



INTERNATIONAL DOCTORAL
SCHOOL OF THE USC

Miguel
Huidobro García

PhD Thesis

Skyrme Neutron Stars

Santiago de Compostela, 2023

Doctoral Programme in Nuclear and Particles Physics

Skyrme Neutron Stars

Miguel Huidobro García



Escuela de Doctorado Internacional de la Universidad de Santiago de
Compostela

Programa de Doctorado en Física Nuclear y de Partículas

Octubre 2023

Supervisor Doctoral:
Christoph Adam

*To my dear mother and sister,
and to my inexhaustible source of
encouragement and happiness, Elena.*

Acknowledgements

Quisiera agradecer en primer lugar a mi director, Christoph Adam, por el apoyo y dedicación recibidos a lo largo de estos últimos años. Con él comencé mi carrera investigadora desde que llegué a Santiago de Compostela, y desde el principio me ayudó a introducirme en este campo de estudio y a plantearme las preguntas que dieron lugar a los resultados obtenidos en esta etapa de mi vida. También debo agradecer, con especial dedicación, a la memoria de Ricardo Vázquez, quien me ayudó también desde el principio y fue un pilar fundamental en mi formación. De él aprendí a enfocar la resolución de la mayoría de los problemas expuestos en esta tesis, siempre con una admirable intuición sobre la física de esos problemas.

A mis colaboradores, pero ante todo buenos amigos, Andrzej, Carlos y Kasia por todas las conversaciones compartidas, tanto sobre física como personales, y hacerme sentir en Cracovia como en casa. Muchas gracias, dziękuję bardzo!

Thanks also to the whole Solitons at Work community for their insightful talks and fruitful discussions. Specially to Paul Leask, with whom I shared great moments and enriching ideas.

Gracias a las personas que me acogieron desde mi llegada a Santiago y con las que he compartido buenos momentos durante estos cuatro años: Manuela, Baladrón, Rivadulla, Gabri y Marcos. También agradecer a quienes me apoyaron desde la distancia, a mi gente, mis chavales: Pablo, Rafa, Diego, Sergio, Bea, Sierra, Héctor, Tomás y Arem. Volver a Gijón con ellos era un verdadero respiro y un impulso para llegar hasta aquí.

Indudablemente debo agradecer a mi familia, concretamente a mi madre y mi hermana, por confiar en mí y apoyarme en todo momento a lo largo de mi vida, realmente os lo debo todo a vosotras. También quiero darle las gracias a la persona que me ha apoyado diariamente, ha vivido toda esta experiencia conmigo y con la que he podido hacer de Santiago mi hogar en estos cuatro años, Elena. Eres una parte fundamental de esta etapa y de mi vida, esta tesis es gracias a ti.

Por último, estos agradecimientos están especialmente destinados para mis compañeros y hermanos en esta experiencia, Alberto y Jorge, sin los que esta tesis tampoco hubiera sido posible. Trabajar con vosotros estos años ha sido un verdadero privilegio, pero sin duda sois dos de las mejores personas que he tenido la suerte de encontrar en mi vida. Me llevo innumerables recuerdos de mi etapa en Santiago que me acompañarán siempre, y en todos ellos estáis vosotros.

Esta tesis ha sido realizada bajo la financiación de la actividad predoctoral a través del Programa de ayudas a la etapa predoctoral 2021 por la Xunta de Galicia (Consellería de Cultura, Educación y Universidad).

Abstract

The description of nuclear matter at high densities, reached in the cores of neutron stars, has become one of the major problems in both experimental and theoretical physics. In this thesis we consider the Skyrme model and its generalizations to reproduce the state of nuclear matter at such densities and the macroscopic properties of neutron stars.

We start in the Introduction with a complete and detailed overview about the physics of neutron stars. First, the concept of a neutron star as one of the possible final fates of the very massive stars is introduced. Then, a brief explanation on the consecutive stages of the core-collapse of the progenitor star is given to present one of the most violent processes in our universe, the supernova explosions. The entire mechanism of supernovae is not included, since it mainly involves neutrino physics, which will not be studied in this thesis. Instead, we rather focus on the general properties of neutron stars. At this point, we mention the typical masses and sizes of neutron stars to establish the physical scales of our problem. Further interesting phenomenology of neutron stars, like rotational velocities or strong magnetic fields, is mentioned and quantified to show the extreme conditions reached in these objects. To end this first introductory part, we explain how the URCA processes rapidly cools down the newly born stellar object to yield a (relatively) cold neutron star, whose description is one of the main objectives of this thesis.

The following entire subsection is devoted to present the prevailing description of the interior of neutron stars based on five different layers. An extensive outline on the size and chemical composition of each layer is given, with a complementary scheme depicted in the text. We remark that the outermost parts are essential for the experimental observations of neutron stars, but they are already well determined from hadronic physics reproducible in terrestrial experiments. Nevertheless, these regions only represent less than a 1% of the total neutron star. At the neutron drip density, the matter adopts different geometries called the nuclear pasta phases, and for larger densities, the equation of state is mainly determined by theoretical simulations. Deeper inside the

neutron star, the nuclei dissolve into free neutrons, protons and leptons in equilibrium under the beta decay and charge neutrality conditions. In the innermost region, the extreme conditions attained hide the specific state of nuclear matter within our current knowledge, but the different possible scenarios are explained. Among them, the kaon condensation in neutron star cores will be considered in the last chapter of this work.

In the next subsection, we comment the evolution of neutron stars throughout the history since their first accepted proposal by Baade and Zwicky in 1934 until the breakthrough discovery of pulsars by J. Bell and A. Hewish. Besides, soon after the works of Baade and Zwicky, the theoretical contributions of Tolman, Oppenheimer and Volkoff (TOV) established the theoretical framework to obtain neutron star solutions from any equation of state for nuclear matter. Indeed, the TOV formalism is used several times throughout this thesis, therefore, it is explained in Appendix B. Eventually, we mention the current theoretical works on neutron star physics, focused on the description of nuclear matter at such high densities and the experimental techniques which are the source of information for the neutron star observables in the present.

In the second chapter, we present and motivate the Skyrme model and its generalization as a theory of nuclear matter and, in particular, for the study of neutron stars. First, we introduce the historical context in which the Skyrme model was proposed. The main feature of this model is the existence of stable topological solitons, called skyrmions, which are identified with atomic nuclei. We present the Lagrangian density, built from two interactions term and a $SU(2)$ group element field which carries three degrees of freedom identified with the pions. The mathematical arguments to understand the existence of the skyrmions are given, but the model is mainly introduced from the physical and modern point of view of low-energy effective field theory of QCD. Furthermore, the energetical stability of the solitons is carefully analyzed, from which the notion of the BPS energy bound is introduced.

The simplest skyrmion is characterized by the topological number $B = 1$ and spherical symmetry, it is aimed to represent the classical state of the proton and neutron. The parametrization of this field configuration is given by the hedgehog ansatz, and yields a single ordinary differential equation of second order. The resolution of this field equation is explained in the text, but an alternative approach based on spectral methods is studied in the Appendix A. Then, the parametrization of larger B skyrmions, out of spherical symmetry,

is performed through the rational map approximation, however, the resulting solutions yield too large binding energies and unrealistic energy density configurations. Additionally, since protons and neutrons are spin and isospin 1/2 quantum particles, the inclusion of these effects is an important step that must be considered in the Skyrme model. The quantization procedure of skyrmions relies on a semiclassical approximation in which the quantum corrections to the energy are obtained from the classical configuration, and the possible quantum states are determined by the symmetries of the specific solution, as stated by Finkelstein and Rubinstein. The introduction to the standard Skyrme model ends up with the inclusion of a pion mass potential term which not only yields a more realistic model, but also improves on some of the incorrect properties of the previous solutions.

A brief outline on the first attempts to construct neutron star solutions is presented in subsection 2.1.2. Although the results were completely unrealistic, the study of neutron stars within the Skyrme model motivated the development of a new kind of low-energy crystalline solutions by Klebanov. Different periodic solutions were proposed and the observables of the neutron stars computed from Skyrme crystals sharply improved, but still the masses were small compared with experimental observations.

The next section is aimed at introducing another Skyrme-based model with a different Lagrangian, composed of a generic potential term and a new term with six derivatives of the Skyrme field. Skyrmions may be obtained from this new model too, and the main property is that they saturate the corresponding BPS energy bound, hence, it is called the BPS model. Despite this model is not physically motivated, the mathematical structure and the great improvement on the solutions have crucial phenomenological implications.

We review the computations of neutron stars within the BPS model for different potentials and compare them with the low-mass standard Skyrme model solutions. Besides, due to the BPS model stress-energy tensor, we may compare between the neutron stars obtained from a full theoretical computation and from the TOV formalism under a mean-field approximation. The high values for the maximum masses of the BPS neutron stars motivate the combination of the two models for an accurate description of highly dense matter from a generalized Skyrme model, which is the seed of this research work.

The first novel research work is shown in subsubsection 2.2.1.1, where BPS neutron stars are coupled to a modification of General Relativity. More specifically,

a new term quadratic in the Ricci scalar is introduced in the Einstein-Hilbert action, motivated as a higher order correction given that the intense gravitational fields convert neutron stars into ideal scenarios to detect these high curvature effects. Although this modification is the simplest choice, the difficulty in the resolution of the problem sharply increases. Nevertheless, solutions are found and the implications on neutron star observations are discussed.

The last section of Chapter 2 introduces a generalization of the Skyrme model, based on the combination of the BPS and standard Skyrme submodels. As a natural starting point, we compute the $B = 1$ skyrmion for different values of the sextic term coupling constant. The pion mass is fixed to the physical value, but the other parameters are fitted to the proton and Δ excitation masses using an iterative method after the quantization of spin and isospin degrees of freedom. For completeness, we also compute the classical energies of the firsts four skyrmions to study the impact of the sextic term on isolated solutions. Finally, the chapter is concluded with an effective analysis about the neutron stars within the generalized Skyrme model. We construct a complete EOS consistently from scaling arguments supported by the results from both submodels explained throughout the entire chapter. The remarkable results on the mass, radius and tidal deformability of the neutron stars are a great motivation to study full theoretical crystal solutions in the generalized Skyrme model.

In Chapter 3, we focus on the construction of Skyrme crystals in order to establish the basis for the description of neutron stars. First, the concept of Skyrme crystals is explained, and we remark that topological solitons are still allowed despite the boundary conditions have changed. The energy of these solutions is obviously infinite, but the structure may be divided into finite-size unit cells with well determined energy and baryon number, such that the energy per baryon number of the whole crystal remains finite.

We follow the Kugler and Shtrikmann approach to construct crystal solutions. The idea consists in the expansion of the fields in truncated Fourier series, such that the coefficients are varied in order to minimize the energy functional. In this way, the scenario is directly translated into a finite-dimensional minimization problem which, indeed, does not require a very large number of coefficients. However, the centre of the skyrmions is fixed such that they cannot move freely in this approach, so we still have to find their optimal distribution and orientation within the unit cell. Different field configurations were studied since the first simple cubic symmetry proposed by Klebanov, we review the symme-

tries and explain how they can be easily implemented in the Fourier expansion formalism.

The minimization of the energy functional implies the simultaneous multidimensional variation of the coefficients, so we first consider the simplest case with two coefficients to develop the numerical algorithm. More coefficients are gradually added, and a fast convergence in the energy is observed, so we fix the final number of coefficients (around 30) for each symmetry by comparing with the original values obtained by Kugler and Shtrikmann. The philosophy of the minimization algorithm is described and the numerical details are also given, then, it is applied for different sizes of the unit cell to obtain the values of the energy. In this way, the energy is obtained as a function of the lattice length (L) and it is parametrized using scaling arguments for an analytical treatment which is extremely useful. The energy curve always takes a minimal value, called the equilibrium, and it grows for smaller values of the lattice length, being equivalent to compress the system. For larger values of L , the energy also increases, generating an unphysical region with negative pressure, but this only indicates that our description is still classical and further effects must be included.

Throughout this study we observe an interesting property of the energy curve, which becomes crucial for the subsequent fit of the parameters. The accuracy of the fit proposed for the energy suggests that each term in the Lagrangian may be actually fitted independently by its own scaling behaviour. Following this idea, we obtain a simpler and universal parametrization of the energy curve which also accounts for a wide range of the parameters without performing the minimization explicitly. This “perfect scaling” is indeed quite accurate at the minimum of energy.

In section 3.2 we introduce the concept of infinite nuclear matter, which is the physical system that we want to describe using Skyrme crystals. The identification of the minimum of energy with the nuclear saturation point fixes the energy and length scales of the crystals. To reproduce these values, we fit the parameters of the standard Skyrme model for different values of the sextic term coupling constant using the perfect scaling approximation. Then, we compute the energy curves for the different crystals in a broad range of densities (or equivalently lattice lengths). The results are carefully analyzed in order to find the ground state at the equilibrium, and also the numerical values at the minimum are given, as well as the coefficients from the parametrization of the

energy curve.

Additionally, the possible phase transitions between the symmetries are extensively studied. At high densities we find a transition of the crystal into a fluid-like behaviour, due to the presence of the sextic term. Another transition between the FCC and BCC symmetries, already noticed by Kugler and Shtrikmann, is found, but we extend the study including the impact of the sextic term on the transition density, and the details to consistently reconstruct the whole energy curve are also given. At low densities we find a second order phase transition from the FCC crystal to its half-skyrmion version. However, it is observed that the FCC crystal is not the true ground state at low densities, instead, a new kind of crystalline solutions are found to be the correct low energy solutions. These new lattices are obtained locating a $B = 4$ skyrmion in the center of a unit cell and imposing periodic boundary conditions. In this way, a lower value of the energy in the $L \rightarrow \infty$ limit is obtained, which is further decreased with the computation of the $B = 32$ and $B = 108$ lattices. The inclusion of these lattices have motivated the study of a new phase transition from infinite nuclear matter into isolated nuclei within the Skyrme model. This is, indeed, a unique property of this model and the final goal of every nuclear model, *i.e.*, a complete description of nuclear matter in the whole range of densities. Under this assumption we try to reproduce the surface energy coefficient in the semi-empirical mass formula. In fact, we construct a consistent argument to identify this contribution in the energy of Skyrme crystals, and the geometry of these lattices predict the correct scaling with the baryon number, however, the obtained value is much larger than the experimentally determined one.

This chapter ends with the construction of the EOS from the Skyrme crystals, considering the different phase transitions studied before, and the resolution of the TOV system to obtain neutron stars solutions. The results confirm that the sextic term is crucial for a correct description of neutron stars, besides, it also has an interesting impact on the speed of sound. The masses obtained agree with the experimental observations, but the radii are slightly higher than the expected values. Therefore, this chapter represents the starting point for a realistic and consistent description of neutron stars within the Skyrme model.

In Chapter 4, we focus on the introduction of new particle species. The first step is the inclusion of isospin quantum effects in Skyrme crystals, as we did with isolated skyrmions in the second chapter. These effects are, actually, of great importance for neutron stars since they account for the difference in en-

ergy between protons and neutrons. Then, the quantization procedure is again reviewed and we obtain the expression of the Hamiltonian for these quantum effects in the Skyrme crystals. The isospin energy will depend on the lattice length, through the isospin inertia tensor, and on the specific quantum state of the crystal. We compute the isospin tensor curve similarly to the classical energy, and we explain how the possible quantum states of the crystals are obtained from the Finkelstein-Rubinstein constraints. For this purpose, an additional approximation is required due to the infinite size of the crystal. Among the states, we find the charge neutral case, however, it is definitely not the most realistic case since we expect to have a small proton fraction inside neutron stars (despite their name). The problem is that the small number of baryons within the unit cell only allows for some specific number of protons which are not realistic either.

This fact motivates a further approximation in which a larger chunk of crystal is considered. In this approximation, we obtain the isospin energy contribution as a function of the density and proton fraction, from which we identify the symmetry energy curve. This curve has been extensively studied in nuclear physics, and it has great implications on the description of neutron stars since it is responsible for many important effects. The symmetry energy has also been tightly constrained from theoretical and experimental results, we give the most fiducial values and compare them with those obtained from Skyrme crystals. This new observable has important implications since it has never been determined in the Skyrme model and it may be used to fix the sextic term parameter. Moreover, it enables the introduction of protons and leptons in the EOS, imposing charge neutrality and beta equilibrium. We computed the symmetry energy curve for several values of the parameters and found that it may be accurately reproduced using Skyrme crystals. Furthermore, the symmetry energy curve in the FCC crystal presents the transition to finite nuclear matter since the same asymptotic behaviour is found in the large L limit. Indeed, the FCC crystal yields remarkable results for the curve in the whole range of densities, even the asymptotic value is close to the semi-empirical mass formula coefficient in the asymmetry term contribution. Additionally, we find the desired behaviour of the isospin energy curve in the low density regime when realistic neutron star matter is considered, however, the classical contribution deteriorates the total energy curve.

We end this section with an extensive analysis of the parameters using the perfect scaling approximation. The introduction of the symmetry energy in

the Skyrme model allows to completely determine all the parameters in the model, hence, it is interesting to check the possibility to reproduce all the observables within the model and still have physically acceptable neutron stars. From this analysis we find difficulties to satisfy all the conditions with arbitrary accuracy, but we find some interesting conclusions on the values of the sextic term coupling constant, the speed of sound and the masses and radii of the neutron stars.

In the next section we consider the possibility to develop a kaon condensed core in neutron stars. This task is addressed using the Callan and Klebanov approach which naturally introduces the strange degrees of freedom perturbatively in a $SU(3)$ -extended Skyrme field. The interactions between kaons and pions are directly given by the model itself, therefore, the final Lagrangian is purely within the Skyrme model with no *ad hoc* extra fields. We follow the standard procedure for the condensation of a scalar field and obtain the contribution to the energy from the kaon condensed field. Then, the isospin degrees of freedom of the whole system (including kaons) are quantized in order to study the impact of kaons on the particle fractions. The quantization procedure is the same, but an additional term is introduced in the energy contribution. Given that the system is more complicated than in the previous section, we must build the thermodynamical grand potential to obtain the equilibrium conditions. The density at which kaons become energetically favourable is computed using four different sets of parameters obtained from the last section, then, the total energy is calculated and we find that the impact of kaons on the Skyrme crystals produces a first order phase transition. In this case, the presence of two conserved charge requires a Gibbs construction to reconstruct a physically acceptable energy curve. Finally, the Skyrme $npe\mu$ with kaon-condensed core EOS is shown and also the mass-radius curves for the resulting neutron stars.

The last result in this chapter is the impact of ρ mesons in the Skyrme lattices with the aim of solving one severe problem in the description of nuclear matter within the Skyrme model, the compression modulus value. We first motivate the inclusion of vector mesons with similar computations carried out in the past. Next, we present the compression modulus, how it is measured, the accepted experimental value and we show the values obtained for the Skyrme crystals computed in the second chapter. Additionally, we argue that the deviations from the correct value are not the result of a wrong set of parameters, but are indeed a problem of the crystal solutions. Then, we motivate the interaction term between ρ mesons and pions, and obtain the energy contribution

and the corresponding Euler-Lagrange equations. A remarkable feature of this interaction is that we may still identify an energy bound for the whole system. Eventually, we show the energy curves of the α -lattice coupled to ρ mesons and the great improvement on the compression modulus value.

Finally, we end with some concluding remarks and additional ideas to extend the research developed throughout this thesis.

Contents

Acknowledgements	I
Abstract	III
Abbreviations	XXIII
List of Publications	XXV
Scope and Methodology	XXIX
1 Introduction	1
1.1 Neutron Stars	1
1.1.1 Structure of Neutron Stars	4
1.1.2 History of Neutron Stars	6
1.2 Current status of Neutron Stars physics	8
1.2.1 Theoretical approaches	9
1.2.2 Experimental detections	11
2 The Skyrme model	15
2.1 The standard Skyrme model	16
2.1.1 Introducing the pion mass	24
2.1.2 Neutron stars in the standard Skyrme model	26
2.2 The BPS Skyrme model	28
2.2.1 Neutron stars in the BPS Skyrme model	34
2.2.1.1 BPS Skyrme neutron stars in modified gravity .	41
2.3 The generalized Skyrme model	56
2.3.1 Neutron stars from a Generalized Skyrme EOS	61
3 Skyrme Crystals	74
3.1 Construction of Skyrme crystals	76
3.1.1 Perfect scaling property	84

3.2	Infinite nuclear matter from Skyrme crystals	86
3.2.1	Comparison between the symmetries	89
3.2.2	Phase transitions	92
3.2.2.1	High density phase transitions	92
3.2.2.2	Low density phase transitions	97
3.3	Neutron stars from generalized Skyrme crystals	103
4	Neutron Star matter in the Skyrme model	109
4.1	Quantization of Skyrme crystals	109
4.1.1	Symmetry energy	115
4.1.2	Realistic $npe\mu$ matter in Skyrme neutron stars	121
4.1.3	Analysis of the parameters	127
4.2	Kaon condensation in Skyrme neutron stars	134
4.2.1	The Bound-State approach of the Skyrme model	135
4.2.2	Kaon condensation in neutron star cores	141
4.3	The inclusion of ρ mesons in the Skyrme model	149
4.3.1	The compression modulus problem	151
4.3.2	Skyrme α -lattice coupled to ρ mesons	153
5	Conclusions and Outlook	161
A	$B = 1$ skyrmion from Spectral Methods	165
B	The TOV formalism	173
C	Gradient Flow methods in the Skyrme model	179
	Bibliography	185

List of Figures

1.1	Depiction of the internal composition by layers of a neutron star.	5
2.1	<i>Left:</i> The EOS for the different models considered so far, in the MF and FT approaches. In the FT cases we considered the EOS resulting from the maximal mass stars. <i>Right:</i> The MR curves from the same models.	39
2.2	Global $\rho_c(p_c)$ EOS for the two potentials from the FT cases in the BPS Skyrme model which determines the presence or not of a crust. We also added three EOS corresponding to NS solutions of different mass.	40
2.3	Profile functions of the solutions obtained from the TOV system for a single NS. Here we compare between three extremely different EOS and a realistic nuclear physics EOS.	41
2.4	$M_{ADM}R$ curve in the MF, for three different potentials, and for different values of α in units of km ²	48
2.5	The same MR curve of Fig. 2.4 in the FT cases.	48
2.6	The ADM mass as a function of the central energy density, for the MF case. It can be clearly seen that for a fixed ρ_c the mass decreases with increasing α for small masses, but increases with increasing α for large masses. The maxima of the curves correspond to the value of p_c where the unstable branch starts. . . .	49
2.7	The same curves of Fig. 2.6 for the FT cases. The same conclusions may be extracted, however, solutions in the unstable branch cannot be found.	50

2.8	Mass function vs radius, for the MF case. For each potential, the solutions are for a fixed value of p_c which is sufficiently large to lead to a rather large mass but, at the same time, sufficiently small such that all solutions belong to the stable branch. The vertical dashed lines indicate the NS radii for different α , which turn out to be very similar.	52
2.9	The surface mass as a function of the NS radius, for the MF case. It can be clearly seen that the surface mass for a given radius shrinks with increasing α	52
2.10	The Ricci scalar as a function of the radius, for the MF case. The solutions are for the same fixed values of p_c as in Fig. 2.8. The Ricci scalar suddenly jumps from a non-zero value to zero in the GR case, but is continuous at R_s for $\alpha > 0$. Again, the vertical dashed lines indicate the NS radii for different α , which turn out to be very similar.	53
2.11	The Newtonian mass at the surface as a function of the star radius, for the MF case. For a fixed radius, it grows with α for small stars but shrinks for large stars.	54
2.12	Radial profile function of the $B = 1$ skyrmion in the generalized Skyrme model for different values of the sextic term coupling constant in units of MeV fm ³	61
2.13	Energy density contour plots in three dimensions of the first four skyrmions. We adopt the Runge colouring convention to represent the orientations of the pion fields.	62
2.14	Speed of sound of the generalized Skyrme EOS (2.90) for different values of the interpolating parameter. The red curves represent (unphysical) superluminical sound velocities, whilst the green curves correspond to acceptable curves.	66
2.15	Comparison of the energy and baryon densities of the Generalized and Hybrid EOS from the Skyrme model with other standard nuclear physics EOS.	68
2.16	MR relation for the hybrid model (red curves) for different combinations of values of $p_* = 0.5, 1, 2$ MeV/fm ³ and $p_{PT} = 25, 40, 50$ MeV/fm ³ . The red shaded region corresponds to the accessible region of the hybrid model with p_* and p_{PT} within the given ranges.	69

2.17	$\tilde{\Lambda}$ as a function of the mass ratio. The orange shaded regions correspond to the 50% (dark) and 90% (light) credible regions for the joint posterior of $\tilde{\Lambda}$ and q as obtained in [3] assuming a low spin prior. The notation for the curves are: Gen ^{p_{PT}} , Hyb ^{p_{PT}} _{p_*} .	70
2.18	$\tilde{\Lambda}(q)$ curves for the EOS considered throughout this chapter with the same GW170817 constraints as in Fig. 2.17.	72
3.1	Top: The 3D energy density plot of the BCC unit cell with $B_{\text{cell}} = 8$. We adopt the Runge colouring convention [91] in this figure to represent the pion fields. Bottom: Energy density contour plots in two dimensions at $z = 0$, $L/4$ and $L/2$ respectively.	79
3.2	Top: The 3D energy density plot of the FCC unit cell with $B_{\text{cell}} = 4$. The colours follow the Runge colouring convention. Bottom: Energy density contour plots in two dimensions at $z = 0$, $L/2$ and L respectively, since the energy density has double the period of the previous crystal.	81
3.3	Top: The 3D energy density plot of the FCC _{1/2} unit cell with $B_{\text{cell}} = 4$. The pion fields are represented following the Runge colouring convention. Bottom: Energy density contour plots in two dimensions at $z = 0$, $L/4$ and $L/4$ respectively, as in the BCC crystal.	82
3.4	Energy per baryon number curves against the lattice length L of the FCC _{1/2} crystal. The circles are the full-numerically minimized values of the energy, the solid lines are the PS approximation curves, and the dots were obtained from the Castillejo ansatz for the fields.	85
3.5	Energy per baryon as a function of the lattice length parameter for the three different crystal symmetries considering the four relevant Skyrme models. The horizontal dashed line represents BPS bound of each model for the specific choice of parameters in each case. The energy and length are both given in adimensional units (2.8).	90
3.6	Ratio between the REPs for the crystal and the fluid at different densities with and without sextic term. The coordinate \bar{r} has been defined as the radial coordinate rescaled by the lattice length.	93

3.7	Comparison between the energies of the BCC and FCC _{1/2} crystals at the same baryon density, showing the phase transition point, denoted by the red cross in the plots. Both n_B and E are shown in Skyrme units.	95
3.8	Mean value of the σ field within the unit cell shows the second order transition from the FCC to the FCC _{1/2} crystal when the pion mass term is not included, and the asymptotic approach when it is included.	98
3.9	Energy per baryon number for the different crystals and lattices considered in this work in the \mathcal{L}_{240} model. The large difference in energy between these lattices and the FCC crystal that indicate the correct ground state is clearly observed. However, the convergence to the same FCC _{1/2} crystal is observed slightly above the minimum.	100
3.10	Energy density contour of the $4N_\alpha^3$ lattices at different sizes of the unit cell. The colours represent the same values as in Fig. 3.3. Here, the transition to the the FCC _{1/2} crystal is visible, whereas the isolated skyrmion is recovered for large values of L	101
3.11	Surface energy of the isolated $4N_\alpha^3$ skyrmions fitted to the semi-empirical mass formula surface term expression.	102
3.12	<i>Top left:</i> The full Skyrme crystal EOS including the possible phase transitions in the different submodels. <i>Top right:</i> The speed of sound obtained from each EOS. <i>Bottom:</i> The MR curves obtained solving the TOV system of equations.	106
4.1	Symmetry energy curve of the Skyrme crystals studied in the previous chapter. We also added a new case (black solid (FCC _{1/2}) and dashed (FCC) lines) which reproduces S_0 , L_{sym} and K_{sym} using the standard parameters (2.21) and $\lambda^2 = 1.5$. The red shaded region comes from the IAS constraints for the symmetry energy obtained from [84], whilst the green area represents the suprasaturation constraints from the GW170817 event analysis [144].	119

4.2	<i>Left:</i> Symmetry energy curves for the α -lattice, FCC crystal and its half-skyrmion version. Here, the transition to finite nuclear matter in the FCC and α -lattice is observed. <i>Middle:</i> . Particle fractions obtained for the α -lattice, with the limits expected from the analysis of (4.37) <i>Right:</i> The total (classical and isospin) energy of the three crystalline configurations for realistic $npe\mu$ matter.	126
4.3	Isospin inertia moment curve of the $FCC_{1/2}$ Skyrme crystal with and without sextic term. We show the numerical data (dots), fitted via the parametrization (4.12) (dashed lines) and the PS approximated curve (solid lines). The minima of the energy curves are represented by the crosses, where the PS is still an accurate approximation.	129
4.4	Symmetry energy of Skyrme crystals as a function of the density. We show 23 different curves from the scanned values. The shaded regions constrains the symmetry energy at sub-saturation [84] and supra-saturation [144] densities.	130
4.5	The EOS for the same 23 values shown before. In black we plot the resulting EOS without isospin effects, whilst in red we consider $npe\mu$ matter. We find a good agreement between our EOS and the shaded regions obtained from the analysis in [30] at high densities. The purple region is an estimation for the range of the maximum central density inside NS, and the dots represent the maximum central energy densities in our models.	131
4.6	MR curves for the 23 representative sets of parameters considered. The colours of the lines represent the same as in Fig. 4.5. The shaded regions correspond to GW (blue and orange) and pulsar (green) constraints.	133
4.7	<i>Left:</i> Energy vs lattice length for the set 1 of parameters. The energy is shown for the classical crystal without isospin contributions (green), isospin asymmetric ($npe\mu$) matter with (black) and without (blue) kaons. We also plot the completely asymmetric neutron matter (magenta) which lies slightly above the blue curve. <i>Right:</i> Particle fractions as a function of baryon density for the set 1 of parameters, both with (solid lines) and without (discontinuous lines) kaon condensate.	144

4.8	Symmetry energy of nuclear matter as a function of baryon density for the sets of parameters considered in this work. The thick line represents the symmetry energy when kaons are considered in the system and the dashed line does not include kaons.	145
4.9	<i>Left:</i> Energy per baryon against the side length of the unit cell and their interpolations. <i>Right:</i> pressure against the energy density, from which we conclude that there is a first order phase transition. Both plots are for the set 1 of parameters.	146
4.10	<i>Left:</i> $E(L)$ curves for the two phases and the two different constructions, for set 1 of the parameter values. <i>Right:</i> MR curves of NS with a kaon condensed core. The different sets of parameters that we consider are shown with different colors. Solid lines represent $npe\mu$ matter, dashed-dotted lines are obtained with a MC and the dashed with the GC.	149
4.11	<i>Left:</i> Adimensional energy of the α -lattice for different values of the coupling with the ρ mesons. <i>Right:</i> The same curves when the minimum of each curve is fitted to the nuclear saturation point.	157

List of Tables

2.1	Exact case: values of the NS radii and the central energy densities for the maximum mass stars for the two potentials considered, and the corresponding values of α	50
2.2	Mean-field case: values of the NS radii and the central energy densities for the maximum mass stars for the three potentials considered, with the corresponding values of α	51
2.3	Sets of parameters that fit the $B = 1$ solution to the masses of the proton and the Δ excitation.	60
2.4	Energy per baryon number and corresponding binding energies for the first four ground state skyrmions in the generalized model. We also included the binding energies of the same solutions in the standard Skyrme model for comparison.	61
3.1	Fitting constants for the PS approximated curves	86
3.2	Values for the parameters of the generalized Skyrme model that fit the minimal energy point of the $\text{FCC}_{1/2}$ crystal to the nuclear saturation point.	88
3.3	$\text{FCC}_{1/2}$ crystal fit coefficients.	90
3.4	BCC crystal fit coefficients.	90
3.5	$\text{FCC}_{1/2}$ crystal values at the minimum of energy.	90
3.6	BCC crystal values at the minimum of energy.	90
3.7	Ratio between the transition density and the density at which the minimum of the energy of the $\text{FCC}_{1/2}$ crystal is achieved. . .	96
4.1	Experimental values for the symmetry energy curve multipoles at the saturation density.	117
4.2	Values of the symmetry energy curve multipoles at saturation for the sets of the parameters given in Table 3.2 and a new set with the standard parameters of [29].	120

4.3	Values of the INM observables obtained from the α -lattice using the set of parameters (4.42). We include in the last column the asymptotic value of the symmetry energy curve.	126
4.4	Perfect scaling parametrization constants of the isospin inertia tensor	129
4.5	Sets of parameter values obtained from the extensive analysis in the last subsection and their corresponding observables at nuclear saturation.	143
4.6	Values for the compression modulus for the crystals studied in Chapter 3.	152
4.7	Values of the adimensional coupling constant between ρ mesons and pions with the corresponding values of the compression modulus and energy ratio. In the third column we show the value of the compression modulus once the minimum has been shifted to the saturation point. In the last two columns we compute the difference between the minimum and the $L \rightarrow \infty$ asymptotic energy and the corresponding value of the physical coupling constant, respectively.	158

Abbreviations

AGD	Accelerated Gradient Descent
BCC	Body Centered Cubic
BCPM	Barcelona-Catania-Paris-Madrid
BPS	Bogomol'nyi-Prasad-Sommefield
EFT	Effective Field Theory
EH	Einstein-Hilbert
EHS	Einstein-Hilbert-Skyrme
EOS	Equation Of State
ETG	Extended Theories of Gravity
FCC	Face Centered Cubic
FR	Finkelstein-Rubinstein
FT	Full Theory
GC	Gibbs Construction
GR	General Relativity
GW	Gravitational Waves
IAS	Isobaric Analog States
INM	Infinite Nuclear Matter
LIGO	Laser Interferometry Gravitational-waves Observatory
MC	Maxwell Construction
MF	Mean-Field
MR	Mass-Radius
NLSM	Non-Linear Sigma Model
NS	Neutron Star
NICER	Neutron Star Interior Composition Explorer
ODE	Ordinary Differential Equation
PN	Post-Newtonian
PS	Perfect Scaling

QCD	Quantum Chromodynamics
QFT	Quantum Field Theory
REP	Radial Density Profile
TOV	Tolman-Oppenheimer-Volkoff
VEV	Vacuum Expectation Value
VPD	Volume-Preserving Diffeomorphisms
WZW	Wess-Zumino-Witten

List of Publications

The research work elaborated throughout this PhD resulted in 13 peer-reviewed publications in total. Some of the results presented in this thesis have been reproduced from these publications, the details of the articles are listed below.

Publications reproduced in this thesis

Title: BPS Skyrme neutron stars in generalized gravity
Authors: Christoph Adam ^a , Miguel Huidobro ^a , Ricardo Vázquez ^a , Andrzej Wereszczynski ^b
^a Departamento de Física de Partículas, Universidad de Santiago de Compostela and Instituto Galego de Física de Altas Enerxías (IGFAE) E-15782 Santiago de Compostela, Spain
^b Institute of Physics, Jagiellonian University, Lojasiewicza 11, Kraków, Poland
Journal and article information
Name: Journal of Cosmology and Astroparticle Physics
Publisher: IOP Publishing and SISSA
Date of publication: 24 August 2020
ISSN: 1475-7516
DOI: 10.1088/1475-7516/2020/08/041
Impact Factor: 5.84 (2020)
Contribution from the PhD student: Development of algorithms for analytical and numerical computations, elaboration of the figures displayed in the manuscript and contribution to its writing.
The results from this article are reproduced in Chapter 2, subsubsection 2.2.1.1, with the author permissions from the JCAP journal

Title: A new consistent neutron star equation of state from a generalized Skyrme model
Authors: Christoph Adam ^a Alberto García Martín-Caro ^a Miguel Huidobro ^a ; Ricardo Vázquez ^a Andrzej Wereszczynski ^b
^a Departamento de Física de Partículas, Universidad de Santiago de Compostela and Instituto Galego de Física de Altas Enerxias (IGFAE) E-15782 Santiago de Compostela, Spain
^b Institute of Physics, Jagiellonian University, Lojasiewicza 11, Kraków, Poland
Journal and article information
Name: Physics Letters B
Publisher: Elsevier
Date of publication: 10 December 2020
ISSN: 1873-2445
DOI: 10.1016/j.physletb.2020.135928
Impact Factor: 4.77 (2020)
Contribution from the PhD student: Development of algorithms for analytical and numerical computations, elaboration of the figures displayed in the manuscript and contribution to its writing.
The results from this article are reproduced in Chapter 2, subsection 2.3.1, with the standard author permissions from Elsevier

Title: Dense matter equation of state and phase transitions from a generalized Skyrme model
Authors: Christoph Adam ^a Alberto García Martín-Caro ^a Miguel Huidobro ^a ; Ricardo Vázquez ^a Andrzej Wereszczynski ^b
^a Departamento de Física de Partículas, Universidad de Santiago de Compostela and Instituto Galego de Física de Altas Enerxias (IGFAE) E-15782 Santiago de Compostela, Spain
^b Institute of Physics, Jagiellonian University, Lojasiewicza 11, Kraków, Poland
Journal and article information
Name: Physical Review D
Publisher: American Physical Society
Date of publication: 22 April 2022
ISSN: 2470-0029
DOI: 10.1103/PhysRevD.105.074019
Impact Factor: 5.0 (2022)
Contribution from the PhD student: Development of algorithms for analytical and numerical computations, elaboration of the figures displayed in the manuscript and contribution to its writing.
The results from this article are reproduced in Chapter 3, with the standard author permissions from the American Physical Society

Title: Kaon condensation in skyrmion matter and compact stars
Authors: Christoph Adam ^a Alberto García Martín-Caro ^a Miguel Huidobro ^a , Ricardo Vázquez ^a , Andrzej Wereszczynski ^b
^a Departamento de Física de Partículas, Universidad de Santiago de Compostela and Instituto Galego de Física de Altas Enerxias (IGFAE) E-15782 Santiago de Compostela, Spain
^b Institute of Physics, Jagiellonian University, Lojasiewicza 11, Kraków, Poland
Journal and article information
Name: Physical Review D
Publisher: American Physical Society
Date of publication: 10 April 2023
ISSN: 2470-0029
DOI: 10.1103/PhysRevD.107.074007
Impact Factor: 5.0 (2022)
Contribution from the PhD student: Development of algorithms for numerical computations, elaboration of the figures displayed in the manuscript and contribution to its writing.
The results from this article are reproduced in Chapter 4, section 4.2 with the standard author permissions from the American Physical Society

Title: Skyrme Crystals, Nuclear Matter and Compact Stars
Authors: Christoph Adam ^a Alberto García Martín-Caro ^a Miguel Huidobro ^a , Andrzej Wereszczynski ^b
^a Departamento de Física de Partículas, Universidad de Santiago de Compostela and Instituto Galego de Física de Altas Enerxias (IGFAE) E-15782 Santiago de Compostela, Spain
^b Institute of Physics, Jagiellonian University, Lojasiewicza 11, Kraków, Poland
Journal and article information
Name: Symmetries and Ultra Dense Matter of Compact Stars special issue, Symmetry
Publisher: MDPI
Date of publication: 12 April 2023
ISSN: 2073-8994
DOI: 10.3390/sym15040899
Impact Factor: 2.7 (2022)
Contribution from the PhD student: Development of algorithms for analytical and numerical computations, elaboration of the figures displayed in the manuscript and contribution to its writing.
The results from this article are reproduced in Chapter 4, subsubsection 4.1.3 with the standard author permissions from the American Physical Society

Other publications

1. C. Adam, A. García Martín-Caro, M. Huidobro, R. Vázquez and A. Wereszczynski, “Quasiuniversal relations for generalized Skyrme stars”
DOI: [10.1103/PhysRevD.103.023022](https://doi.org/10.1103/PhysRevD.103.023022)
2. C. Adam, A. García Martín-Caro, M. Huidobro, R. Vázquez and A. Wereszczynski, “Quantum skyrmion crystals and the symmetry energy of dense matter”
DOI: [10.1103/PhysRevD.106.114031](https://doi.org/10.1103/PhysRevD.106.114031)
3. C. Adam, J. Castelo, A. García Martín-Caro, M. Huidobro, R. Vázquez and A. Wereszczynski, “Universal relations for rotating boson stars”
DOI: [10.1103/PhysRevD.106.123022](https://doi.org/10.1103/PhysRevD.106.123022)
4. C. Adam, P. Dorey, A. García Martín-Caro, M. Huidobro, K. Oles, T. Romancukiewicz, Y. Shnir and A. Wereszczynski, “Multikink scattering in the ϕ^6 model revisited”
DOI: [10.1103/PhysRevD.106.125003](https://doi.org/10.1103/PhysRevD.106.125003)
5. C. Adam, A. García Martín-Caro, M. Huidobro, K. Oles, T. Romancukiewicz and A. Wereszczynski, “Constrained instantons and kink-antikink collisions”
DOI: [10.1016/j.physletb.2023.137728](https://doi.org/10.1016/j.physletb.2023.137728)
6. A. García Martín-Caro, M. Huidobro and Y. Hatta, “Gravitational form factors of nuclei in the Skyrme model”
DOI: [10.1103/PhysRevD.108.034014](https://doi.org/10.1103/PhysRevD.108.034014)
7. C. Adam, J. Castelo, A. García Martín-Caro, M. Huidobro and A. Wereszczynski, “Effective no-hair relations for spinning boson stars”
DOI: [10.1103/PhysRevD.108.043015](https://doi.org/10.1103/PhysRevD.108.043015)
8. P. Leask, M. Huidobro and A. Wereszczynski, “Generalized skyrmion crystals with applications to neutron stars”
DOI: [10.1103/PhysRevD.109.056013](https://doi.org/10.1103/PhysRevD.109.056013)

Scope and Methodology

The study of neutron stars is crucial for the understanding of the behaviour of nuclear matter at extreme densities (up to ten times the density of atomic nuclei). This information is encoded in the so-called equation of state, which is the relation between the pressure applied on a system and its density. At low densities, the equation of state is completely determined by terrestrial experiments, but its extension to higher densities must lead to neutron star observables that agree with astrophysical measurements.

Since the number of neutron star observations, as well as their accuracy, is still low, it is important to obtain the maximal possible amount of observables from simulations and the comparison between different theoretical models. In this thesis, we will extract the results from the Skyrme model because of its natural and inherent description of nuclear matter.

It is also known that, despite their name, neutron stars are not completely made up of neutrons, but protons and leptons are present. Indeed, the number of protons is mainly determined by the symmetry energy, hence, it is a crucial ingredient for a realistic description of matter inside neutron stars. Besides, recent progress in the determination of the symmetry energy from different experiments and theoretical analyses may establish this observable as a new source of information to constrain the Skyrme model.

Finally, one of the main problems in neutron stars physics is known as the hyperon puzzle. This is related to the possible appearance of strange degrees of freedom inside neutron stars at high densities, implying a sharp reduction of the masses and radii. This effect rules out many equations of state from the list of possible candidates to describe nuclear matter at high densities. Besides, the inclusion of strangeness is highly non-trivial in some models, and it is interesting to study how they can be included in the Skyrme model. Furthermore, once these new degrees of freedom are included, the kaon condensation in the core of neutron stars has a similar impact, and its formation is also of great interest.

The previous physical motivations establish the following main goals for this thesis:

1. The understanding of the Skyrme model and its generalization as a nuclear theory and its motivation for the description of neutron stars.
2. Computation of crystal configurations from the generalized Skyrme model for a first classical description of the mass and radius of neutron stars.
3. Addition of isospin effects and leptons to obtain a realistic description of nuclear matter inside neutron stars and the computation of the symmetry energy, which has never been obtained from the Skyrme model.
4. Inclusion of strangeness in the equation of state, without any *ad hoc* extra fields but purely within the Skyrme model to predict the density at which kaons condense inside neutron stars.
5. Extend the Skyrme model with the addition of ρ mesons to solve the compression modulus problem in the description of infinite nuclear matter.

The methodology to carry out the goals presented above consists of the following steps:

Bibliographic revision: The study of topological soliton solutions is an interesting task in many different models due to their properties. To get familiarized with these solutions and with the aim of obtaining them in extensions of the Skyrme model, it is important to review the previous works in which they were obtained in the same context.

Conversely, it is important to understand which observables can be extracted from nuclear terrestrial experiments and astrophysical events, and how they are computed from theoretical models. Hence, the study of the nuclear matter behaviour at low densities as well as how it is extrapolated and constrained to higher densities is of great importance.

Development of symbolic and numerical codes to setup and solve the problem: The problems presented in this thesis join two different fields of study, and it is important to find the optimal way to proceed in each case. For instance, in General Relativity, the problems are usually translated into a system of differential equations which must be first obtained from the Einstein equations in some specific system of coordinates. Alternatively, in the Skyrme model we frequently need first to consider the possible symmetries of the so-

lutions, with a correct parametrization, and then find the field equations from the energy functional. Both scenarios require efficient symbolic algorithms to obtain the expressions that we will finally solve. Besides, it is also interesting to develop a sufficiently flexible framework to introduce possible modifications, like extensions of General Relativity or additional terms in the Skyrme lagrangian.

Once the problem has been translated into a numerical issue, we need to consider different algorithms to find the solution. Specifically, in the Skyrme model a shooting method is frequently used to integrate the field equations for the simplest solution, however, this is not the only possibility. For the rest of solutions, a better alternative is a minimization problem rather than a system of differential equations, where a gradient flow method is implemented. Besides, it is straightforward to implement periodic boundary conditions on the solutions using a gradient flow method, however, although this algorithm is more effective and versatile, it requires a high computational capacity even for an efficient code, so the development of this framework to obtain the solutions from the Skyrme model is an important step.

Additionally, we will also consider other solutions which are more efficiently obtained using other approaches. This is the case of the FCC or BCC Skyrme crystals, which are better obtained varying the coefficients of the Skyrme fields expanded in truncated Fourier series to minimize the energy. Despite this method is basically a minimization as well, the procedure is completely different.

Analysis of the results and the comparison with experimental data:
Finally, when the solution is obtained it is important to reproduce the results from previous works to trust our numerical method. Then, the physical observable of interest must be extracted from the solution. This may not be a trivial task since it may require accurate integrations or even further minimizations. Besides, the estimation and consideration of errors both experimentally and theoretically are essential to accept or disprove the result.

Chapter 1

Introduction

Didn't know how but I always had a feeling I
was gonna be that one in a million. Always had
high, high hopes.

Panic! at the Disco

1.1 Neutron Stars

Neutron stars (NS) are one of the most compact objects in the universe, such that matter reaches its most exotic states in their interiors. More specifically, NS are the remnant cores of very massive stars, typically those with masses larger than $8M_{\odot}$ during their main-sequence stage [140], where $M_{\odot} = 1.98841 \times 10^{30}$ kg is the mass the Sun. These high masses induce strong gravitational interactions, but the stars remain stable under collapse due to the energy released from the nuclear fusion reactions. An increasing sequence of nuclei in the baryon number occurs in these reactions until the most stable nuclei are achieved in the last stages of the stars. At this point, nuclear fusion is not energetically favoured anymore and the gravitational collapse takes place. The outermost layers are so squeezed towards the core, so that the matter inside the star is greatly compressed until the degeneracy pressure stops the collapse and bounces, producing one of the most violent events in the universe, a type II supernova explosion.

The whole mechanism of these type of supernovae may be split in six different stages [70], in which the different neutrino emissions play a crucial role, but a detailed description remains unclear [71]. In this process, a large amount of mass from the star is expelled, leaving a extremely compact object of $\sim 2M_{\odot}$ and around 10 km of radius, the NS [139, 201]. Additionally, the atomic matter

present in the former star is so compressed in the collapse, that the electrons and protons combine via electron capture processes. This produces a vast amount of neutrons, and it is the reason for their name.

Nevertheless, NS are not the only fate of a very massive star. If the gravitational attraction is sufficiently strong, so that the degeneracy pressure of nuclear matter is not enough to stop the collapse, then the final remnant is a black hole. Recent simulations estimate that stars in the main-sequence with masses larger than $20M_{\odot}$ are more likely to produce a black hole [118].

The main characteristic of NS is their high compactness, $C := GM/R \sim 0.2 - 0.3$, being the closest to the maximal values of the spherically symmetric black holes, $C_{\text{BH}} = 0.5$. This induces a huge surface gravity, which may be roughly estimated in the Newtonian limit, $g = GM/R^2 \sim 10^{10}g_{\oplus}$, where g_{\oplus} is the surface gravity on Earth. The intense gravity present in NS convert them into unique scenarios where the four fundamental known interactions are simultaneously important. Moreover, the high curvature effects around the NS bends the photons trajectory that much, so that we could see the 85% of the star surface.

Furthermore, the conservation of angular momentum imply that the rotation of the original star induces high rotational velocities in the much smaller resulting NS. The largest rotational frequencies observed have reached $\Omega \sim 700$ Hz [119], quite close to the maximal Keplerian frequency, $\Omega_K \sim 1.4$ kHz [140]. Indeed, the high speed rotations induce measurable deformations in the NS being, in fact, a valuable source of information. NS are also characterized for having the strongest detected magnetic fields $\sim 10^8 - 10^{15}$ G, the highest magnetized NS are called magnetars. The origin of such intense magnetic fields is indeed more intricate than that of the fast rotations, but there exist some possible justifications [214]. The fast rotations combined with the strong magnetic fields produce the emission of beams of electromagnetic radiation, which, when aligned with the Earth, provides an effect analog to a cosmic lighthouse. These objects are known as pulsars, and they are responsible for the discovery of NS with the subsequent interest in their study.

Additionally, despite they are called stars, nuclear reactions do not occur in the

NS interiors. Indeed, the temperature of NS reaches the highest values $\sim 10^{13}$ K during their formation, but the lack of nuclear reactions and the emission of neutrinos cools down the NS to $\sim 10^6$ K in the next million years [142]. Indeed, The NS cooling is governed by the direct URCA process in the first seconds of existence. This mechanism is the result from the combined reactions,

$$n \rightarrow p + e^- + \bar{\nu}_e, \quad p + e^- \rightarrow n + \nu_e. \quad (1.1)$$

The name URCA was given by Mário Schenberg referring to a casino in Rio after telling to Gamow: “The energy in a supernova must disappear as quickly as the money at the roulette table.” The temperature drops to $\sim 10^9$ K, then neutrinos are emitted by the modified URCA processes, which involve interactions between the nucleons, and the NS cooling sharply slows down. Actually, the direct URCA process might continue if the fraction of protons is larger than 1/9 in the NS, so the accurate description of nuclear at high densities is crucial to distinguish not only the static properties of NS but also many dynamical effects. However, already at these temperatures, the energy associated to thermal fluctuations ~ 0.1 MeV is much smaller than the nuclear matter binding energies ~ 10 MeV. For this reason, the NS computations with no interest in the cooling physics are carried out under the zero temperature assumption.

It is widely accepted that nuclear matter is so compressed inside NS, that the baryon density in the center might surpass several times the average baryon density of stable nuclei, which is known as the nuclear saturation density $\rho_0 = 2.68 \times 10^{17}$ kg/m³. Therefore, the extreme conditions reached inside NS convert them into ideal laboratories to study how nuclear matter behaves at these regimes which are not reproducible on Earth. Indeed, the complete knowledge of nuclear matter is encoded in the so-called equation of state (EOS), and its determination has become one of the most outstanding problems in nuclear physics in the present [56].

1.1.1 Structure of Neutron Stars

Our current understanding of NS interiors is based on layers [113] as it is shown in Fig. 1.1.

The outermost part of a NS is a thin layer mainly made of light atoms (^1H , ^{12}C , ^{14}Si) of density $\rho \sim 10^3 \text{ kg/m}^3$ called the atmosphere, where the thermal spectrum is created and emitted. The specific thickness ranges from millimeters to some ten centimeters, depending on the temperature and the radiation transports. It is possible to extract valuable information from this external part about the surface properties of the stars, like the radius, surface temperature, chemical composition and the shape of the surface magnetic field.

The next layer is called the outer crust (or envelope), it extends up to some hundred meters starting with a very thin layer of a non-degenerate gas of electrons for $\rho \leq 10^7 \text{ kg/m}^3$ and positive ions from light nuclei. Going deeper, for densities $\rho \lesssim 10^9 \text{ kg/m}^3$, this layer is mainly made of ^{56}Fe nuclei [140] displayed on a lattice [78] surrounded by a degenerate gas of ionized electrons. At this point, the degeneracy pressure induces electron capture processes, producing neutrons in the present nuclei. The outer crust ends when the energy density reaches the neutron drip value $\rho_{\text{ND}} \approx 4 \times 10^{14} \text{ kg/m}^3$.

For larger densities, we enter the ($\sim 1 \text{ km}$ thick) inner crust (or simply the crust), where neutrons leak out of nuclei and very large baryon number $B \gtrsim 200$ clusters are produced. Here, close to the nuclear saturation density, $\rho_0 = 2.5 \times 10^{17} \text{ kg/m}^3$, the neutron enriched matter starts to deform due to the competition between the Coulomb and surface energies [186], so that a well-established sequence of different shapes occurs. Specifically, around $\rho \approx 0.1\rho_0$ the nuclear matter adopts the shape of gnocchi, spaghetti, waffles, lasagna, antispaghetti and antignocchi [74]. For obvious reasons, this stage is known as the nuclear pasta phases [205].

This phase ends at $\rho \approx \rho_0/2$, where we enter in the outer core. At these regimes, the excess of neutrons at high pressures suggest that nuclei dissociate and a superfluid state of neutrons might occur [207]. Actually, the interaction of vortices, created due to the superfluid state, with the surface of the NS

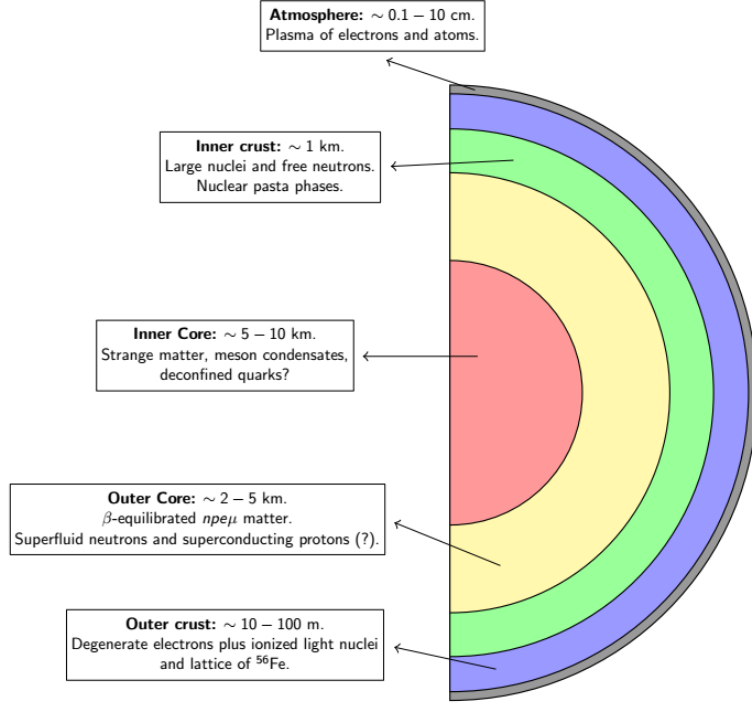


Figure 1.1: Depiction of the internal composition by layers of a neutron star.

could explain the pulsar glitches, in which a fast and momentary acceleration in their period is observed [31]. In this layer of several kilometers thick, matter is composed of a small amount of protons, electrons and mainly neutrons under charge and beta equilibrium. Furthermore, the high energy of electrons at some point favours the production of muons to ensure charge neutrality, both lepton species are well described by relativistic ideal Fermi gases.

Finally, in the beginning of the inner core, the densities surpass $\rho \gtrsim 2\rho_0$, but the value at the centre is still unknown. Different simulations suggest that the energy density might reach the values $\rho \sim 10 - 15\rho_0$, depending on the model. The size of this part is still unknown, but it might be of several kilometers as well. The specific composition is also obscure, but different hypothesis, which are mainly model dependent, have been proposed. The high densities reached in the core of NS might be the idoneous conditions to produce condensation of mesons, like pions or, if the electron degeneracy pressure is sufficiently high, kaons. Simulations estimate the emergence of kaon condensates around 2 – 3 times the saturation density. Indeed, the presence of strangeness might occur as well from the baryonic particles production, called hyperons. This possibility has also been studied, but these particles are expected to appear between 3 – 4

times the saturation density. Moreover, this phenomenon induces a release of the energy, which sharply decreases the masses of the NS. This effect may be problematic if the EOS does not reach the values that have been experimentally determined. Nevertheless, these are purely hadronic phase transitions, but quark deconfinement has also been suggested to occur at some point in the cores of very massive NS. All these transitions affect significantly the properties of the NS, so they have crucial importance to describe the EOS correctly.

One last possibility is the strange quark matter hypothesis [55, 204, 234]. It is based on the simple bag model, which simulates the quark confinement considering the system of quarks as a highly compressed Fermi gas in a finite region of space. To be consistent with the observations, a constant is introduced *ad hoc* to penalize energetically the free quark matter at low temperatures. However, if a strange quark is added to the bag, there is a narrow window of values for the bag constant that might sharply decrease the energy per baryon of the three-flavour quark system, implying that strange quark matter is the absolute stable state of matter. This hypothesis introduced the idea of the so-called strange stars as the ultimate stable state of matter in compact stars.

1.1.2 History of Neutron Stars

The theoretical prediction of NS is attributed to Baade and Zwicky in 1934, when they analyzed the enormous amount of energy released in the supernova explosions. Indeed, the term *super-nova* was first used in their original work [38]. Although they correctly identified the supernova with the formation of a NS, they indicated that the resulting object would be formed by the accumulation of neutrons falling down from the surface to the core of the star, due to the almost zero pressure applied on them.

The concept of EOS was soon introduced to predict the chemical composition of NS at different densities. The first β -equilibrated *npe* system was proposed in 1933 by Sterne [217], where the neutronization of nuclear matter for increasing densities was confirmed. Later, a systematic study of the mass and radius of a NS was developed independently (in fact in the same day) by Tolman [223], Oppenheimer and Volkoff [181] in 1939, deriving the stellar structure equations directly from general relativity (GR). In those studies, the Mass-Radius (MR)

curve is reconstructed for an EOS describing a degenerate Fermi gas of neutrons, and the concept of maximal mass NS was introduced with a value of $M_{\max} \approx 0.7M_{\odot}$. They realized that this small value of M_{\max} was due to the simplicity of the EOS, but after the Second World War, the inclusion of nuclear interactions increased the maximal mass up to $2M_{\odot}$. The further development of realistic EOS with additional vector meson interactions, strangeness, magnetic fields, superfluid cores and the thermal evolution of NS via neutrino emissions has been an increasing field of study since the 1960s.

The interest in the refinement of the EOS was mainly motivated by the first experimental X-ray detections in the 60s decade. The first measured X-ray source of non-solar origin was called Sco X-1, discovered in 1962 by Giacconi and his collaborators [98], but it was not identified as a NS at that moment. In the present we know that Sco X-1 is actually a binary system with a NS accreting matter from the companion.

The next remarkable X-ray source observation was the Crab nebula in 1964, however, this case was neither identified with a NS given the large size measured $\sim 10^{13}$ km. Surprisingly, the Crab nebula is actually a plerion, *i.e.*, an active pulsar surrounded by the supernova remnant gas, which is expanding and radiating due to the interactions with the central NS strong magnetic fields. Indeed, the observation of the supernova explosion from this specific stellar object has been dated to the year 1054 by historical records of Chinese astronomers. It is indicated in these manuscripts that the light emitted in the explosion would have been visible even during the daylight.

Probably the most famous NS observation was made by Jocelyn Bell in 1967 [120], using a radiotelescope designed by her supervisor, Anthony Hewish. She discovered a radio source emitting strictly periodic pulses with a very short and stable period $P = 1.3373$ s. The identification of this source with an oscillating star was ruled out since the fast rotational velocity would fly apart the star, and the stability in the period made them even think of a possible artificial origin. Indeed, they denoted the source by “LGM” (little green men) due to the obscure origin of the signals, so the publication was postponed until the situation was clarified. Finally, the discovery of three more similar objects suggested that the source might be a pulsating NS. However, over a hundred of pulsars, some of

then in the range of millisecond period, were observed by the end of 1968, then the idea of Gold [102], that the pulsar is a fast rotating NS with strong magnetic fields, was finally accepted. The original object discovered by Bell is now called PSR B1919+21, and Hewish was awarded in 1974 with the Nobel Prize for the discovery of pulsars, albeit with some controversy for not considering J. Bell in the award.

1.2 Current status of Neutron Stars physics

In the present, theoretical computations of NS are focused on the numerical simulations of the possible scenarios mentioned before in the deepest layers of NS and their comparison with the current observations. Specifically, the final goal of every study is the full description of nuclear matter for all densities, positioning the EOS as the cornerstone in NS physics.

Quantum Chromodynamics (QCD) has been established as the fundamental theory of strong nuclear interactions. In particular, it is a non-abelian quantum field theory (QFT) which describes the interactions between quarks and gluons, the fundamental degrees of freedom of nuclear matter. Then, a first naive thinking would suggest the derivation of the EOS using QCD as the starting point, but it is not the case. In QFT, the standard description of the interactions between particles is carried out via the evolution of the coupling constant as a function of the energy scale. The non-abelian structure of QCD induces self-interactions between gluons, this triggers an asymptotic decrease of the coupling constant at high energies. Hence, quarks and gluons become weakly coupled in this regime, a phenomenon called asymptotic freedom, and it is of great importance given that it allows to perform computations in the perturbative framework of Feynman diagrams.

In the opposite direction, the QCD coupling constant grows arbitrarily as the energy scale decreases, which causes quarks and gluons to be strongly bounded. This effect is known as the color confinement, and it is responsible for the fact that isolated quarks cannot be observed at low energies, instead they are strongly tied in bound states which are the mesons and baryons. It also prevents us to compute quark-gluon dynamics in the standard perturbative approach, indeed the energy scale at which QCD is not reliable anymore has been estimated

around $\Lambda_{\text{QCD}} \sim 200$ MeV [95]. Therefore, other approaches are necessary to describe nuclear matter in the low energy scale regime. Lattice QCD has become an interesting proposal of non-perturbative formalism to extract information from the fundamental theory at high temperatures and low baryon densities. However, as we have seen, NS are the prototypical scenarios of very high baryon densities and relatively low temperatures, hence this approach is not a correct choice for our purposes.

1.2.1 Theoretical approaches

The most frequent approaches to develop an EOS are called many-body interaction methods, which are built from nucleons, as the fundamental degrees of freedom, and the couplings extracted from the few-body (two or three) nucleon interactions. The further inclusion of strange degrees of freedom and deconfined quark matter in the EOS is a more complicated task which requires additional interactions terms, including strange mesons and hyperons, and *ad hoc* hadron-quark phase transitions [48]. The few-body computations extract the dominant two-body (or higher order) nuclear forces, based on experimental data or from theoretical approaches, like meson-exchange models [137], potential models [146, 231] or even from Lattice QCD using high computational resources. A detailed description of the different few-body techniques may be found in [68, 179] and the references therein. Once the information of the nucleon-nucleon interactions has been obtained, it is introduced as an input in the many-body computational methods, which are classified into ab-initio microscopic methods or phenomenological models.

One of the most used ab-initio methods is the relativistic Dirac-Brueckner-Hartree-Fock. This method is actually the lowest-order Hartree-Fock approximation of the energy density in the Brueckner-Bethe-Goldstone theory [113]. The basic idea of this theory is the introduction of a self-energy term to split consistently the single-nucleon Hamiltonian and the interactions terms between nucleons. This step is crucial to ensure the convergence of the method. Then, all the interaction diagrams must be considered to compute the energy of the system [41], but the summation on the whole set of diagrams is replaced by the so-called G-matrix. Thus, the G-matrix may be regarded as the effective

in-medium interaction between two nucleons. It is obtained as a solution to an integral equation at different densities, so that the self-energy term is also determined, and the total energy of the system may be computed. In this way, the EOS is constructed, however, in this approach, the three body forces must be included since they are essential to reproduce the properties of nuclear matter at the saturation point.

Another popular and successful case are the Chiral Effective Field Theories [150]. These are based on the effective field theory (EFT) philosophy, considering only the appropriate degrees of freedom for a specific physical phenomenon in some energy and length scales, instead of considering the possibly more complicated underlying fundamental theory. Other fundamental ingredients in an EFT are the symmetries of the problem and the expansion parameter, also known as the power counting. The main advantage of EFT is the consistent description order by order in the expansion parameter, focusing on the key physical properties of the scenario. In particular, chiral EFT provide a model-independent systematic framework to describe the low energy interactions between hadrons, introduced as external effective fields, through the interchange of mesons as the fundamental degrees of freedom. These theories rely on the chiral symmetry, which is the invariance under the interchange of quarks in the massless Lagrangian of QCD. Thus, the expansion parameter typically relates the chiral symmetry breaking scale Λ_χ with the quarks masses or the meson momentum transfer. The inclusion of chiral EFT results allowed to constrain the EOS slightly above the saturation density, $\sim 1.1n_0$ [221].

Specifically, the Skyrme model may be enclosed in the chiral EFT paradigm, but not in the traditional sense, since baryons appear naturally within the model, in opposition to the other methods explained above. It was already considered in 2012 to describe NS, but the results did not correspond to the mass constraints. Nevertheless, the Skyrme model recently gained some interest in the study of dense nuclear, from the promising results using a specific extension of the model [12]. Then, it is natural, and the aim of this thesis, the combination of these models to extend the computations for NS.

On the other hand, phenomenological models are often called effective energy density functionals. Among them, relativistic mean-field theories [100] are built

from an effective Lagrangian of nucleons described by Dirac spinor fields, which interact through the exchange of different type of mesons. The coupling constants are usually fitted to some nuclear matter properties, and each meson is responsible of different effects, for instance, the short and long range interactions are carried by the σ and ω mesons respectively, and the neutron-proton asymmetry contributions are accounted by ρ mesons. Then, the whole system of highly coupled nonlinear equations is solved under a mean-field approximation, in which the mesons are replaced by their spatially integrated mean value.

1.2.2 Experimental detections

The multiples approaches explained above produce a wide variety of EOS [68, 69, 183], and each one yields different observables like the mass, radius and rotational or tidal deformations for NS. Therefore, these results must be compared with experimental measurements to confirm the reliability of the EOS. Indeed, the low density regime has already been constrained up to 1 – 2 times the saturation density, from heavy ion collisions [125].

Many different observational techniques have been developed to extract the NS properties [196]. The Shapiro delay method [206] is an effective way to measure the mass of a NS. In a binary system, in which one of the compact objects is a pulsar, the strong gravitational effects induce a periodic delay in the received pulse. The delay is a correction to the classical Newtonian motion, so it is an example of post-Newtonian (PN) parameter and it is related to the mass of the companion. Then the NS mass may be extracted from the binary mass function, which is easier to measure. Many important detections have been determined using this technique [82, 87], indeed, these observations ruled out some EOS whose maximal mass could not reach the values $M \gtrsim 2M_\odot$.

An additional PN parameter in binary-NS systems may be related to the moment of inertia [83], which depends directly on the mass and radius of the compact object. The moment of inertia has already been estimated in this way, but the current measurements produce large uncertainties, then this observable does not further constrain the EOS. The reason is that it is obtained from a second order $\mathcal{O}(v^4/c^4)$ PN parameter in the orbital velocity of the NS, extracted from the apsidal precession of the orbits. However, it is expected that longer

timing baselines will resolve the accuracy.

Interestingly, the moment of inertia has been recently related to other physical observables, specifically the deformability and quadrupolar moment of rotating NS, in the so-called universal relations [237]. Hence, even though different observables cannot be measured simultaneously for the same NS, the unknown observables may be estimated from the others using these relations.

X-ray observational techniques represent an important source of information given that the emitted photons are greatly affected by the mass and radius of the NS. The Neutron Star Interior Composition Explorer (NICER) experiment is now the main responsible for the mass and radius measurements from X-ray emissions of spinning NS [164, 165, 197, 198]. It is a NASA telescope located in International Space Station which is collecting the photons in the $0.2 - 12$ keV spectrum emitted by pulsars. In this way, the compactness may be constrained by the flux curve due to the gravitational light-bending effect, besides, there are promising expectations in the independent constraint of the mass and radius from the spectroscopy analysis [184].

Finally, from a completely different perspective, gravitational wave (GW) observations has become an increasing field of study. The propagation of gravitational radiation emitted by the accelerated motion of masses is a strong prediction of GR, and it encodes valuable information from the source. However, due to the low intensity of gravity, these waves must be emitted from very massive, compact and rapidly moving sources (mainly binary NS or black hole mergers), and yet their observation requires an extremely accurate detector.

The first GW detection of a binary neutron stars coalescence is attributed to the LIGO scientific and Virgo collaborations [2] in 2017. Furthermore, the combined detection of the GW emission and the electromagnetic counterpart from this source [1] established the starting point of the new multimessenger detection era. This event not only allowed to constraint the MR diagram of NS, but also imposed an upper bound for the tidal deformability. This new observable may be extracted from the PN expansion of the GW waveform just before the merging, and it is a direct indication on how much nuclear matter is compressed inside the NS, also known as the stiffness of the EOS.

The LIGO and Virgo detectors have measured more events since the first GW observation, imposing tight constraints on the EOS. They have been recently complemented by other detectors like KAGRA, and extensions of LIGO and Virgo in other places. Besides, new detectors are expected to be introduced in the next decade, like LISA or the Einstein Telescope [39].

Chapter 2

The Skyrme model

The outcome of the battle depends on how you handle weakness and strength.

Gichin Funakoshi

In the beginning of the 1960s, T. H. Skyrme proposes a theory purely built from mesons to reproduce the nuclear interactions and describe baryonic solutions [210, 211]. In this theory, which in the present is commonly known as *The Skyrme model* [156, 240], baryons naturally appear as nonperturbative collective excitations from the non-linear interactions between mesons. More specifically, these solutions are topological solitons [154, 193] and, in the context of the Skyrme model, they are called *skyrmions*. The model was introduced before the appearance of QCD, so it is originally based on the Yukawa's idea, prevalent since the 1930s, in which nuclear interactions between baryons were mediated by mesons. The success of this idea is due to the reasonable description of long range interactions between nucleons and the discovery of the pions.

The computational difficulty to obtain solutions from the model at that moment, together with the advent of QCD in the beginning of the 1970s, induced a loss of interest in the model for some years. It was in 1983 when Witten [233] established a relation between QCD in the large N_c limit [220] and the Skyrme model, which drew attention to the model again. In his work, it is shown how the fundamental theory of strong interactions becomes an effective theory of weakly interacting mesons, in which the baryons satisfy the typical properties of solitons [122, 149, 202]. Hence, the Skyrme model might be understood as an EFT of QCD at low energies, regime at which results cannot be obtained from the standard perturbative methods. This result strengthened the basic

ideas of the Skyrme model, and many analogies between the two theories may be extracted.

2.1 The standard Skyrme model

The Skyrme model is built from a field, denoted by U , which is an element of the $SU(2)$ Lie group. This implies that the field satisfies the following conditions:

$$U^\dagger U = UU^\dagger = \mathbb{I}_2, \quad \det\{U\} = 1. \quad (2.1)$$

In practice, this field is parametrized in terms of other scalar fields. Specifically, the exponential map establishes a correspondence between the elements of a Lie group and its associated Lie algebra. Besides, any element of a Lie algebra may be expanded in terms of the algebra generators, which in the $\mathfrak{su}(2)$ case, these are the Pauli matrices,

$$\tau_1 = \begin{pmatrix} 0 & 1 \\ 1 & 0 \end{pmatrix}, \quad \tau_2 = \begin{pmatrix} 0 & -i \\ i & 0 \end{pmatrix}, \quad \tau_3 = \begin{pmatrix} 1 & 0 \\ 0 & -1 \end{pmatrix}. \quad (2.2)$$

Then, the Skyrme field may be written in terms of the new fields, π_a ($a = 1, 2, 3$), which are identified with the pions,

$$U = \exp\{i\tilde{\pi}_a \tau_a\} = \cos(\tilde{\boldsymbol{\pi}})\mathbb{I}_2 + i \sin(\tilde{\boldsymbol{\pi}})\tilde{\pi}_a \tau_a := \sigma \mathbb{I}_2 + i\pi_a \tau_a, \quad (2.3)$$

where \mathbb{I}_2 is the 2×2 identity matrix, and $\tilde{\boldsymbol{\pi}} = \sqrt{\tilde{\boldsymbol{\pi}}^2} = \sqrt{\tilde{\pi}_a \tilde{\pi}_a}$. We also have defined the σ field, which must satisfy the unitary constraint $\sigma^2 + \boldsymbol{\pi}^2 = 1$.

Hence, the Skyrme model is a scalar field theory of pions which was originally represented by the following Lagrangian density,

$$\mathcal{L}_{24} = \mathcal{L}_2 + \mathcal{L}_4 = -\frac{f_\pi^2}{16} \text{Tr}\{L_\mu L^\mu\} + \frac{1}{32e^2} \text{Tr}\{[L_\mu, L_\nu]^2\}. \quad (2.4)$$

It is usual to express the Lagrangian in terms of $L_\mu = U^\dagger \partial_\mu U$, the left-invariant Maurer-Cartan form, which is an element of the $\mathfrak{su}(2)$ Lie algebra. The subscript in each term is just a notation to represent the number of derivatives in the specific term, for this reason, we will often refer to them as the quadratic (\mathcal{L}_2)

and the quartic (\mathcal{L}_4) terms. We remark here that, throughout this thesis, we will work with different versions of the model, therefore, we will refer to the previous Lagrangian (2.4) as the standard Skyrme model.

There are two parameters (f_π, e) in this theory. The coefficient f_π , present in the quadratic term may be identified with the pion decay constant, which has the physical value 186 MeV within our convention. The other one is known as the Skyrme parameter, e , and it has no direct identification with any observable. However, it is usual to consider both as free parameters and use them to fit the solutions to nuclear observables.

The Skyrme model is invariant under a $SU(2)_L \times SU(2)_R$ chiral transformation of the field,

$$U \rightarrow LUR^\dagger. \quad (2.5)$$

However, in order to obtain finite energy solutions, we need to impose the vacuum boundary conditions on the Skyrme field at spatial infinity. There is no unique choice for the vacuum, but it is standard, and natural, to consider the limit $U \xrightarrow{x \rightarrow \infty} \mathbb{I}_2$. This condition corresponds to the spontaneous chiral symmetry breaking in the Skyrme model, which modifies the previous internal invariance to the diagonal symmetry group, $SU(2)_L \times SU(2)_R \rightarrow SU(2)_V$. Then, the model is now invariant under the so-called *isospin* transformation,

$$U \rightarrow AUA^\dagger. \quad (2.6)$$

These features of the Skyrme model are also present in QCD, whose Lagrangian for massless quarks is chiral invariant. Besides, it is known that this symmetry is also spontaneously broken to the isospin symmetry in the fundamental theory [149]. Moreover, the Nambu–Goldstone theorem [104, 168] states that any spontaneously broken symmetry in a relativistic system induces a number of massless Goldstone bosons equal to the number of broken generators. These bosons are, indeed, the pions [149].

In general, we may extend the symmetry of the Skyrme model to $SU(N_f)$, where N_f is the number of flavours that we want to consider. However, we aim

at describing atomic nuclei and nuclear matter inside NS, hence, we just need to reproduce protons and neutrons, which are composed by the two lightest quarks, u and d . The inclusion of strangeness is considered at the end of this thesis, since it is of huge interest for NS physics, thus, we will maintain $N_f = 2$ until the last chapter.

For any fixed time, the Skyrme field defines a map from the three dimensional real space to the $SU(2)$ group. From the unitary condition we see that the fields (σ, π_a) lie on a three-sphere, so the $SU(2)$ group may be regarded as the S^3 manifold. Then, the Skyrme field is the map $U : \mathbb{R}^3 \rightarrow SU(2) \sim S^3$. Furthermore, once the vacuum condition is imposed on the field, the whole spatial infinite of \mathbb{R}^3 is compactified into a point, becoming the base manifold the S^3 too. This implies that the field configurations may be classified by the third homotopy group which, in this case, satisfies $\pi_3(S^3) = \mathbb{Z}$. Therefore, there is an integer number, denoted by B , associated to each field configuration, which is different for topologically distinct configurations. This integer number was identified by Skyrme with the baryon number of nuclear matter, and it may be calculated from the topologically conserved current B^μ :

$$B = \int d^3x B^0, \quad B^\mu = \frac{\epsilon^{\mu\nu\alpha\beta}}{24\pi^2} \text{Tr}\{L_\nu L_\alpha L_\beta\}. \quad (2.7)$$

It is trivial to see that the divergence of the topological current vanishes ($\partial_\mu B^\mu = 0$), therefore, the topological charge is conserved. In addition, the zero component B^0 of the current is the pullback of the target space volume form, so the integer number B counts the number of times the field configuration winds around the target space. For this reason, the topological charge is also known as the winding number.

For computational purposes, it is usual to work with an adimensional model, scaling out the energy and length units. Indeed, we may choose these units such that the two parameters in the Lagrangian (2.4) are eliminated,

$$E_s = \frac{3\pi^2 f_\pi}{e}, \quad x_s = \frac{1}{f_\pi e}. \quad (2.8)$$

These are called the Skyrme units, and the Lagrangian is expressed as follows,

$$\mathcal{L} = \frac{1}{24\pi^2} \left[-\frac{1}{2} \text{Tr}\{L_\mu L^\mu\} + \frac{1}{4} \text{Tr}\{[L_\mu, L_\nu]\} \right]. \quad (2.9)$$

In these units, solutions are obtained independently of the parameters, so that we have the freedom to fit the energy and length scale to some physical observables, which is translated into the fit of the parameters f_π and e .

The quadratic term may be expressed as a kinetic energy term for the Skyrme field,

$$\mathcal{L}_2 = -\frac{1}{2} \text{Tr}\{L_\mu L^\mu\} = \frac{1}{2} \text{Tr}\{\partial_\mu U^\dagger \partial^\mu U\}. \quad (2.10)$$

However, when it is expanded in terms of the pion fields, it yields a kinetic energy contribution plus self-interaction terms. In fact, this term is also known as the non-linear σ -model (NLSM).

Even though this term already reproduces some long distance phenomenology of nuclear matter, it is not enough to provide energetically stable solutions. Under a simple rescaling of the spatial coordinates $x \rightarrow x/\sigma_s$ on a field configuration $U(x) \rightarrow U(x/\sigma_s)$, it may be shown that the energy is minimized for $\sigma_s = 0$, *i.e.*, the solution collapses. This is anticipated by the Derrick scaling theorem [88], which states that stationary localized solutions to a nonlinear wave equation in three or higher spatial dimensions are unstable.

However, the inclusion of the quartic term in the model avoids the Derrick theorem restriction and yields stable solutions. Applying the scaling argument in the static energy functional $E = -\int d^3x \mathcal{L}$ of the Skyrme model,

$$E = E_2 + E_4 = \frac{1}{24\pi^2} \int d^3x \left[-\frac{1}{2} \text{Tr}\{L_i^2\} - \frac{1}{4} \text{Tr}\{[L_i, L_j]^2\} \right], \quad (2.11)$$

we find a non-zero size of the minimal energy configuration.

$$E(\sigma_s) = \sigma_s E_2 + \frac{E_4}{\sigma_s}, \quad (2.12)$$

$$\partial_{\sigma_s} E = 0 \longrightarrow \sigma_s^2 = \frac{E_4}{E_2} \neq 0. \quad (2.13)$$

Then, the quartic term is crucial to stabilize the solutions. It was introduced by Skyrme himself, this is also a reason for which the quartic term is frequently referred to as the Skyrme term. Given that the Skyrme model is identified as a low-energy effective field theory of QCD, the quartic term may be seen as a higher derivative correction to the NLSM. It is not, in fact, the only term that we can construct with four derivatives that satisfies chiral symmetry, but it is the only one that yields a Hamiltonian of second order in time derivatives.

Furthermore, a lower energy bound for the field configurations may be obtained in the standard Skyrme model. The energy functional (2.11) may be written in terms of strictly positive terms using the following relations:

$$L_\mu^\dagger = -L_\mu, \quad (2.14)$$

$$\text{Tr}\{[L_i, L_j]^2\} = 2 \text{Tr}\{(\epsilon_{ijk} L_i L_j)^2\} = -2 \text{Tr}\{|\epsilon_{ijk} L_i L_j|^2\}. \quad (2.15)$$

Then, the perfect square may be reconstructed from the two terms in the energy to obtain the so-called Bogomol'nyi-Prasad-Sommerfield (BPS) bound [57, 190].

$$\begin{aligned} E &= \frac{1}{24\pi^2} \int d^3x \left[\frac{1}{2} \text{Tr}\{|L_i|^2\} + \frac{1}{2} \text{Tr}\{|\epsilon_{ijk} L_i L_j|^2\} \right] = \\ &\quad \frac{1}{24\pi^2} \int d^3x \left[\frac{1}{2} \text{Tr}\{(|L_k| - |\epsilon_{ijk} L_i L_j|)^2\} + \text{Tr}\{|\epsilon_{ijk} L_i L_j L_k|\} \right] \geq |B| \end{aligned} \quad (2.16)$$

Indeed, the Skyrme units have been defined such that the BPS bound is exactly the topological charge. The equality cannot be saturated in the standard Skyrme model since no solutions, other than the trivial (vacuum) solution $L_k = 0$, can be obtained from the BPS equation,

$$L_k = \epsilon_{ijk} L_i L_j. \quad (2.17)$$

Solutions to the field equations for different values of B may be obtained using different approaches. The simplest solution is the $B = 1$ skyrmion, which has spherical symmetry, therefore, the field equation is just an ordinary differential equation (ODE) that only depends on the radial coordinate. This solution may be parametrized by the hedgehog ansatz: $\pi_a = f(r)n_a$, where $f(r)$ is the profile function and n_a is the S^2 unit vector.

$$U = \exp\{if(r)n_a\tau_a\} = \sin(f)\mathbb{I}_2 + \cos(f)n_a\tau_a. \quad (2.18)$$

Inserting the hedgehog ansatz in the Lagrangian we obtain a second order ODE for the profile function $f(r)$. Recall that we chose \mathbb{I}_2 to be the vacuum state of the Skyrme field, hence the topologically non-trivial boundary conditions for the $B = 1$ skyrmion are: $f(r = 0) = \pi$, $f(r \rightarrow \infty) = 0$. However, in order to solve the field equation, we need to know the value of f and its derivative at the same value of r . The usual way to solve this issue, is to integrate the equation starting with an initial seed for $f'(r = 0)$, using any standard ODE integrator, like a Runge-Kutta method. The input value for the first derivative will not produce a solution with the correct boundary condition at infinity, but a shooting method may be implemented to reach the correct value iteratively.

Nevertheless, the solution may be obtained using other techniques which are not usually found in the Skyrme model literature, but they are often used in other studies. Spectral methods [105, 106] are a powerful tool to solve many kinds of differential equations, which are vastly used in numerical relativity [107], specifically for the study of collisions between compact objects [176, 203] or fast rotating NS [59]. This technique has also been used to solve other (non-topological) solitonic systems like rotating boson stars [108], but no applications, to our knowledge, have been found in the Skyrme model. Then, the $B = 1$ skyrmion field equation may serve as another interesting test in which this approach could be implemented to compute skyrmions, as well as a representative example to show how to solve non-linear ODE using spectral methods. The resolution of the $B = 1$ skyrmion is detailed in appendix A using this technique.

Once the solution for the field profile is found, the energy obtained for the skyrmion is $E = 1.2315$, and it represents the classical state for a nucleon, *i.e.*, the proton or neutron.

Solutions for higher values of B have been extensively studied. The standard procedure to obtain the low- B skyrmions consists in the identification of the symmetries for the field configuration, then the field equations may be solved using different approaches. The $B = 2$ solution was first identified to be axially symmetric in [153], and then the system of PDE was solved in [62].

The extension to the tetrahedral $B = 3$ and cubic $B = 4$ skyrmions [64] was also performed following this approach [64], but a new method was soon developed to simplify the resolution of the field equations. The rational map approximation [124, 157] splits the radial and angular dependent parts of the Skyrme field in the energy functional. In this approach, the skyrmion is parametrized using (2.18), but with a generic angular distribution,

$$n_a^{(\mathcal{R})} = \frac{1}{1 + |\mathcal{R}(z)|^2} \left(2\text{Re}(\mathcal{R}(z)), 2\text{Im}(\mathcal{R}(z)), 1 - |\mathcal{R}(z)|^2 \right), \quad (2.19)$$

where $\mathcal{R}(z)$ is the rational map, which is a holomorphic function of the stereographic coordinate $z(\theta, \phi)$ of the S^2 . Specifically, $\mathcal{R}(z)$ is the ratio between two polynomials, $p(z)$ and $q(z)$, which have no common roots. The rational map is fixed by considering the most general polynomials of degree B , which is the baryon number of the resulting skyrmion. Then the symmetries are imposed on $\mathcal{R}(z)$, constraining some of the coefficients in the polynomials.

The part that only depends on z in the energy functional is minimized first, by varying the remaining coefficients of the polynomials $p(z)$ and $q(z)$. Thus, we end up with an expression that only depends on the radial coordinate through the profile function $f(r)$, which is minimized as we did in the spherically symmetric case. Recall that skyrmions obtained from rational maps are not solutions of the field equations, since in this approximation we minimize different parts individually, but it is a powerful tool to obtain symmetric field configurations.

Comparisons between the energy of the solutions and the rational map configurations show quite similar results up to $B = 8$. This encouraged the computation of higher B -skyrmions to reproduce heavier nuclei. However, the energy density of these field configurations was concentrated in hollow and shell-like distributions [47], which does not correspond to the physical nuclei.

An additional problem in the standard Skyrme model, as pointed out in [63], is the large difference between the binding energies obtained from the solutions [154] and the experimental values, which are not larger than 1%. They are defined as follows,

$$\text{BE}_B(\%) := \frac{E_{B=1} - E_B/B}{E_{B=1}}. \quad (2.20)$$

However, these binding energies have been computed from the classical energies of the skyrmions, hence, this discrepancy might be due to the lack of some corrections that we are not considering. Indeed, it was recently shown [112] that the quantum corrections from vibrational modes yield remarkable results in order to solve this longstanding problem.

Further effects of realistic nuclear matter are the spin and isospin quantum corrections. Indeed, nucleons are spin $\frac{1}{2}$ particles, but the higher spin excitation of the proton (Δ particle), as well as different isospin excitations (isotopes) of many nuclei, have been observed. Furthermore, it is known that an important correction to the mass of the nuclei comes from the difference between the number of protons and neutrons. Hence, it is of great interest to consider this quantum effects in the Skyrme model.

However, we have seen that nucleons appear as collective excitations from the nonlinear interactions between pions, which are bosonic particles. Then, the natural question of how fermionic particles are obtained in a purely bosonic theory arises. This question was addressed by Finkelstein and Rubinstein in [92], where they stated that fermionic quantum states may be obtained since the wave functions may change the sign under a 2π rotation due to the existence of non-contractible loops in the configuration space of wave functions [134, 156]. This is, indeed, the requirement for the correct quantization of the Skyrme model or similar low-energy EFT of QCD. Furthermore, they introduced the constraints that determine the possible quantum states of a skyrmion depending on the specific symmetries of the solution.

Having said that, a canonical quantization as in standard QFT is not possible since the Skyrme model is non-renormalizable, therefore, a semi-classical quantization must be applied. The usual procedure [29, 63] considers the quan-

tization of a finite number of collective coordinates which correspond to the zero modes (symmetries) of the Skyrme Lagrangian *i.e.*, translations, spatial rotations and isorotations of the field. This approach is motivated from the approximate description of slowly moving soliton dynamics using the geodesic motion on the moduli space of static configurations [152]. It also involves an approximation in which the skyrmion of baryon number B is transformed under these symmetries rigidly, such that no deformations are allowed. Translations of the skyrmion are usually ignored, but the quantization of spin and isospin has been extensively studied, indeed due to the simplicity of the rational map, for different values of the baryon number [134, 135, 151].

Despite the great phenomenological interest of (iso-)spin quantum correction in the Skyrme model, they are not helpful in the previously mentioned binding energies problem.

In [29], the $B = 1$ skyrmion was quantized obtaining from the same classical solution a splitting in the energy to describe the proton and the Δ baryon. Then the parameters were calibrated to reproduce their masses, and the values obtained are usually referred to as the standard parameters in the Skyrme model,

$$f_\pi = 129 \text{ MeV}, \quad e = 5.45. \quad (2.21)$$

The quantization of the $B = 1$ skyrmion will be briefly explained in the last section to recalibrate the parameters in a generalization of the Skyrme model and to compare them with those obtained from NS. Furthermore, in the upcoming chapters we will show in detail how the quantization of the isospin in Skyrme crystals opens a broad phenomenology in the Skyrme model.

2.1.1 Introducing the pion mass

So far, we have seen some of the problems of the Skyrme model in which pions are massless particles. However, it is known that pions have mass, $m_\pi = 138$ MeV, which means that chiral symmetry is explicitly broken into the isospin symmetry. Then, since the model is expected to describe QCD at low energies, the inclusion of a pion mass term in the Lagrangian seems a natural requirement.

Additionally, isospin symmetry implies that the pions have the same mass, which is also false. Hence, a further isospin symmetry breaking mechanism would be required in the Skyrme model. However, the difference between the masses (~ 1 MeV) is rather small in comparison to the energy scales considered in this work, besides, it is still not clear how isospin symmetry might be broken in the model. Therefore, we neglect this effects and maintain the isospin symmetry in this work.

The simplest choice to add a pion mass to the original theory (2.4) is the following,

$$\mathcal{L}_0 = \frac{m_\pi^2 f_\pi^2}{8} \text{Tr}\{U - \mathbb{I}_2\}. \quad (2.22)$$

This term explicitly breaks chiral symmetry because now the only possible vacuum state is precisely $U = \mathbb{I}_2$. As well as the quadratic term, this potential term may also be expanded on the pion fields around the vacuum and we would obtain the usual mass term of a scalar field.

The solutions obtained from the massive Skyrme model (following our previous notation we will denote it as \mathcal{L}_{240}) improve some of their properties. In the original model the profile function of the $B = 1$ skyrmion decays to zero at infinity under a power-law, $f \sim 1/r^2$. However, the inclusion of the pion mass term introduces a new term in the field equation which induces an exponential decay on the profile function. This is a standard phenomenon in field theory, as it occurs, for instance, with the long range interaction of electromagnetism, mediated by the massless photon, as opposed to the weak interactions, whose gauge bosons have mass. It is also an important effect from the computational point of view, since now the exponential decay reduces the size of the skyrmion and a smaller grid may be used in the numerical resolution of the field equations.

The major improvement of the pion mass term is the $B = 3$ and $B = 4$ clustering effect for some large $B \geq 10$ skyrmions. It is known that the α -particle model correctly describes the properties of some large nuclei with zero isospin [66]. Fortunately, the pion mass term (2.22) penalizes the hollow solutions [45, 46], and yield solutions with more realistic structures [44].

Additionally, solutions in the massive model have larger energies, however, the BPS bound is also expected to increase with the inclusion of the new term. Indeed, it is possible to redefine a BPS bound [115], but now it will depend on the parameters (f_π , e , m_π) given that we cannot erase them from the Lagrangian with any change of units. The knowledge of these generalized bounds is important to find the minimal energy configurations, and they will be specially helpful for the study of Skyrme crystals in the next section.

The quantization of the $B = 1$ skyrmion was also computed including the pion mass term [28]. Although potential terms do not directly enter in the quantization procedure, they modify the classical solution, hence, different values for the parameters, $f_\pi = 108$ MeV, $e = 4.84$, were obtained to reproduce the masses of the proton and Δ baryon.

2.1.2 Neutron stars in the standard Skyrme model

From a simple analysis we may see that NS contain the order of $M_\odot/m_N \sim 10^{57}$ baryons, being $m_N = 939$ MeV the mass of the nucleon. Hence, a naive thinking would suggest that in order to describe a neutron star from the Skyrme model, we would have to obtain the $B \sim 10^{57}$ skyrmion. This is obviously an impossible task from the computational point of view, however, some attempts to obtain enormously large- B solutions yield some results in the description of NS from the standard Skyrme model.

The first studies of self-gravitating skyrmions to describe NS involved the resolution of the full Einstein–Hilbert–Skyrme (EHS) system using the rational map approximation for the Skyrme field [188]. In this approach, NS are obtained for different values of the baryon number until a maximal value is attained, for which stars are no longer stable under radial oscillations. The results yield NS with quite small maximal baryon number and unnatural hollow shell-like configurations, where the solutions had a step-like behaviour. Besides, the solutions were obtained using unphysical values for the gravitational constant to facilitate the computations, given that the thickness of the solutions decreased with the value of G .

Nevertheless, motivated by this effect, they further considered large B rational

map configurations based on N shells of smaller baryon number rational maps, first introduced in [157]. These multilayer field configurations, combined with additional approximations on the profile and metric functions [132, 133], allowed to obtain solutions for the physical values of G . Furthermore, the values of the maximal baryon number increased to $\approx 10^{56}$, however, the NS obtained had small values of the masses and radii [172], compared to the typical values for a NS.

A much more promising result in the NS description within the Skyrme model concerns a new type of solutions called Skyrme crystals. A detailed explanation on how these configurations are constructed will be given in the next chapter, but at this point we will only comment the main results of their application to NS modelling.

The lowest energy configuration (up to now) in the massless standard Skyrme model was found almost simultaneously in two different works [77, 136] in 1988. This solution is an infinite lattice of unit cells, each one with $B = 4$, and its energy is just a 3.8% above the unattainable BPS bound. Hence, it represents a suitable configuration to describe infinite nuclear matter and to be a model for NS from the standard Skyrme model.

The energy of this solution depends on the size l of the unit cell, and it is a convex function which has a single minimum value E_0 at some value l_0 of the length. It has been computed for a large range of values of l , and follows the simple relation [77],

$$E(l) = E_0 \left[\left(\frac{l}{l_0} + \frac{l_0}{l} \right) \frac{(1 - \varepsilon)}{2} + \varepsilon \right], \quad (2.23)$$

where $E_0 = 727.4$ MeV, $l_0 = 1.666$ fm are precisely the energy and the lattice length of the minimum respectively, and $\varepsilon = 0.0515$. In this parametrization, l is the size of the unit cell with volume $V = l^3$, which has $B = 1$ within it. The parameters (f_π, e) used to obtain this curve correspond to the standard values (2.21).

The Skyrme crystal may also be used to obtain NS, but from a different approach. Rather than solving the full EHS system, an EOS might be obtained

from a mean-field (MF) approximation using the thermodynamical definitions,

$$\rho = \frac{E}{V}, \quad p = -\frac{dE}{dV}, \quad n_B = \frac{B}{V}, \quad (2.24)$$

where V is the volume of the unit cell. The three variables ($\rho(l)$, $p(l)$, $n_B(l)$) are functions of the lattice length, hence, we may associate a value of the pressure, energy and baryon densities to each value of l and find the relations $\rho(p)$ and $n_B(p)$.

Then we assume the stress-energy tensor of a perfect fluid,

$$T^{\mu\nu} = (\rho + p)u^\mu u^\nu - pg^{\mu\nu}, \quad (2.25)$$

where the pressure and the energy density are related by the EOS extracted from the Skyrme crystal. NS are obtained following the TOV formalism [181, 223, 229], which is the standard approach to describe the stellar equilibrium in GR. The details of the TOV formalism are explained in Appendix B.

The resulting NS yield better values than the previous attempts, leading to a maximal mass of $M_{\max} = 1.49M_\odot$, with a radius of $R \approx 10$ km and $B \approx 2 \times 10^{57}$ [171]. The whole MR curve has been obtained for comparison with other Skyrme EOS, and it is shown in Fig. 2.1.

These results have been consistently considered as the minimal energy configuration and they have definitely improved the NS description within the Skyrme model. However, the maximal mass turns out to be quite small compared to the NS measurements, which require a maximal mass of $2M_\odot$ at least. Moreover, as we have seen in the Introduction, a crystalline configuration is an acceptable description in the outer crust of NS, but it is not expected to be present for the innermost layers.

2.2 The BPS Skyrme model

The perspective of the Skyrme model as an EFT of QCD at low energies suggest that the Lagrangian (2.4) only considers the first contributions of an expansion in field derivatives. Therefore, there is no reason not to consider additional

higher derivative terms as corrections to the model to solve the problems mentioned above.

The most natural extension is a term with six derivatives of the field. Among the possibilities, as also occurred with \mathcal{L}_4 , the only term that provides a Hamiltonian of second order in time derivatives is the following [16, 17],

$$\mathcal{L}_6 = -\lambda^2 \pi^4 B_\mu B^\mu. \quad (2.26)$$

We will refer to this as the sextic term which, when combined with a generic potential term $\mathcal{L}_0 = -\mu^2 \mathcal{U}$, yields a special model with very interesting properties.

The coupling constant λ^2 of the sextic term is a new parameter that may be used to fit nuclear observables from the solutions. In fact, we may relate this parameter to the coupling constant between the pions and the ω meson in an extended version of the Skyrme model coupled to vector mesons [27, 161–163], hence, it is possible to give an estimation of its value. More specifically, when the ω meson is integrated out in the extended Lagrangian, the interaction term yields a sextic term with $\lambda^2 = g_\omega^2 / (2\pi^4 m_\omega^2)$ [7], where m_ω and g_ω are the mass and coupling constant of the ω meson respectively. For the empirical values $m_\omega = 783$ MeV and $g_\omega^2/(4\pi) \sim 10 - 12$ [162], we obtain $\lambda^2 \sim 8 - 10$ MeV fm³.

In this section, we will consider different potential terms, then the parameter μ^2 will have very different values. For the pion mass potential term (2.22) we identify $\mu^2 = m_\pi^2 f_\pi^2/4$, so it will be interesting to study how the parameters change when they are used in the standard or in the BPS Skyrme model. We will also compare them when they are fitted to isolated atomic nuclei or to infinite nuclear matter and NS.

Despite we are going to study a different Lagrangian in this section, all the previous topological considerations on the Skyrme field are independent of the theory. Hence, the \mathcal{L}_{60} model still allows the existence of topological solitons. Besides, the solitons are also energetically stable in this theory due to the

opposite scaling of the sextic and the potential term:

$$E_{60}(\sigma_s) = \frac{E_6}{\sigma_s^3} + \sigma_s^3 E_0, \quad (2.27)$$

$$\partial_{\sigma_s} E_{60} = 0 \longrightarrow \sigma_s^6 = \frac{E_6}{E_0} \neq 0. \quad (2.28)$$

The BPS bound, and the corresponding BPS equation, may also be obtained in this model as follows,

$$E = \int d^3x \left[\lambda^2 \pi^4 (B^0)^2 + \mu^2 \mathcal{U} \right] = \quad (2.29)$$

$$\begin{aligned} & \int d^3x \left[\lambda^2 \pi^4 (B^0)^2 + \mu^2 \mathcal{U} \pm 2\lambda\mu\pi^2 B^0 \sqrt{\mathcal{U}} \right] = \\ & \int d^3x \left[(\lambda\pi^2 B^0 - \mu\sqrt{\mathcal{U}})^2 + 2\lambda\mu\pi^2 B^0 \sqrt{\mathcal{U}} \right] \geq \lambda\mu|B| \int \text{vol}_{S^3} \sqrt{\mathcal{U}}. \end{aligned} \quad (2.30)$$

To obtain the bound in the last line we have made use of the following property of B^0 :

$$\text{vol}_{\mathbb{R}^3} B^0 = \frac{U^*(\text{vol}_{S^3})}{2\pi^2}. \quad (2.31)$$

Specifically, in cartesian coordinates $\text{vol}_{\mathbb{R}^3} = d^3x$.

Then, the BPS equation is:

$$\lambda\pi^2 B^0 = \mu\sqrt{\mathcal{U}}. \quad (2.32)$$

The main property of this model is the possibility to obtain solutions to the BPS equation. For this reason, the \mathcal{L}_{60} model is also known as the *BPS model*.

Moreover, the BPS equation may be solved analytically for any value of B . The reason for the integrability lies in the infinite amount of symmetries on the target space [8]. In particular, the sextic term is the pullback of the volume form on the target space, S^3 in our case. Therefore, all diffeomorphisms that preserve the volume form of this manifold will not produce changes on the

topological current, therefore, the sextic term remains invariant.

This volume-preserving diffeomorphisms (VPD) invariance is broken in the BPS model once the potential term is introduced. However, potential terms which only depend on the trace of the Skyrme field, $\mathcal{U} := \mathcal{U}(\text{Tr}\{U\})$, like the pion-mass term (2.22), are still invariant under area-preserving diffeomorphisms on the S^2 . This may be checked from the expansion (2.3) of U , such that any transformation on the pion fields that leaves the norm π invariant has no effect on the trace of the field, given that $\text{Tr}\{U\} \sim \sigma \sim 1 - \pi^2$. These infinitely many symmetries are responsible for the integrability of the model for any value of B [16].

Furthermore, the static energy functional (2.29) of the BPS model satisfies a similar set of symmetries as well. Specifically, all volume-preserving diffeomorphisms on the base space \mathbb{R}^3 will not affect the energy functional [6]. This is trivial to see for the potential term, which does not depend on the base space coordinates. The sextic term, on the other hand, depends on the spatial coordinates, but it is also invariant under these transformations since the topological current contracts the indices of the derivatives with a Levi-Civita symbol. Therefore, it has the same structure as the base space volume form, $d^3x \sim \epsilon_{ijk}\partial_i U \partial_j U \partial_k U$. These symmetries imply that any change of coordinates which remain the volume invariant will have zero cost of energy. As a consequence, all the solutions of the BPS model may have arbitrary shapes. This facilitates the resolution of the BPS equation since we may always use the generalization of the hedgehog ansatz (2.18) to higher topological charges,

$$U : (r, \theta, \phi) \mapsto (f = f(r), \Theta = \theta, \Phi = B\phi), \quad (2.33)$$

which is called the axially symmetric ansatz when $B > 1$.

In addition, the VPD invariance on the base space are precisely the symmetries of an incompressible ideal fluid. This suggests a close connection to nuclear matter due to the success of the liquid drop model in the description of atomic nuclei. Moreover, the spherical symmetry for arbitrarily high B solutions totally differs from the shapes of the solutions obtained in the standard Skyrme model, but it is in excellent agreement with the experimentally known shapes of the

large baryon number nuclei.

Besides, solutions to the BPS equation satisfy the $E \propto |B|$ energy curve, implying that the binding energies are exactly zero. Although a realistic description of nuclear matter requires non-zero binding energies, these are indeed very small $\sim 1\%$. Then, the BPS model may serve as the starting point of a more complete model that reproduces the correct binding energies. One possibility might be to consider small perturbations around the BPS model, in a kind of *near-BPS model* [12, 49, 60].

Another fundamental property of the BPS model lies in the stress-energy tensor, which may be extracted from the action [9]

$$\begin{aligned} T^{\mu\nu} = & -\frac{2}{\sqrt{|g|}} \frac{\delta S}{\delta g_{\mu\nu}} = -\frac{2}{\sqrt{|g|}} \frac{\delta \int d^4x \sqrt{|g|} \mathcal{L}}{\delta g_{\mu\nu}} = \\ & 2\lambda^2 \pi^4 \frac{B^\mu B^\nu}{|g|} - \left(\lambda^2 \pi^4 g_{\alpha\beta} \frac{B^\alpha B^\beta}{|g|} - \mu^2 \mathcal{U} \right) g^{\mu\nu}. \end{aligned} \quad (2.34)$$

The following variations of the metric are useful to derive the previous result,

$$\delta \left(\frac{1}{\sqrt{|g|}} \right) = -\frac{1}{\sqrt{|g|}} \delta \sqrt{|g|} \quad (2.35)$$

$$\delta \sqrt{|g|} = \frac{1}{2} \sqrt{|g|} g^{\alpha\beta} \delta g_{\alpha\beta}. \quad (2.36)$$

Recall that in a generic (non-flat) spacetime, the topological current is actually $\tilde{B}^\mu = B^\mu / \sqrt{|g|}$, where g is the determinant of the metric and B^μ is the flat spacetime (2.7) current. Now, considering the following definitions:

$$u^\mu = \frac{B^\mu}{\sqrt{g_{\alpha\beta} B^\alpha B^\beta}}, \quad (2.37)$$

$$p = \lambda^2 \pi^4 g_{\alpha\beta} \frac{B^\alpha B^\beta}{|g|} - \mu^2 \mathcal{U}, \quad \rho = \lambda^2 \pi^4 g_{\alpha\beta} \frac{B^\alpha B^\beta}{|g|} + \mu^2 \mathcal{U}, \quad (2.38)$$

the stress-energy tensor has an expression equivalent to a perfect fluid (2.25). The identification of the energy density ρ yields precisely the integrand of the

energy functional (2.29) for static field configurations. However, the identification of p is, for the moment, just a mathematical definition, so we still cannot consider it as the physical pressure of the system.

The conservation of the stress-energy tensor in a flat spacetime for static solutions implies that p is constant,

$$\partial_i T^{ij} = \delta^{ij} \partial_i p = 0 \rightarrow P := p \equiv \text{const.} \quad (2.39)$$

The pressure definition in (2.38) generalizes the BPS equation (2.32). Indeed, this generalized equation may be obtained by integrating the field equations [9], where P is precisely the integration constant:

$$\lambda \pi^2 B^0 = \mu \sqrt{\mathcal{U} + P/\mu^2}. \quad (2.40)$$

We will only consider the positive P case.

The volume and energy of the solutions to the non-BPS equation (2.40) may be easily obtained:

$$V(P) = \frac{\pi^2 \lambda}{\mu} |B| \left\langle \frac{1}{\sqrt{\mathcal{U} + P/\mu^2}} \right\rangle_{S^3}, \quad (2.41)$$

$$E(P) = \pi^2 \lambda \mu |B| \left\langle \frac{2\mathcal{U} + P/\mu^2}{\sqrt{\mathcal{U} + P/\mu^2}} \right\rangle_{S^3}, \quad (2.42)$$

where we have adopted the notation used in [12] for the integration of a generic function on the S^3

$$\langle F \rangle_{S^3} := \frac{1}{2\pi^2} \int \text{vol}_{S^3} F. \quad (2.43)$$

Interestingly, neither the volume nor the energy depend on the specific solution. In fact, solutions with the same pressure will occupy the same volume.

It is now easy to show that P actually is the pressure of the system.

$$\left. \frac{\partial E}{\partial V} \right|_B = \frac{\partial E / \partial P}{\partial V / \partial P} = -P. \quad (2.44)$$

Surprisingly, the BPS model yields the standard thermodynamical relation naturally, although the variables E , V and p have been introduced from a pure field theoretical definition. Thus, (2.38) is the generalization of the BPS equation to the non-zero pressure case in a generic spacetime, where p is not constant anymore.

Combining the expressions in (2.38), we obtain a relation between the energy density and the pressure of the system, *i.e.*, the EOS of the BPS model,

$$\rho = p + 2\mu^2 \mathcal{U}. \quad (2.45)$$

Recall that the potential term depend on the Skyrme field, so the energy density is not only a function of the pressure. Hence, the BPS Skyrme model EOS is non-barotropic.

Another relation may be extracted by adding the expressions in (2.38),

$$\rho = -p + 2\lambda^2 \pi^4 (B^0)^2. \quad (2.46)$$

Since B is the baryon number in the Skyrme model, it is natural to identify B^0 with the baryon density n_B . Indeed, this expression represents the Euler thermodynamical relation, from which we may identify the baryon chemical potential of the BPS model, $\mu_B = 2\lambda^2 \pi^4 B^0$.

Finally, we have seen that the spin and isospin quantization in the standard Skyrme model allows to reproduce some interesting phenomenology of nuclear matter. In the BPS model, the inclusion of these and further effects is much easier, due to the spherical symmetry, and produces an extremely accurate reproduction of the nuclear binding energies [13, 14].

2.2.1 Neutron stars in the BPS Skyrme model

NS have also been obtained in the BPS model [10, 11], leading to promising results for their study within the Skyrme model. The main advantage of the BPS model is that, owing to the symmetries, the ground state solutions may be parametrized with the ansatz (2.33) for arbitrarily high B . Indeed, this is compatible with the spherically symmetric ansatz of the spacetime metric

(B.12), hence, we may solve the full EHS system without MF approximation. Nonetheless, this fact may also be regarded as an interesting scenario to compare the results from a MF approximation and the full-theory (FT) [11].

In the MF approximation we use the thermodynamical definitions of the energy and baryon densities,

$$\bar{\rho}(p) = \frac{E(p)}{V(p)} = \mu^2 \frac{\left\langle \frac{2U+p/\mu^2}{\sqrt{U+p/\mu^2}} \right\rangle}{\left\langle \frac{1}{\sqrt{U+p/\mu^2}} \right\rangle}, \quad (2.47)$$

$$\bar{n}_B(p) = \frac{B}{V(p)} = \frac{\mu}{\pi^2 \lambda \left\langle \frac{1}{\sqrt{U+p/\mu^2}} \right\rangle}. \quad (2.48)$$

The dependence on the pressure is naturally introduced from the non-BPS equation (2.40), however, once the skyrmions are coupled to gravity, the pressure is not constant anymore.

The parameters (λ^2, μ^2) of the BPS model must be fixed to some values in order to solve the TOV system. Given that we want to describe NS, instead of the proton and Δ masses, we may fit the parameters to reproduce the saturation energy and baryon density of infinite nuclear matter (INM),

$$E_0 = 923 \text{ MeV}, \quad n_0 := \frac{\rho_0}{m_N} = 0.16 \text{ fm}^{-3}. \quad (2.49)$$

This choice seems more appropriate for our purpose since nuclear matter inside NS is more similar to an infinitely extended system than to isolated nuclei. An extensive explanation of the INM properties will be given in the next chapter.

Different potentials yield different expressions for the densities, specifically, we will compare between three potentials with their respective value for the parameters:

- Step-Function potential

$$\mathcal{U} := \Theta = \Theta(\text{Tr}\{\mathbb{I} - U\}) \quad (2.50)$$

From a phenomenological point of view, this is not a correct choice given that a constant potential term yields a linear EOS in the BPS model, which is not expected at all in the whole interior of NS. Besides, the sharp behaviour of this potential in the surface of NS represents the lack of a crust, which neither is correct. However, this case is interesting (and helpful) because the EOS obtained in the MF and FT are the same. The parameters obtained from this potential are,

$$\mu^2 = 73.8335 \text{ MeV/fm}^3, \quad \lambda^2 = 29.6083 \text{ MeV fm}^3. \quad (2.51)$$

- Pion mass potential

$$\mathcal{U} := \mathcal{U}_\pi = 1 - \cos(f) \quad (2.52)$$

The obvious choice is the pion mass term, which was introduced in the last section (2.22). This potential has a non-constant behaviour and yields a nontrivial EOS. The parameters obtained in this case are,

$$\mu^2 = 92.2919 \text{ MeV/fm}^3, \quad \lambda^2 = 25.6836 \text{ MeV fm}^3. \quad (2.53)$$

As mentioned before, the physical constants of the pion may be identify from $\mu^2 = \frac{m_\pi^2 f_\pi^2}{4}$, which yields $f_\pi = 385.93 \text{ MeV}$ when $m_\pi = 138 \text{ MeV}$. This indicates that the parameters of the BPS model must be significantly larger than the physical values to describe nuclear matter, however, the introduction of other terms ($\mathcal{L}_2, \mathcal{L}_4$) might alleviate this situation.

- Squared pion mass potential

$$\mathcal{U} := \mathcal{U}_\pi^2 = (1 - \cos(f))^2 \quad (2.54)$$

This potential has previously been studied for isolated skyrmions, and the interest lies in its repulsive behaviour [110]. Here, it represents a different case that yields an interesting EOS to compare. The parameters obtained differ substantially from the previous values,

$$\mu^2 = 147.6670 \text{ MeV/fm}^3, \quad \lambda^2 = 14.8042 \text{ MeV fm}^3. \quad (2.55)$$

We show in Fig. 2.1 the EOS curves for the different potentials explained before, and their explicit expressions may be found in [11]. Actually, since the EOS is non-barotropic in the FT cases, a different curve is obtained for every value of the baryon number, hence, we first have to solve the Einstein equations to extract an EOS. The curves of the FT computations represented in Fig. 2.1 have been obtained for the corresponding maximal mass in each case. For comparison with the stars obtained from the BPS model, we also consider the EOS obtained from the crystal solution in the standard Skyrme model using the standard parameters (2.23) and the same crystal curve when fitted to the nuclear saturation point (2.49). The specific values of the parameters for this last fit are $f_\pi = 138.17$ MeV, $e = 4.60$.

The whole set of EOS covers a wide range of different possibilities. The first observed feature is that all the MF cases have a nonzero value of the energy density in the zero pressure limit. This is directly related to the fact that the low density regime is not correctly reproduced in these models. For instance, the Skyrme crystal reaches the $p = 0$ equilibrium point at a finite value of the lattice length l_0 with a nonzero value of the energy E_0 .

A correct description for lower densities would not present a minimum value of the energy, instead the $E(L)$ curve decreases asymptotically for larger lengths than the minimum. This, in NS terminology, is translated into the absence of crust in the resulting NS. On the other hand, the FT curves seem to have the correct $\rho \rightarrow 0$ limit for vanishing pressure, as it occurs with the standard nuclear physics EOS obtained from the different methods explained in the Introduction. We use for comparison the Barcelona-Catania-Paris-Madrid (BCPM) [208] EOS, since it reaches the minimal accepted values for the mass and satisfies the most fiducial radius constraints. This EOS is based on the combination of the Brueckner-Hartree-Fock approach for the inner parts of the NS, and the BCPM energy density functional for the inhomogeneities in the crust.

Additionally, the stiffness of each EOS may be easily compared from the same plot. It is often said that an EOS is softer or stiffer than other EOS when the energy density is, in general, larger or smaller for the same values of the pressure respectively. For instance, in our case we would conclude that the Skyrme

crystal EOS is clearly softer than the BPS EOS in the FT case. Indeed, a careful analysis on the stiffness may extract valuable information of the masses and radii of the resulting NS. Specifically, the softer an EOS is in the range of $p \gtrsim 1 \text{ MeV/fm}^3$, the more compressed the nuclear matter will be, therefore, soft EOS yield NS with smaller radii. Besides, the accumulation of nuclear matter in the core of the NS induce an earlier gravitational collapse, producing much smaller maximal masses.

The TOV equations may be solved for each EOS in the MF case as explained in Appendix B, and the MR curve is obtained. On the other hand, the resolution of the EHS system in the FT case is slightly different. Since the stress-energy tensor of the BPS model is already a perfect fluid, the expressions of the differential equations obtained from the TOV system apply to this case too. The energy density and pressure are defined in (2.38), besides, we also have naturally identified $n_B \equiv B^0$. However, these definitions depend on the Skyrme profile function, hence, in order to close the TOV system of equations, a further equation must be added to determine the Skyrme field. We take the definition of the pressure (2.38) as the differential equation for the profile function.

In the MF case, the pressure in the centre of the star p_c determines the solution, but in the FT the baryon number B of the star is the input parameter, and determines the solution. Then, the system must be solved using a shooting method for the value of the pressure in the center of the star, such that the condition $p(R) = 0$ is fullfilled.

The MR curves of both the MF and FT cases are shown in the right plot of Fig. 2.1 for different values of the p_c and B respectively. We also added the MR curve obtained from the crystal configuration in the standard Skyrme model for the original parameters and the nuclear saturation fit.

The main feature in the MR plot is the wide difference between the maximal masses attained in the BPS and the standard Skyrme models. Whilst the smallest mass for the BPS model obtained is $\approx 3M_\odot$ for the squared potential in the MF case, the standard Skyrme model hardly reaches the values $1.5M_\odot$. This completely agrees with the previous analysis on the stiffness of the EOS. Besides, the small value of the maximal mass in the standard Skyrme model is a problem

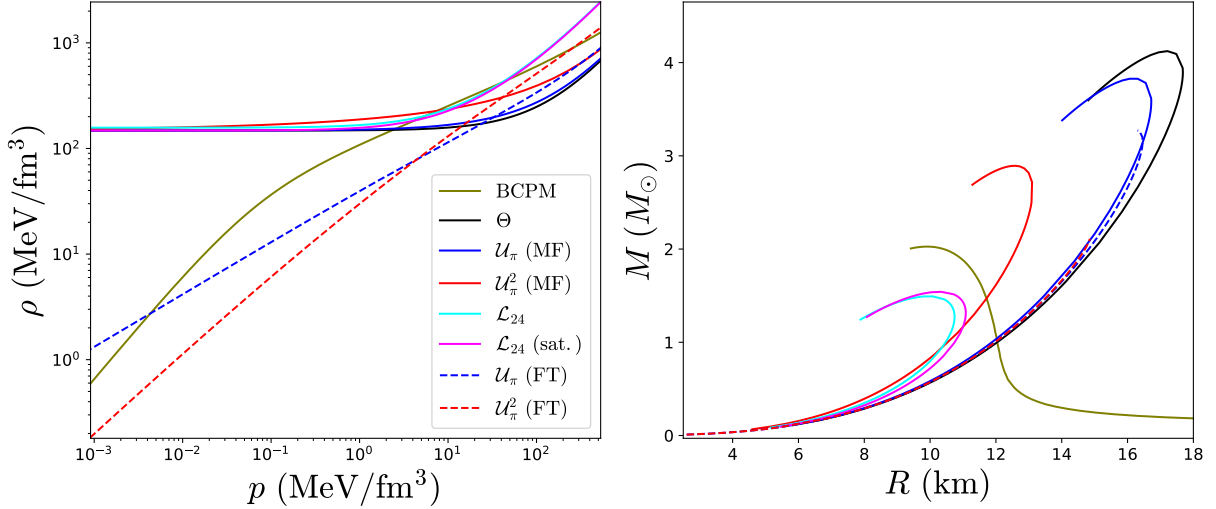


Figure 2.1: *Left:* The EOS for the different models considered so far, in the MF and FT approaches. In the FT cases we considered the EOS resulting from the maximal mass stars. *Right:* The MR curves from the same models.

of the model itself, given that we obtain quite similar masses for different choices of the parameters. Although the results obtained from the BPS model are much higher than the current measurements, this is indeed a nice result since it is actually really hard for standard nuclear physics EOS to reach very high masses. Interestingly, these computations motivate the combination of both submodels given that desirable values for the maximal masses lie precisely in the middle $\sim 2 - 2.5 M_\odot$.

The next interesting feature concerns the low mass region in the MR curve. All the Skyrme EOS satisfy the limit $M(R \rightarrow 0) \rightarrow 0$, contrary to the BCPM case. This, as explained before, is due to the lack of a crust in the Skyrme EOS, *i.e.*, because of the limit $\rho(p = 0) \neq 0$. Actually, the EOS obtained from the FT cases represented in Fig. 2.1 seem to reproduce the correct behaviour in the zero pressure limit, however, the MR curves do not present the typical behaviour of NS with crust, like BCPM. Indeed, all the EOS obtained for every baryon number satisfy the correct zero pressure limit in the FT cases. The reason for these apparently contradictory results, is that the FT cases of the BPS model are actually special cases in which different EOS may be defined. The relations $\rho(p)$ of every star are unique EOS that only apply for the specific solution, but we may associate the values of the pressure and energy density at the centre of each NS to construct a new global $\rho_c(p_c)$ EOS.

We show the new global EOS for the FT cases in Fig. 2.2, which display the same behaviour as the EOS of the MF cases. Therefore, we conclude that the correct EOS to study the presence of crust is the $\rho_c(p_c)$ relation. The corresponding EOS obtained from the solutions for different values of mass are also plotted to show that they all emerge from the global EOS and exhibit the zero density limit. We remark that the existence of different EOS in the BPS model is due to the field-dependent EOS, which is not a frequent phenomenon, but it is a more general statement that might apply for other non-barotropic EOS.

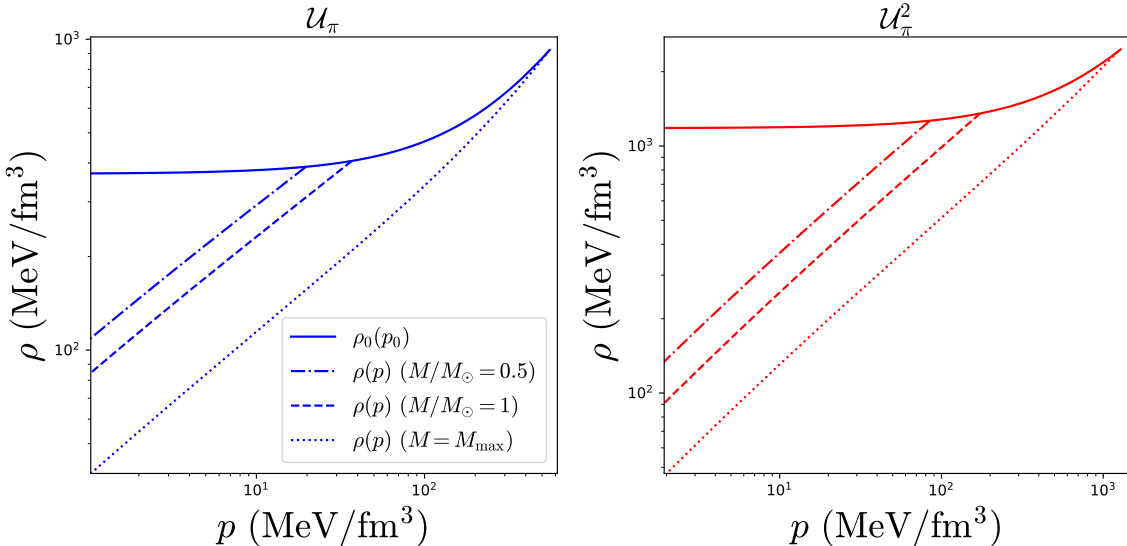


Figure 2.2: Global $\rho_c(p_c)$ EOS for the two potentials from the FT cases in the BPS Skyrme model which determines the presence or not of a crust. We also added three EOS corresponding to NS solutions of different mass.

Finally, we want to show how the different EOS affect some of the solutions of the TOV system in Fig. 2.3. For this purpose, we consider the Θ potential with nonzero energy density at the surface of the NS, the pion mass potential \mathcal{U}_π with the correct zero pressure limit of the energy density but not for the derivative, and the BCPM and squared potential which both reproduce the correct limit for the energy density and its derivative. We plot the g_{rr} metric function and the mass, pressure and energy density profiles inside the $\sim 1.4M_\odot$ NS for each model.

The metric function $B(r)$ is determined by the compactness function of the star. The BCPM and FT curves show a nontrivial behaviour for this function with a maximum value in the outer parts ($r/R \geq 0.6$), contrary to the monotonously increasing simple trend in the MF case. The mass and energy density functions

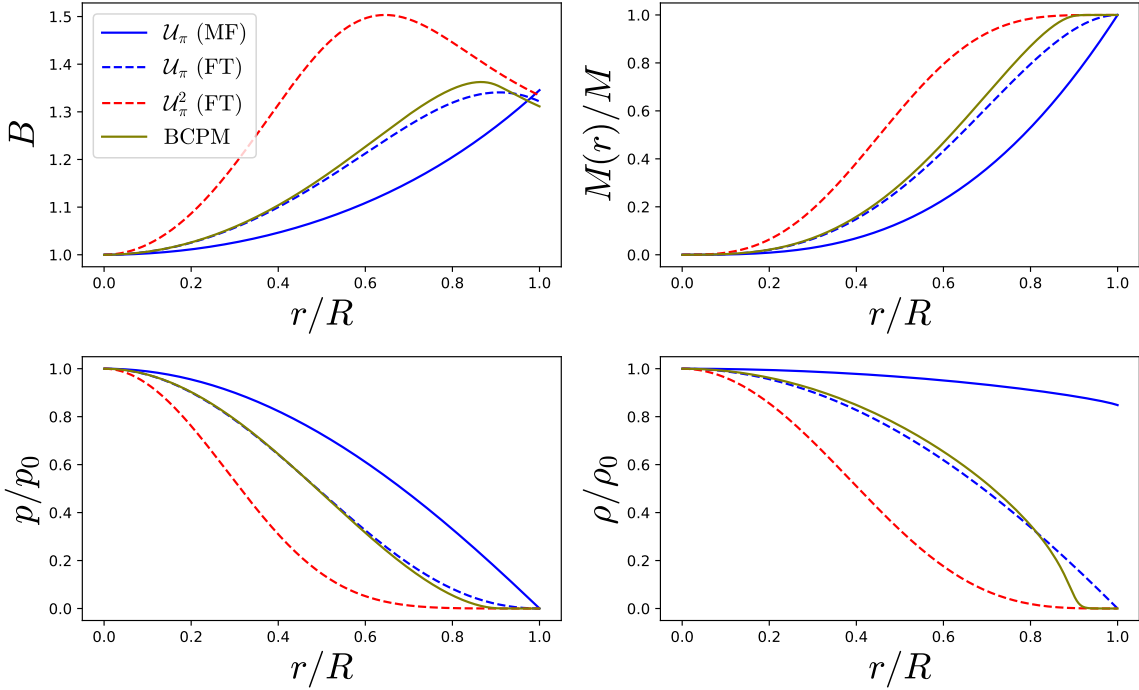


Figure 2.3: Profile functions of the solutions obtained from the TOV system for a single NS. Here we compare between three extremely different EOS and a realistic nuclear physics EOS.

mainly show how the mass is distributed along the radius of the NS. In the MF case, the energy density profile is almost constant, which is not a realistic description for a NS and induces the $M \propto r^3$ mass curve. The remarkable result is the highly concentrated core of the quadratic potential with the 90% of the mass reached already at the 67% of the radius of the star, whilst for the BCPM and FT pion mass potential, the same ratio of the mass is attained at the 85% of the radius. The three different behaviours may also be seen in the pressure plot, which always reaches the zero value at the surface of the star.

2.2.1.1 BPS Skyrme neutron stars in modified gravity

NS are affected by intense gravitational fields (namely, by high curvature effects) more strongly than any other currently observable physical system in the universe. They are, therefore, perfect natural laboratories to investigate the consequences of this high curvature. In particular, they allow us to study deviations from GR and to constrain the free parameters in theories describing these deviations, or even to discard them by comparing their predictions with the observed data. Such deviations, or Extended Theories of Gravity (ETG), are completely natural from an effective field theory point of view, where quan-

tum gravity corrections should induce further terms in the low-energy effective action of the gravitational field, in addition to the Einstein–Hilbert (EH) action. The $f(R)$ theories [76, 85, 175, 213] are a specific class of these ETG in which the EH action linear in the Ricci scalar R is replaced by a generic function $f(R)$. These theories are motivated, first, by their relative simplicity when it comes to solve the modified Einstein equations and, second, from a cosmological point of view, by the possibility to explain the acceleration of the universe (the dark energy problem) or the abundance of non-baryonic matter in the galaxies (the dark matter problem). These motivations are based on the presence of an additional degree of freedom, which is usually related to a scalar field known as the scalaron. Besides, these $f(R)$ theories lead to modified Einstein equations which are of more than second order, but they avoid the Ostrogradski instability [182, 235].

In particular, we shall consider the theory

$$f(R) = R - \alpha R^2, \quad (2.56)$$

also known as the Starobinsky model [215]. The reason for this choice is that standard GR is in excellent agreement with all current astrophysical and cosmological observations. Any extension of GR, therefore, should approach GR in the limit of small curvature, but the most natural way to achieve this is by a power series expansion $f(R) = R + \sum_{i=2}^{\infty} c_i R^i$. Then, the term quadratic in R is the leading-order correction to the EH action.

The $f(R)$ theories consist in the following modification of the EH action,

$$S = \frac{1}{16\pi G} \int d^4x \sqrt{|g|} f(R) + S_{\text{matter}}, \quad (2.57)$$

where $f(R)$ is a generic function of the Ricci scalar R . GR can be recovered by setting $f(R) = R$.

The new Einstein equations may be obtained, as we did in Appendix B, by

varying this action with respect to the metric. Following [53],

$$\begin{aligned} \delta S = & \int d^4x \left[\delta \sqrt{|g|} f + \sqrt{|g|} \delta f \right] = \\ & \int d^4x \sqrt{|g|} \left[-\frac{1}{2} f g_{\mu\nu} \delta g^{\mu\nu} + f_R \delta R \right] = \\ & \int d^4x \sqrt{|g|} \left[-\frac{1}{2} g_{\mu\nu} f + f_R R_{\mu\nu} - (\nabla_\mu \nabla_\nu - g_{\mu\nu} \nabla_\alpha \nabla^\alpha) f_R \right] \delta g^{\mu\nu}, \end{aligned} \quad (2.58)$$

where we have defined $f_R = \partial f / \partial R$ and for the last expression we have made use of the results (B.5–B.9) from Appendix B. Then, the modified Einstein equations in $f(R)$ gravity are

$$\tilde{G}_{\mu\nu} = 8\pi G T_{\mu\nu}, \quad (2.59)$$

$$\tilde{G}_{\mu\nu} = f_R R_{\mu\nu} - \frac{1}{2} g_{\mu\nu} f - (\nabla_\mu \nabla_\nu - g_{\mu\nu} g^{\alpha\beta} \nabla_\alpha \nabla_\beta) f_R. \quad (2.60)$$

Since we want to consider static NS we maintain the spherically symmetric ansatz for the spacetime metric. Besides, since in the BPS model the baryon number appears explicitly, we will denote it as N only in this section, to avoid confusion with the metric component B . Additionally, in order to distinguish between the Ricci scalar and the radius of the stars we will denote, along this section, as R_s the last one.

The first difference with respect to GR is that now the Ricci scalar is not fixed (algebraically) just by the value of the pressure and the energy density. Instead, tracing the equation (2.60) we obtain a second order differential equation for R that we have to solve,

$$R'' = -\frac{f_{3R}}{f_{2R}} R'^2 - \frac{B}{3f_{2R}} (4\pi G(\rho - 3p) + 2f - f_R R) + \left(-\frac{A'}{2A} + \frac{B'}{2B} - \frac{2}{r} \right) R' \quad (2.61)$$

The key point is that we now have an additional degree of freedom in comparison to the GR case, precisely provided by the $f_R(R)$ term. The components of the generalized Einstein tensor may be computed, and the equations for the metric components A and B can be obtained combining the (t, t) and (r, r) components

as in the GR case,

$$\frac{A''}{A} = \frac{A'B'}{2AB} + \frac{A'^2}{2A^2} + \frac{2B'}{rB} + \frac{2}{f_R} \left(-4\pi GBp + \frac{Bf}{2} + \left(\frac{A'}{2A} + \frac{2}{r} \right) f_{2R}R' \right) \quad (2.62)$$

$$B' = \frac{2rB}{3f_R} \left[4\pi GB(\rho + 3p) - Bf - f_R \left(-\frac{BR}{2} + \frac{3A'}{2Ar} \right) - \left(\frac{3A'}{2A} + \frac{3}{r} \right) f_{2R}R' \right] \quad (2.63)$$

Following our notation we have defined $f_{2R} = \partial^2 f / \partial R^2$, and we denote $d/dr \equiv '$. Finally an equation for the pressure of the star is obtained from the conservation of the stress-energy tensor $\nabla_\mu T^{\mu\nu} = 0$, which leads to the same equation.

We may prove that $f(R)$ theories are completely equivalent to scalar-tensor theories. This will be important to fix the sign of the parameter α in our modified gravity.

The Brans-Dicke action [65] takes the form

$$S_{BD} = \frac{1}{16\pi G} \int d^4x \sqrt{|g|} \left[\phi R - \frac{\omega}{\phi} g^{\mu\nu} \nabla_\mu \nabla_\nu \phi - V(\phi) \right]. \quad (2.64)$$

To see the correspondence, we can rewrite the action (2.57) in a new dynamically equivalent form with a new scalar field χ ,

$$S = \frac{1}{16\pi G} \int d^4x \sqrt{|g|} (f(\chi) + f'(\chi)(R - \chi)). \quad (2.65)$$

From the scalar field equation we find that $R = \chi$ iff $f_{2R}(\chi) \neq 0$, then redefining the scalar field as $\phi := f'(\chi)$ and $V(\chi) = \chi(\phi)\phi - f(\phi)$ we arrive at the Brans-Dicke action for $\omega = 0$.

The mass of the scalar field ϕ may be defined from the action (2.64), by obtaining its equation of motion and identifying the terms with those of the Klein-Gordon equation,

$$\square\phi - \frac{1}{3+2\omega} (8\pi GT + \phi V'(\phi) - 2V(\phi)) = 0. \quad (2.66)$$

The equation of motion for the field can be expressed as a Klein-Gordon equa-

tion, defining an effective potential [75, 90], $dV_{\text{eff}}/d\phi = -\frac{1}{3+2\omega}(\phi V' - 2V)$. Then the mass is related to the second derivative of this effective potential, and equation (2.66) admits the usual Yukawa-like solution $\phi(r) \propto \exp\{-m(\phi)r\}/r$ with m defined as explained above. Now we can obtain the mass of the new degree of freedom in our theory in terms of $f(R)$ and its derivatives. Setting $\omega = 0$ and the potential given above we have for a generic $f(R)$ theory [90]

$$m^2 = -\frac{f_R - R f_{2R}}{3 f_{2R}}. \quad (2.67)$$

In our case $f(R) = R - \alpha R^2$, we obtain that the mass of the field is $m^2 = \frac{1}{6\alpha}$, thus the sign of α must be positive in order to have a real scalar field.

In order to solve the system of differential equations, we need first to know the boundary conditions of all the variables and also of their derivatives. These conditions are obtained analysing the Einstein equations (2.60) and the system (2.61–2.63) and (B.15). As explained in Appendix B, we expand the field variables close to the center in even powers of r , but in this case the Ricci scalar is also added to the system.

From the (θ, θ) component of (2.60) we immediately obtain $b_0 = 1$. In $f(R)$ gravity we still have the problem of finding the value of a_0 , because the system of differential equations can be re-expressed in terms of A'/A . Therefore, a_0 is again determined only up to a multiplicative factor, so we give it an arbitrary value for the integration.

Again in the MF case, the pressure in the centre p_c is an input parameter. This means that for each (not too large) value p_c we will find a NS solution. In the FT case, on the other hand, the input parameter is the baryon number N , so for fixed N there is only one correct value for the pressure in the center, which we have to determine with a shooting method. Recall that we have the additional differential equation (2.38) of the pressure in the FT case, which determines the Skyrme profile function.

Finally, we need the initial value R_0 of the Ricci scalar. Unlike in GR, the Ricci scalar is now not determined algebraically but satisfies its own second-order differential equation and, therefore, we do not know its initial value. The way

to solve this problem is, again, by a shooting method imposing the Minkowski spacetime condition at large distances, $R \xrightarrow{r \rightarrow \infty} 0$. In order to be able to satisfy this condition, we have to integrate the system up to large distances, in contrast to the GR case where we just have to integrate until the radius of the star.

The shooting to determine R_0 required by $f(R)$ gravitational theories has been solved already for cases which are similar to our MF case, *i.e.*, with a barotropic EOS (see for example [37, 129]). On the other hand, we have to solve a double shooting problem for the pressure and the Ricci scalar in the FT case. To solve this problem, we perform several shootings for the pressure until a sufficient accuracy is reached, then we change the value of the Ricci scalar. Besides, when we change the value of the Ricci scalar we also constrain the range of values in the shooting of the pressure. Repeating this iteration we obtain the required solutions.

It is crucial to constrain the pressure after each iteration when solving the system because, as we explained, the solutions of the scalar field are Yukawa-like, *i.e.*, exponential functions. We will have both the positive and the negative ($\exp(\pm mr)$) solutions, and as we want a finite solution and the mass is a real value, the growing exponential must be cancelled, but this can be obtained only with a very accurate initial condition for R . Another interesting feature that supports this argument is found when we change the values of α . When α grows we are deviating more from GR, but the mass of the field decreases, and we find that it is easier to reach a good accuracy in our solutions.

Finally, as we have two second-order equations, we have to start the integration at a small but nonzero value of r and, therefore, we need the values of a_1 and R_1 . To obtain them, we just have to insert the expansions of the variables in the equations and take the limit $r = 0$,

$$A''(0) = 2a_1 = \frac{2}{9(1 - 2\alpha R_0)} \left(16\pi G (2\rho_c + 3p_c) + \frac{R_0}{2} - \frac{3}{4}\alpha R_0^2 \right), \quad (2.68)$$

$$R''(0) = 2R_1 = \frac{1}{18\alpha} (16\pi G (\rho_c + 3p_c) + R_0). \quad (2.69)$$

Results and Discussion

We have solved the Einstein equations with a 4th order Runge-Kutta method, so we can extract now the observables of the NS (the mass and radius) from the solutions. We find some interesting differences with respect to the GR case, but before showing the figures we will explain how to calculate the mass.

Once we integrate the system for a given value of the pressure in the center, we extract the radius of the star as the point R_s where the pressure is zero. Then, we maintain the integration with $p = \rho = 0$. In GR, the mass can be obtained by solving the differential equation,

$$\frac{dM_\rho}{dr} = 4\pi Gr^2\rho(r), \quad (2.70)$$

which is obtained from the TOV system by taking the parametrization $B(r) = [1 - 2GM(r)/r]^{-1}$ and by using the field equations of GR which imply $M(r) = M_\rho(r)$. In the region outside of the star, the spacetime is described by the Schwarzschild metric (where $R = 0$ and $M = \text{const.}$), thus, we can identify the surface mass value $M_s \equiv M(R_s)$ with the mass of the star.

However, in $f(R)$ gravity, we do not have the Schwarzschild solution for $r \geq R_s$, because R satisfies its own differential equation and, in general, is nonzero for $r \geq R_s$, approaching zero only in the limit of large distances $r \rightarrow \infty$. As a consequence, the mass function

$$M(r) = \frac{r}{2}(1 - B^{-1}(r)), \quad (2.71)$$

is no longer constant outside the star, and the surface mass $M_s = M(R_s)$ is different from the asymptotic or ADM (Arnowitt-Deser-Misner) mass $M_{\text{ADM}} = \lim_{r \rightarrow \infty} M(r)$ as seen by a distant observer. M_s is also different from $M_\rho(R_s)$, because it receives additional contributions from the curvature scalar inside the star radius (for a detailed discussion see [200]).

We show the curves of the asymptotic (ADM) mass against the radius R_s for both the FT and the MF cases in Figs. 2.4 and 2.5. Further, in Figs. 2.6 and 2.7 we plot the same mass against the central energy density. Here α is always

given in units of km^2 .

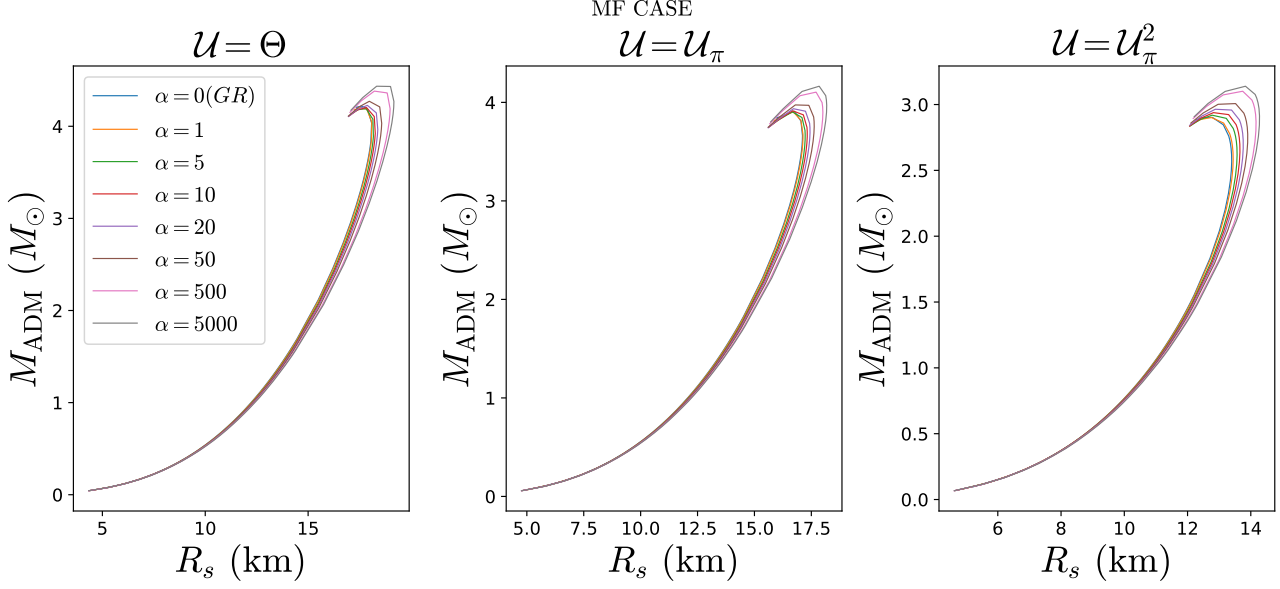


Figure 2.4: $M_{\text{ADM}}R$ curve in the MF, for three different potentials, and for different values of α in units of km^2 .

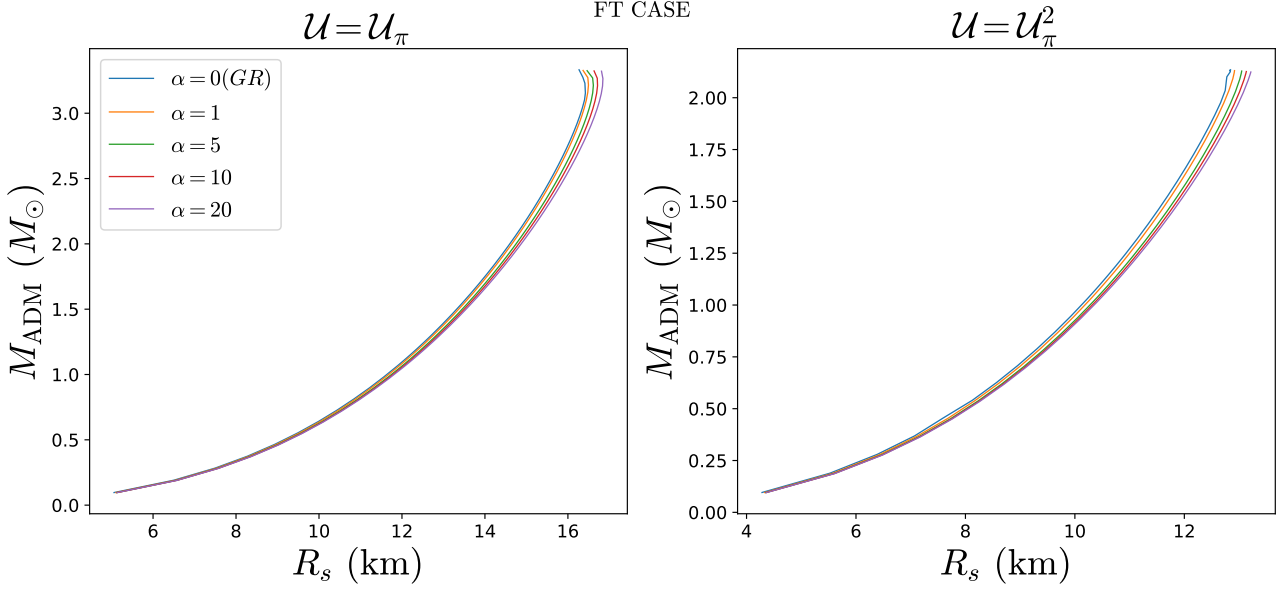


Figure 2.5: The same MR curve of Fig. 2.4 in the FT cases.

We find that for stars with small masses (*i.e.*, for sufficiently small central pressures or, equivalently, central energy densities), the radius and the value of the ADM mass for a fixed p_c decrease with increasing α so they are smaller than the GR case. The decrease in M_{ADM} can be directly seen in Figs. 2.6 and 2.7, whereas the corresponding decrease in the star radius follows from Figs. 2.4 and 2.5. For small masses, the MR curves in Figs. 2.4 and 2.5 are

almost identical for different α , so smaller masses correspond to smaller radii. For higher values of the central pressure (corresponding to larger masses), the radii and the masses of the stars for fixed p_c increase with increasing α (*i.e.*, stronger deviations from GR). Again, the increase of the masses can be directly seen in Figs. 2.6 and 2.7, whereas the corresponding increase of the radii can be inferred from Figs. 2.4 and 2.5. For the maximum ADM masses we provide the corresponding values also in Tables 2.1 and 2.2.

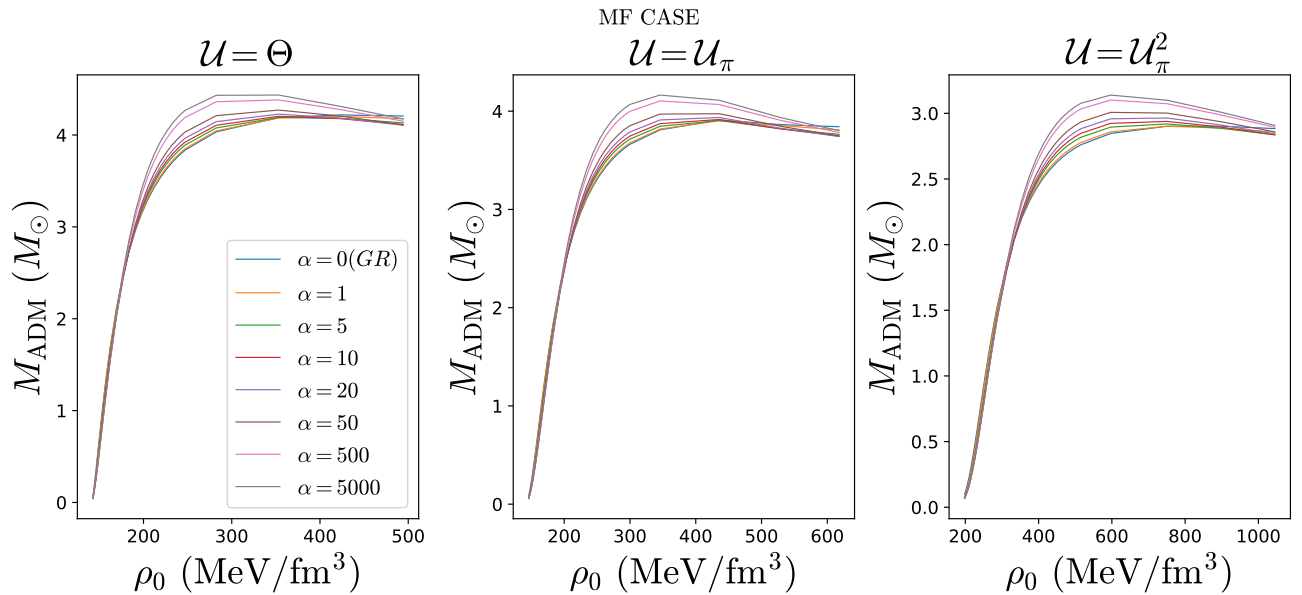


Figure 2.6: The ADM mass as a function of the central energy density, for the MF case. It can be clearly seen that for a fixed ρ_c the mass decreases with increasing α for small masses, but increases with increasing α for large masses. The maxima of the curves correspond to the value of p_c where the unstable branch starts.

From Figs. 2.4 and 2.5 it appears as if the MR curves for different α approached each other for small masses. This is, however, not entirely correct. The different MR curves for different α for a given model, in fact, always cross each other in the region of small M . In particular, for each α there exists a NS mass $M_*(\alpha)$ which has exactly the same radius as its GR counterpart ($\alpha = 0$). For all our models, however, this occurs for very small masses (always smaller than $0.15M_\odot$). As such small masses are most likely phenomenologically irrelevant, we did not try to zoom into this region to make this behavior more visible. The fact that this crossing of different MR curves occurs for very small masses is probably related to the very stiff nature of our EOS even for small density. BPS Skyrme NS, by construction, do not have a crust region, although a crust can be added without difficulty [15]. Other EOS, which are much softer in the

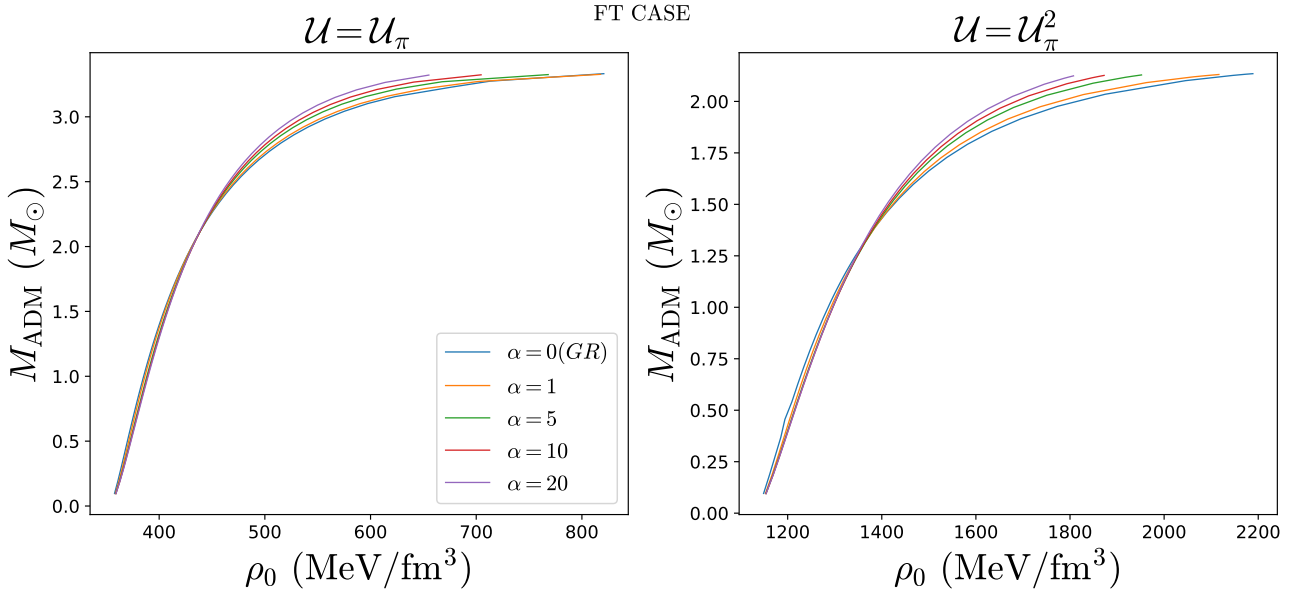


Figure 2.7: The same curves of Fig. 2.6 for the FT cases. The same conclusions may be extracted, however, solutions in the unstable branch cannot be found.

low-density region, produce pronounced crust regions for small mass NS and, thus, the crossing happens for much larger masses, see, *e.g.*, [200].

$\mathcal{U} = \mathcal{U}_\pi$ (FT)					
α (km^2)	0	1	5	10	20
M_{ADM} (M_\odot)	3.332	3.327	3.325	3.323	3.321
R_s (km)	16.26	16.36	16.46	16.63	16.81
ρ_c (MeV/fm 3)	820.73	817.64	786.10	704.61	655.20

$\mathcal{U} = \mathcal{U}_\pi^2$ (FT)					
α (km^2)	0	1	5	10	20
M_{ADM} (M_\odot)	2.134	2.130	2.128	2.126	2.124
R_s (km)	12.84	12.91	13.05	13.13	13.21
ρ_c (MeV/fm 3)	2188.60	2116.41	1951.95	1872.46	1807.41

Table 2.1: Exact case: values of the NS radii and the central energy densities for the maximum mass stars for the two potentials considered, and the corresponding values of α .

Another interesting quantity is the mass at the surface of the star, M_s , which in $f(R)$ gravity is a second, independent and invariant mass observable, as explained in [200]. It may be understood as a sum of the mass contributions of matter and curvature inside the star. As in [37], we find that its value decreases when we deviate from GR (*i.e.*, for increasing α), see Figs. 2.8 and

$\mathcal{U} = \Theta$ (MF)							
α (km ²)	0	5	10	20	50	500	5000
M_{ADM} (M_{\odot})	4.218	4.219	4.221	4.227	4.275	4.402	4.447
R_s (km)	17.58	17.60	17.79	17.92	18.08	18.55	18.95
ρ_c (MeV/fm ³)	430.70	374.21	360.09	345.97	338.91	317.73	289.49

$\mathcal{U} = \mathcal{U}_{\pi}$ (MF)							
α (km ²)	0	5	10	20	50	500	5000
M_{ADM} (M_{\odot})	3.918	3.919	3.921	3.944	3.990	4.113	4.170
R_s (km)	16.56	16.70	16.82	16.93	17.09	17.50	17.69
ρ_c (MeV/fm ³)	489.46	426.80	408.83	399.83	390.82	372.75	363.70

$\mathcal{U} = \mathcal{U}_{\pi}^2$ (MF)							
α (km ²)	0	5	10	20	50	500	5000
M_{ADM} (M_{\odot})	2.905	2.921	2.944	2.974	3.019	3.106	3.143
R_s (km)	12.63	12.90	13.00	13.12	13.29	13.61	13.69
ρ_c (MeV/fm ³)	825.34	705.17	689.90	674.56	659.15	628.06	596.59

Table 2.2: Mean-field case: values of the NS radii and the central energy densities for the maximum mass stars for the three potentials considered, with the corresponding values of α .

2.9. It turns out, however, that the non-vanishing curvature scalar outside the star produces a further contribution to the ADM mass which essentially compensates this decrease. The region outside the star, in which the Ricci scalar does not vanish, is also referred to as the gravisphere [37], and it can be seen explicitly in Fig. 2.10. We only include the MF plots because they are quite similar to the FT case.

An even further mass definition (the ‘‘Newtonian mass’’ M_n [200]) is provided by the (t, t) metric function $A(r)$,

$$M_n(r) = \frac{r}{2} (1 - A(r)), \quad M_{n,s} = M_n(R_s), \quad (2.72)$$

and this mass is relevant for the surface redshift,

$$z_s = \left(1 - \frac{2GM_{n,s}}{R_s} \right)^{-1/2} - 1. \quad (2.73)$$

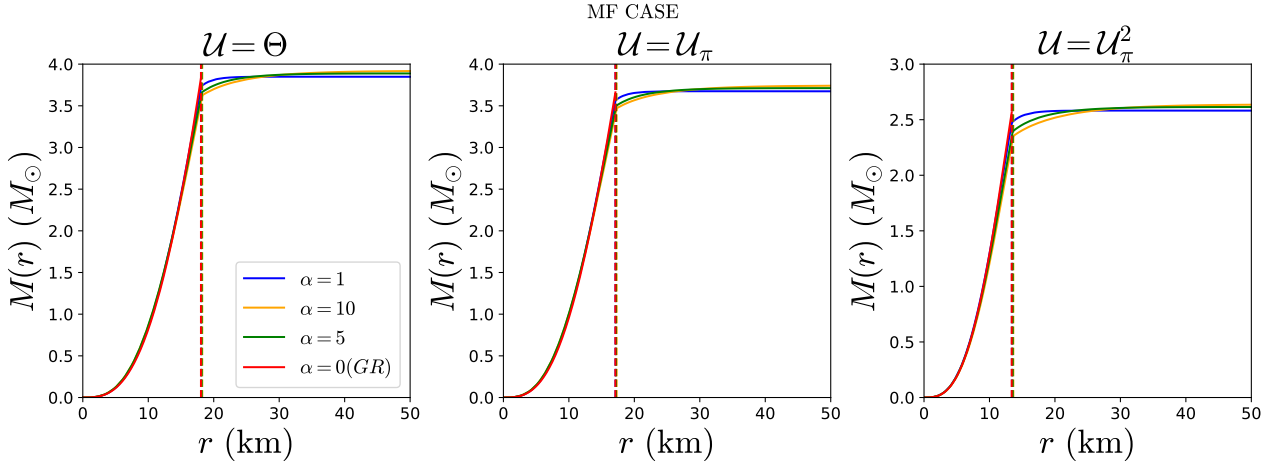


Figure 2.8: Mass function vs radius, for the MF case. For each potential, the solutions are for a fixed value of p_c which is sufficiently large to lead to a rather large mass but, at the same time, sufficiently small such that all solutions belong to the stable branch. The vertical dashed lines indicate the NS radii for different α , which turn out to be very similar.

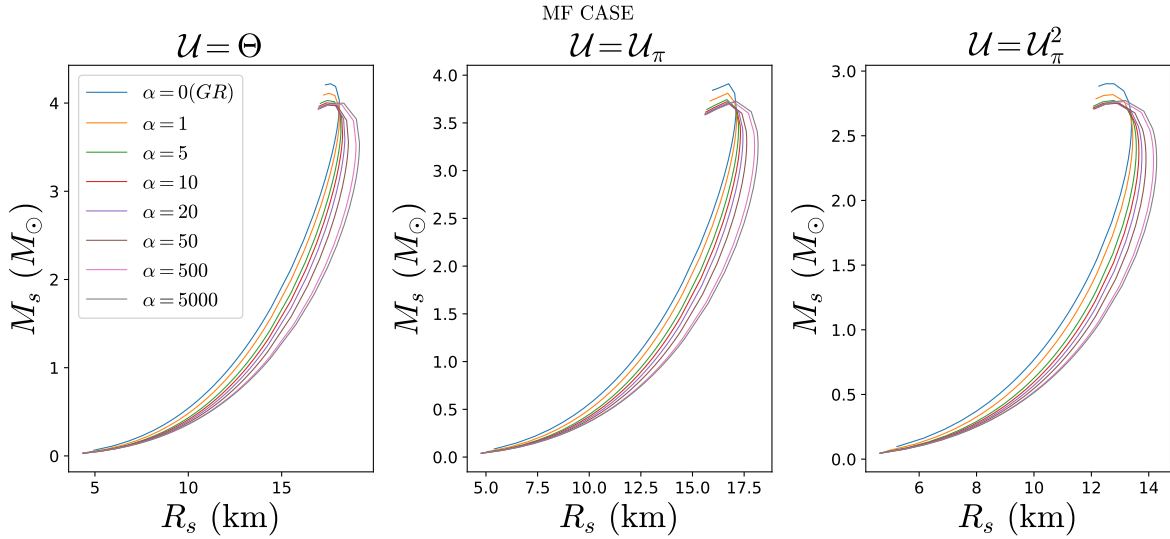


Figure 2.9: The surface mass as a function of the NS radius, for the MF case. It can be clearly seen that the surface mass for a given radius shrinks with increasing α .

Interestingly, it turns out that $M_{n,s}$ is larger than M_{ADM} such that the value of z_s for a star of a given mass increases in comparison to the one predicted in GR. This is probably related to the particularly stiff nature of the EOS of the BPS Skyrme model, because for the soft EOS used in [200] they find the opposite behavior. In any case, this difference could be important to discriminate between different extended theories of gravity.

The Ricci scalar curves for the MF case shown in Fig. 2.10 are continuous at the NS radius for the modified gravity $\alpha > 0$, but discontinuous for the GR case.

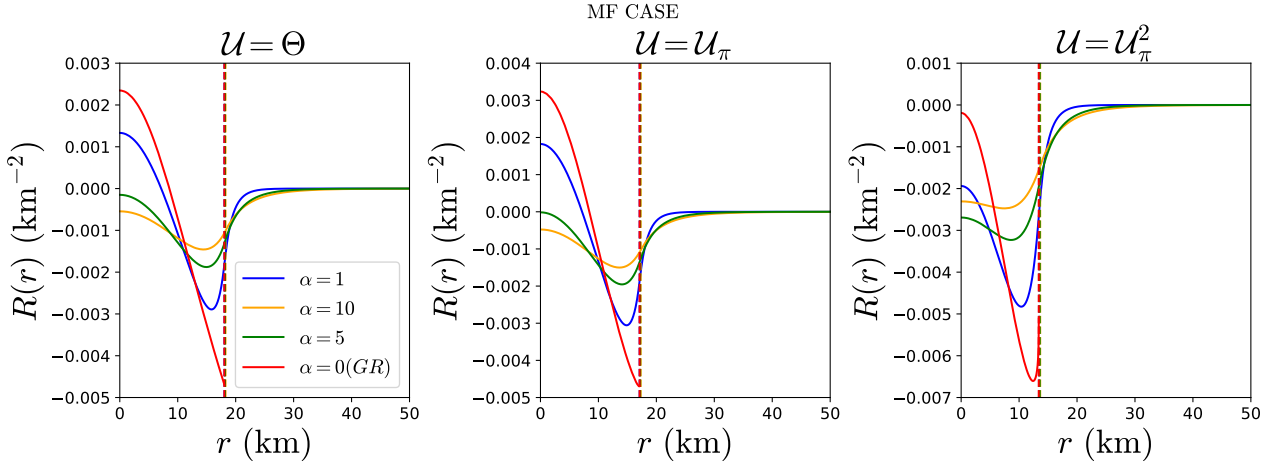


Figure 2.10: The Ricci scalar as a function of the radius, for the MF case. The solutions are for the same fixed values of p_c as in Fig. 2.8. The Ricci scalar suddenly jumps from a non-zero value to zero in the GR case, but is continuous at R_s for $\alpha > 0$. Again, the vertical dashed lines indicate the NS radii for different α , which turn out to be very similar.

This discontinuity is a consequence of the EOS of the BPS model in the MF case because, in GR, the Ricci scalar obeys a purely algebraic equation given by the trace of the Einstein equations,

$$R = 8\pi G (3p - \rho). \quad (2.74)$$

Therefore, if the EOS leads to a non-vanishing energy density at the NS surface, the Ricci scalar will also show that discontinuity. In the modified gravity, on the other hand, the curvature satisfies its own differential equation until the end of the integration, which results in a continuous curve.

Finally, we remark a possible singularity which, interestingly, is always avoided by solutions of our system. Indeed, the first derivative of $f(R)$,

$$f_R(R) = 1 - 2\alpha R, \quad (2.75)$$

may, in principle, become zero for a positive R , which would introduce a singularity in the equation (2.63). In GR, R is always negative close to the surface, where ρ dominates over p , see (2.74). Whether it may become positive in the center of the star depends on the EOS. It may become positive in our case, because in the high-pressure limit the EOS of the BPS Skyrme model approximates the maximally stiff EOS $\rho = p + \text{const}$. Indeed, it can be seen

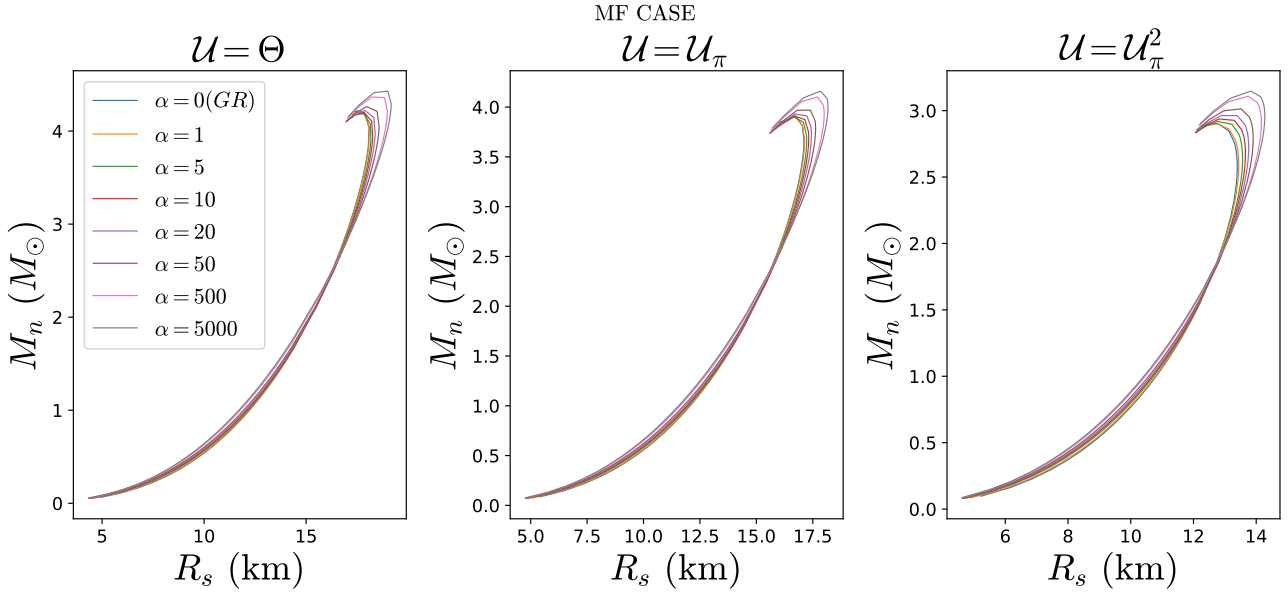


Figure 2.11: The Newtonian mass at the surface as a function of the star radius, for the MF case. For a fixed radius, it grows with α for small stars but shrinks for large stars.

in Fig. 2.10 that $R(0)$ takes positive values in the GR case ($\alpha = 0$). On the other hand, we also see that $R(0)$ diminishes with increasing α . In particular, it seems that $R(0)$ always becomes negative for sufficiently large α . In any case, $f_R(R(r)) = 1 - 2\alpha R(r)$ always remains positive for all r for all solutions considered (even for extremely large α), and the singularity never occurs. In general, these results are compatible with those obtained in other investigations [36, 37, 86, 129, 200, 216].

In more detail, our $M(R_s)$ curves are quite similar to the curves resulting from quark stars [36], although the deviations for different values of α are slightly larger in the quark star case (probably related to the fact that the quark star EOS for high densities is softer than the BPS Skyrme EOS). The underlying reason for their similarity is that in both cases (quark stars and BPS Skyrme stars) the EOS does not become extremely soft in the low-density region, such that the MR curves always have positive slope for small masses. In other words, the radius grows with the mass, and light stars do not have a pronounced tail (or crust). For EOS which approach the very soft EOS of nuclear physics for low densities, on the other hand, the resulting $M(R_s)$ curves lead to larger radii for smaller masses (a negative slope) in the low-density region. For such EOS, the effect of varying α is much stronger, particularly for small mass NS, there

seems to exist an overall tendency that the variation of α has a stronger effect for softer EOS.

It is interesting to compare the values of α used here, which are similar to those in [36, 37, 200], with some observational astrophysical bounds. In [35] the bound $\alpha \lesssim 1 \text{ km}^2$ was suggested, based on NS masses constraints. That bound, however, was derived within a perturbative approach to the Starobinsky model which is not capable of reproducing the gravisphere contribution to the NS mass and, therefore, underestimates this mass. Taking into account this correction, the bound becomes much weaker [36]. Other astrophysical bounds [167] are much weaker, as well, such that the values considered in the present article are, at this moment, compatible with those astrophysical bounds. Further, we restricted to positive values of α to avoid tachyonic instabilities. For $\alpha < 0$ we found solutions of the Ricci scalar that show damped oscillations outside the stars, see [34] for a detailed investigation.

We find that the radius increases with α , while the maximum mass also slightly increases in the MF case, see Table 2.2. In the FT case, instead, the maximum ADM mass seems to slightly decrease with increasing α , although the effect is tiny, as may be seen in Table 2.1. So, in principle, we could constrain the values of α with observational NS data, however, such data are still not very precise. Besides, the maximum masses that the NS can reach strongly depend on the EOS that we are using, hence, those EOS that are slightly below the minimum accepted value $2M_\odot$, could be reconsidered with these results. A priori one might think that the maximum mass can be arbitrarily large when the value of α is increased, but we find that this is not the case. For instance, for the large value $\alpha = 5000 \text{ km}^2$ we find an increase of about 5%, also found in [216].

One further interesting result is that the Newtonian surface mass $M_{n,s}$ relevant for the redshift of radiation emitted from the star surface is larger than the ADM mass, in contrast to results for softer EOS. This implies that if generalized gravity turns out to be indeed relevant for NS, then the redshift will be able to distinguish different EOS and, in particular, their stiffness.

We also find that the Ricci scalar is a smooth function at the surface of the stars. In the GR case, an EOS leading to a non-vanishing energy density at

the surface of the star leads to a discontinuity in the Ricci scalar, but in $f(R)$ gravity that discontinuity is cured, because R satisfies its own differential equation. We required that the Ricci scalar tends to zero at infinity to recover an asymptotically flat spacetime but, in principle, this would not be necessary, and we could have imposed the Schwarzschild solutions just at the surface of the star. This has been done in [96, 178] for some EOS, but this matching condition cannot be imposed for an arbitrary EOS, therefore it is highly unnatural. The results shown here are, thus, a straightforward violation of the Jepsen-Birkhoff theorem in $f(R)$ gravity.

These results also open a new possibility in the description of NS. It consists in the study of the differences of these results performed in the Einstein frame as is done in [129], although they present their final results in the Jordan frame. Indeed, we have posed the problem and solved the equations in the Jordan frame, in which GR is usually expressed. However, the introduction of modified theories of gravity, concretely the scalar-tensor theories, motivates the introduction of the Einstein frame via a conformal transformation of the metric.

In any case, the BPS Skyrme model does yield rather high values for the maximum mass even in GR, up to $\sim 3.5M_\odot$ for realistic potentials, and the computations in generalized gravity does not help in this respect. For a more complete and more reliable description of nuclear matter, the BPS Skyrme submodel should be combined with the standard Skyrme model, which, as we have seen in the last section, leads to much smaller values of the maximum mass.

2.3 The generalized Skyrme model

The properties of the BPS model, concerning isolated nuclei and NS, encourages the generalization of the standard Skyrme model including the contribution of the sextic term. Therefore, we present the generalized Skyrme model:

$$\mathcal{L}_{2460} = -\frac{f_\pi^2}{16} \text{Tr}\{L_\mu L^\mu\} + \frac{1}{32e^2} \text{Tr}\{[L_\mu, L_\nu]^2\} - \lambda^2 \pi^4 B_\mu B^\mu + \frac{m_\pi^2 f_\pi^2}{8} \text{Tr}\{U - \mathbb{I}_2\}. \quad (2.76)$$

In this model, the stability of the skyrmions is also ensured due to the opposite scaling of the terms. Moreover, a generalized BPS bound may be also extracted

[18], with explicit dependence on the parameters.

The starting point and natural procedure is the resolution of the $B = 1$ skyrmion, which is the simplest solution. We first write the previous Lagrangian in Skyrme units, however, due to the presence of the sextic and potential terms we cannot completely eliminate the parameters from the Lagrangian,

$$\begin{aligned} \mathcal{L}_{2460} = & \frac{1}{24\pi^2} \left[-\frac{1}{2} \text{Tr}\{L_\mu L^\mu\} - \frac{1}{4} \text{Tr}\{[L_\mu, L_\nu]^2\} \right. \\ & \left. - 4\pi^4 c_6 B_\mu B^\mu - \frac{c_0}{2} \text{Tr}\{\mathbb{I}_2 - U\} \right]. \end{aligned} \quad (2.77)$$

The parameters have been encompassed into the adimensional coupling constants $c_6 = 2\lambda^2 f_\pi^2 e^4$ and $c_0 = 2m_\pi^2 / (f_\pi e)^2$. Introducing the hedgehog ansatz (2.18) in the Lagrangian, the field equation of the profile function $f(r)$ is obtained, and it may be solved for any given values of c_6 and c_0 .

In order to fix the parameters f_π and e , we follow the ideas in [28, 29], in which the $B = 1$ skyrmion is quantized to reproduce the masses of the proton and the Δ excitation. As mentioned before, for the zero mode quantization, we perform a time-dependent transformation of the full symmetry group on the Skyrme field,

$$U(x) \rightarrow A(t)U(R(B(t))x + X(t))A^\dagger(t) \quad (2.78)$$

The transformed field is introduced in the Lagrangian and we obtain the static energy term plus additional kinetic energy terms,

$$L = -M + \frac{1}{2}M\dot{X}^2 + \frac{1}{2}a_i V_{ij}a_j + \frac{1}{2}b_i U_{ij}b_j - \frac{1}{2}a_i W_{ij}b_j. \quad (2.79)$$

We have identified the static energy functional with the mass M of the skyrmion, and the different kinetic energies come from translations, rotations, isorotations and a mixed spin-isospin term. We also have defined the corresponding inertia tensors V_{ij} , U_{ij} , W_{ij} and the angular frequencies a_i , b_i associated to rotations and isorotations respectively,

$$a_i = -i \text{Tr}\{\tau_i B^\dagger \dot{B}\}, \quad b_i = -i \text{Tr}\{\tau_i \dot{A} A^\dagger\}. \quad (2.80)$$

We drop the translational kinetic energy contribution, and for the $B = 1$ skyrmion all the inertia tensors are equal and proportional to the identity due to the spherical symmetry of the field configuration, $U_{ij} = V_{ij} = W_{ij} = \Lambda \delta_{ij}$. Their expressions may be easily obtained in terms of the profile function.

The Hamiltonian is obtained via the Legendre transformation of the Lagrangian (2.79), from the angular velocities to the canonical spin and isospin angular momenta. The possible quantum states, which are characterized by the spin and isospin quantum numbers $|j, i\rangle$, are found from the Rubinstein-Finkelstein (FR) constraints in spherical symmetry [151]. Finally, the quantum corrections to the $B = 1$ skyrmion may be obtained for the $j = i = \frac{1}{2}$ ground state and the $j = i = \frac{3}{2}$ first excited state, which correspond to the proton and Δ particle respectively,

$$\begin{aligned} M_p &= M + \frac{3\hbar^2}{8\Lambda}, \\ M_\Delta &= M + \frac{15\hbar^2}{8\Lambda}. \end{aligned} \tag{2.81}$$

We fix the pion mass to its physical value ($m_\pi = 138$ MeV) and we compute the solutions for different values of λ^2 to study the impact of the sextic term on the skyrmion. For each value of λ^2 , the field equation is solved with an initial seed of values (f_π, e) , and the isospin inertia tensor is computed. This process is repeated iteratively until the values for $M_p = 939$ MeV and $M_\Delta = 1232$ MeV are satisfied.

The results obtained for the parameters from the $B = 1$ fit in the generalized Skyrme model are shown in Table 2.3. Interestingly, when the sextic term coupling constant increases, the required Skyrme parameter to fit the solutions also grows, which implies that the quartic term becomes less important. Indeed, the Skyrme parameter rapidly blows up if the sextic term is present in the massless model, whilst it remains stable when the mass term is included. The main reasons for this discrepancy between the two models are the repulsive behaviour of the sextic term and the slow decay of the massless model. In particular, when the sextic term is included the solution expands, increasing the value of the inertia tensor, thus, reducing the importance of the quantum

energy in (2.81). However, the difference between the two physical masses is precisely given by this correction which, after recovering the physical units, depends proportionally to $f_\pi e^3$, whilst the classical contribution is proportional to f_π/e . This implies that the Skyrme parameter must increase to counteract the growth of the inertia tensor in order to maintain the fits. Additionally, we may see from the definition of $c_6 \propto e^4$ that if e increases so does the presence of the sextic term, which is precisely the main cause of this effect. Hence, the presence of the sextic term induces a feedback process that may not have solution for a given maximal value of λ^2 if the size of the solution is not restricted by an exponential decay.

Conversely, the parameter f_π also increases, but much more slowly since the energy is much less affected by the sextic term than the isospin inertia tensor. In fact, it is still far from its physical value (186 MeV).

The energies of the solution are larger than for the standard fit (2.21), but also the BPS bound increases. However, the difference in energy between the solution and the BPS bound broadens for both the massless and massive models, contrary to a first naive intuition from the BPS model. This indicates a nontrivial interaction between the sextic and the other terms for these values of λ^2 , however, for sufficiently high values of both c_6 and c_0 this difference in energy should decrease, given that we are approaching the BPS model.

We show in Fig. 2.12 the profile function solutions against the radial coordinate in the massive case for the different values of λ^2 . There, the expansion of the solution in space is clearly visible. Indeed, the repulsive behaviour of the sextic term may have an interesting effect in the $r \rightarrow 0$ limit of $f(r)$. In this region, the profile function has always positive second derivative in the models without sextic term, see right part of Fig. 2.12. However, if the sextic term is included, we may find a sufficiently large value of c_6 for which the second derivative is negative near the $r = 0$ region, in which the sextic term is the most relevant. This effect might have important consequences in the description of the electric charge density profile functions for the nucleons within the Skyrme model [89].

Finally, we solve the next skyrmions (up to $B = 4$) to compute the classical

$m_\pi = 0$			$m_\pi = 138 \text{ (MeV)}$		
f_π (MeV)	e	λ^2 (MeV fm 3)	f_π (MeV)	e	λ^2 (MeV fm 3)
135.97	6.30	1	112.24	5.24	1
145.98	9.77	3	118.34	6.27	3
149.36	39.59	5	123.18	7.99	5

Table 2.3: Sets of parameters that fit the $B = 1$ solution to the masses of the proton and the Δ excitation.

binding energies (2.20) in the generalized model. The quantization of these solutions follows the same procedure, and their corresponding quantum states have also been identified in the standard Skyrme model. However, we will only be interested in the classical energies. The reason is that the quantum corrections already increase the energy of the $B = 1$ ground state an 8% of the total energy, but the next skyrmions will typically have smaller or even zero (for the $B = 4$ ground state) contributions [151]. In conclusion, these corrections induce even more bounded isolated skyrmions, hence, they cannot be considered as a solution for the binding energies problem.

These skyrmions do not have spherical symmetry anymore, hence we obtain the solutions using an accelerated gradient descent (AGD) minimization algorithm for the fields in the three-dimensional space. This procedure is extremely useful to obtain minimal energy configurations, so we explain the details in Appendix C. We start with the rational map field configuration for each skyrmion [157] and let the algorithm vary the fields in the direction of maximal decreasing energy. The set of parameters that we are going to consider correspond to the $\lambda^2 = 3$ case of Table 2.3 in the massive model. The energies of the resulting solutions are shown in Table 2.4.

The skyrmions have inherited the symmetries initially imposed by the rational map, but the density distributions are more spread in space, due to the repulsive behaviour of the sextic term. The energy density distribution is shown in Fig 2.13 using the Runge colouring convention [91], which turns out to be quite helpful to see the orientation of the pion fields.

Unfortunately, the binding energies computed are even worse than in the standard Skyrme model, both values are shown in Table 2.4. Hence, a substantial decrease of the binding energies purely within the generalized model would re-

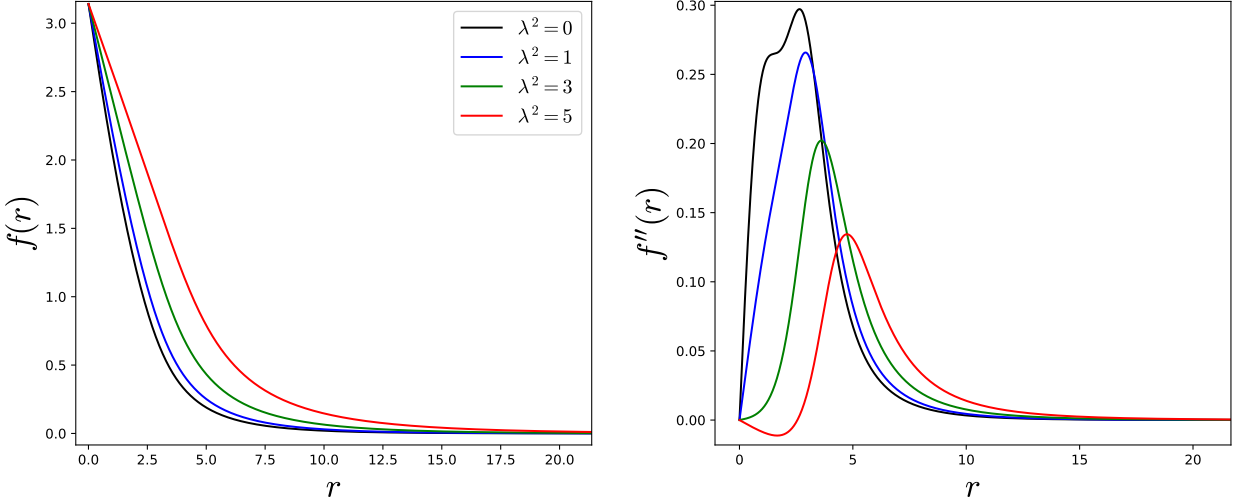


Figure 2.12: Radial profile function of the $B = 1$ skyrmion in the generalized Skyrme model for different values of the sextic term coupling constant in units of MeV fm³.

B	E/B	$BE_B (\%)$	$BE_B (\%) (\mathcal{L}_{24})$
1	1.541	0	0
2	1.451	5.84	4.31
3	1.400	9.16	6.98
4	1.362	11.62	9.10

Table 2.4: Energy per baryon number and corresponding binding energies for the first four ground state skyrmions in the generalized model. We also included the binding energies of the same solutions in the standard Skyrme model for comparison.

quire very large values of c_6 and c_0 simultaneously, however, the computations become extremely hard numerically in this limit using the AGD.

Nonetheless, it has been shown that the classical energies should receive significant corrections from the quantization of the vibrational modes. This is still a task ahead, but it is for sure an interesting direction to improve the results of the Skyrme model for isolated nuclei.

2.3.1 Neutron stars from a Generalized Skyrme EOS

The aim of this final part is to consider a first approximated description of INM to reproduce NS from the generalized Skyrme model, in which we consider the contributions from the standard and the BPS submodels from an effective approach.

As mentioned before, the lowest energy solution of the standard Skyrme model

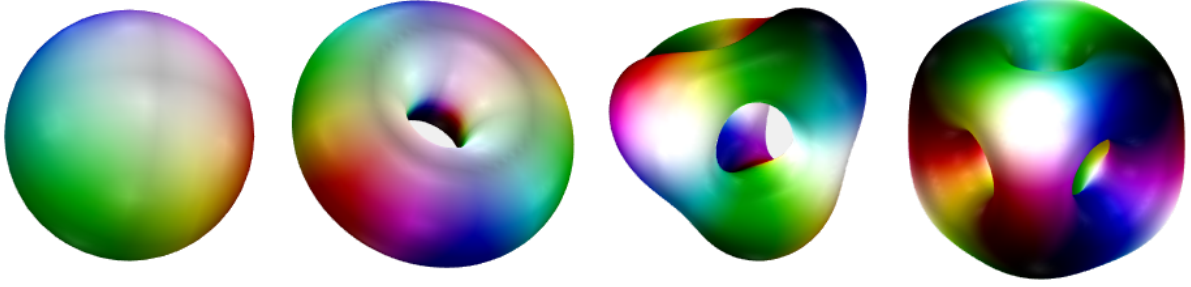


Figure 2.13: Energy density contour plots in three dimensions of the first four skyrmions. We adopt the Runge colouring convention to represent the orientations of the pion fields.

(2.4), for very large baryon number consist of a crystalline lattice of cubic unit cells. The energy per baryon of such solution as a function of the lattice parameter of the unit cell (l) is given by (2.23). The pressure, using the thermodynamical definition (2.24), is

$$p(l) = \frac{E_0}{3l^2} \left(\frac{l_0}{l} - \frac{1}{l_0} \right) \frac{(1 - \varepsilon)}{2}. \quad (2.82)$$

This expression vanishes at the finite length $l = l_0$, which is a well-known property of INM at the saturation density n_0 . Further, we shall argue below that the standard Skyrme crystal should provide the leading contribution to the nuclear EOS close to the nuclear saturation. This explains the fit of the Skyrme crystal parameters l_0 and E_0 to the INM values (2.49) that we have considered in the previous section.

At sufficiently high densities, for instance those at the core of a NS, the sextic term (2.26) provides the most important contribution to the EOS, related to the ω meson repulsion of nuclear matter [23]. The sextic term alone defines a barotropic perfect fluid with energy density $\rho_6 = \lambda^2 \pi^2 (B^0)^2 = p$, see the definition (2.38). The EOS $\rho_6 = p$ is maximally stiff with a speed of sound equal to one, which explains its dominance at high density.

In the case of interest here, we will introduce a constant effective potential $\mu^2 \mathcal{U} = \rho_U$, which is supposed to take into account the effects of the subleading contributions above a certain threshold value p_{PT} for the pressure. This is equivalent to choosing the Θ potential (2.50) and implies the barotropic EOS

$$\rho = \rho_6 + \rho_U = p + 2\rho_U \quad (2.83)$$

already at the full FT level.

It is clear from the previous sections that the true equation of state for Skyrme matter should take into account both models in a unified fashion. Nevertheless, we may still obtain some information of the full description within the generalized model by scaling arguments of the energy terms for the different submodels.

Indeed, consider the case of the Skyrme crystal and let $\sigma_s \in (0, 1]$. A scale transformation of the space coordinates of the form $x \rightarrow x/\sigma_s$ can be understood as a mapping between crystalline solutions, respectively, with lattice size l and $\sigma_s l$. On the other hand, the lattice length is a function of the pressure, inverting (2.82):

$$\frac{l_0^2}{l^2} = \frac{1}{2} \left(1 + \sqrt{1 + \frac{24l_0^3}{E_0(1-\varepsilon)} p} \right). \quad (2.84)$$

Then, we conclude that two solutions at different pressures p and p' which have a lattice length of $l(p)$ and $l'(p')$ respectively, are related through a scale transformation $\sigma_s(p, p')$ such that $l'(p') = \sigma_s(p, p')l(p)$. In particular, any configuration with lattice length $l(p)$ will be related to the zero pressure crystal (minimum energy configuration) via $l(p) = \sigma_s(p)l_0$, where $\sigma_s(p) = \sigma_s(0, p)$ can be seen as a function relating the pressure of the crystal and the scaling parameter. Furthermore, taking into account (2.84), we find

$$\sigma_s(p) = \sqrt{\frac{2}{1 + \sqrt{1 + \frac{24l_0^3}{E_0(1-\varepsilon)} p}}}. \quad (2.85)$$

Indeed, this expression has the correct limits $\sigma_s(p \rightarrow \infty) \rightarrow 0$ and $\sigma_s(p = 0) = 1$.

This equivalence between pressure and scaling allows us to write the energy of the Skyrme crystal at any pressure (*i.e.* $\sigma_s \neq 1$) as a simple function of

$$\sigma_s = l/l_0,$$

$$E(\sigma_s) = E_0 \left[(\sigma_s + \sigma_s^{-1}) \frac{(1 - \varepsilon)}{2} + \varepsilon \right]. \quad (2.86)$$

Obviously, the contribution from the term proportional to σ_s becomes negligible for large pressure, whereas the term proportional to σ_s^{-1} dominates in this regime ($\sigma_s \ll 1$).

Next, consider the sextic term contribution to the energy per baryon of a fluid element Ω

$$\frac{E_6}{B} = \frac{\int_{\Omega} d^3x \sqrt{|g|} \rho_6}{\int_{\Omega} d^3x \sqrt{|g|} B^0} \quad (2.87)$$

which transforms as $E_6 \rightarrow \sigma_s^{-3} E_6$ under a scaling of the spacetime coordinates. This implies that the sextic contribution will dominate the energy per baryon at sufficiently high pressure. Therefore, we may assume that a solution of the complete model will provide an EOS which tends to the EOS of the submodel ρ_6 at high pressure, with an asymptotic energy per baryon of $E_6/B = \rho_6/B^0 = \lambda^2 \pi^2 \sqrt{p}$. This is, therefore, the asymptotic behavior of the energy per baryon at high pressure also for the full model.

On the other hand, as the pressure decreases to a certain value, E_6/B becomes of the order of the energy per baryon of the Skyrme crystal, and the BPS approximation to the complete solution will start to fail. For even lower p , the contribution of E_6/B will be subleading in comparison to the Skyrme crystal. This supports the idea that a transition of some kind must take place within this generalized model, between the crystalline phase of the standard Skyrme model and the perfect fluid phase of the BPS model. A quantitative prediction of the pressure value p_{PT} where this transition occurs, as well as the determination of its character (first or second order) would require the knowledge of the full solution. In [10], the BPS submodel was used to model the full NS core so the parameters λ^2 and μ^2 were fitted to match with the infinite nuclear matter approximation at zero pressure. In the present case, however, the Skyrme crystal describes the low-pressure region, therefore, it should be fitted to nuclear matter. In this section, we will propose an EOS for the generalized model. The

value of λ^2 will be determined, instead, by the behavior of the EOS in the limit of very high pressure, in which, as argued, it can be approximated by only the sextic term.

From the previous considerations, we can construct a generalized EOS which takes into account both the standard Skyrme and BPS submodels at different regimes, based on simple assumptions on the behaviour of the solutions in the low and high pressure regimes, without knowing these solutions explicitly. Indeed, we will assume that the low pressure solutions of the complete model are still Skyrme crystals and the energy is approximately described by (2.23). In the fluid high-pressure phase, we will assume that the sextic term provides the most important contribution, and the complete solutions can be well described by a BPS Skyrme model. We can model this behaviour by introducing a certain value of the pressure, p_{PT} , above which the solutions are described by a BPS fluid. Therefore, the generalized EOS $\rho_{\text{Gen}}(p)$ must satisfy

$$\rho_{\text{Gen}}(p) := \begin{cases} \rho_{\text{Sk}} & \text{if } p \ll p_{PT} \\ p + \text{const.} & \text{if } p \gg p_{PT} \end{cases} \quad (2.88)$$

A simple way of parametrizing this behavior that yields a smooth transition between these two regimes is to consider an EOS of the form

$$\rho_{\text{Gen}}(p) = (1 - \alpha(p)) \rho_{\text{Sk}} + \alpha(p) (p + \rho_{\text{Sk}}(p_{PT})) , \quad (2.89)$$

where $\alpha(p)$ is a function that interpolates between the two regimes, $\alpha \rightarrow 0$ for $p/p_{PT} \rightarrow 0$ and $\alpha \rightarrow 1$ for $p/p_{PT} \rightarrow \infty$. Specifically, we consider the interpolating function,

$$\alpha(p, p_{PT}, \beta) = \frac{(p/p_{PT})^\beta}{1 + (p/p_{PT})^\beta}, \quad (2.90)$$

as in [15]. Here, smaller values of β produce a more gradual transition, whereas larger values correspond to a faster transition between the two regimes. For the transition between the Skyrme crystal and the BPS fluid at p_{PT} , we have to choose the rather gradual transition $\beta = 0.9$, because otherwise the resulting energy density (2.89) would lead to acausal propagation (a speed of sound

larger than one), in some regions inside the star, see Fig. 2.14. As a result of this interpolation, the energy density contribution from the crystal becomes less important as p grows, freezing at its value at p_{PT} for sufficiently high pressures, playing the role of an effective potential energy for the BPS Skyrme model. The p dependence for $p > p_{PT}$ is taken into account by ρ_6 , which is known to provide the leading contribution for large p . Therefore, the generalized EOS (2.89) is effectively equivalent to that of a BPS Skyrme model with a Θ potential (2.50) for $p \gg p_{PT}$. In the following section, we will see that the value of p_{PT} determines the maximum mass of a NS, so we may adjust the value of p_{PT} to agree with the current maximum mass limit for NS.

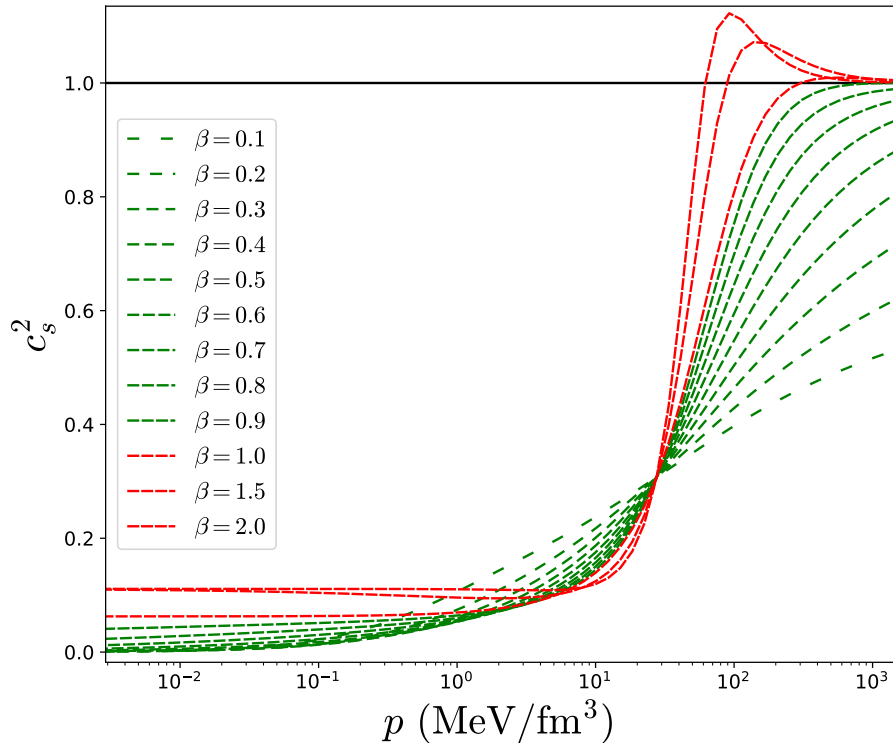


Figure 2.14: Speed of sound of the generalized Skyrme EOS (2.90) for different values of the interpolating parameter. The red curves represent (unphysical) superluminal sound velocities, whilst the green curves correspond to acceptable curves.

To obtain the baryon density n_B as a function of the pressure in the generalized model, we use the well-known Euler relation $\rho = -p + \frac{\partial \rho}{\partial n_B} n_B$, which yields a differential equation for n , that we integrate using $n_B(p=0) \equiv n_0 = 0.16 \text{ fm}^{-3}$ as initial condition. The result, and the corresponding EOS $\rho(p)$, are shown in Fig. 2.15, where other EOS have been included for comparison.

Addition of crust: the Hybrid EOS

The generalized Skyrme EOS (2.89) only describes, by construction, nuclear matter above nuclear saturation. Below saturation density, nuclear matter in a NS is known to be in a rather inhomogeneous state, resulting from a competition between nuclear and electromagnetic forces (*e.g.*, the nuclear pasta phases). In principle, the (generalized) Skyrme model can be coupled to the electromagnetic interaction, so these low-density phases are fundamentally within its scope. Full field-theoretical calculations for this coupled system and for large B are, however, not feasible, and a macroscopic treatment is currently unknown. On the other hand, the standard methods of nuclear physics, such as many-body techniques, can be used to describe these low-density NS crust regions and are completely reliable there. This motivates us to consider a hybrid version of (2.89), in which at a sufficiently low density, n_* (or equivalently p_*), a realistic EOS for a NS crust, like $\rho_{\text{BCPM}}(p)$, is glued,

$$\rho_{\text{Hyb}}(p) := \begin{cases} \rho_{\text{BCPM}} & \text{if } p \ll p_* \\ \rho_{\text{Gen}} & \text{if } p \gg p_* \end{cases} \quad (2.91)$$

We choose again the BCPM EOS to reproduce the low density regime. For the crust and the outer core ($n_B \lesssim n_0$), nuclear matter is well understood, and standard nuclear physics EOS should provide a precise description of NS matter. Again, we choose a smooth transition between the two regimes, using the interpolating function (2.90). Now we choose the faster transition $\beta = 2$, as was done in [15] (replacing p_{PT} by p_*).

Results

We solve the TOV system of equations to determine the static properties of the NS resulting from the new generalized and hybrid EOS. In the hybrid EOS, there are two free parameters, namely the values of p_* and p_{PT} corresponding to the low and high density parts. Here, we show that recent astrophysical and gravitational wave observations actually tightly constrain the value ranges for both parameters. For instance, from the MR curves, we find that only the value of p_{PT} affects the maximum NS mass in the model. Thus, we could

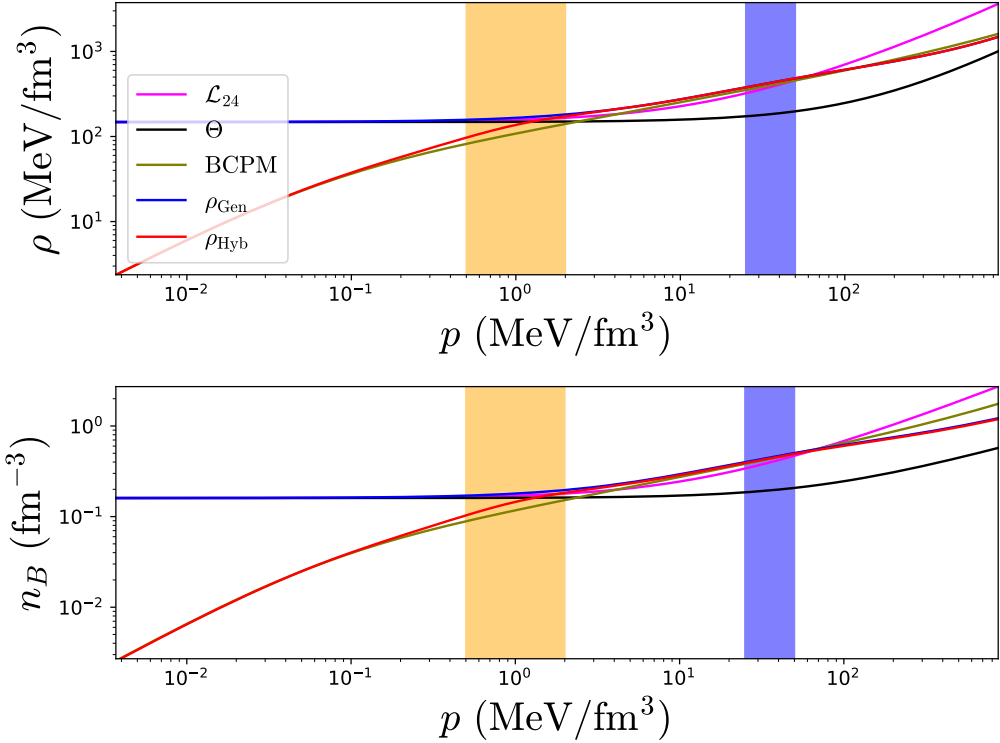


Figure 2.15: Comparison of the energy and baryon densities of the Generalized and Hybrid EOS from the Skyrme model with other standard nuclear physics EOS.

constrain the value of p_{PT} using the maximum mass limit for nonrotating NS of $M/M_\odot = 2.16^{+0.17}_{-0.15}$ proposed in [195]. However, given the GW observations of GW190425, with a total mass of $3.4^{+0.3}_{-0.1}$ and mass ranges of components varying from 1.12 to $2.52M_\odot$ [4], and GW190814, a compact binary merger between a $22.2 - 24.3M_\odot$ black hole and a secondary object within the mass gap ($2.50 - 2.67M_\odot$) [5], we have allowed the range of values of p_{PT} to yields stars of maximum mass up to $\sim 2.5M_\odot$.

In Fig. 2.16 we show different MR curves of the hybrid model corresponding to different values of p_{PT} . We can see a good agreement, for any pair (p_*, p_{PT}) within the ranges $p_* \in [0.5, 2]$ MeV/fm³ and $p_{PT} \in [25, 50]$ MeV/fm³, with the most likely MR relation for the NS corresponding to the GW170817 event [2]. We have not included the corresponding data of the second BNS event, namely, GW190425, since it was less informative on matter effects than GW170817, although our data is also compatible with this event, specially for lower values of p_{PT} . In the same figure, we represent the most updated measured masses of some heavy pulsars, PSR J1614-2230 ($1.928 \pm 0.017M_\odot$) [94], PSR J0348+0432

$(2.01 \pm 0.04 M_{\odot})$ [33] and PSR J0740+6620 ($2.14^{+0.10}_{-0.09} M_{\odot}$) [82], as well as the most probable MR region from combined observations of GW and these heavy pulsars [138]. Also, other constraints from NICER, chiral EFT and multimesenger observations are represented, adapted from [79] and [109].

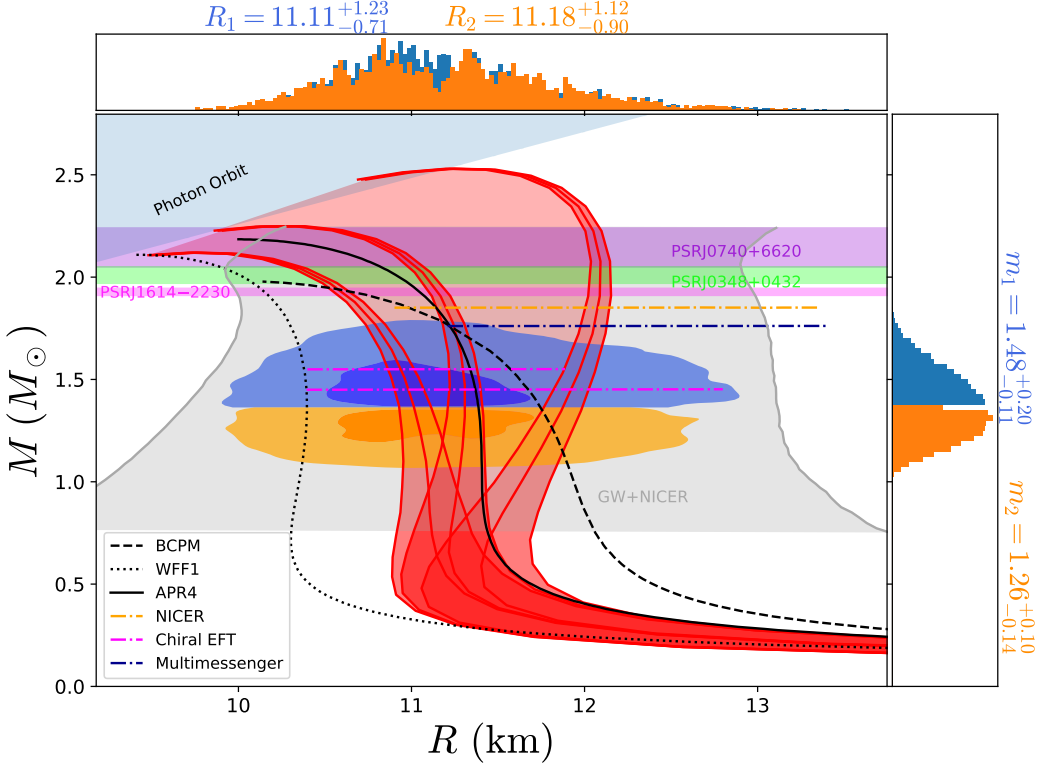


Figure 2.16: MR relation for the hybrid model (red curves) for different combinations of values of $p_* = 0.5, 1, 2$ MeV/fm 3 and $p_{PT} = 25, 40, 50$ MeV/fm 3 . The red shaded region corresponds to the accessible region of the hybrid model with p_* and p_{PT} within the given ranges.

The observed gravitational waveform can also be used to place direct constraints on the tidal deformability of NS. Indeed, the waveform produced by the coalescence of two NS at the early phase of the inspiral depends on the underlying EOS mostly through the tidal Love number [121]. However, the individual Love numbers for the two stars cannot be disentangled in the observed gravitational waveform. Instead, what is measured is the so-called effective tidal deformability $\tilde{\Lambda}$, a mass weighted average of the deformabilities of the individual stars in the merger [93]. Similarly, the two component masses are not measured directly, but the chirp mass, $M_c = (m_1 m_2)^{3/5} / (m_1 + m_2)^{1/5}$ where $q = m_1/m_2$ is the mass ratio, can actually be tightly constrained. In the case of the GW170817 event, the chirp mass was constrained to $1.188^{+0.004}_{-0.002}$ at the 90% confidence level, and the mass ratio was constrained to be in the range $0.7 - 1$ within the same

confidence level, whereas the effective tidal deformability was inferred to be smaller than 800 [3].

$$\tilde{\Lambda} = \frac{16}{13} \frac{(m_1 + 12m_2) m_1^4 \Lambda_1 + (m_2 + 12m_1) m_2^4 \Lambda_2}{(m_1 + m_2)^5} \quad (2.92)$$

Such measurements allow to reduce the set of Skyrme models able to reproduce the NS properties. Following [237], we have solved the Einstein equations for slowly rotating Skyrmion stars with the hybrid EOS using the Hartle-Thorne formalism [117, 222] and obtained the dimensionless tidal deformability of stars described by this model as a function of their TOV mass. On the other hand, since the chirp mass of the binary progenitor of GW170817 is well measured, for any given EOS the effective deformability reduces to a simple EOS-dependent function of the mass ratio. These curves, together with the constraints commented above, are represented in Fig. 2.17, from where it follows that our new EOS is compatible with the data from [3] for the ranges of p_* and p_{PT} considered. Future measurements of the tidal deformability of NS will allow us to further constrain these ranges, since we find that the curves $\tilde{\Lambda}(q)$ depend on the particular values of both parameters.

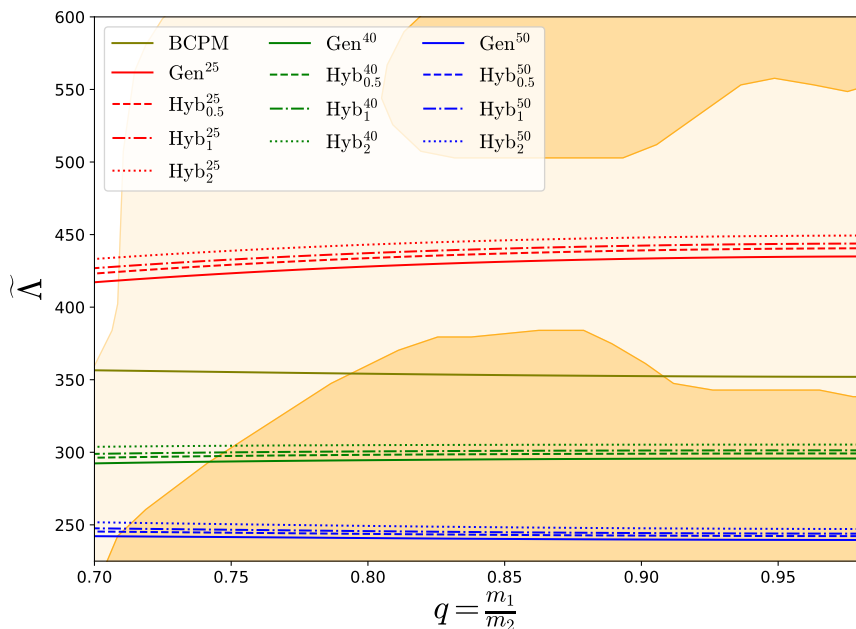


Figure 2.17: $\tilde{\Lambda}$ as a function of the mass ratio. The orange shaded regions correspond to the 50% (dark) and 90% (light) credible regions for the joint posterior of $\tilde{\Lambda}$ and q as obtained in [3] assuming a low spin prior. The notation for the curves are: $\text{Gen}^{p_{PT}}$, $\text{Hyb}_{p_*}^{p_{PT}}$.

For completeness, we also compute the effective deformability for the EOS considered in the previous section. This observable completely rules out the Θ and pion mass MF potentials in the BPS model due to the huge deformabilities. The MF quadratic pion mass potential is within the 90% confidence level with quite similar values to the FT pion mass potential, contrary to their MR curves. The BCPM curve lies perfectly in the main region of the inferred tidal deformability, slightly below the hybrid EOS. At the bottom we find the FT quadratic pion mass term which has the lowest deformability, but still within the accepted values.

Interestingly, we find quite extreme differences in the tidal deformability within the BPS model. On the one hand, we find the maximally stiff EOS, given by the Θ potential, which reaches the highest deformabilities, and the quadratic potential with the lowest values. We find a possible explanation about this difference in the energy density distribution inside the NS. From Fig. 2.3 we may see that the FT quadratic potential concentrates the vast majority of matter in the core, whilst the MF pion mass potential, which has an almost identical behaviour to the Θ potential, nuclear matter is homogeneously distributed along the star. Then, for two equal mass NS from the different models, the one with the largest amount of matter concentrated in the core would be the least deformed since matter in the surface is more gravitationally bounded. Additionally, it was suggested in [127] that the behaviour of the energy density profile might also be the origin of some universal relations like the inertia moment and compactness of the stars, with which the tidal deformability is also related.

The λ^2 coupling constant appearing in front of the sextic term in the generalized Lagrangian does not directly show up in the generalized EOS proposed in this work, whose parameters are constrained by the observations of maximum mass and deformability. However, the generalized Skyrme model EOS approaches the EOS of the BPS submodel for sufficiently large pressure, by assumption. We can, therefore, extract an effective value of λ^2 by taking the limit of infinite pressure and using the Euler relation of the BPS model (2.46) to obtain an effective value of λ^2 ,

$$\lambda_\infty^2 = \lim_{p \rightarrow \infty} \frac{p + \rho}{2\pi^4 n_B^2}. \quad (2.93)$$

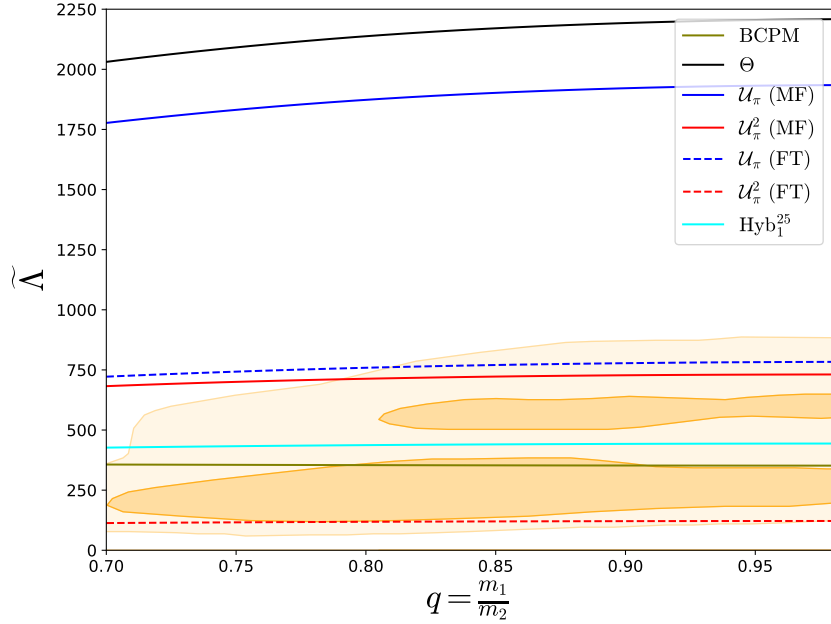


Figure 2.18: $\tilde{\Lambda}(q)$ curves for the EOS considered throughout this chapter with the same GW170817 constraints as in Fig. 2.17.

For the range of values $p_{PT} \in [25, 50]$ MeV/fm 3 , we find that $\lambda_\infty^2 \in [8.6, 11.9]$ MeV fm 3 . The values so obtained for λ_∞^2 are, therefore, compatible with the values obtained by assuming that the sextic term in the generalized Lagrangian results from integrating out the ω vector meson.

Finally, there exists the possibility to consider a quark-hadron phase transition in the cores of very massive NS [100, 201]. Indeed the density at which deconfinement is expected to occur is around $\sim 40n_0$ [32]. In this work we have found a correct description of NS observables with the generalized and hybrid EOS, reaching the highest density of $n_{\max} = 7.7n_0$ and $\rho_{\max} = 1577$ MeV/fm 3 for $p_{PT} = 50$ MeV/fm 3 in the maximal mass NS. Hence the presence of quark-deconfined matter inside NS is completely dismissed within our approach.

Chapter 3

Skyrme Crystals

But in the end, it's only a passing thing, this shadow. Even darkness must pass. A new day will come. And when the sun shines it will shine out the clearer. Those were the stories that stayed with you. That meant something. Even if you were too small to understand why.

Samwise Gamgee

Skyrmions have been extensively studied, and solutions for finite values of B were found both in the standard and the BPS submodels with different shapes and properties. The usual procedure to find a minimal energy solution considers the different possible symmetries for the skyrmion and then, the solution is the one with the lowest energy. However, it becomes more difficult to find the minimal energy solutions for increasing B since the number of possible configurations quickly grows [111].

Skyrme crystals are solutions obtained imposing periodic boundary conditions, therefore, they are infinitely spatially extended solutions so they formally have infinite baryon number. For this reason, skyrmion crystals are good candidates to describe infinite nuclear matter and to reproduce the conditions inside NS. To obtain these periodic solutions, we split the crystal in finite unit cells where we construct the skyrmion configuration, then, the main difference between the crystals and isolated skyrmions lies in the boundary conditions. Now Skyrme crystals compactify the real space into T^3 , however, since the T^3 is still an oriented and compact manifold, the Hopf's degree theorem ensures the existence of topological solitons labelled by an integer number.

From all the possible unit cells in three dimensions that we may use to construct

a Skyrme crystal, we will consider cubic unit cells throughout this work, but we will allow for different symmetries within them. Additionally, since the crystal is infinitely extended, it has infinite energy and baryon number, however, the unit cell is finite in size, hence, it carries a finite amount of energy and baryon number. Then, the energy per unit cell, as well as the energy per baryon number of the crystal, are completely well defined and finite,

$$\frac{E_{\text{crystal}}}{B_{\text{crystal}}} = \frac{N_{\text{cells}} E_{\text{cell}}}{N_{\text{cells}} B_{\text{cell}}} = \frac{E_{\text{cell}}}{B_{\text{cell}}}. \quad (3.1)$$

The first Skyrme crystal was proposed in 1985 for the standard Skyrme model by Klebanov [130], motivated by the phenomenological application of crystals to the interior of NS. He considered the simplest possible crystal with a simple cubic (SC) unit cell, in which eight $B = 1$ skyrmions were located in the corners of the cube in the maximal attractive channel with respect to their nearest neighbors. Then, he computed the minimal energy field configuration respecting these conditions for different values of the unit cell side length and found that the lowest value of the energy was just 8% above the BPS bound. In the following, we will explain how we construct Skyrme crystals via the procedure given in [136] with the different symmetries that have been proposed, and we will compare them within the generalized Skyrme model.

3.1 Construction of Skyrme crystals

The starting point in the construction of the Skyrme crystal proposed in [136] is the expansion of the fields in the following Fourier series,

$$\begin{aligned}\sigma &= \sum_{a,b,c}^{\infty} \beta_{abc} \cos\left(\frac{a\pi x}{L}\right) \cos\left(\frac{b\pi y}{L}\right) \cos\left(\frac{c\pi z}{L}\right), \\ \pi_1 &= \sum_{h,k,l}^{\infty} \alpha_{hkl} \sin\left(\frac{h\pi x}{L}\right) \cos\left(\frac{k\pi y}{L}\right) \cos\left(\frac{l\pi z}{L}\right), \\ \pi_2 &= \sum_{h,k,l}^{\infty} \alpha_{hkl} \cos\left(\frac{l\pi x}{L}\right) \sin\left(\frac{h\pi y}{L}\right) \cos\left(\frac{k\pi z}{L}\right) \\ \pi_3 &= \sum_{h,k,l}^{\infty} \alpha_{hkl} \cos\left(\frac{k\pi x}{L}\right) \cos\left(\frac{l\pi y}{L}\right) \sin\left(\frac{h\pi z}{L}\right).\end{aligned}\tag{3.2}$$

Here, the unit cell extends from $-L$ to L (being L an input parameter) in all three Cartesian directions, so the volume of the unit cell is $V = 8L^3$. Then, the symmetries of a given crystal impose some conditions on the Skyrme field which, in the end, are translated into constraints on the coefficients of the expansions β_{abc} and α_{hkl} . Finally, the constrained coefficients are varied in order to obtain the lowest energy configuration. These expansions of the fields break the normalization condition of the Skyrme field (2.1), a renormalization is required,

$$n_A \longrightarrow \frac{n_A}{\sqrt{n_B n_B}}.\tag{3.3}$$

Although the expansion series of the fields are infinite, the truncation to the first coefficients provides a good approximation to the solution. Therefore, the addition of higher modes produces corrections to the energy, which become smaller for higher orders. Indeed, we find that the energy converges very fast with an increasing number of coefficients considered in the expansion. This conclusion is also seen numerically; while the first coefficients are of order ~ 1 , we have calculated that the next orders decay to the $\sim 4\%$, $\sim 0.3\%$ and $\sim 0.06\%$

of the first-order results. Hence, we may safely truncate the series to a finite number of coefficients; we take around 30 coefficients to obtain the solution for each crystal.

The crystal considered by Klebanov has the simplest unit cell. It is invariant under cubic symmetry transformations:

$$\begin{aligned} A_1 : (x, y, z) &\rightarrow (-x, y, z), \\ (\sigma, \pi_1, \pi_2, \pi_3) &\rightarrow (\sigma, -\pi_1, \pi_2, \pi_3), \end{aligned} \quad (3.4)$$

$$\begin{aligned} A_2 : (x, y, z) &\rightarrow (y, z, x), \\ (\sigma, \pi_1, \pi_2, \pi_3) &\rightarrow (\sigma, \pi_2, \pi_3, \pi_1), \end{aligned} \quad (3.5)$$

and it has an additional periodicity symmetry on the side length of the unit cell,

$$\begin{aligned} A_3 : (x, y, z) &\rightarrow (x + L, y, z), \\ (\sigma, \pi_1, \pi_2, \pi_3) &\rightarrow (\sigma, -\pi_1, \pi_2, -\pi_3), \end{aligned} \quad (3.6)$$

Owing to the translational invariance of A_3 , the energy (2.76) and baryon (2.7) densities are periodical in L , as well as reflection invariant due to the symmetry A_1 . Since each skyrmion contributes $1/8$ to the baryon number and the cube has eight corners, the baryon number of this cube is 1. However, the fields are periodical in $2L$ (as follows again from the symmetry A_3), hence the unit cell is a cube of length $2L$.

Body Centered Cubic (BCC) Crystal of half-skyrmions

This unit cell was proposed in [103] to be the one with the lowest energy for small values of L . It introduces an additional symmetry,

$$\begin{aligned} B_4 : (x, y, z) &\rightarrow (L/2 - z, L/2 - y, L/2 - x), \\ (\sigma, \pi_1, \pi_2, \pi_3) &\rightarrow (-\sigma, \pi_2, \pi_1, \pi_3). \end{aligned} \quad (3.7)$$

to those of the Klebanov crystal (A_1 , A_2 and A_3). The motivation of this new crystal comes from the appearance of an additional symmetry when two $B = 1$ skyrmions are brought together and form the lower energy $B = 2$ field configuration, in which the $B = 1$ skyrmions have lost their individual identity. This new symmetry involves an $O(4)$ transformation that produces a BCC unit cell of half-skyrmions. A half-skyrmion is a solution with $\sigma = -1$ at the centre until some radius r_0 for which $\sigma = 0$. It carries a half of baryon charge and it is undefined outside r_0 . This solution is located in the centre of the cube of side length L . Additionally, a new half-skyrmion solution can be defined via the transformation $(\sigma, \pi_a) \rightarrow (-\sigma, -\pi_a)$. These new solutions are located in the corners of the cube, connected to the $\sigma = 0$ value of the central half-skyrmion at $r = r_0$, forming a cube of side length L .

As a result, the mean value of the σ field in this cube is exactly zero, so the energy coming from the potential term $\mathcal{L}_0 \sim (\sigma - 1)$ will scale exactly as $8c_0 L^3$. Further, the eight half-skyrmions in the corners contribute a total baryon number of $1/2$, so the cube of side length L contains a baryon charge of $B = 1$.

The energy and baryon densities are also periodic in L , but the fields have again a $2L$ periodicity, then, we have $B_{\text{cell}} = 8$ within our unit cell of side length $2L$. The energy density iso-contour plots of the unit cell are shown both in two and three dimensions in Fig. 3.1.

The restrictions imposed on the Fourier coefficients by the last symmetries are:

- h, k are odd, l is even.
- a, b and c are even.
- $\beta_{abc} = \beta_{bca} = \beta_{cab}$.
- $\alpha_{hkl} = -(-1)^{\frac{h+k+l}{2}} \alpha_{khl}$.
- $\beta_{abc} = -(-1)^{\frac{a+b+c}{2}} \beta_{bac}$.

Face Centered Cubic (FCC) Crystal of skyrmions

This symmetry was proposed in [136] in order to have a new solution with lower energy for very large values of L . It shares symmetries A_1 and A_2 and also has

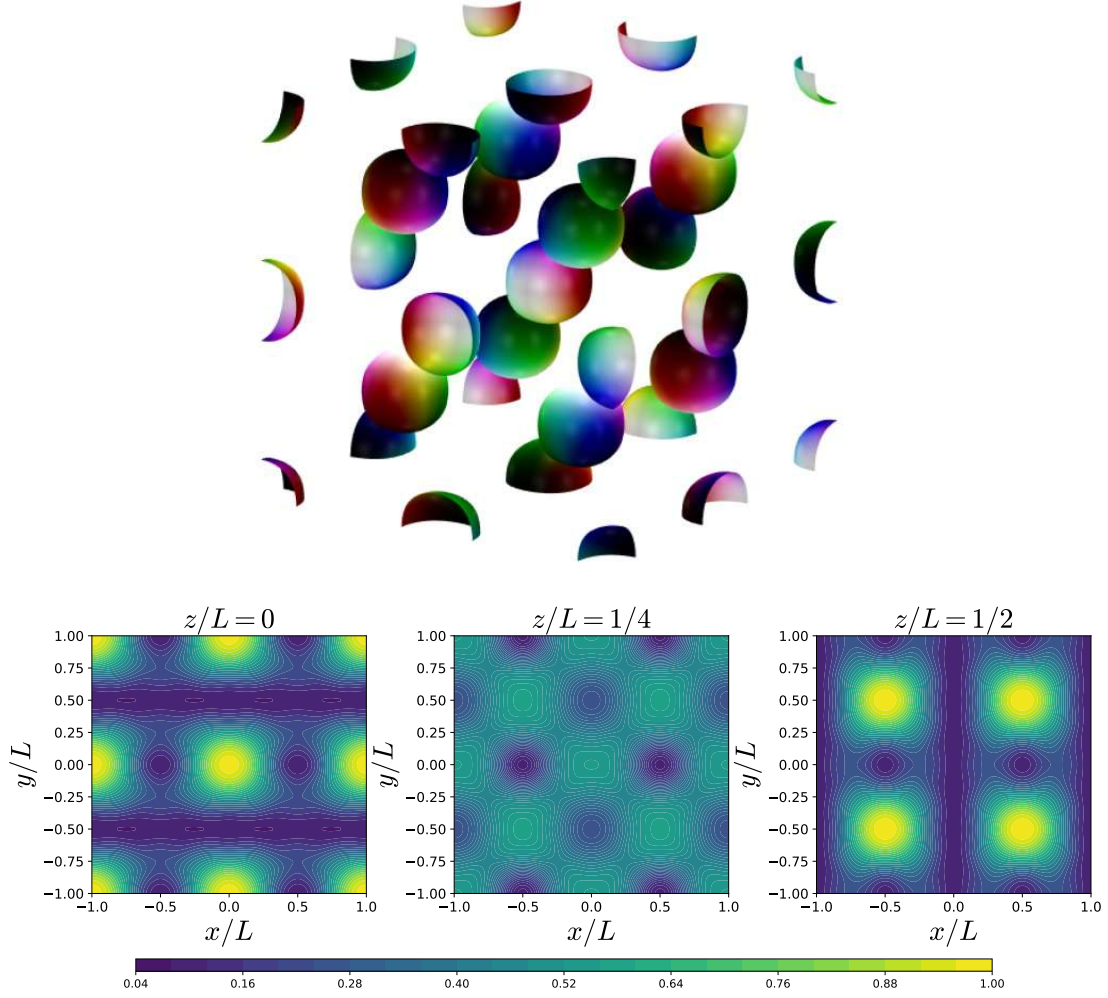


Figure 3.1: Top: The 3D energy density plot of the BCC unit cell with $B_{\text{cell}} = 8$. We adopt the Runge colouring convention [91] in this figure to represent the pion fields. Bottom: Energy density contour plots in two dimensions at $z = 0$, $L/4$ and $L/2$ respectively.

two additional symmetries,

$$\begin{aligned} C_3 : (x, y, z) &\rightarrow (x, z, -y), \\ (\sigma, \pi_1, \pi_2, \pi_3) &\rightarrow (\sigma, -\pi_1, \pi_3, -\pi_2), \end{aligned} \quad (3.8)$$

$$\begin{aligned} C_4 : (x, y, z) &\rightarrow (x + L, y + L, z), \\ (\sigma, \pi_1, \pi_2, \pi_3) &\rightarrow (\sigma, -\pi_1, -\pi_2, \pi_3). \end{aligned} \quad (3.9)$$

In this case, the energy and baryon number are periodic in $2L$, and the unit cell has the shape of an FCC lattice of skyrmions. We have eight $B = 1$ skyrmions in the corners of the cube, and symmetry C_4 locates other six skyrmions in the

centre of the faces and it also isorotates them by π with respect to their nearest neighbours. Thus, this lattice differs from the first in that each skyrmion is surrounded by 12 nearest neighbours, all of them in the maximal attractive channel. Since we have the eight skyrmions in the corners and other six in the faces of the cube, the total baryon number in this unit cell is $B_{\text{cell}} = 4$. Again, the same energy density contour plots are shown in Fig 3.2 for this new crystal.

As we mentioned before, these symmetries impose some constraints on the Fourier coefficients and they can be easily obtained imposing the symmetries on the field ansätze (3.2). In this case, the non-vanishing coefficients are determined from the combination of the following restrictions:

- h is odd, k and l are even or h is even, k and l are odd,
- a, b, c are all odd or a, b, c are all even.

Face Centered Cubic ($\text{FCC}_{1/2}$) Crystal of half-skyrmions

This crystal configuration was almost simultaneously found, in two different publications [77, 136], to be the one with the lowest energy in the standard Skyrme model. It may be seen as the half-skyrmion version of the FCC crystal explained before, since each kind of half-skyrmion (with $\sigma = \pm 1$ in their centre) form a FCC lattice, similar to the NaCl crystal structure. Indeed it shares the symmetries A_1, A_2, C_3 plus an additional symmetry,

$$\begin{aligned} D_4 : (x, y, z) &\rightarrow (x + L, y, z), \\ (\sigma, \pi_1, \pi_2, \pi_3) &\rightarrow (-\sigma, -\pi_1, \pi_2, \pi_3), \end{aligned} \tag{3.10}$$

then, some of the FCC crystal Fourier coefficients are set to zero in this crystal. Specifically, this new unit cell only allows the Fourier coefficients which satisfy the conditions:

- h is odd, k and l are even,
- a, b, c are all odd.

As a consequence, the $\text{FCC}_{1/2}$ crystal will always have equal or larger energy than the FCC crystal. This may lead to phase transitions between the crystals

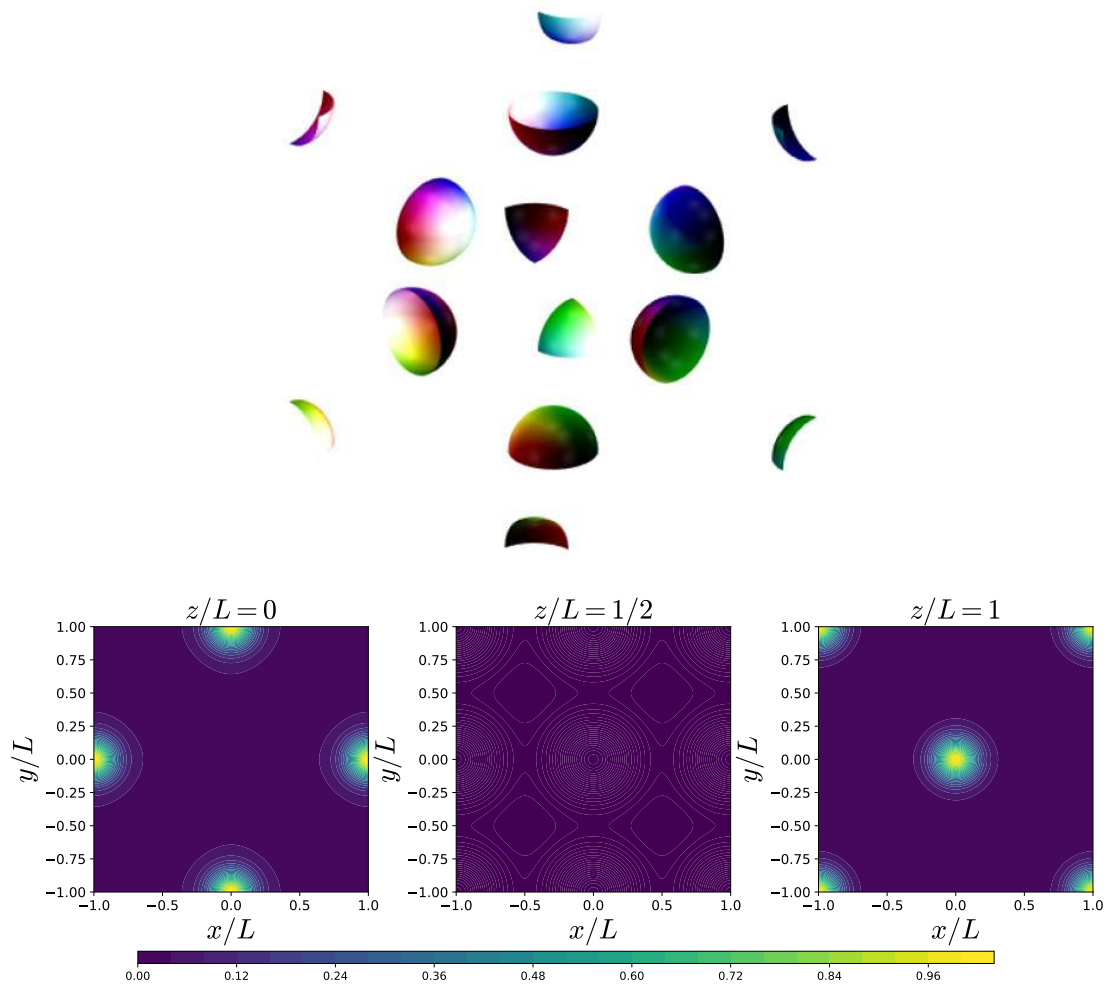


Figure 3.2: Top: The 3D energy density plot of the FCC unit cell with $B_{\text{cell}} = 4$. The colours follow the Runge colouring convention. Bottom: Energy density contour plots in two dimensions at $z = 0$, $L/2$ and L respectively, since the energy density has double the period of the previous crystal.

at some length of the unit cell as we will see later.

Equivalently to the FCC crystal, the half-skyrmion solutions with $\sigma = -1$ in their centre are located at the corners and faces of the unit cell. Further, the opposite half-skyrmions with $\sigma = 1$ occupy the body centre and the link centres of the unit cube. Then, the mean value of the σ field is zero, again, as in the BCC crystal. We show the same contour plots of the half-crystal in Fig. 3.3.

The energy and baryon densities are periodic in L and they have the appearance of a simple cubic unit cell of half-skyrmions. However, since the fields are periodic in $2L$ we take that to be the side length of the unit cell, hence, the unit cell still has the shape of an FCC crystal with the alternating half-skyrmion

solutions. In this case, the baryon content within our unit cell is again $B_{\text{cell}} = 4$. This crystal is precisely the one studied in the second section of Chapter 2,

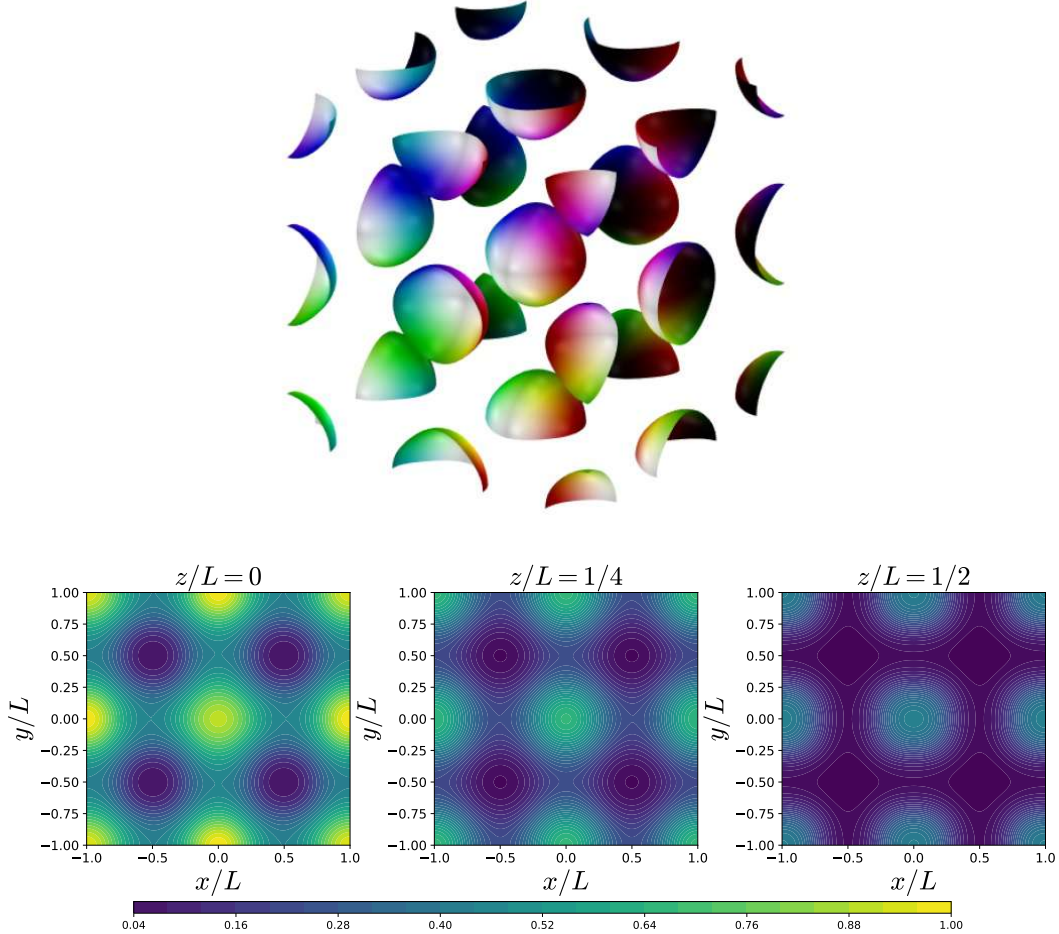


Figure 3.3: Top: The 3D energy density plot of the $\text{FCC}_{1/2}$ unit cell with $B_{\text{cell}} = 4$. The pion fields are represented following the Runge colouring convention. Bottom: Energy density contour plots in two dimensions at $z = 0$, $L/4$ and $L/2$ respectively, as in the BCC crystal.

where we denoted with l the size parameter of the $B = 1$ unit cell. Therefore, the equivalence between the size parameter l in (2.23) and the side length L is $l = 2^{1/3}L$.

Numerical procedure

The full minimization of the energy functional becomes a computationally hard task when the number of coefficients increases. For this reason, in a first step, we will consider the simplest ansatz with only the first non-vanishing coefficients for the $\text{FCC}_{1/2}$ crystal.

The minimal energy configuration of this crystal in the \mathcal{L}_{24} model has been found at $L = 4.71$ with $E/B = 1.038$. The first nonzero coefficients under the restrictions explained before are β_{111} and α_{100} . We may impose $\alpha_{100} = 1$ without loss of generality and leave the other coefficient to minimize the energy. The minimum is attained for $\beta_{111} = -1$ at $L = 4.92$ with an energy per baryon of $E/B = 1.071$, which is already smaller than the minimum of the Klebanov crystal.

The minimum is shifted towards the correct values when more coefficients are included in the minimization. The convergence is indeed quite fast, the number of coefficients for which we reproduce the values of the minimum is 32. This number slightly changes for the other crystals, given that the restrictions change. For instance, the BCC crystal required more modes in the expansion (3.2) since many of the coefficients vanish due to the high symmetry.

The minimization is performed through the variation of the coefficients via a Nelder-Mead algorithm [170], implemented in the GSL library of C++. This algorithm is also known as the downhill simplex method [192], and it is a numerical method based on a direct comparison of the function at each iteration for multidimensional minimization. The algorithm maps the n -dimensional parameter space via a triangulation using the concept of $n + 1$ -simplex, which is the generalization of the triangle in higher dimensions. The worst vertex in the simplex is replaced by the centroid of the remaining n points, so that the algorithm proceeds. The minimization ends when the size of the simplex reaches some desired tolerance.

Additionally, the ansätze of the Skyrme fields are known analytically, and they have been fixed to reproduce the properties of the specific crystal, like the baryon number in the unit cell and the orientations of the skyrmions, independently on the specific values that yield the minimal energy configuration. Hence, the derivatives of the fields are known analytically as well, so the integrals of the baryon and energy densities may be accurately estimated numerically since the expressions may be evaluated at any point in space. We use a Gaussian quadrature method for the computation of the integrals, which induces a negligible error. It has been estimated to be less than 10^{-5} for the baryon number.

Therefore, the main source of error in this minimization comes from the variations of the coefficients, which we estimate to induce around 1% of error in the energy. This is contrary to the AGD minimization, where the derivatives and integrations are estimated using finite differences and Riemann sums respectively. However, in the AGD method, the error is induced in both the baryon number and energy, hence, a common way to erase this effect is to compute the ratio between both values.

Once the values of the curve $E(L)$ have been obtained, we fit the points with the following function,

$$\frac{E}{B} = k + k_2 L + \frac{k_4}{L} + c_6 \frac{k_6}{L^3} + c_0 k_0 L^3, \quad (3.11)$$

which is motivated from the scaling behaviour of the different terms that appear in the Lagrangian.

This fit reproduces the numerical points with great accuracy, being the largest difference between the fit and the data point less than 0.5%. Furthermore, this fit is extremely useful since it allows for the analytical manipulation of the energy curve in order to compute the important magnitudes, like the pressure, energy density and speed of sound.

3.1.1 Perfect scaling property

An interesting observation is that the contribution to the energy of each term can be approximately parametrized as $E(L) = c_i K_i L^{3-i}$, at least for $L \leq L_{\min}$ in the FCC_{1/2} crystal. Here, K_i is a universal constant in the sense that different parameters will not change its value, and i is the scaling dimension of each term. Then, the energy can be expressed as the sum of the individual contributions of each term in the Lagrangian. This suggests that at least in the high density regime (which is the one of interest), there is an approximate perfect scaling of each term. The accuracy of this approximation is given by the differences $K_i \neq k_i$ and $k \neq 0$. This perfect scaling (PS) property at medium ($L \sim L_{\min}$) densities will be useful to fit the values of the constants f_π and e in the next sections. To obtain the perfect scaling parametrization, we calculate the energy for a single value of L and we compute the contribution of the different terms

individually to extract the constants K_i . Specifically, we calculate the constants K_i in the case $c_6 = c_0 = 1$ for simplicity and for a value of the length near the minimum. Then, the curve $E(L)$ can be approximated by

$$\frac{E_{\text{PS}}}{B} = K_2 L + \frac{K_4}{L} + c_6 \frac{K_6}{L^3} + c_0 K_0 L^3. \quad (3.12)$$

The universal constants K_i of the PS approximation are given in Table 3.1.

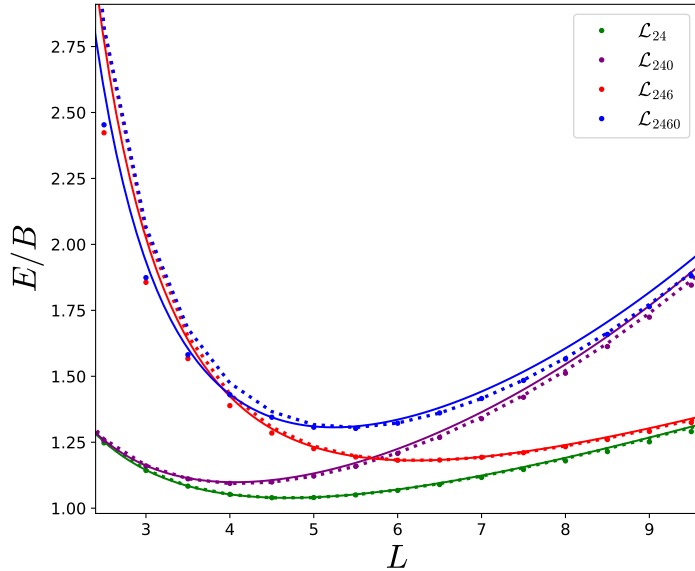


Figure 3.4: Energy per baryon number curves against the lattice length L of the $\text{FCC}_{1/2}$ crystal. The circles are the full-numerically minimized values of the energy, the solid lines are the PS approximation curves, and the dots were obtained from the Castillejo ansatz for the fields.

We show in Fig. 3.4 the comparison between the curves of the energy per baryon number of the $\text{FCC}_{1/2}$ crystal for the four different submodels. We have considered the standard values of the parameters (2.21) for f_π and e and we just turn on and off the sextic term coupling constant to $\lambda^2 = 5 \text{ MeV/fm}^3$ and the pion mass to its physical value. The PS curve is also represented in order to compare this approximation with the fully minimized energy values. We also consider the energy curve obtained from the approximated ansatz for the Skyrme fields given in [77] by Castillejo et al. In this figure, we may see that the Castillejo ansatz for the Skyrme field is a better approximation for large values of L whilst the PS deviates more from the numerical values in that region, but it is more accurate in the large density regime. Both approximations are quite accurate around the minimum of the curve, and this fact will be of great importance to describe realistic nuclear matter inside NS. It is also clearly visible how the dif-

ferent terms that we include in the Lagrangian have the expected impact on the energy per baryon curve. The sextic term, due to its repulsive behaviour, shifts the length of the minimum to larger values, whereas the attractive potential term has the opposite effect.

Model	K_2	K_4	K_6	K_0
\mathcal{L}_{24}	0.1108	2.4373	0	0
\mathcal{L}_{240}	0.1136	2.4089	0	0.0085
\mathcal{L}_{246}	0.1111	2.4319	1.2435	0
\mathcal{L}_{2460}	0.1164	2.4042	1.0824	0.0084

Table 3.1: Fitting constants for the PS approximated curves

3.2 Infinite nuclear matter from Skyrme crystals

The binding energies of isolated nuclei are a measure of how much a particular nucleus is bounded to lighter nuclei. They have been experimentally measured up to very high baryon numbers, and it is known that they are accurately reproduced by the semi-empirical mass formula:

$$\text{BE}_B := m_N B - E_B = a_V B - a_S B^{2/3} - a_A \frac{(N_n - N_p)^2}{B} - a_C \frac{N_p (N_p - 1)}{B^{1/3}}, \quad (3.13)$$

where E_B is the mass of the nucleus with baryon number B , and N_p, N_n are the number of protons and neutrons respectively.

The first contribution corresponds to a bulk term which just takes into account the number of baryons that the nucleus has. The second term is the contribution from the finite-size effects, *i.e.* a correction from the surface of the nucleus. The third term is the quantum isospin correction to the energy, which does not break isospin symmetry but penalizes any asymmetry between protons and neutrons, it is also called the pairing term. The last term is just the contribution from the Coulomb energy between protons in the nucleus.

This model is based on theoretical arguments in which nuclei are considered spherical drops of incompressible fluid, but the values of the coefficients (a_V, a_S, a_A, a_C) are obtained from the fit of the experimental data for physical nuclei, so this is why it is called semi-empirical. Under these assumptions the nuclei lie in a

constant density curve which is called the nuclear saturation density n_0 . This value has been measured from the interior of very large nuclei [123] and the most fiducial value is given by (2.49).

The system that we want to describe using the Skyrme crystals, with the final aim of reproducing NS, is commonly known as infinite nuclear matter (INM). It is an idealized system where the surface, Coulomb and isospin contributions are neglected. Then, we can extract the value of the energy $E_0 := m_N - a_V$ (2.49) of INM at the saturation density from the semi-empirical mass formula. Hence, we will be interested in the fit of the minimum of the Skyrme crystals, at which the skyrmions are at zero pressure, to the values of the INM at the saturation point.

A remarkable property of the standard Skyrme model without potential term is that, with a suitable choice of units (2.8), one can factor out all dimensionful constants from the energy functional, so that the constants remaining inside it are just dimensionless numbers. As a consequence, one can just forget about the numerical values of the coupling constants and numerically find the different crystalline solutions at different unit cell lengths. Once the relation between the energy and length $E(L)$ is found, the values of the coupling constants can be adjusted a posteriori in order to fit whatever observable we are interested in. Unfortunately, the addition of the sextic and mass potential terms to the energy functional spoils this property, as there is no choice of units that allows to factor out all coupling constants in the energy functional. This means that, in order to be able to obtain solutions, one needs first to give specific values to the coupling constants appearing in the problem. However, this is problematic if one wants to fit the values of energy and density to some physical values. In our case, we want to identify the energy and the density at the minimum of the crystal ($L_0 := L_{\min}$) with the nuclear saturation point, however, one cannot know the value of L_0 without performing the numerical simulations, but in order to do so you need to fix the values of the parameters. Hence, the fitting of the skyrmion crystal parameters in the generalized model to values at nuclear saturation is, in principle, a very difficult problem that needs to be solved iteratively until a self consistent solution is achieved. Given the computational cost of simulating a single unit cell at a given length, following this naive approach would make

it almost impossible to realize a significant scan of parameters in a reasonable time. However, due to the PS property at the minimum, we take advantage of this approximation in order to fit the magnitudes obtained from generalized Skyrme crystals to their physical values (up to a certain error).

We fix the physical value of the pion mass, and we will use two different values to the sextic term coupling constant λ^2 . As we mentioned before, the values of

$m_\pi = 0$			$m_\pi = 138 \text{ (MeV)}$		
f_π (MeV)	e	λ^2 (MeV fm 3)	f_π (MeV)	e	λ^2 (MeV fm 3)
137.81	4.59	0	118.76	4.32	0
147.75	5.51	3	125.33	4.90	3
160.30	8.59	7	134.80	6.26	7

Table 3.2: Values for the parameters of the generalized Skyrme model that fit the minimal energy point of the FCC $_{1/2}$ crystal to the nuclear saturation point.

f_π and e which reproduce (2.49) can, in fact, be calculated exactly in the \mathcal{L}_{24} , since the dimensionless Lagrangian does not depend on them,

$$\frac{f_\pi}{e} = \frac{B_{\text{cell}}}{3\pi^2 E_{\min}} E_0, \quad f_\pi e = (2n_0)^{1/3} L_{\min}. \quad (3.14)$$

where L_{\min} and E_{\min} denote the values of the length and energy at the minimum, and B_{cell} is the baryon number of the unit cell (recall that we consider the unit cell with volume $8L^3$). In the FCC $_{1/2}$ phase, $B_{\text{cell}} = 4$, and for the model \mathcal{L}_{24} the exact values have been previously shown, $f_\pi = 138.17$ MeV, and $e = 4.60$, being quite close to those obtained from the perfect scaling approximation. These values are, in fact, not far from those obtained fitting the hedgehog solution to the proton and the Δ excitation [29]. For the other models, we do not attempt to calculate f_π and e exactly. Instead, we calculate them from the coefficients obtained from perfect scaling approximation, and then use (2.49) to fit the pairs of values (L_{\min} , E_{\min}) by varying f_π and e .

The results for the fits are given in Table 3.2. Interestingly, we find the same effect as with the isolated $B = 1$ skyrmion, where the Skyrme parameter increases due to the presence of the sextic term, but it is less pronounced. Besides, the constant f_π is more affected in this fit, but still smaller than its physical value.

As a first, and interesting, check we also have computed the energy of the $\text{FCC}_{1/2}$ crystal with the parameters obtained from the previous chapter to compare with the energies given in Table 2.4. The minimal value is reached for $L_0 = 5.20$ with $E_0/B = 1.280$, being a 6% smaller than the $B = 4$ isolated skyrmion.

3.2.1 Comparison between the symmetries

We show the curves E/B for the different symmetries and for different models in Fig. 3.5. The left upper plot (model \mathcal{L}_{24}) reproduces the known results described in the Chapter 2. A more detailed discussion of the remaining plots will be given below, where we describe the resulting phases of skyrmionic matter at different densities. In Fig. 3.5 we also use the fact that for all models, except for the simplest model \mathcal{L}_{24} , there exist topological energy bounds [18] which are tighter than the Skyrme-Faddeev bound. We plot these topological energy bounds for each model together with the energy curves for the values of the parameters specified in Table 3.2. Although the crystals do not reach the bounds, they are very close to it at the minimum. We show the values of these bounds and how far the minimal energy of the crystals are above it in Tables 3.5 and 3.6.

Further, we find that the half-skyrmion phases are well fitted to the proposed parametrization (3.11) even for $L \geq L_{\min}$. However, this parametrization breaks down for large L for the FCC phase, and a more complicated behaviour is observed in this region. Indeed, $\langle \sigma \rangle$ does not vanish for large L in the FCC phase, but has a nontrivial dependence on L which requires a different fitting curve rather than (3.11). A possible choice for the large L regime might be a hyperbolic tangent, but we cover the whole curve using a spline cubic interpolation. However, for small L the FCC phase is either exactly equal to the $\text{FCC}_{1/2}$ phase (a phase transition occurs) or very close to it. In particular, the region where the FCC phase differs significantly from the $\text{FCC}_{1/2}$ phase is always beyond the minimum, *i.e.*, for $L > L_{\min}$. As we shall argue below, in this region the FCC crystal is not relevant for the nuclear EOS. We will, therefore, ignore this problem and we will work with the parameters of the fit k_i that reproduce the half-skyrmion curves, which are given in Table 3.3. The fit for the $\text{FCC}_{1/2}$ phase serves as a good approximation for the FCC phase in the small L region.

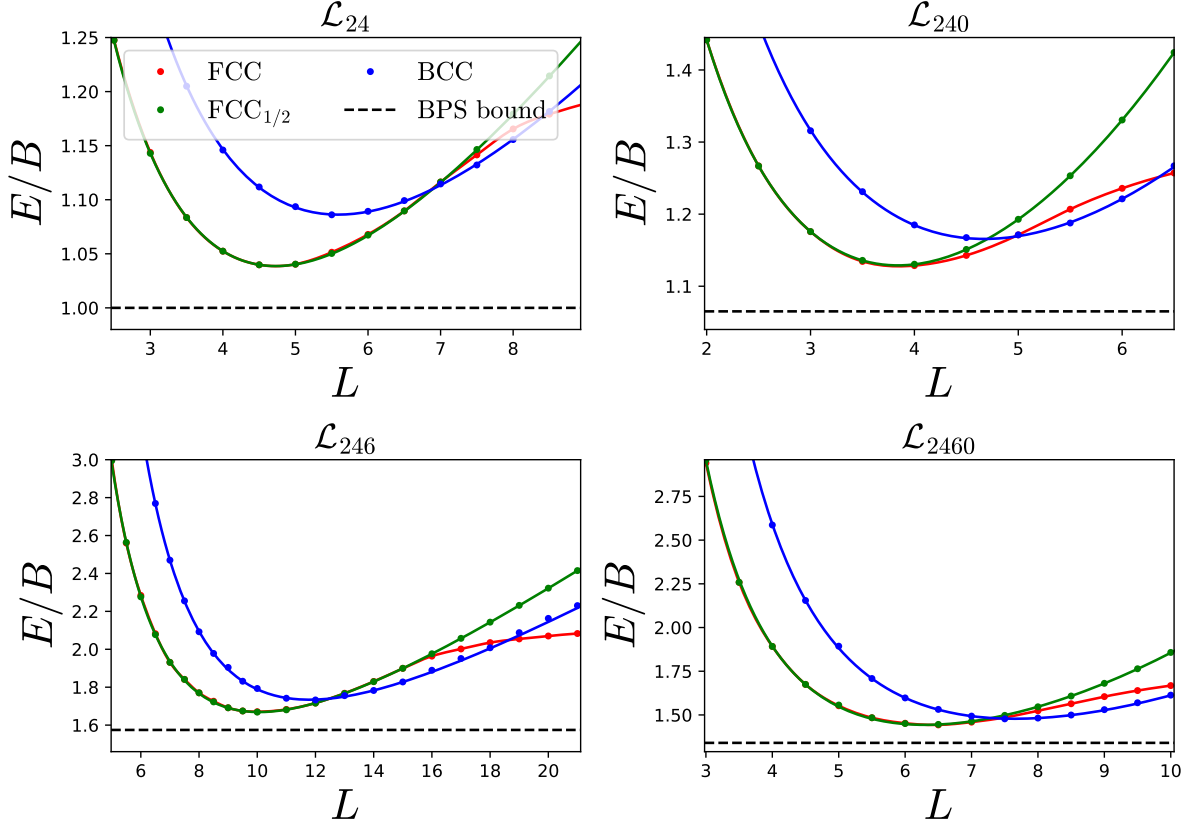


Figure 3.5: Energy per baryon as a function of the lattice length parameter for the three different crystal symmetries considering the four relevant Skyrme models. The horizontal dashed line represents BPS bound of each model for the specific choice of parameters in each case. The energy and length are both given in adimensional units (2.8).

Model	k_0	k_2	k_4	k_6	k_0
\mathcal{L}_{24}	0.0467	0.1049	2.3448	0	0
\mathcal{L}_{240}	0.0201	0.1094	2.3866	0	0.0082
\mathcal{L}_{246}	0.0440	0.1027	3.8966	0.8183	0
\mathcal{L}_{2460}	0.1221	0.0956	2.6941	0.8650	0.0087

Table 3.3: FCC_{1/2} crystal fit coefficients.

Model	k_0	k_2	k_4	k_6	k_0
\mathcal{L}_{24}	0.0168	0.0957	2.9876	0	0
\mathcal{L}_{240}	-0.0760	0.1114	3.1247	0	0.0034
\mathcal{L}_{246}	0.1618	0.0885	3.1918	1.6589	0
\mathcal{L}_{2460}	0.1367	0.0840	3.0337	1.6915	0.0046

Table 3.4: BCC crystal fit coefficients.

Model	L_0	E_0/B	Bound
\mathcal{L}_{24}	4.72	1.04	1
\mathcal{L}_{240}	3.84	1.13	1.06
\mathcal{L}_{246}	9.97	1.67	1.57
\mathcal{L}_{2460}	6.30	1.44	1.34

Table 3.5: FCC_{1/2} crystal values at the minimum of energy.

Model	L_0	E_0/B	Bound
\mathcal{L}_{24}	5.56	1.08	1
\mathcal{L}_{240}	4.66	1.16	1.06
\mathcal{L}_{246}	11.76	1.73	1.57
\mathcal{L}_{2460}	7.65	1.48	1.34

Table 3.6: BCC crystal values at the minimum of energy.

As expected, we conclude that the FCC crystal reaches the lowest energy in the \mathcal{L}_{240} and \mathcal{L}_{2460} cases, but the FCC_{1/2} crystal is the energetically favourable phase

at the minimum when the pion mass term is not included. This conclusion is visible in Fig. 3.5, but the details on which phase is preferable will be clarified in the next section. Another set of parameters was considered in [22] and the conclusions were the same as here, however, from Tables 3.5 and 3.6 it may be seen that the difference in energy between the FCC_{1/2} and BCC crystals is significantly smaller when the pion mass term is present. Therefore, it seems possible to find a set of parameters with sufficiently large c_0 for which the BCC has lower energy than the FCC crystals, however, a physical motivation for that choice of parameters is required.

Again, the impact of each term in the $E(L)$ curve is visible in Fig. 3.5, where the minimal energy configuration is shifted towards larger or smaller values of the lattice length. Also the energy increases when new terms are added, although the energy of the \mathcal{L}_{246} is higher than the full generalized Skyrme model. This effect may seem contradictory, but the comparison in this case is harder than in Fig. 3.4, where we just turn on and off each term in the Lagrangian. In this case, the parameters are changed among the different models in order to fit to the same physical energy and length scales. Then, by comparing the values of the adimensional coupling constants (c_6, c_0) present in the energy, we see that the sextic term contribution is much larger in the \mathcal{L}_{246} term than in the full model, producing the larger adimensional energy.

Besides, the energy of the minimum moves away from the BPS bound when more terms are added in the Lagrangian. This is, again, surprising when the sextic term is introduced since we are closer to the BPS Skyrme model, then, the difference should decrease. As stated in the previous chapter, for very large values of the sextic and potential terms, the difference between the minimum and the bound will finally decrease. However, for the values considered here, the non-trivial interaction between the different terms deviates the generalized Skyrme model from a BPS theory.

We also found larger deviations from the PS constants in Table 3.1 when large values of the sextic term are considered. This is visible from the fitting constants in Table 3.3 for the \mathcal{L}_{246} case. This reflects a change in the behaviour of the Skyrme crystal under scale transformations when the sextic term (which behaves like a fluid) is dominant in the Lagrangian. Indeed, we will see in the

next subsection how a phase transition to a fluid phase may be observed.

3.2.2 Phase transitions

We may anticipate from Fig. 3.5 that even though the FCC_{1/2} crystal reaches the lowest energy at the minimum, it may not be the crystal with the lowest energy for all values of L . This is clear in the region with large values of L , for which the FCC crystal has lower energy than the FCC_{1/2}. We will also see that there is a phase transition from the FCC to the BCC crystal at small values of L , however, since they do not have the same baryon content within the unit cell, a more careful comparison is necessary. We will study in the following the possible phase transitions that we may have since it may lead to an interesting phenomenology of the Skyrme crystals. For simplicity, since L is a measure of the size of unit cell it is also a measure of the baryon density, then we will also refer to the region of small values of L as the high density regime and for large values of L the low density regime.

3.2.2.1 High density phase transitions

Fluid-like phase transition

As stated in the Chapter 2, the BPS model shares the properties of a perfect fluid [16]. The inclusion of the sextic term in the Lagrangian should, therefore, lead to a skyrmionic matter that reflects this fluidity, at least in the high density regime where the contribution from this term to the energy becomes relevant. More specifically, we will find that in the range of densities considered here, a perfect fluid is never reached exactly. Instead, the sextic term has the effect of homogenizing the energy densities in the unit cell of a crystal configuration at high densities.

A measure of this homogeneity may be obtained by comparing the exact, field-theoretic energy density and its mean value over the unit cell, $\rho_{\text{mean}} = E_{\text{cell}}/B_{\text{cell}}$. Since the sextic term scales as $1/L^3$, we expect to have a highly inhomogeneous crystal at the minimum of the energy, where the skyrmions are surrounded by regions of vacuum, whereas for decreasing values of L a more homogeneous energy density (fluid-like behaviour) will appear, *i.e.*, the field configuration will

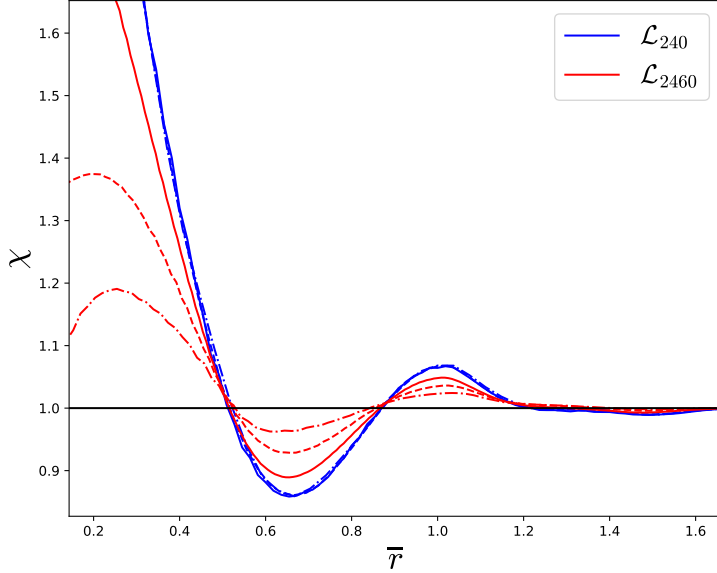


Figure 3.6: Ratio between the REPs for the crystal and the fluid at different densities with and without sextic term. The coordinate \bar{r} has been defined as the radial coordinate rescaled by the lattice length.

get closer to a perfect fluid with homogeneous energy density, without exactly reaching it. We will compare the \mathcal{L}_{240} and \mathcal{L}_{2460} cases, since we want to consider the more realistic cases in which pions have mass, however, we remark that the pion mass term is irrelevant for these high-density effects.

To compare the energy densities within the unit cell we define the radial energy profile (REP) enclosed within a sphere of radius r ,

$$E(r) = \int_0^r d^3x \rho \quad (3.15)$$

where ρ is substituted by the ρ_{mean} in the case of the constant energy density unit cell and by the energy density of the generalized Skyrme model (2.76) in the full field-theoretical case. We calculate both REPs for each case at the baryon density of the minimal energy (n_0), and at the higher densities $3n_0$ and $7n_0$. We show in Fig. 3.6 the ratio $\chi = E(r)/E_{\text{mean}}(r)$ of the two REP for each case, since it tells us how far we are from the fluid-like behaviour. For this concrete calculation, we only consider the BCC phase, because (i) this is the relevant phase for high densities, and (ii) the effect of homogenization is stronger for this phase. The resulting REP will grow with the radius until $r = \sqrt{3}L$ and take a constant value equal to the energy of the unit cell for larger values.

In Fig. 3.6 we can see that the homogeneity of the energy density strongly increases with density, *i.e.*, with decreasing values of the lattice parameter, when the sextic term is included. For the model \mathcal{L}_{240} without the sextic term, on the other hand, the ratio χ between the lattice and the fluid REPs is almost independent of the density and strongly deviates from unity. In other words, without the sextic term skyrmionic matter remains in a crystalline phase with an essentially unchanged rigidity up to very high densities. When the sextic term is included, instead, the resulting crystal becomes less rigid against volume-preserving deformations at high densities, but without completely losing its crystalline structure.

In contrast to the volume-preserving deformations, the inclusion of the sextic term is known to lead to much more resistance against these deformations like compressions, resulting in a much stiffer EOS for skyrmionic matter at high densities [23]. The stiffer EOS of the generalized model is important, since it allows for more realistic NS maximum masses than the standard Skyrme model. This observation led us to consider an EOS based on an interpolation between the standard Skyrme crystal at intermediate densities and the perfect fluid of the BPS model at high densities in the last chapter. On the other hand, the nature of the transition between the crystalline and the fluid phases remained undetermined. Our current results imply that the fluid phase is approached asymptotically rather than via a phase transition.

FCC_{1/2} to BCC phase transition

The energies per baryon number of the FCC_{1/2} and BCC phases have been compared in Fig. 3.5. An important point here is that whilst the FCC_{1/2} unit cell contains 4 baryons, the BCC unit cell has 8 baryon units, so if we want to compare both crystals we need to do it at the same baryon density.

We find that the different terms that we consider in the Lagrangian have an important impact on the transition point. Specifically, the sextic term locates the transition at physically reasonable densities, *i.e.*, the same order of magnitude as the density at the energy minimum. Without the sextic term, we find the transition point at very high densities, and the addition of the pion-mass term shifts the transition density to even higher values, therefore, we only plot

the cases in which we have the sextic term.

We show in Fig. 3.7 the two phases and the density at which the transition takes place, and the numerical values for this point are given in Table 3.7.

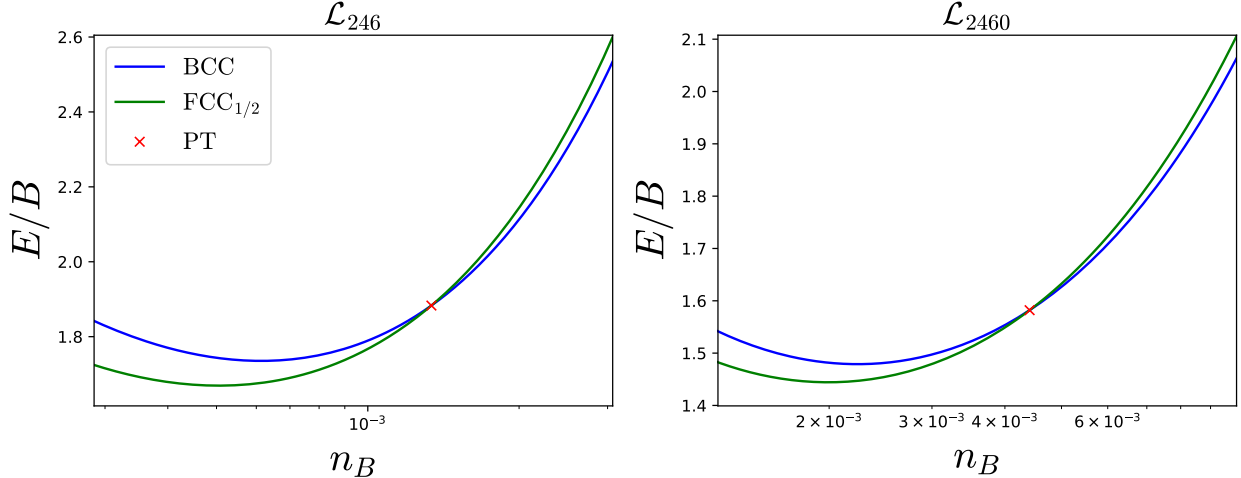


Figure 3.7: Comparison between the energies of the BCC and FCC_{1/2} crystals at the same baryon density, showing the phase transition point, denoted by the red cross in the plots. Both n_B and E are shown in Skyrme units.

Since the energy curves have different slopes at the transition point there is a discontinuity in the derivative of the energy. This implies that the FCC-to-BCC is a first order phase transition and we must perform a Maxwell construction (MC) in order to avoid unphysical regions.

The pressure of a system acquires great relevance when phase transitions are present since it must remain finite and continuous in order to have a physical transition. The pressure, as well as the energy density of the crystal, can be obtained from their thermodynamical definition (2.24).

From these expressions we may conclude that there is a discontinuity in the pressure of the crystal and this is contradiction with the Gibbs conditions that must be preserved in every phase transition,

$$p^I = p^{II}, \quad \mu_B^I = \mu_B^{II} \quad (3.16)$$

For this analysis we will identify the FCC_{1/2} crystal as the phase I and the BCC crystal as the phase II. Besides, in our system the baryon charge is conserved so we must find the mixed phase which has the associated chemical potential

(μ_B) common to both phases.

Model	n_{PT}/n_0	p_{PT} (MeV/fm 3)
\mathcal{L}_{24}	62.21	1321
\mathcal{L}_{240}	46.93	1048
\mathcal{L}_{246}	2.65	30.92
\mathcal{L}_{2460}	2.21	20.14

Table 3.7: Ratio between the transition density and the density at which the minimum of the energy of the FCC $_{1/2}$ crystal is achieved.

The MC introduces a mixed phase which preserves the Gibbs conditions in this case. The main idea of this construction is to find one point in each of the energy curves which have the same pressure, we denote it by p_{PT} , and join them with the curve which has the same value of μ_B for the two phases. Mathematically this means that we have to find the points (V_I, V_{II}) of each phase that have the same slope in the $E(V)$ diagram and are both tangent to the straight line with the same slope (which is p_{PT}). We remark that, although we denote as p_{PT} the pressure at which the phase transition occurs, it is not related to the effective transition between the Skyrme crystal and the BPS model considered in the previous chapter.

We must be careful for this calculation since we are dealing now with the volumes of the unit cells. This means that same volumes have different baryon content in each crystal, so we need to rescale them in order to have the same baryon number,

$$n_B^{\text{FCC}} = n_B^{\text{BCC}} \longrightarrow V_{\text{FCC}} = \frac{V_{\text{BCC}}}{2} \quad (3.17)$$

The final energy curve with a physical phase transition starts at low densities in the FCC $_{1/2}$ crystal until we find the mixed phase which joins to the BCC crystal,

$$E(V) = \begin{cases} E_{\text{FCC}}(V), & V \geq V_1 \\ E_{\text{FCC}}(V_1) - p_{PT}(V - V_1), & V_1 \geq V \geq V_2 \\ E_{\text{BCC}}(V), & V \leq V_2 \end{cases} \quad (3.18)$$

Actually, from the arguments given before and the curves displayed in Fig. 3.5

we would have to compute the transition between the BCC and FCC crystal of single skyrmions. However, we may use the $\text{FCC}_{1/2}$ energy curve for these calculations since the density at which the transition occurs, the FCC and $\text{FCC}_{1/2}$ crystals are the same in the \mathcal{L}_{246} case and the difference between them in the \mathcal{L}_{2460} case is negligible. The final curve, with the first order phase transition, after the MC is applied, may be seen in Fig. 3.12.

3.2.2.2 Low density phase transitions

FCC_{1/2} to FCC phase transition

As we noted in the construction of the crystals, the $\text{FCC}_{1/2}$ crystal will always have larger or equal energy than the FCC. In Fig. 3.5 we see that the energies of both crystals are indistinguishable at high densities, but at some value of the length the curves split and the FCC crystal becomes the ground state. This behaviour in the $E(L)$ curves suggests a phase transition between the crystals, but the presence of the pion-mass potential term is crucial in the understanding of this possible transition. Concretely, this potential term explicitly breaks chiral invariance, then, it is not compatible with the $\text{FCC}_{1/2}$ symmetry $\sigma \rightarrow -\sigma$. However, the relevance of the potential term in the energy decreases at high densities, so both crystals tend to the same energy in the chiral limit. Hence, when this term is not included in the Lagrangian both crystals are allowed and we find a FCC to $\text{FCC}_{1/2}$ second order phase transition, but when the potential term is present the FCC crystal is always the ground state and the energy curves approach asymptotically.

This phase transition has been extensively studied in [143], where the mean value of the σ field was proposed to be the order parameter of the transition.

We show in Fig. 3.8 the curve of the σ field mean value in the unit cell for the cases \mathcal{L}_{24} and \mathcal{L}_{240} to represent the cases without and with pion-mass potential term respectively. The addition of the sextic term does not qualitatively change the curves.

Although the $\text{FCC}_{1/2}$ is not the ground state crystal it is a good approximation to the FCC crystal at large densities. Indeed, for the values of the parameters that we have considered, the transition point always occurs at densities smaller

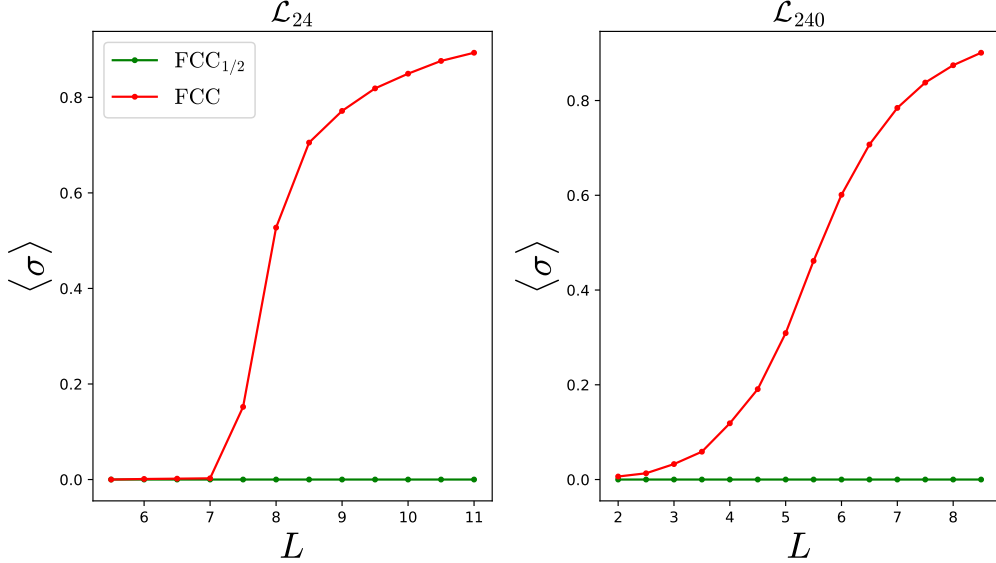


Figure 3.8: Mean value of the σ field within the unit cell shows the second order transition from the FCC to the $\text{FCC}_{1/2}$ crystal when the pion mass term is not included, and the asymptotic approach when it is included.

than the minimum of energy in the case without potential term. Besides, even with potential term the $\text{FCC}_{1/2}$ crystal is already a good approximation to the FCC crystal for densities larger than the minimum.

$B = 4N_\alpha^3$ Skyrme lattices

For the moment, we have mostly focused on the behaviour of Skyrme crystals under the Kugler and Shtrikman construction procedure. It is the aim of this section to show that there is a new branch of solutions which have different energies in the low density regime and tend to the $\text{FCC}_{1/2}$ crystal at high densities.

The fact that the Skyrme crystal has a minimum is not a bad behaviour, since this is expected to occur in symmetric nuclear matter. However, the energy of the half-crystals seems to diverge with L , but this is due to the Fourier expansion that we use to construct the Skyrme crystal, in which we impose the skyrmions to be in fixed positions and we do not allow them to move freely within the unit cell to find the lowest energy configuration.

This is a correct procedure for small values of L , however, if we increase the size of the unit cell the skyrmion is only allowed to spread instead of clustering to form a compact configuration surrounded by vacuum.

This motivated us to find new lower energy configurations with a new numerical minimization method which lets the skyrmions move with no restrictions within the unit cell. We use the AGD method to find the field configurations with minimal energy, locating the $B = 4$ skyrmion in the centre of the unit cell. We use the rational map approximation (2.19) found in [124] as initial configuration for the minimization, and periodic boundary conditions are imposed on the faces of box after each iteration. The $B = 4$ skyrmion has octahedral symmetry, the rational map with this symmetry and degree four explicitly reads,

$$\mathcal{R}(z) = \frac{z^4 + 2\sqrt{3}iz^2 + 1}{z^4 - 2\sqrt{3}iz^2 + 1}. \quad (3.19)$$

The motivation for this new lattice starts with the similarities between the isolated $B = 4$ skyrmion, which has cubic symmetry, and the FCC_{1/2} crystal. Indeed, the energy density contour of the isolated skyrmion is quite similar to the crystal in the sense that it is composed by eight half-skyrmions located in the corners of a cube.

Besides, the study of the $B = 4$ skyrmion in periodic boundary conditions under different deformations showed the phase transitions it may experiment [209]. Concretely, the phase transition between the FCC_{1/2} and the $B = 4$ skyrmion lattice was found at a certain value of L , then the new lattice becomes a more energetically favourable crystal.

Since the isolated $B = 4$ skyrmion aims to describe an alpha particle, we will refer to this configuration as the α -lattice. We calculated the energy of this new lattice for different values of L in the \mathcal{L}_{240} model. The reason for not considering the sextic term is that the AGD is extremely sensitive to high values of c_6 , and we have rather large presence of the sextic term in this specific case.

As a result, it turns out that the α -lattice has lower energy than the crystal at a certain value of L , furthermore, it tends to a constant value at $L \rightarrow \infty$. Indeed, the asymptotic constant value is precisely the energy of the isolated $B = 4$ skyrmion. This motivates the construction of other cubic lattices with larger values of B , since it is known that the energy per baryon of skyrmions decreases for increasing values of the baryon charge [91].

The next simplest cubic skyrmions, which are the N_α^3 multiples of the $B = 4$ skyrmion, are the $B = 32$ and $B = 108$ solutions. The way to construct these higher B skyrmions is, in fact, by cutting chunks of the Skyrme crystal, and then joining the fields with appropriate vacuum boundary conditions as explained in [42]. Once these isolated solutions are obtained they are introduced in the AGD method with periodic boundary conditions in order to solve the corresponding $4N_\alpha^3$ -lattices.

The constant value for $L \rightarrow \infty$ is also found for the FCC crystal, given that the single skyrmions are moved apart from each other in this limit. However, it settles much more slowly than the cubic lattices considered in this section. Besides, all these new lattices have less energy than the FCC crystal at low densities, since they achieve the more compact and energetically favourable configuration of $B = 4N_\alpha^3$ skyrmion, rather than $4N_\alpha^3$ isolated $B = 1$ skyrmions of the asymptotic FCC crystal.

Decreasing the size of the unit cell forces the skyrmion to recover the $\text{FCC}_{1/2}$ crystal configuration. The transition in the energy curve for these lattices may be seen in Fig. 3.9 at a slightly smaller density than the minimum.

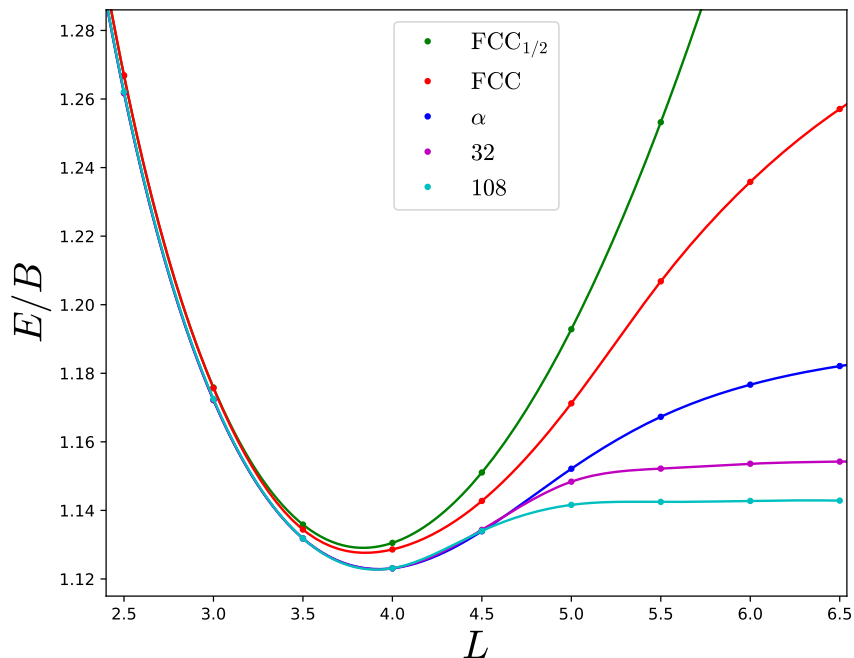


Figure 3.9: Energy per baryon number for the different crystals and lattices considered in this work in the \mathcal{L}_{240} model. The large difference in energy between these lattices and the FCC crystal that indicate the correct ground state is clearly observed. However, the convergence to the same $\text{FCC}_{1/2}$ crystal is observed slightly above the minimum.

The explicit transition to the half crystal is represented in Fig. 3.10 via the corresponding energy density contours at different lattice length values.

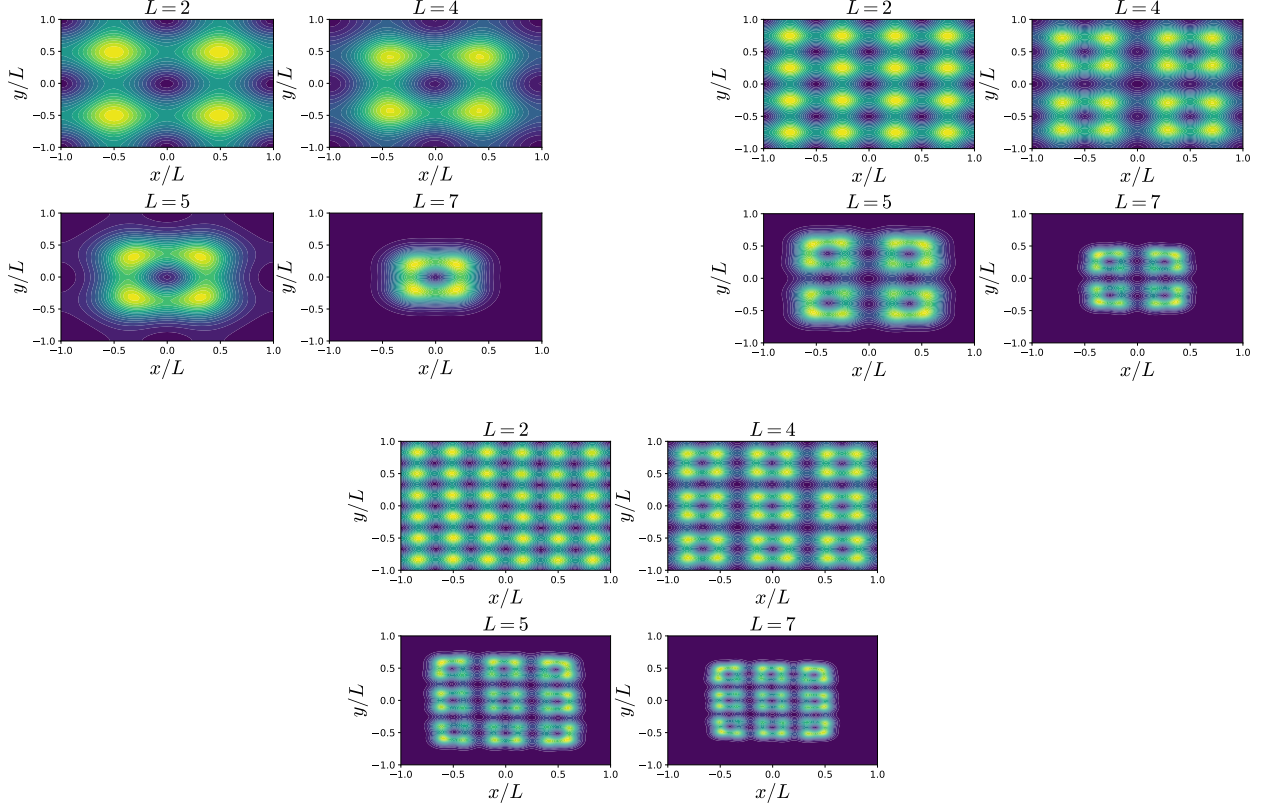


Figure 3.10: Energy density contour of the $4N_\alpha^3$ lattices at different sizes of the unit cell. The colours represent the same values as in Fig. 3.3. Here, the transition to the the FCC_{1/2} crystal is visible, whereas the isolated skyrmion is recovered for large values of L .

Transition to finite nuclear matter

In addition to the great improvement in the low density regime of the $E(L)$ curve with these new lattices, a smooth transition from infinite to finite nuclear matter is found. Increasing the value of the lattice length, the neighbouring unit cells are moving apart from each other, ending up with an isolated skyrmion in the infinite L limit. This is actually the physical reason of the asymptotic finite value at the end of the energy curve. Furthermore, this fact has great interest since it is possible to extract an estimation of the surface term present in (3.13) entirely within the Skyrme model.

For this purpose, we first assume that the energy of a B -skyrmion is just the energy at the minimum of the energy curve, and the difference between the minimum and the asymptotic value (*i.e.* the energy of the isolated skyrmion)

is the contribution from the surface energy. This is a reasonable assumption since quantum corrections are not considered, and we can see from Fig. 3.9 that the minimum of the curve is the same for all the lattices, covering a wide range of baryon numbers, at least up to 108. Then, the surface energy may be parametrized in terms of the number of faces of each skyrmion and the number N_α of alpha particles. Specifically, due to the cubic symmetry of the lattices that we are considering, each skyrmion will have six faces covered by N_α^2 alpha particles, hence, the surface energy and the baryon number may be easily related,

$$B = 4N_\alpha^3, \quad (3.20)$$

$$E_B = E_0 B + 6E_{\text{surface}} N_\alpha^2 = E_0 B + \frac{6E_{\text{surface}}}{4^{2/3}} B^{2/3}. \quad (3.21)$$

From this simple analysis we found the same scaling of the surface contribution in (3.13) in terms of the baryon number. We remark that this behaviour does not have to be necessarily true in the Skyrme model since it simply comes from geometrical arguments, however, we fitted the difference between the energy of the isolated skyrmion and the minimum of energy and we found a great agreement with the correct power-law.

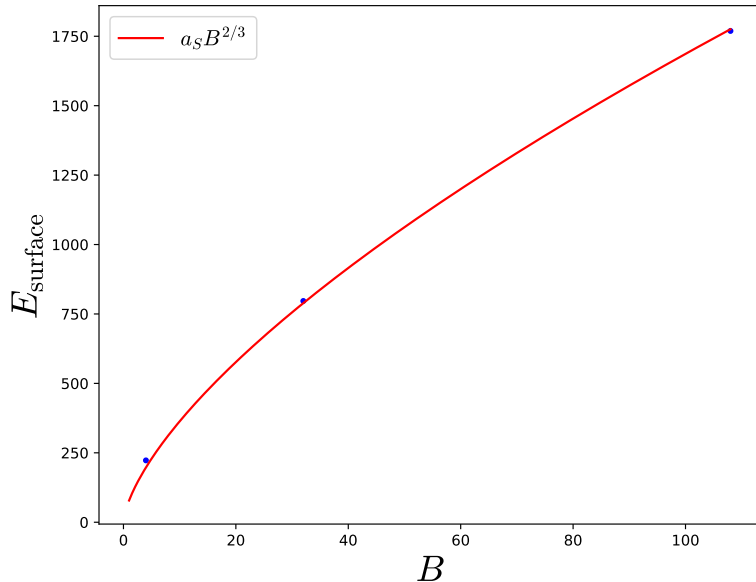


Figure 3.11: Surface energy of the isolated $4N_\alpha^3$ skyrmions fitted to the semi-empirical mass formula surface term expression.

From the fit we can extract a value for a_S , though it turns out to be too high compared to the most fiducial experimental value,

$$a_S^{\text{Skyrme}} = 78.3 \text{ MeV} \gg a_S^{\text{exp.}} = 18.3 \text{ MeV}. \quad (3.22)$$

This discrepancy may be directly related to the problem of the high binding energies in the Skyrme model. Correct values for the asymptotic difference between the isolated skyrmions would yield the precise value for the surface energy coefficient, hence the resolution of the binding energies problem also implies great enhancement in the infinite nuclear matter description. Indeed, we will see in the next section that this problem also prevents the correct description in the low density regime of the EOS, specifically the region of the crust.

3.3 Neutron stars from generalized Skyrme crystals

We have performed an exhaustive study of skyrmionic matter at different densities in order to describe nuclear matter. The main result is that Skyrme crystals are the most appropriate candidates to describe INM in the Skyrme model not only because they are infinitely extended configurations with the lowest energy, but also because we found a nontrivial phenomenology at different densities.

In this final section we obtain the EOS from the Skyrme crystals and solve the TOV system of differential equations to study the impact that the sextic term has in the NS from a complete field theoretical approach. Despite the results obtained so far are not a completely realistic description of INM, it may serve as a first indication for the maximal mass of the NS. Besides, it is interesting for a direct comparison with the results obtained combining the two submodels in the previous chapter.

The equation of state may be easily obtained from the crystals using the definitions (2.24). Besides, since the energy has been parametrized by (3.11), the pressure and energy density are obtained analytically in terms of L as well,

$$p(L) = -\frac{1}{24L^2} \frac{dE}{dL}, \quad \rho(L) = \frac{E}{8L^3}, \quad (3.23)$$

where the coefficients of the energy are given in Tables 3.3 and 3.4 for each crystal. Recall that there is a first order phase transition between the FCC_{1/2} and the BCC crystals which is solved by the piecewise function (3.18). This produces a discontinuous jump in the EOS since the pressure is required to be constant during the mixed phase in the MC, but the energy changes along the $p \equiv$ constant path. The values of the phase transition have also been obtained from the fit of the energy (3.11), and they are given in Table 3.7.

The EOS are represented in the upper left plot of Fig. 3.12 for the different models considered. All the curves tend to the same energy density in the zero pressure limit since we have fixed the parameters in each case in order to fit the nuclear saturation point. However, the \mathcal{L}_{246} case seems to deviate from the rest of EOS. The reason is that the fit has been obtained from perfect scaling approximation, which is not arbitrarily accurate, and we have seen that the sextic term tends to deviate from the crystal configuration into a fluid. Besides, the \mathcal{L}_{246} case has the largest value of $c_6 \sim 250$ among the four sets of parameters, being extremely far from the values $c_6 = c_0 = 1$ used to compute the perfect scaling constants. We might have recomputed the constants for a better accuracy, however, the deviation is around a 5%, although the logarithmic scale magnifies this effect in the plot.

The phase transitions are present in each curve, but they are only visible in the cases where the sextic term is included. Furthermore, this figure displays the stiffening on the EOS when more terms are added in the Lagrangian, specially the sextic term. This, indeed, produces the increase in the masses and radii.

The speed of sound is another informative magnitude in the EOS, it is directly related to the stiffness so it has great implications on the observables of NS [30]. As explained before, it must always be less than one, and it may be computed

analytically as well,

$$c_s^2 = \frac{dp}{d\rho} = \frac{dp}{dL} \frac{dL}{d\rho}, \quad (3.24)$$

$$\frac{dp}{dL} = \frac{1}{12L^3} \frac{dE}{dL} - \frac{1}{24L^2} \frac{d^2E}{dL^2}, \quad (3.25)$$

$$\frac{d\rho}{dL} = \frac{1}{8L^3} \frac{dE}{dL} - \frac{3E}{8L^4}. \quad (3.26)$$

The speed of sound curve depends on L and on the energy fit constants, but the asymptotic value at high densities turns out to be a constant value for each case. In the $L \rightarrow 0$ limit we have,

$$\mathcal{L}_{2460} : c_s^2 \longrightarrow 1, \quad (3.27)$$

$$\mathcal{L}_{240} : c_s^2 \longrightarrow 1/3. \quad (3.28)$$

These values also apply for the massless versions since the potential term is irrelevant at high densities. Interestingly, the speed of sound without sextic term tends to the conformal value of deconfined quark matter. There is, indeed, an intense debate on the possibility of surpassing the conformal bound inside NS cores [50]. It is known that hadronic matter must deconfine into quark matter at some point for high densities, hence, the speed of sound must tend asymptotically to the conformal value. One possibility is that the sound velocity is always subconformal and it tends to $1/\sqrt{3}$ from below, but this is in tension with the most massive NS observations and most of simulations, which suggest that the conformal bound is violated inside NS.

The speed of sound curve as a function of the pressure is shown in the upper right plot in Fig. 3.12. The main conclusion obtained so far is that the sextic term is necessary for a correct description of NS using the Skyrme model. Therefore, it is clearly observed from Fig. 3.12 that if this term is included, the conformal bound is widely exceeded for reasonable densities. Then, the best description hitherto for NS purely within the Skyrme model also predict that the conformal bound is violated.

Additionally, the speed of sound may be affected by other effects previously to

the quark deconfinement. Indeed, the decrease in the speed of sound is usually a sign for the appearance of new particle species inside NS.

The value of c_s^2 in the zero pressure limit may also be determined, however, it explicitly depends on the values of the constants in the energy fit. Besides, the low density part is not correctly reproduced in the Skyrme crystals due to the absence of crust, therefore, it requires further development.

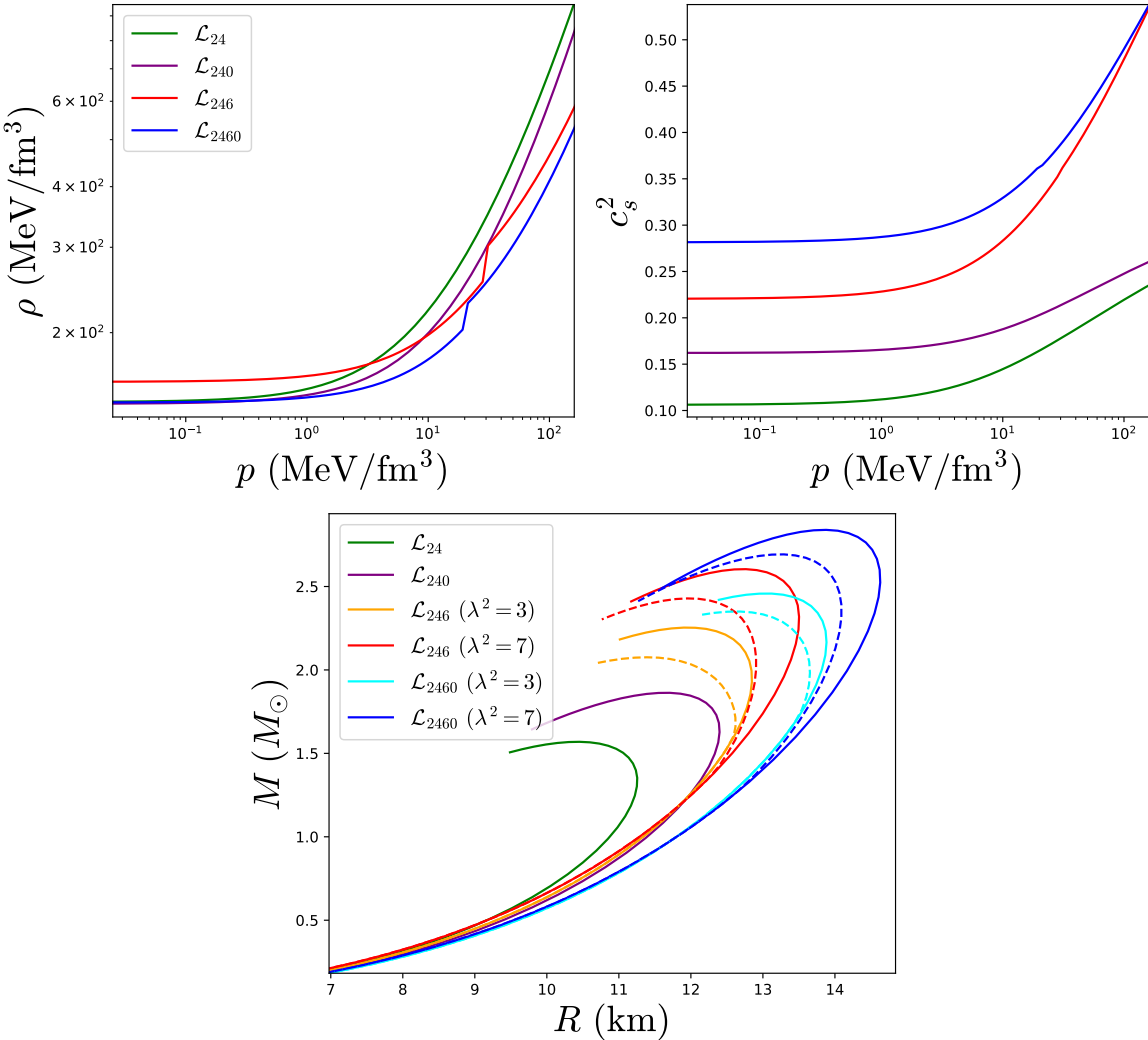


Figure 3.12: *Top left:* The full Skyrme crystal EOS including the possible phase transitions in the different submodels. *Top right:* The speed of sound obtained from each EOS. *Bottom:* The MR curves obtained solving the TOV system of equations.

The resolution of the TOV system for these EOS yields the MR curves shown in the lower plot of Fig. 3.12. We have included the MR curve with (dashed lines) and without (solid lines) MC to clearly see the impact of the phase transition on the NS. This phase transition is not attained in the models without sextic term

since the NS become unstable earlier. Additionally, we have also computed the curves for the \mathcal{L}_{246} and \mathcal{L}_{2460} models with $\lambda^3 = 3 \text{ MeV fm}^3$, where the other parameters have been again fitted to the nuclear saturation point.

The masses obtained from the crystalline solutions reach the minimal mass constraints from experimental observations. Interestingly, we obtain values for the mass similar to the effective description of the generalized EOS in the previous chapter, even though the values for the sextic term coupling constant are significantly smaller. This may be interpreted as an underestimation of the sextic term in the effective description. Conversely, the radii turn out substantially larger than the expected values, which suggests that the EOS might be too stiff. This effect might be attributed to a prominent presence of the sextic term, however, the large radii already for the low mass NS indicate that this might be a problem intrinsic to the crystalline solutions near the minimum. Nonetheless, the radius is highly affected by the low density regime of the EOS, which is not correctly described for the moment since the energy curves considered here still present a minimum.

Chapter 4

Neutron Star matter in the Skyrme model

Happiness can be found, even in the darkest of times, if one only remembers to turn on the light.

Albus Dumbledore

4.1 Quantization of Skyrme crystals

The crystalline solutions obtained so far correspond to classical solutions in which no quantum effects have been considered. Specifically, the isospin correction to the energy, like the third term in the semi-empirical mass formula (3.13), is crucial for a realistic description of nuclear matter. Indeed, inside NS (as the name suggests) a high asymmetry between protons and neutrons is expected, implying a large contribution to the energy. Hence, since Skyrme crystals aim to describe NS, the quantum isospin contribution to the energy needs to be considered.

This is the goal of this section, in which we will extensively explain the standard isospin quantization procedure in the Skyrme model, showing explicitly the expressions for the isospin inertia tensors in general. Then, the specific case of the FCC_{1/2} crystal is considered and the physical implications are studied.

The quantization of the Skyrme crystal was already discussed by Baskerville [43] in the massless model. The vacuum boundary conditions of isolated skyrmions break the chiral symmetry of the Lagrangian (2.4) to the diagonal isospin subgroup. However, this does not occur for periodic boundary conditions, and there

is not natural way to define the isospin subgroup. More specifically, there is an ambiguity in the reduction of the 4-dimensional representation of the crystal symmetry, into a trivial 1-dimensional irrep and 3-dimensional irrep, such that one dimension in isospace is singled out. We take the σ field to transform under the trivial representation, since this is the natural decomposition when the specific pion mass term (2.22) is introduced. Therefore, we will only consider the quantization of Skyrme crystals in the massive model.

The starting point, as we did in the last section of Chapter 2, is the transformation of the Skyrme field under the symmetries of the Lagrangian (2.78). However, in this section we will only consider the quantization of isospin degrees of freedom. The reason is that a global spatial rotation of an infinite crystal requires infinite energy, however, for a rotation in the isospace a finite amount of energy per baryon is required [43]. Besides, global isorotations may be decomposed in the individual isorotations of each unit cell, but that decomposition does not apply for spin rotations. Then, we only promote the isospin transformation to be time-dependent,

$$U(x) \rightarrow A(t)U(x)A^\dagger(t), \quad (4.1)$$

and the transformed field is inserted into the Lagrangian. This produces a kinetic energy term in the Lagrangian,

$$T = \frac{1}{24\pi^2} \int d^3x \left[-\frac{1}{2} \text{Tr}\{L_0^2\} - \frac{1}{2} \text{Tr}\{[L_0, L_i]^2\} + 4\pi^4 c_6 (B^i)^2 \right]. \quad (4.2)$$

The time component of the Maurer-Cartan current, as well as the spatial components of the topological current, are now excited due to the time dependence of the isospin transformation. The expressions after the transformation (4.1) are the following:

$$L_0 = AU^\dagger \left[A^\dagger \dot{A}, U \right] A^\dagger, \quad (4.3)$$

$$L_i = AU^\dagger \partial_i U A^\dagger, \quad (4.4)$$

$$B^i = \frac{1}{8\pi^2} \epsilon^{ijk} \text{Tr}\{L_0 L_j L_k\}. \quad (4.5)$$

Recall that the potential term does not explicitly contribute to the kinetic energy due to the lack of derivative terms. However, the presence of a potential term changes the classical solution, so it will affect indirectly the isospin inertia tensor. Nonetheless, the standard range of parameters that we usually consider in the Skyrme model yields $c_0 \lesssim 0.5$, which produces an almost negligible difference.

Now, we make use of the isospin angular frequency definition, $A^\dagger \dot{A} = \frac{i}{2}\omega_a \tau_a$. Then, we may identify the isospin inertia tensor, Λ_{ab} , from the isorotational kinetic energy definition, $T = \frac{1}{2}\omega_a \Lambda_{ab} \omega_b$, and extract the following expression:

$$\Lambda_{ab} = \frac{1}{24\pi^2} \int d^3x \left[\text{Tr}\{T_a T_b\} + \text{Tr}\{[T_a, L_i][T_b, L_i]\} - \frac{c_6}{16} (\epsilon_{ijk} \text{Tr}\{T_a [L_j, L_k]\}) (\epsilon_{ilm} \text{Tr}\{T_b [L_l, L_m]\}) \right], \quad (4.6)$$

where we have defined the $\mathfrak{su}(2)$ -valued current,

$$T_a = \frac{i}{2} U^\dagger [\tau_a, U]. \quad (4.7)$$

Expanding the three terms in the isospin inertia tensor,

$$\Lambda_{ab} = \frac{1}{24\pi^2} \int d^3x \left[\Lambda_{ab}^{(2)} + \Lambda_{ab}^{(4)} + c_6 \Lambda_{ab}^{(6)} \right], \quad (4.8)$$

we obtain an expression depending on the fields which, in the case of the Skyrme crystal, are known since the classical solution has already been solved in the previous chapter. Indeed, due to the symmetries (3.4) and (3.5) that all Skyrme crystals share, it might be proven that the isospin inertia tensor is diagonal and proportional to the identity [20], $\Lambda_{ab} \equiv \Lambda \delta_{ab}$, where its eigenvalue Λ is the isospin moment of inertia. In general, we can always diagonalize the isospin inertia tensor, however, the fact that it is proportional to the identity is a special property of some field configurations, like the Skyrme crystal. This will not be the case of the $B = 4N^3$ lattices studied in the last parts of the previous chapter, where the third component of the isospin tensor is different to the others. The reason is that those lattices only have spatial cubic symmetry, but not in isospace.

The diagonal components of the isospin inertia tensor are shown below,

$$\Lambda_{aa}^{(2)} = 2(\pi_b^2 + \pi_c^2), \quad b \neq c \neq a, \quad (4.9)$$

$$\Lambda_{aa}^{(4)} = 8 \left(\partial_i \sigma^2 (1 - \pi_a^2) + (\partial_i \pi_a)^2 (1 - \sigma^2) + 2\sigma \pi_a \partial_i \sigma \partial_i \pi_a \right), \quad (4.10)$$

$$\Lambda_{aa}^{(6)} = (\partial_i \sigma \partial_j \pi_a - \partial_j \sigma \partial_i \pi_a)^2. \quad (4.11)$$

We remark that these expressions have been obtained from (4.6) in general, and no symmetry has been imposed. It is also important to note that in the last expressions we do not use the Einstein summation convention for repeated pionic indices (a, b, c). Instead we just want to show that the only components of interest are the diagonal terms, and the others vanish for Skyrme crystals.

We computed the isospin inertia tensor as a function of the lattice length in the \mathcal{L}_{24} case and compared with the values previously obtained by Baskerville [43]. As we noted before, the inclusion of a potential term does not impact the isospin inertia tensor directly, however, the sextic term induces a new term. Following the scaling behaviour of each term we consider the parametrization

$$\Lambda(L) = \Lambda_c + \Lambda_2 L^3 + \Lambda_4 L + c_6 \frac{\Lambda_6}{L}, \quad (4.12)$$

to fit the isospin inertia tensor in the generalized Skyrme model, see Fig. 4.3. The sextic term has, indeed, an important impact since the isospin tensor is an increasing monotonic function in the \mathcal{L}_{24} theory, vanishing in the infinite baryon density limit. However the inclusion of the sextic term changes this behaviour, then, the isospin tensor now diverges in the same limit. On the other hand, in the zero baryon density limit (or alternatively the $L \rightarrow \infty$ limit) the sextic term vanishes, and the isospin tensor also diverges. We find good agreement between the numerical data and the fit (4.12) for a wide range of densities.

The kinetic energy of the isospinning crystal with N_{cells} unit cells is the sum of each unit cell kinetic energy,

$$T = \frac{N_{\text{cells}}}{2} \omega_a \Lambda_{ab} \omega_b = \frac{N_{\text{cells}}}{2} \omega_a \Lambda \omega_a. \quad (4.13)$$

Then, the Hamiltonian for the isospin corrections may be obtained via a Legendre transformation of the Lagrangian between the angular frequency and the canonical body-fixed angular momentum definition,

$$K_a = \frac{\partial \mathcal{L}}{\partial \omega_a} = N_{\text{cells}} \Lambda \omega_a. \quad (4.14)$$

The standard quantization procedure promotes the angular momenta to operators ($K_a \rightarrow \hat{K}_a$) in the Hamiltonian,

$$\hat{H}_{\text{iso}} = \frac{\hat{\mathbf{K}}^2}{2N_{\text{cells}}\Lambda} = \frac{\hat{\mathbf{I}}^2}{2N_{\text{cells}}\Lambda}, \quad \hat{K}_a \hat{K}_a = \hat{\mathbf{K}}^2 \quad (4.15)$$

In the last part, we have made use of the relation between the Casimir invariant operators ($\hat{\mathbf{K}}^2 = \hat{\mathbf{I}}^2$) of the body-fixed (K_a) and space-fixed (I_a) isospin angular momentum.

In order to add the contribution of this Hamiltonian to the classical energy of the crystal, we need to know the quantum state of the whole crystal. This is, of course, impossible since the crystal is infinitely extended so that the number of particles is infinite. Therefore, the following assumptions are imposed on the quantum state of the crystal to simplify the task:

- The quantum state of the full crystal $|\Psi\rangle$ is strictly written as a superposition of each individual unit cell quantum state $|\psi\rangle$.
- The quantum state of the crystal inherits the point symmetry group of the classical configuration and it is also shared by the quantum state of each unit cell.

The first assumption neglects any quantum correlation between neighbouring unit cells so that the full crystal quantum state may be decomposed in the tensor product of each unit cell state, $|\Psi\rangle = \bigotimes_{N_{\text{cells}}} |\psi\rangle$. The second assumption ensures that any isorotation of the crystal occurs equivalently in each unit cell. Then, the total isospin of the crystal is expressed as the sum of each unit cell isospin, $i_{\text{tot}} = i_{\text{cell}} N_{\text{cells}}$.

Now, the FR constraints resulting from the symmetries of the crystal must

be solved in order to obtain the possible quantum states in the unit cell. How these states are obtained will be briefly described in the following, for a detailed explanation see [20]. In general, the symmetries of the configuration must be written in terms of the generators of the spin and isospin groups which act on a state. Then, the FR constraints are imposed,

$$e^{i\theta_1 \mathbf{n}_1 \cdot \mathbf{L}} e^{i\theta_2 \mathbf{n}_2 \cdot \mathbf{K}} = \chi_{FR} |\psi\rangle, \quad (4.16)$$

where \mathbf{L} , \mathbf{K} are the body-fixed spin and isospin angular momentum vectors respectively, and $\chi_{FR} = \pm 1$ is the constraint.

In the FCC_{1/2} Skyrme crystal, the relevant symmetries that relate spin and isospin transformations are A_2 (3.5) and C_3 (3.8). They are expressed as follows,

$$A_2 : \quad e^{i\frac{\pi}{2\sqrt{3}}(K_1+K_2+K_3)} = \mathcal{R}(0, -\pi/2, -\pi/2), \quad (4.17)$$

$$C_3 : \quad e^{i\frac{\pi}{2}K_1} = \mathcal{R}(\pi/2, -\pi/2, \pi/2), \quad (4.18)$$

where the $\mathcal{R}(\alpha, \beta, \gamma)$ rotation represents the specific operator in the *ZYZ* convention of Euler angles. Spin rotations are represented by the same operators, but we will focus on the quantum isospin states.

The representation in terms of $\mathcal{R}(\alpha, \beta, \gamma)$ rotations is important since it is known how these operators act on the states in terms of Wigner D-matrices [20]. Thus, the problem reduces to finding the eigenstates of the Wigner D-matrix corresponding to each symmetry for the different possible values of isospin in the unit cell of $B_{\text{cell}} = 4$. Additionally, given that the baryon number in the unit cell is even, we have imposed the constraint $\chi_{FR} = +1$ following the results in [135].

We found a unique quantum state for each isospin value, $i = 0, 1, 2$ which is common to both symmetries. The energy for each of these states may be computed from the Hamiltonian (4.15). We might think that the $i = 0$ state has the lowest energy since it has exactly zero isospin energy. However, since this state is symmetric in isospin, the presence of protons require the inclusion of electrostatic interaction in the energy. It has already been noticed in [130] that if this contribution is taken into account in the infinite crystal, even the

energy per baryon number would diverge due to the long range interaction of Coulomb energy. Therefore, we conclude that the charge neutral state, is in fact the ground state of the Skyrme crystal.

The charge neutral case is made up of B_{cell} neutrons in each unit cell and it induces the largest isospin contribution to the energy, since it fixes the highest isospin value in the unit cell, $i_{\text{cell}} = \frac{1}{2}B_{\text{cell}}$. In this case, the total isospin of the full crystal is $i_{\text{tot}} = \frac{1}{2}N_{\text{cells}}B_{\text{cell}}$, and the isospin energy of the crystal may be obtained,

$$E_{\text{iso}} = \frac{\hbar^2}{2N_{\text{cells}}\Lambda} i_{\text{tot}}(i_{\text{tot}} + 1) \xrightarrow{N_{\text{cells}} \rightarrow \infty} \frac{\hbar^2}{8\Lambda} N_{\text{cells}} B_{\text{cell}}^2. \quad (4.19)$$

Again, the energy of the entire crystal diverges, but it does so linearly, such that the energy per unit cell (or per baryon number) remains finite.

We have explicitly introduced the \hbar factor in the isospin energy since it is a contribution of quantum origin. In order to be consistent with the Skyrme units, in which the isospin inertia tensor is computed (4.6), it is important to know the value of the quantum scale in the same units, $\hbar = \frac{e^2}{3\pi^2}$.

It might also be crucial to consider the impact that the isospin contribution might have on the classical configuration. This possibility has been considered for the isolated $B = 1$ skyrmion in [147], but not for skyrmion crystals. However, we have confirmed in [20] that the isospin effects are always smaller than the classical energy contribution. Hence, we may safely neglect the backreaction due to the isospin effects and include them as a quantum correction.

4.1.1 Symmetry energy

The energy of isospin-asymmetric infinite nuclear matter is often expressed as a function of the baryon density and the asymmetry parameter $\delta = \frac{N_n - N_p}{B}$. Indeed, isospin-asymmetry is in general parametrized as an expansion of the energy in powers of δ up to second order,

$$\frac{E}{B}(n_B, \delta) = E(n_B) + S(n_B)\delta^2 + \mathcal{O}(\delta^3). \quad (4.20)$$

The zero order is the energy curve of the symmetric INM, which we identify with the energy curves $E(L)$, obtained from the classical Skyrme crystals in the previous chapter. The function $S(n_B)$ is known as the symmetry energy curve [141, 199], which measures the change in the energy due to the proton-neutron difference at a given baryon density.

The symmetry energy may also be defined as the difference between pure neutron and symmetric nuclear matter. This curve is of great importance since it affects many different phenomena of nuclear matter. It has been constrained up to $n_B \sim n_0$ but, again, it is difficult to experimentally extend nuclear matter up to much higher densities. Instead, the curve is expanded in powers of the baryon density,

$$S(n_B) = S_0 + \frac{1}{3}L_{\text{sym}} \left(\frac{n_B - n_0}{n_0} \right) + \frac{1}{9}K_{\text{sym}} \left(\frac{n_B - n_0}{n_0} \right)^2 + \dots \quad (4.21)$$

and parametrized by the the symmetry energy at the saturation density, S_0 . The higher multipoles in the expansion,

$$L_{\text{sym}} = 3n_0 \frac{\partial S}{\partial n_B} \Bigg|_{n_B=n_0}, \quad K_{\text{sym}} = 9n_0^2 \frac{\partial^2 S}{\partial n_B^2} \Bigg|_{n_B=n_0}, \quad (4.22)$$

are the slope and the curvature of the symmetry energy at saturation respectively.

The three multipoles in the expansion (4.21) have been inferred from the combined theoretical predictions and experimental measurements of the symmetry energy curve [40]. This curve has been mainly constrained at subsaturation densities by the Isobaric Analog States (IAS) method [84] for finite nuclei, however, the extension of the restrictions above the saturation was performed through the analysis of NS observables. Indeed, the discovery of GW170817 induced an extensive study on the radii of NS in which the symmetry energy is involved. Here, we shall consider the most fiducial values obtained from an averaged survey of 53 analysis from nuclear experiments [180] for S_0 and the combination of other analysis extracted from NS observables [144] for the higher multipoles. The numerical values with their corresponding uncertainties are given in Table 4.1.

Actually, the L_{sym} multipole, which is also called the slope, is directly related to the neutron skin thickness [227], and it may be determined from terrestrial experiments. The neutron skin is the accumulation of neutrons in the surface of the large baryon number nuclei due to the Pauli pressure from the excess of neutrons with respect to protons. The thickness of this skin is the result of the competition between this repulsive behaviour and the symmetry energy (more specifically to the slope) since large asymmetries increase the energy. However, the recent determination of the neutron skin thickness of ^{208}Pb [25] yield unexpected high values for the slope, $L_{\text{sym}}^{\text{(PREX)}} = 106 \pm 37$ MeV. This induced serious tensions with the rest of estimations [236], which require further studies on this topic.

S_0 (MeV)	L_{sym} (MeV)	K_{sym} (MeV)
31.7 ± 3.2	57.7 ± 19	-107 ± 88

Table 4.1: Experimental values for the symmetry energy curve multipoles at the saturation density.

It may be noticed that our previous result of the isospin energy for the Skyrme crystal (4.19) naturally follows the same behaviour to the symmetry energy (4.20) since it is proportional to i_{cell}^2 , which is indeed a measure of the isospin asymmetry. For the computation of the energy, we have imposed the zero charge condition in the unit cell, where we have fixed the isospin numbers to $i = 2$, $i_3 = -2$, describing a pure neutron crystal. This corresponds to the highest isospin asymmetry of nuclear matter, similar to what is expected to occur in the core of NS. However, realistic models of the nuclear matter inside NS do not predict a totally asymmetric state, but a small fraction of protons must be allowed. Although the real values are unknown, simulations yield some estimations of the proton fraction $\gamma := \frac{N_p}{B} \sim 10^{-2} - 10^{-1}$ [158, 187].

Since the Skyrme crystal has $B_{\text{cell}} = 4$, there is a finite number of possible quantum states which physically correspond to the different combinations of protons and neutrons within the unit cell. Nonetheless, even the minimal possible number of protons in the unit cell yields a too high proton fraction $\gamma = 0.25$ compared to the expected values. We could consider the total quantum state resulting from the combination of several unit cell quantum states, following the standard spin composition procedure in representation theory. Then, in

order to reproduce realistic values of the proton fraction, a simple estimation indicates that we would need to combine the order of $\frac{1}{\gamma B_{\text{cell}}} \sim 15$ unit cells, which becomes an unhandleable task.

Following the same philosophy, we consider an arbitrary number N of unit cells enclosed in a larger chunk of crystal with $B = NB_{\text{cell}}$. Then, we perform a mean-field approximation in which the third isospin eigenvalue of the quantum state is generically defined,

$$i_3 = \frac{N_p - N_n}{2} = -N \frac{B_{\text{cell}}}{2} \delta. \quad (4.23)$$

Now, the proton fraction is not an input, but it is left as an independent variable introduced by the asymmetry parameter, $\delta = 1 - 2\gamma$. Once the third isospin component has been established from the mean-field approximation, the total isospin value of the crystal is fixed by $i = i_3$, given that $i^2 \geq i_3^2$, and that is the condition that minimizes the isospin energy.

Then, the isospin energy of the Skyrme crystal per unit cell with an arbitrary proton fraction is:

$$E_{\text{iso}} = \frac{\hbar^2 B_{\text{cell}}^2}{8\Lambda} \delta^2. \quad (4.24)$$

Finally, this energy may be compared with (4.20) and we can extract the symmetry energy curve,

$$S(n_B) = \frac{\hbar^2}{2\Lambda}, \quad (4.25)$$

where the dependence on the baryon density lies entirely on the isospin inertia tensor. Indeed, this is precisely the same expression that is obtained from the difference between pure neutron (4.19) and symmetric nuclear matter energies, which is an equivalent definition of the symmetry energy [141].

We show in Fig. 4.1 the symmetry energy curves for the Skyrme crystals obtained for the massive model from the previous chapter. However, despite the energy and baryon density at saturation are correctly fitted, the values for the symmetry energy multipoles come out too low. Surprisingly, the values of S_0

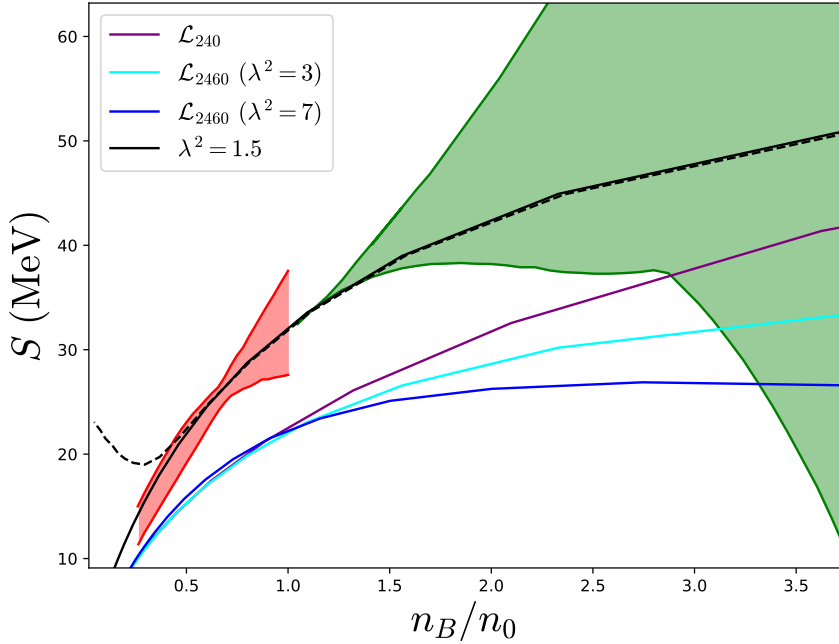


Figure 4.1: Symmetry energy curve of the Skyrme crystals studied in the previous chapter. We also added a new case (black solid (FCC_{1/2}) and dashed (FCC) lines) which reproduces S_0 , L_{sym} and K_{sym} using the standard parameters (2.21) and $\lambda^2 = 1.5$. The red shaded region comes from the IAS constraints for the symmetry energy obtained from [84], whilst the green area represents the suprasaturation constraints from the GW170817 event analysis [144].

are indeed quite similar, independently on the model, which might be a sign of the difficulty on the simultaneous fit of E_0 , n_0 and S_0 using Skyrme crystals.

We have also added a new curve for which we have fixed the standard parameters (2.21) and the sextic term coupling constant has been tuned to fit the symmetry energy at saturation, with a final value of $\lambda^2 = 1.5$ MeV fm³. In fact, all the multipoles are quite accurately reproduced with this set of parameters, however, the energy and baryon density at the minimum deviate from the correct values, $E_0 = 822$ MeV and $n_0 = 0.22$ fm⁻³.

In general, we find that the sextic term has significant impact in the isospin inertia tensor already at the minimum of energy. It generally decreases the values of $S(n_B)$, which is actually quite hard to fit at saturation if the other observables are below the 20% of error. Hence, although the results obtained in this section are highly dependent on the fit of f_π and e , small values of the sextic term, around $\lambda^2 \sim 1 - 3$ MeV/fm³, seem to be preferred by the symmetry energy curve. This is indicated not because of the value of S_0 itself, but the sextic term is in particular penalized by the multipole L_{sym} . Nevertheless, the

whole symmetry energy curve obtained from Skyrme crystals is well within the experimental uncertainties if S_0 is well fitted. This is a great result which is intrinsic to Skyrme crystals and encourages their use to describe INM for densities above the saturation point.

Model	λ^2 (MeV fm 3)	S_0 (MeV)	L_{sym} (MeV)	K_{sym} (MeV)
\mathcal{L}_{240}	0	22.67	36.03	-71.99
\mathcal{L}_{2460}	3	22.16	30.48	-93.56
\mathcal{L}_{2460}	7	22.26	24.22	-118.43
\mathcal{L}_{2460} $f_\pi = 129$ MeV, $e = 5.45$	1.5	31.94	46.40	-131.64

Table 4.2: Values of the symmetry energy curve multipoles at saturation for the sets of the parameters given in Table 3.2 and a new set with the standard parameters of [29].

We may also obtain the symmetry energy curve from the FCC crystal of skyrmions since it satisfies the symmetries considered for the quantization of the crystal. The values at the saturation point are the same as those for the half crystal in Table 4.2, however, an interesting effect is observed in the $L \rightarrow \infty$ limit.

The asymptotic behaviour of the FCC crystal produced a constant value for energy in the large L limit, and the same is observed for the symmetry energy curve. This constant value of the symmetry energy is indeed another manifestation of the transition to finite nuclear matter explained in the end of the last chapter. Hence, we may directly compare the asymptotic value of the symmetry energy with the asymmetry coefficient present in (3.13),

$$S^{(\text{FCC})}(n_B = 0) = 24.2 \text{ MeV} \approx a_A^{\text{exp.}} = 23.2 \text{ MeV}. \quad (4.26)$$

The value is surprisingly close the experimental fit when the symmetry energy is well fitted at the saturation point, at least for the FCC crystal. Therefore, this asymptotic behaviour is an extremely remarkable property of crystalline configurations in the Skyrme model since it allows to describe symmetric and asymmetric nuclear matter in the whole range of densities.

4.1.2 Realistic $npe\mu$ matter in Skyrme neutron stars

The inclusion of the symmetry energy in the Skyrme model enables the presence of an arbitrary number of protons in our system. However, for a consistent description in which protons are present, we must include the Coulomb electrostatic interaction in the energy. Furthermore, as we mentioned before, the inclusion of the Coulomb interaction yields an infinite contribution to the energy per baryon.

In order to solve this problem, we introduce a negatively charged background of leptons such that the Coulomb interaction is exponentially suppressed and we may neglect the electrostatic contribution between neighbouring unit cells in a first approximation. Additionally, NS are charge neutral objects in which the system of protons, neutrons and leptons is stabilized via the neutron β decay and electron capture processes, which is called β -equilibrium,

$$n \rightarrow p + l + \bar{\nu}_l, \quad p + l \rightarrow n + \nu_l. \quad (4.27)$$

Leptons are typically described by a relativistic Fermi gas at zero temperature, whose energy depends on the number of particles N_l and the volume,

$$E_l(N_l, V) = \frac{m_l^4}{8\pi^2\hbar^3} V \left[(x + 2x^3) - \ln \left(x + \sqrt{1 + x^2} \right) \right], \quad (4.28)$$

where m_l is the mass of the corresponding lepton, $x = \hbar k_F/m_l$, and the dependence on N_l is implicit in the Fermi momentum $k_F = (3\pi^2 N_l/V)^{1/3}$.

All thermodynamical properties of interest, like the chemical potential (μ_l) and pressure, for the system of leptons may be extracted from the energy expression,

$$\mu_l = \left. \frac{\partial E}{\partial N_l} \right|_V, \quad p = - \left. \frac{\partial E}{\partial V} \right|_{N_l}. \quad (4.29)$$

Specifically, the chemical potential acquires the simple expression,

$$\mu_l = \sqrt{(\hbar k_F)^2 + m_l^2}. \quad (4.30)$$

In the outer crust of NS we only expect to have electrons since other leptonic species are unstable under weak interactions. However, since electrons are fermions, the increase of the density in deeper layers of the NS rises the chemical potential (4.30) up to $\mu_e \geq m_\mu = 105.658$ MeV. At this point muons become energetically more favourable than electrons, so they start to appear in the system.

The number of each particle species is solved imposing β -equilibrium and charge neutrality, which yield the following conditions,

$$\mu_n - \mu_p := \mu_I = \mu_l, \quad l = e, \mu, \quad (4.31)$$

$$N_p = N_e + N_\mu, \quad (4.32)$$

respectively. We have introduced in the system the isospin chemical potential μ_I using its thermodynamical definition. The lepton chemical potentials are already known from (4.30), but the explicit form of μ_I may be obtained in two different, but equivalent, ways from the Skyrme crystal. In one way, one can introduce a nonzero isospin chemical potential through a covariant derivative in the Skyrme model, this is formally equivalent to the quantization procedure explained above [20, 212], and μ_I may be easily related to the isospin energy. From another thermodynamical point of view, we may rewrite the variables of our system,

$$E = E_{\text{class}}(V, B) + E_{\text{iso}}(V, \delta) + E_e(V, N_e) + E_\mu(V, N_\mu) = \quad (4.33)$$

$$- pV + \mu_p N_p + \mu_n N_n + \mu_e N_e + \mu_\mu N_\mu, \quad (4.34)$$

in terms of other degrees of freedom of interest. Specifically, we may define the isospin number of particles $N_I := \frac{N_p - N_n}{2}$, which is the same as the third isospin component i_3 , and the baryon number $B = N_p + N_n$,

$$E = -pV + \mu_B B - \mu_I N_I + \mu_e N_e + \mu_\mu N_\mu, \quad (4.35)$$

where the definitions $\mu_B = \frac{\mu_n + \mu_p}{2}$ and $\mu_I = \mu_n - \mu_p$ are satisfied. Then, the isospin chemical potential is canonically obtained from the isospin energy since

it is the only one that depends on $N_I = -\frac{B\delta}{2}$,

$$\mu_I = -\frac{\partial E_{\text{iso}}}{\partial N_I} = -\frac{\hbar^2}{\Lambda} N_I. \quad (4.36)$$

Hence, the equilibrium conditions (4.32) become a system of equations, and yield the following equation for γ ,

$$\frac{\hbar B_{\text{cell}}}{2\Lambda} (1 - 2\gamma) = \left[3\pi^2 \left(\frac{\gamma B_{\text{cell}}}{V} - n_\mu \right) \right]^{1/3}, \quad (4.37)$$

$$n_\mu = \frac{1}{3\pi^2} \left[\left(\frac{\hbar B_{\text{cell}}}{2\Lambda} (1 - 2\gamma) \right)^2 - \left(\frac{m_\mu}{\hbar} \right)^2 \right]^{3/2}, \quad (4.38)$$

which may be solved at every value of the baryon density. For very low densities, the chemical potential of electrons is too low and we must impose the condition $n_\mu = 0$. Besides, electrons quickly become ultrarelativistic particles, *i.e.*, $k_F \gg m_e = 0.511$ MeV, therefore, we have imposed the condition $\mu_e = k_F$ in the beginning to simplify the expressions.

The main properties of the curve $\gamma(n_B)$ may be directly extracted from (4.37) since the main nontrivial behaviour comes from the isospin inertia moment. As we have seen, in the limit $L \rightarrow 0$, the inertia moment vanishes if the sextic term is not included. From this we conclude that $\gamma = 1/2$ is the solution in that limit, implying that we would have symmetric nuclear matter in the inner core of NS. The sextic term produces a divergence in the isospin moment of inertia in this limit, then the solution in this case is $\gamma = 0$, which implies that all electrons have been captured by the protons and the core is full of neutrons. This is, indeed, a more plausible situation than without the sextic term since the increase of the pressure in the center of NS would enhance the electron capture process. However, it is believed that the proton fraction do not completely vanishes in the core of NS, due to the appearance of the other particles. Then, we conclude that the sextic term improves the phenomenology of Skyrme NS, and for a complete description we need to include other particles in the system.

In the opposite limit, $L \rightarrow \infty$, the isospin inertia tensor always diverges for

the half Skyrme crystals. This yields again a zero proton fraction in the zero baryon density limit, which is not realistic at all. What we actually expect in the surface of NS is a lattice of ^{56}Fe nuclei [78], since it is the most stable nucleus, then, the proton fraction in this region of the star is $\gamma_{\text{Fe}} = 0.464$.

For this reason, we want to focus in this section on the $B = 4N_\alpha^3$ Skyrme lattices which reproduces the high density behaviour of Skyrme crystals, but they have a different description at low densities. The same qualitative arguments for the proton fraction apply for the FCC crystal of single skyrmions. We first found that the isospin inertia tensor is not proportional to the identity in the lattices, but instead it has two eigenvalues, $\Lambda_1 := \Lambda_{11} = \Lambda_{22} \neq \Lambda_3 := \Lambda_{33}$. Therefore, we have to review the previous calculations carried out for an inertia tensor proportional to the identity.

The difference enters in (4.15), where the three components of the isospin operator are splitted,

$$\hat{H}_{\text{iso}} = \frac{\hat{K}_1^2 + \hat{K}_2^2}{2N_{\text{cells}}\Lambda_1} + \frac{\hat{K}_3^2}{2N_{\text{cells}}\Lambda_3} = \frac{\hat{\mathbf{I}}^2}{2N_{\text{cells}}\Lambda_1} + \frac{\hat{K}_3^2}{2N_{\text{cells}}} \left(\frac{1}{\Lambda_3} - \frac{1}{\Lambda_1} \right). \quad (4.39)$$

Since the Hamiltonian depends on the third body-fixed isospin angular momentum, fixing the value of i_3 is not enough, and an explicit computation of the isospin quantum state via the FR constraints is required. However, the contribution to the energy from this additional term is modulated by the difference between the two eigenvalues. Then, we propose the relation $\Lambda = \Lambda_3(1 + \epsilon)$ and expand in perturbation theory to obtain,

$$\hat{H}_{\text{iso}} = \frac{\hat{\mathbf{I}}^2}{2N_{\text{cells}}\Lambda_3} + \frac{(\hat{K}_3^2 - \hat{\mathbf{I}}^2)}{2N_{\text{cells}}\Lambda_3} \epsilon. \quad (4.40)$$

Moreover, we may find a maximal bound for the contribution to the energy in this approximation. The third body-fixed isospin eigenvalue takes values in the interval $k_3 \in [-i, i]$, then $k_3^2 \leq i^2$. Besides, $\Lambda_3 > \Lambda_1$ for all the values of L considered here, hence ϵ is always negative and it is never larger than a 20%. Therefore, the linear correction in the Hamiltonian (4.40) is positive, so it underestimates the symmetry energy, but always strictly smaller than a 20%.

For simplicity in the computations, we neglect the linear correction, therefore, the main contribution in (4.40), combined with the previous conditions $i = i_3$ and (4.23), in the limit $N_{\text{cells}} \rightarrow \infty$, yields the following expression of the isospin energy per unit cell for the Skyrme lattices,

$$E_{\text{iso}} = \frac{\hbar^2 B_{\text{cell}}^2}{8\Lambda_3} \delta^2. \quad (4.41)$$

Then, we may study the symmetry energy and the particle fractions for Skyrme lattices using the third component of the isospin inertia tensor. As expected, the curve $\Lambda_3(L)$ settles down to a constant value in the limit $L \rightarrow \infty$ in the same way as it occurs with the FCC crystal. Furthermore, we may now conclude that this behaviour implies that the solution to (4.37) is $\gamma = 0.5$ in the zero density limit, which is extremely close to the iron proton fraction. This is an additional impressive result for the Skyrme model since we are still considering an incomplete description without Coulomb effects. However, this contribution will slightly suppress the presence of protons, then it would bring us even closer to the real value.

We consider the set of parameters that fits the symmetry energy for comparison with the FCC crystal,

$$f_\pi = 129 \text{ MeV}, \quad e = 5.45, \quad \lambda^2 = 1.5 \text{ MeV fm}^3, \quad m_\pi = 138 \text{ MeV} \quad (4.42)$$

The resulting values for the main observables computed with the α -lattice are given in Table 4.3. The same values apply for the higher $B = 32$ and 108 lattices at saturation since they are all the same at the minimum of energy, but the different asymptotic behaviour of the lattices yield other values for the asymmetry coefficient. Unfortunately, this coefficient is too high in the α -lattice, and the smaller isospin inertia tensor of the bigger 108-lattice yields a larger contribution to the symmetry energy producing an even worse result for a_{sym} .

We show in the left plot of Fig. 4.2 the symmetry energy curve of the Skyrme crystals and the α -lattice for comparison. The three curves tend to the same value at high densities, since they finally recover the same half-skyrmion struc-

ture. Although the α -lattice seems to diverge from the crystals curves, this is an artificial effect due to the logarithmic scale in the x-axis. Indeed, the largest difference in the symmetry energy for larger densities than the minimum is smaller than a 2%.

E_0 (MeV)	n_0 ($\text{fm}^{-1/3}$)	S_0 (MeV)	L_{sym} (MeV)	K_{sym} (MeV)	$a_A^{(\alpha)}$ (MeV)
820	0.21	31.44	43.21	-89.90	27.90

Table 4.3: Values of the INM observables obtained from the α -lattice using the set of parameters (4.42). We include in the last column the asymptotic value of the symmetry energy curve.

We have also solved the equilibrium equation (4.37) for the three configurations, the results from the α -lattice are shown in the middle plot of Fig. 4.2.

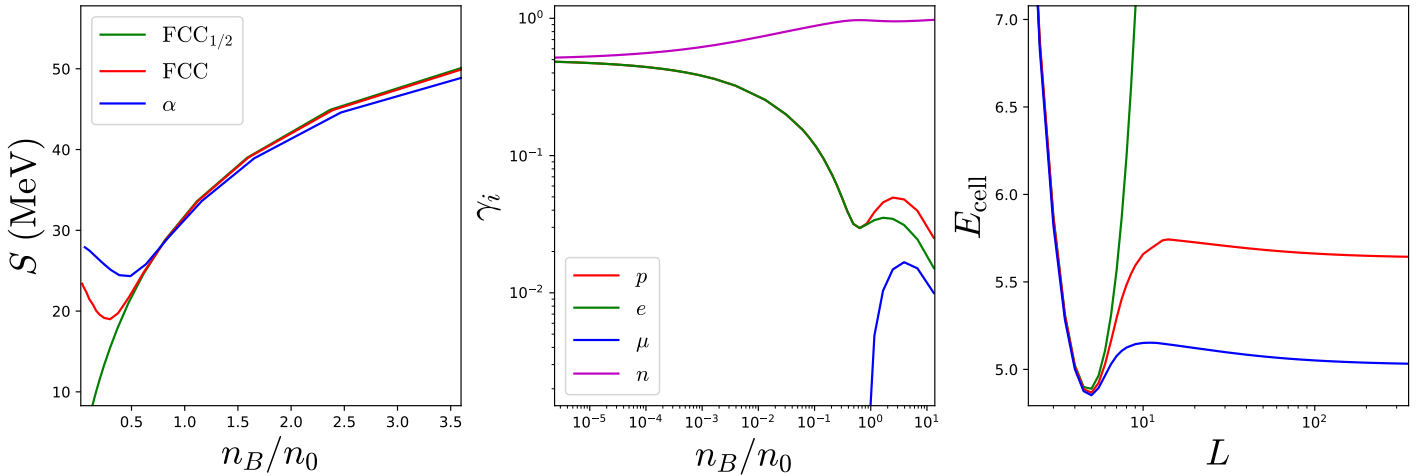


Figure 4.2: *Left:* Symmetry energy curves for the α -lattice, FCC crystal and its half-skyrmion version. Here, the transition to finite nuclear matter in the FCC and α -lattice is observed. *Middle:* Particle fractions obtained for the α -lattice, with the limits expected from the analysis of (4.37) *Right:* The total (classical and isospin) energy of the three crystalline configurations for realistic $npe\mu$ matter.

As we had anticipated, the proton fraction (and because of the baryon number conservation the neutron fractions too) tends to 1/2 in the zero density limit. Along the curve the number of electrons and protons is the same to ensure charge neutrality, until muons become energetically favourable at $n_B/n_0 \sim 0.85$. Finally, at high densities, due to the sextic term impact on the inertia tensor the proton fraction tends to zero.

Lastly, we may compute the total energy resulting from the classical contribution of the lattice and the other contributions coming the isospin quantization and lepton Fermi gases (4.33). The energy of symmetric nuclear matter is ex-

pected to have a minimum of energy in the point (E_0, n_0) , but once asymmetric β -equilibrated $npe\mu$ matter is considered, the minimum should be sharply softened or even removed, such that the resulting NS develops a crust. The Skyrme lattices are great candidates for this to occur given that they have the smallest asymptotic value. This is shown in the right plot of Fig. 4.2 for the three configurations again. However, the difference in energy between the minimum and the energy in the $L \rightarrow \infty$ limit is still too high in the α -lattice to completely erase the minimum from the isospin contribution. Instead, the minimum is slightly displaced and an interesting effect is observed. Although we still have a displaced minimum, the energy curve develops a bump which is above the minimum by a 6%, then the energy asymptotically decreases in the $L \rightarrow \infty$ limit. This asymptotic behaviour is a great feature of this energy curves and it is related to the smooth vanishing of the isospin contribution in the $\gamma \rightarrow 0.5$ limit.

The bump in the energy curve may be directly associated to the high binding energies in the Skyrme model. However, the correct asymptotic behaviour of the energy curve suggests that the presence of this bump might also be related to the compression modulus problem, which is a severe problem in the Skyrme model when it comes to reproduce INM. We will explain in more detail this problem in the last section of this chapter, where we propose a solution for it, but the compression modulus is basically related to the curvature of the energy curve at the minimum. If the compression modulus is too high, which is the case in the Skyrme model (~ 4 times the experimental value), the energy curve rapidly increases around the minimum. Thus, the isospin corrections cannot compete with this growth in the classical energy, so that the total energy increases. If the curvature around the minimum is, instead, sufficiently smaller, then the total energy would decrease, erasing the minimum and developing a crust.

4.1.3 Analysis of the parameters

The computation of the symmetry energy curve with the crystals opens the possibility to consider this new observable as a source of information to fix the values of the parameters present in the Skyrme model. In Chapter 3 we used the energy and baryon density at saturation to fix the pion decay constant

and the Skyrme parameter. The sextic term coupling λ^2 was used as a free parameter to study the effects that it had on the NS maximal masses. In the previous section, we have seen that λ^2 may be tuned to fit the symmetry energy at saturation and the higher multipoles. Then a natural exercise is to check if the set of three parameters in the Skyrme Lagrangian can be used to fit the three observables simultaneously at the saturation point.

From the results of our numerical simulations we have observed that the FCC_{1/2} crystal displays an almost *perfect scaling* property [24] with the unit cell length. Recall that this property is stronger than the fact that each $E(L)$ curve may be fitted by (3.11), it means that each of the terms in the energy functional scales with L independently as $E_i \propto L^{-i+3}$, where i is again the number of spatial derivatives appearing in that particular term. The values of the perfect scaling constants, which we have labelled by K_i , are then universal in the sense that they will not change for different values of the parameters.

Furthermore, this perfect scaling property is a characteristic of the field configuration, and not only of its energy. It is observed that also the isospin moment of inertia of the unit cell displays a sufficiently well perfect scaling for the minimal energy configuration, which we have identified with the saturation point. This is important in our analysis since we also want to fit the values of the symmetry energy at saturation.

Although the scaling is not perfect, in general the biggest deviations from the full numerical values of energy start far from the minimum, at which the perfect scaling fit is most precise.

Thus, we take advantage of this property in order to fit the magnitudes obtained from generalized Skyrme crystals to their physical values (up to a certain error). We do so following an iterative process based on five main steps:

1. Due to the perfect scaling property, the (adimensional) energy follows the curve (3.12), and the isospin moment of inertia approximately satisfy the expression (4.12) with $\Lambda_c = 0$, see Fig. 4.3. The values of Λ_i are again "universal", *i.e.*, they do not depend on the parameters or on L . Hence, these values are obtained from the contribution of each term independently, for the same choice of the parameters and length of the unit cell length L

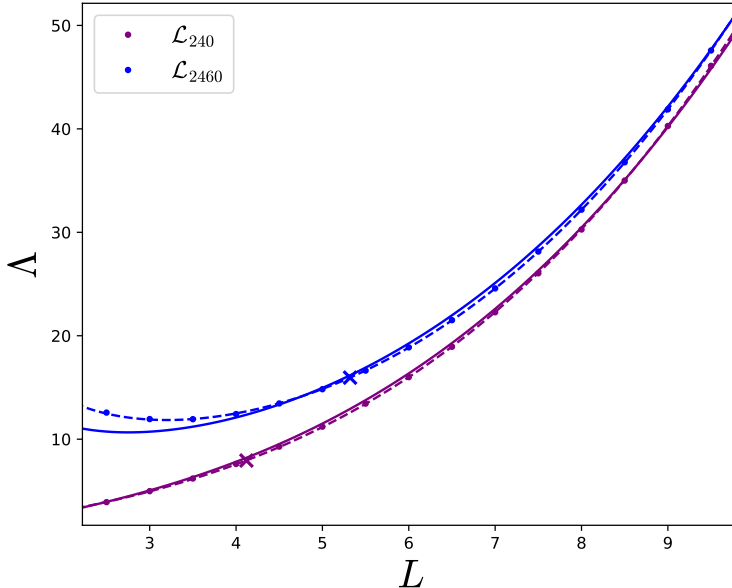


Figure 4.3: Isospin inertia moment curve of the FCC_{1/2} Skyrme crystal with and without sextic term. We show the numerical data (dots), fitted via the parametrization (4.12) (dashed lines) and the PS approximated curve (solid lines). The minima of the energy curves are represented by the crosses, where the PS is still an accurate approximation.

as we did with the energy constants in Table 3.1. The values of the new Λ_i universal scaling constants in the generalized \mathcal{L}_{2460} model are shown in the table below,

n	2	4	6
Λ_n	0.0380	1.3931	0.8831

Table 4.4: Perfect scaling parametrization constants of the isospin inertia tensor

2. We fix the energy scale E_s to an arbitrary value in MeV. This is equivalent to fixing one of the three free parameters of the model, for instance, f_π .
3. Then, we calculate L_0 by minimizing (3.12), and the values of E_0, n_0, S_0 and L_{sym} for different pairs of values (e, λ^2) .
4. When we find a set of parameters (f_π, e, λ^2) that fits the nuclear magnitudes within their respective errors of at most 15% then we calculate the corresponding EOS and solve the TOV system to obtain the mass-radius curve.
5. Finally, we accept the sets of values that satisfy the constraints, $M_{\max} \geq 2M_\odot$ and $R_{1.4M_\odot} \leq 12.5$ km. These constraints are motivated from pulsar

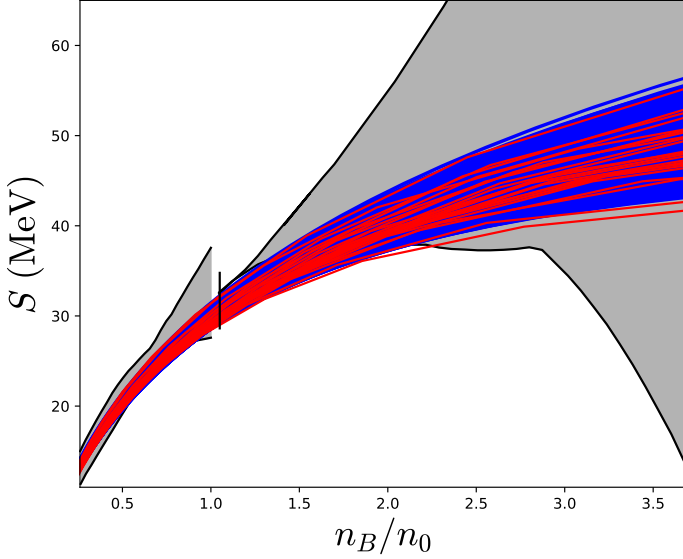


Figure 4.4: Symmetry energy of Skyrme crystals as a function of the density. We show 23 different curves from the scanned values. The shaded regions constrains the symmetry energy at sub-saturation [84] and supra-saturation [144] densities.

measurements [33, 87, 198]. We find that there is more than one set of parameters, so there is a residual freedom in the choice of these values that satisfy the nuclear physics magnitudes at saturation and NS observables.

The scan of parameters underscores the motivation for the generalized Skyrme model. The nuclear physics magnitudes are better fitted for very low or even null values of λ^2 since the sextic term reduces the value of the symmetry energy multipoles, confirming what the result of the previous section suggested. However, those sets of parameters are not accepted since they do not satisfy the maximum mass requirement. This reflects the importance of the sextic term in the extension of the Skyrme model to very high densities as inside NS.

In Fig. 4.4 we plot 560 symmetry energy curves obtained from a first quick scan in blue, and in red we plot 23 representative cases from the larger set which have been fully minimized. We also represent at densities larger than n_0 some restrictions obtained from the most recent constraints of the analysis of neutron star observations, and at densities smaller than the saturation point which are more restrictive.

We have obtained the EOS from these 23 sets of parameters and compare them with some constraints obtained from a recent analysis [30]. In that work they build a huge number of physically well motivated EOS and compare the result-

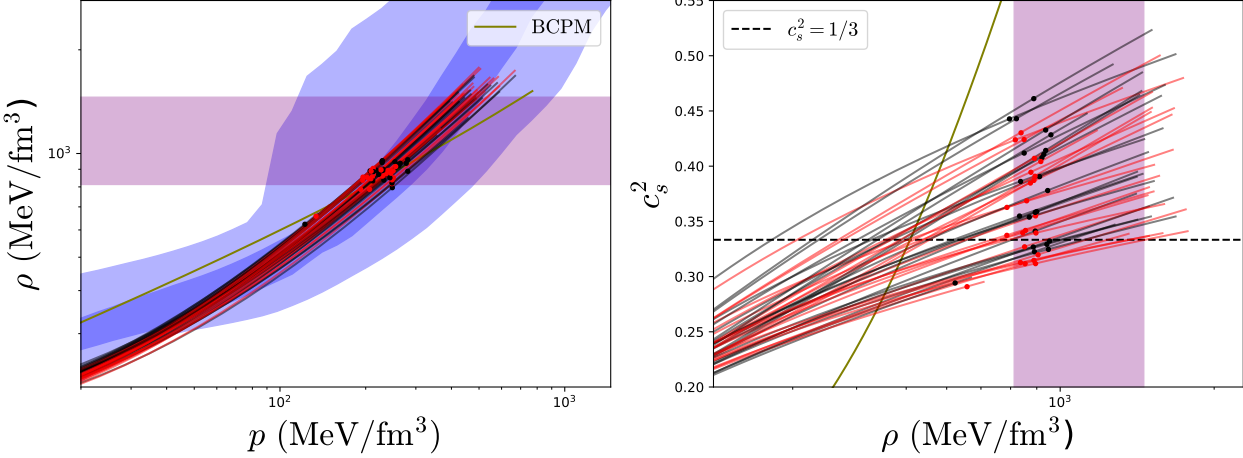


Figure 4.5: The EOS for the same 23 values shown before. In black we plot the resulting EOS without isospin effects, whilst in red we consider $npe\mu$ matter. We find a good agreement between our EOS and the shaded regions obtained from the analysis in [30] at high densities. The purple region is an estimation for the range of the maximum central density inside NS, and the dots represent the maximum central energy densities in our models.

ing NS with pulsars and GW observations. They conclude that the conformal limit in the speed of sound ($c_s^2 = 1/3$) is expected to be surpassed inside NS. In Fig. 4.5 we show the EOS obtained from our analysis and a good agreement is found with their results. The majority of our EOS exceeds the conformal bound too, and all of them lie inside the constrained region in the (ρ, p) diagram. We have cut the low density region in Fig. 4.5 due to the absence of a crust in our EOS. However it is remarkable how the Skyrme model correctly describes the high density regime, which corresponds to the core of the NS and hence the main responsible for the mass of the star. Also the BCPM [208] EOS is represented as an accepted candidate to compare with in the diagram.

In a more extensive analysis of the parameters, we found $\sim 10,000$ accepted sets of parameters. In order to obtain these values, we made the scan with the following steps: $\Delta E_s = 5$ MeV, $\Delta e = 0.01$, $\Delta \lambda^2 = 0.01$ MeV fm 3 . As briefly mentioned before, the constraints on the symmetry energy yield rather stringent upper bounds on the sextic term coupling constant, we find that $\lambda^2 \lesssim 3.4$ MeV fm 3 . Nevertheless, we remark that a lower bound for this constant can also be obtained from the maximum mass requirement of neutron star EOS [19]. In this analysis we have found a lower bound of $\lambda^2 \gtrsim 0.29$ MeV fm 3 .

We solved the system for the same 23 cases and in Fig. 4.6 we plot the MR curves, again with and without isospin effects for each case. The main conclu-

sion is that the isospin always increases the radii of the stars. On the other hand, the isospin increases the masses of the stars with $M \lesssim 2.3M_{\odot}$, for larger values the masses are reduced. This effect is also visible in 4.5, where the red curves lie below the black lines at lower densities, hence the reds are stiffer, whilst for very high densities the situation is slightly the opposite. Another keypoint is that all the sets of parameters obtained in this analysis allow to have a wide range of maximum masses, $M_{\max} \sim 2 - 2.5M_{\odot}$. This was an important feature in the NS obtained in the last section, and it is still possible using the fully minimized Skyrme crystals. This is of great importance for the Skyrme model since it would be able to describe possible high-mass measurements like [4]. In addition, despite the difference in the maximum masses, the radii of the stars do not change as much when choosing some parameters or others, $R_{1.4M_{\odot}} \sim 12 - 13$ km. However a final comment about the radii of the NS requires the presence of a crust, since it will affect the radii of low mass NS.

As can be seen all the black lines satisfy (in good approximation) our M_{\max} and $R_{1.4M_{\odot}}$ restrictions although they were imposed on the mass-radius curves resulting from the PS approximation. We have checked that the mass-radius curves obtained via the PS approximation are indeed quite similar to those of the fully minimized results for these 23 cases, so it confirms the PS approximation as a powerful and accurate tool for skyrmion crystals.

We also plot in 4.6 the most likely mass-radius relations for the NS corresponding to GW170817 [2] and GW190425 [4] events. The green regions represent the estimations for the mass and radius values of J0030+0451 (bottom) [164], and a more recent analysis of the PSR J0740+6620 mass and radius from NICER (top) [198]. The purple region constraints the mass-radius curves from the statistical analysis done in [30], besides they also give an estimation for the maximum central energy density that a NS may support. We also do the comparison in Fig. 4.5 between the range of values that they obtain (purple region) and our values (dots).

The greatest difference between the NS obtained using the interpolation between the submodels in the last section and those obtained from the minimization of the generalized Skyrme model using crystal solutions is found in the radii. Although we still have freedom to reach very high masses $\sim 2.5M_{\odot}$,

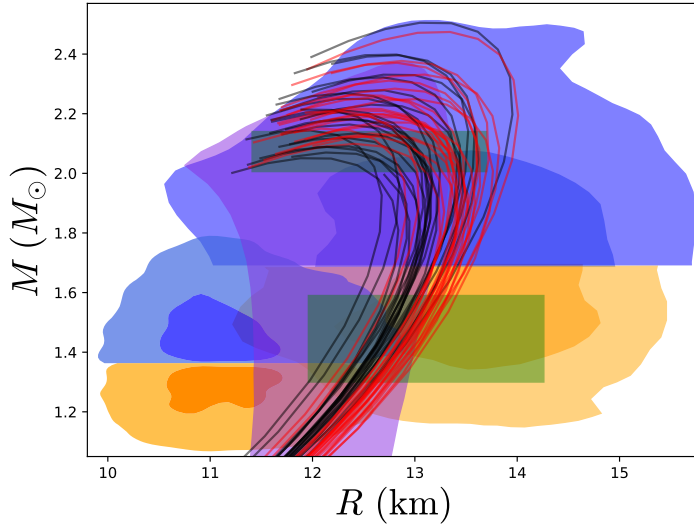


Figure 4.6: MR curves for the 23 representative sets of parameters considered. The colours of the lines represent the same as in Fig. 4.5. The shaded regions correspond to GW (blue and orange) and pulsar (green) constraints.

the radius increases when we consider the full model. The low-mass region ($\sim 1.4M_{\odot}$) in the MR curves of Fig. 2.16 and Fig. 4.6 differ due to the presence of a crust in the first case. We do not include a crust in the EOS shown in this section since it would be more interesting to consider an EOS which already has a crust entirely obtained from the Skyrme model. This is still an open problem due to the behaviour of the Skyrme crystals at low densities, but the study of the new lattices presented in the first section may lead to the correct description of the full EOS within the Skyrme model. Nonetheless we have seen that the inclusion of a crust via the simple quadratic interpolation (2.90) increases the radius of the NS around 1 km.

On the other hand, the $2.5M_{\odot}$ NS radius in Fig. 2.16 is around 11.5 km, while the radius for the same mass in Fig. 4.6 reaches 13 km. These high-mass NS are hardly affected by the presence of a crust, so the numerical simulation of the Skyrme crystal leads to a stiffer EOS. Nevertheless, the high-mass region of the last plot may be sharply improved with the inclusion of strangeness degrees of freedom in the system. Taking into account this effect provides even more realistic EOS, besides it is known that it will decrease the maximal mass as well as the radius, leading to a softer EOS at high densities.

4.2 Kaon condensation in Skyrme neutron stars

The computation of the symmetry energy enabled a natural way to include leptons in Skyrme crystals, which corresponds to a more realistic description of NS. However, it is believed that in the deepest layers of NS, new particles like Δ resonances [145], strange degrees of freedom [224, 228] or even deconfined quark matter [159, 160] would appear similarly as muons, which become more energetically favourable than electrons.

Specifically, the appearance of kaons and their subsequent condensation was firstly proposed in 1987 by Kaplan and Nelson [128], and it has been extensively studied [194], even in the present. The idea is based on the sufficient reduction of the in-medium mass of the antikaon K^- , due to the interactions between the nuclear potential. Besides, the appearance of kaons is a phase transition which may be of first or second order [101], with great impact on the masses of NS. Hence, the study of this phenomenon might shed some light not only in the internal composition of NS, but also in the parametrization of the nuclear potentials.

Actually, the presence of strange degrees in NS is a wider study in which also hyperons may be considered. Simulations have inferred that baryonic particles with strangeness may be produced around $2 - 3$ times the saturation density, whilst kaon condensation is believed to occur at $3 - 4$ times n_0 . However, both processes provide, as the main effect, the decrease the maximal masses of the NS, since the EOS gets softened. This, indeed, may be problematic for some EOS which cannot support NS with maximal masses much larger than those already measured $\sim 2M_\odot$, and it is commonly known as the *hyperon puzzle* [58, 225].

In this section we perform a detailed study on the possibility to have condensation of kaons in the FCC_{1/2} Skyrme crystal, the order of the phase transition, and how this affects the resulting NS.

4.2.1 The Bound-State approach of the Skyrme model

Throughout this thesis we have been working with the Skyrme model based on the $N_f = 2$ isospin symmetry, which is able to describe successfully nucleons and their spin and isospin excitations. Including strangeness in the model is translated into adding one more flavour.

First attempts considered the most natural extension, which is the $SU(3)$ flavour symmetry in the model. However, it seems that treating strangeness in the same way as isospin does not produce suitable results [80, 191]. This failure is not quite surprising given that the mass of the s quark, $m_s \sim 100$ MeV, is much higher than the u and d quarks, $m_u \approx m_d \sim 4$ MeV, to consider the full symmetry. Instead, Callan and Klebanov [72, 73, 131] introduced the strangeness as $SU(3)$ perturbations of the non-strange $SU(2)$ solitonic solutions, in the so-called Bound-State model. This approach remains as one of the simplest and most successful models for hyperons due to the agreements in the masses and the correct identification in the particles spectrum. The idea of this procedure is the inclusion of strange mesonic degrees of freedom, *kaons*, in the model and construct topologically nontrivial solutions from the pionic theory with nonzero kaon solutions. We want to develop this formalism specifically in the FCC_{1/2} Skyrme crystal to derive an EOS in which kaons are included. This would imply that the Skyrme model is able to produce a quite complete description of the high density regime of NS matter.

The starting point in the Bound-State model is the inclusion of the kaon fluctuations as the $SU(3)$ extension on top of a purely pionic $SU(2)$ skyrmion background. Two different ansätze have been proposed to describe the field configuration. Although many static properties, studied so far, yield the same results in both cases, it may be argued that form factors will come out differently [177]. We will consider the one proposed in [54],

$$U = \sqrt{U_K} U_\pi \sqrt{U_K}, \quad (4.43)$$

$$U_\pi = \begin{pmatrix} u & 0 \\ 0 & 1 \end{pmatrix}, \quad U_K = \exp \left\{ i \frac{2\sqrt{2}}{f_\pi} \mathcal{D} \right\}, \quad (4.44)$$

which differs from the original proposal by Callan and Klebanov. In this parametrization, the pionic field U_π is the trivial $SU(3)$ embedding of the usual $SU(2)$ Skyrme field, here denoted by u . The fundamental kaon field is imprinted in the \mathcal{D} matrix, which has the form,

$$\mathcal{D} = \begin{pmatrix} 0 & K \\ K & 0 \end{pmatrix}, \quad (4.45)$$

$$K = \begin{pmatrix} K^+ \\ K^0 \end{pmatrix}, \quad K^\dagger = (K^-, \bar{K}^0). \quad (4.46)$$

The Lagrangian is extended by a new potential term which accounts for the of the pions and kaons,

$$\begin{aligned} \mathcal{L}_0^{\text{new}} = & \frac{f_\pi^2}{24} (m_\pi^2 + 2m_K^2) \text{Tr}\{U - \mathbb{I}_3\} + \\ & \frac{\sqrt{3}}{24} (m_\pi^2 - m_K^2) \text{Tr}\{\lambda_8 (U + U^\dagger)\}, \end{aligned} \quad (4.47)$$

where $m_K = 490$ MeV is the kaon mass, and λ_8 is the eighth component of the Gell-Mann matrices λ_A , which are the $\mathfrak{su}(3)$ Lie algebra generators.

Furthermore, in the $SU(3)$ case, the Wess-Zumino-Witten (WZW) term [230, 232, 233] must be included in the total action. Although it was first introduced to break the C, P and T transformations, this term describes the parity-violating kaon decay $K^+ K^- \rightarrow \pi^+ \pi^0 \pi^-$. Additionally, it also needs to be included when the Skyrme model is coupled to the electromagnetism since it accounts for the π^0 decay into a pair of photons. Actually, it can only be expressed in terms of a five-dimensional action term,

$$S_{\text{WZW}} = -i \frac{N_c}{240\pi^2} \int d^5x \epsilon^{\mu\nu\alpha\beta\rho} \text{Tr}\{L_\mu L_\nu L_\alpha L_\beta L_\rho\}, \quad (4.48)$$

where $N_c = 3$ may be directly identified with the number of QCD colour degrees of freedom. Nevertheless, it is finally expressed as an integral in the standard four-dimensional spacetime integral using the Stokes theorem. As a further comment, this term has crucial importance regarding the spin-statistics

of skyrmions, however, this only applies in the exact $SU(3)$ symmetry since it vanishes in the $SU(2)$ case.

Kaons become energetically favourable when μ_e is larger than the kaon mass. If this condition is attained, since kaons are bosons, they occupy the lowest energy state in the large pressure regime of NS, forming a condensate. Then, we follow the standard formalism for the condensation of a scalar field [204] to describe the kaon field (4.46). We will focus on the condensation of the electrically charged kaons, hence we impose the conditions $K^0 = \bar{K}^0 = 0$. A condensed scalar field is determined by the vacuum expectation value (VEV) $\langle K^\pm \rangle$, which is constant in space, and has a simple time-dependent phase,

$$\langle K^\pm \rangle = \phi e^{\pm i\mu_K t}. \quad (4.49)$$

The constant field VEV, ϕ , becomes nonzero when the kaon condition is satisfied, it will change for different values of the lattice length, and its specific value will be determined by the minimization of kaon potential energy. The phase, μ_K , is the kaon chemical potential, and it will be fixed by the equilibrium condition to the electron chemical potential. We introduce (4.49) in the generalized $SU(3)$ Skyrme field and use the relation $\mathcal{D}^3 = \phi^2 \mathcal{D}$, which is valid for the specific condensed kaon field. Then, we redefine the field $\phi \rightarrow \frac{\sqrt{2}}{f_\pi} \phi$ and obtain,

$$\sqrt{U_K} = \begin{pmatrix} \cos \phi & 0 & ie^{i\mu_K t} \sin \phi \\ ie^{-i\mu_K t} \sin \phi & 0 & \cos \phi \end{pmatrix} \quad (4.50)$$

We assume that the kaon backreaction to the classical configuration of the Skyrme crystal is negligible. Then, the skyrmion solution and the classical energy contribution remain unaffected, but there will be additional contribution to the total energy when kaons condense. Introducing the extended Skyrme field (4.43) in the Lagrangian we obtain the usual Skyrme Lagrangian and an additional potential term which depend on the kaon field ϕ ,

$$S_{\text{Skyrme}}(U) + S_{\text{WZW}}(U) = \int dt d^3x \mathcal{L}_{2460}(u) - \int dt V_K(\phi). \quad (4.51)$$

The new term comes from the time dependence of the kaon field (4.49), it is often called the optical kaon potential, and we will split it in different contributions,

$$V_K = \frac{1}{24\pi^2} \int d^3x \left[V_K^{(2)} + V_K^{(4)} + V_K^{(6)} + V_K^{(0)} \right] + V_K^{(\text{WZW})}. \quad (4.52)$$

Each contribution comes from each term in the Skyrme lagragian, introducing the explicit expression of the field configuration (4.43) and the kaon condensed field ansatz (4.49) we obtain,

$$V_K^{(2)} = \mu_K^2 \sin^2 \phi [(1 + \sigma^2 + \pi_3^2) \sin^2 \phi - 2(1 + \sigma \cos^2 \phi)], \quad (4.53)$$

$$\begin{aligned} V_K^{(4)} = & -2\mu_K^2 \sin^2 \phi \{ (1 + \sigma) \partial_i n^2 \cos^2 \phi + \\ & + 2 [\partial_i \sigma^2 (1 - \pi_3^2) + \partial_i \pi_3^2 (1 - \sigma^2) + 2\sigma \pi_3 \partial_i \sigma \partial_i \pi_3] \sin^2 \phi \}, \end{aligned} \quad (4.54)$$

$$V_K^{(6)} = -\mu_K^2 \frac{c_6}{2} \sin^4 \phi (\partial_i \pi_3 \partial_j \sigma - \partial_i \sigma \partial_j \pi_3)^2, \quad (4.55)$$

$$V_K^{(0)} = 2 \frac{m_K^2}{f_\pi^2 e^2} (1 + \sigma) \sin^2 \phi, \quad (4.56)$$

$$V_K^{(\text{WZW})} = -\mu_K N_c B_{\text{cell}} \sin^2 \phi. \quad (4.57)$$

The quadratic, quartic and potential terms require lengthy but straightforward computations. However, for the WZW and sextic terms, the Lie algebra-valued differential forms formalism is extremely helpful. An extensive derivation of both terms using this formalism may be found in [21].

Finally, we have to consider quantum isospin corrections as we did in the previous sections. Since kaons also have isospin quantum number they will contribute to the isospin inertia moment. We perform the new time-dependent isospin transformation on the extended Skyrme field,

$$U \rightarrow A(t) U A^\dagger(t), \quad A(t) = \begin{pmatrix} a(t) & 0 \\ 0 & 1 \end{pmatrix}, \quad (4.58)$$

where $a(t)$ is the usual $SU(2)$ isospin transformation.

The expressions of the excited currents are equivalent to those obtained before

(4.5), but in this case the time component of the Maurer-Cartan form is separated into two different contributions, one comes from the time dependence of the kaon field (which yields the potential term V_K computed before) and the other from the isospin transformation,

$$U^\dagger \partial_0 U \rightarrow A L_0 A^\dagger + A U^\dagger [A^\dagger \dot{A}, U] A^\dagger. \quad (4.59)$$

The angular frequency is now defined in terms of the Gell-Mann matrices $A^\dagger \dot{A} = \frac{i}{2} \omega_a \lambda_a$, where $a = 1, 2, 3$. The angular frequency is again a three-vector since the simple extension (4.58) of A implies that $A^\dagger \dot{A}$ belongs to the $\mathfrak{su}(2)$ subalgebra of $\mathfrak{su}(3)$. Introducing everything in the Lagrangian we obtain the corresponding kinetic energy contribution,

$$T = \frac{1}{24\pi^2} \int d^3x \left[-\frac{1}{2} (\text{Tr}\{L_0^2\} + 2 \text{Tr}\{L_0 T_a\} \omega_a + \text{Tr}\{T_a T_b\} \omega_a \omega_b) - \frac{1}{2} (\text{Tr}\{[(L_0 + T_a \omega_a), L_k][(L_0 + T_b \omega_b), L_k]\}) + 4\pi^4 c_6 (\mathcal{B}^i)^2 \right], \quad (4.60)$$

which has an equivalent expression to (4.2), quadratic in the angular frequency, and an additional contribution linear in ω_a . We have defined $T_a = \frac{i}{2} U^\dagger [\lambda_a, U]$, equivalently as before.

Again, we identify the kinetic energy with an isorotational energy, from which we may extract the isospin inertia tensor,

$$T = \frac{1}{2} \omega_a \Lambda_{ab} \omega_b - \Delta_a \omega_a, \quad (4.61)$$

and the isospin kaon current Δ_a . Both expressions are rather straightforward

to obtain,

$$\Lambda_{ab} = \int d^3x [-\text{Tr}\{T_a T_b\} - \text{Tr}\{[T_a, L_k][T_b, L_k]\} - \frac{c_6}{8}\epsilon^{lmn} \text{Tr}\{T_a L_m L_n\} \epsilon_{lrs} \text{Tr}\{T_j L_r L_s\}], \quad (4.62)$$

$$\Delta_a = \int d^3x [-\text{Tr}\{L_0 T_a\} - \text{Tr}\{[T_a, L_k][L_0, L_k]\} - \frac{c_6}{8}\epsilon^{lmn} \text{Tr}\{L_0 L_m L_n\} \epsilon_{lrs} \text{Tr}\{T_a L_r L_s\}]. \quad (4.63)$$

As before, the symmetries A_1 (3.4) and A_2 (3.5) of the Skyrme crystals produce an isospin inertia tensor proportional to the identity. However, when the kaon field is nonzero, this property is lost and the isospin inertia tensor becomes anisotropic, with two different eigenvalues, $\Lambda := \Lambda_{11} = \Lambda_{22}$ and Λ_3 . Besides, the operator Δ_a is also excited, but the only non-vanishing component is $\Delta := \Delta_3$ and the others, $\Delta_{1,2}$ are zero. This produces a different third component of the isospin angular momentum,

$$K_3 = \Lambda_3 \omega_3 + \Delta, \quad (4.64)$$

which yields the following Hamiltonian,

$$\hat{H} = \frac{\hat{K}_1^2 + \hat{K}_2^2}{2\Lambda} + \frac{(\hat{K}_3^2 - \Delta^2)}{2\Lambda_3}. \quad (4.65)$$

This Hamiltonian is similar to the one obtained from the Skyrme lattices (4.39) with an additional scalar term. Following the same arguments we finally obtain the quantum energy of the Skyrme crystal with kaons,

$$E_{\text{quantum}} = \frac{\hbar^2 B_{\text{cell}}^2}{8\Lambda_3} \delta^2 - \frac{\Delta^2}{2\Lambda_3}, \quad (4.66)$$

where the first term is the isospin energy obtained previously, but now the isospin moment of inertia depend on the kaon field.

The derivation of the explicit expressions for Λ_3 and Δ requires a careful treat-

ment, and the group properties of the Skyrme field must be used several times in some key points. We finally obtained the following simplified expressions,

$$\Lambda_3^{(2)} = \frac{\pi_1^2 + \pi_2^2}{2}(1 + \cos^2 \phi)^2 + (1 + \sigma) \frac{\sin^2(2\phi)}{4}, \quad (4.67)$$

$$\begin{aligned} \Lambda_3^{(4)} &= 2(1 + \cos^2 \phi) [(1 - \pi_3^2)\partial_i \sigma^2 + \sigma \pi_3 \partial_i \sigma \partial_i \pi_3] + \\ &\quad + \partial_i n^2 (1 + \sigma) \frac{\sin^2(2\phi)}{4}, \end{aligned}$$

$$\Lambda_3^{(6)} = \frac{\mu_K^2 c_6}{4} (1 + \cos^2(\phi))^2 (\partial_i \pi_3 \partial_j \sigma - \partial_i \sigma \partial_j \pi_3)^2 \quad (4.68)$$

$$\Delta^{(2)} = -i\mu_K \left[(\pi_1^2 + \pi_2^2)(\cos^4 \phi - 1) + (1 + \sigma) \frac{\sin^2(2\phi)}{2} \right], \quad (4.69)$$

$$\begin{aligned} \Delta^{(4)} &= -2i\mu_K [2(1 - \cos^4 \phi) (\pi_1^2 \partial_i \pi_2^2 + \pi_2^2 \partial_i \pi_1^2 - 2\pi_1 \pi_2 \partial_i \pi_1 \partial_i \pi_2 \\ &\quad - \partial_i n^2 (\pi_1^2 + \pi_2^2)) + \partial_i n^2 (1 + \sigma) \frac{\sin^2(2\phi)}{4}], \end{aligned} \quad (4.70)$$

$$\Delta^{(6)} = i \frac{\mu_K c_6}{2} (1 + \cos^2 \phi) \sin^2 \phi (\partial_i \pi_3 \partial_j \sigma - \partial_i \sigma \partial_j \pi_3)^2 \quad (4.71)$$

$$\Delta^{(\text{WZW})} = -\frac{N_C B_{\text{cell}}}{2} \sin^2(\phi) \quad (4.72)$$

4.2.2 Kaon condensation in neutron star cores

When the kaon field develops a nonzero VEV, apart from the neutron decay and lepton capture processes of (4.27), additional processes involving kaons may occur:

$$n \rightarrow p + K^-, \quad l \rightarrow K^- + \nu_l \quad (4.73)$$

such that the chemical equilibrium conditions

$$\mu_n = \mu_p + \mu_K, \quad \mu_l = \mu_K \quad (4.74)$$

are satisfied. The last expressions are the extension of (4.32) to the condensate phase.

The total energy within the unit cell may be obtained as the sum of the baryon, lepton and kaon contributions:

$$E = E_{\text{class}} + E_{\text{iso}}(\gamma, \phi) + E_e(N_e) + E_\mu(N_\mu) + \Omega_K(\mu_K, \phi). \quad (4.75)$$

We remark that the above expression does not fully correspond to the (relativistic version of the) internal thermodynamical energy for nonzero kaon condensate. The reason is that the kaon chemical potential μ_K has been introduced as the independent variable in the system, whereas the chemical potentials μ_l of the remaining particles are functions of the corresponding particle numbers, N_l , as must be the case for an internal energy. We have combined the contributions coming from the optical potential and the quantum energy in the same term,

$$\Omega_K(\mu_K, \phi) = V_K - \frac{\Delta^2}{2\Lambda_3}, \quad (4.76)$$

which depends on the condensed kaon field ϕ and on the kaon chemical potential through the explicit dependence on μ_K of both V_K and Δ .

Now we want to determine the values of the proton fraction and the kaon condensate that minimize the total energy for a given baryon density n_B (or equivalently, fixed L) under the modified β -equilibrium (4.73). For this purpose, we perform the systematic thermodynamical derivation of the equations. We first define the new degrees of freedom, $N_Q = N_p - N_e - N_\mu$ and $B = N_p + N_n$, and we perform a Legendre transformation to define the thermodynamical grand potential,

$$\Omega(B, \mu_e, \phi) = E(B, N_Q, \phi) + \mu_e N_Q, \quad (4.77)$$

where we have already imposed the equilibrium conditions (4.74) implying $\mu_I = \mu_e = \mu_\mu = \mu_K$. Recall that the isospin chemical potential is related to the proton fraction through (4.36), and therefore μ_e too. The grand potential must now be minimized with respect to its variables, *i.e.* ϕ and μ_e ,

$$\left. \frac{\partial \Omega}{\partial \mu_e} \right|_{n_B, \phi} = \left. \frac{\partial \Omega}{\partial \phi} \right|_{n_B, \mu_e} = 0. \quad (4.78)$$

Using (4.75) we have:

$$\gamma n_B - \frac{(\mu_e^2 - m_e^2)^{3/2} + (\mu_e^2 - m_\mu^2)^{3/2}}{3\pi^2 \hbar^3} + \frac{n_B}{4} \left. \frac{\partial E_K}{\partial \mu_K} \right|_{\mu_K = \mu_e} = 0, \quad (4.79)$$

$$\frac{\partial V_K}{\partial \phi} - \frac{\Delta}{\Lambda_3} \frac{\partial \Delta}{\partial \phi} + \frac{\partial \Lambda_3}{\partial \phi} \left(\frac{\Delta^2}{2\Lambda_3^2} - \frac{\mu_e^2}{2\hbar^2} \right) = 0. \quad (4.80)$$

The first expression is precisely the charge neutrality condition, where we have partially recovered the proton fraction in the first term for clarity. The second one is the minimization of the grand canonical potential with respect to the kaon field. We note here that we drop the ultrarelativistic consideration for electrons since the appearance of kaons may decrease hugely the electron fraction. By solving the system of equations (4.79) and (4.80) for μ_e and ϕ we obtain all the needed information for the new kaon condensed phase. Then we may compare the particle fractions and energies between both phases, which we will denote by $npe\mu$ and $npe\mu\bar{K}$.

Before solving the full system for different values of the lattice length L , we must obtain the value of the length L_{cond} at which kaons condense. This value is indeed important since it will determine whether or not a condensate of kaons will appear at some point in the interior of NS. This is accomplished with the same system of (4.79) and (4.80) by factoring the $\sin \phi$ from the second equation and setting $\phi = 0$. Then we may see the system as a pair of equations to obtain the values of γ_{cond} and L_{cond} , the values of the proton fraction and the length parameter for which the kaons condense.

We show in Table 4.5 the density at which kaons condense for different values of the parameters. All the values are given in units of MeV and fm, respectively.

label	f_π	e	λ^2	E_0	n_0	S_0	L_{sym}	n_{cond}/n_0
set 1	133.71	5.72	5.00	920	0.165	23.5	29.1	2.3
set 2	138.11	6.34	5.78	915	0.175	24.5	28.3	2.2
set 3	120.96	5.64	2.68	783	0.175	28.7	38.7	1.6
set 4	139.26	5.61	2.74	912	0.22	28.6	38.9	1.6

Table 4.5: Sets of parameter values obtained from the extensive analysis in the last subsection and their corresponding observables at nuclear saturation.

We choose some representative parameter values such that, for the parameter sets 1 and 2, the energy per baryon and baryon density at saturation are reasonably close to their experimental values, whereas the sets 3 and 4 reasonably fit the symmetry energy and slope at saturation. The aim is to study the impact that the different observables have on the condensation density.

In Fig. 4.7, we show the $E(L)$ curves both without and with kaon condensation, in dimensionless Skyrme units. It is clearly visible that for sufficiently small L a nonzero kaon condensate is preferred. In the same figure, we also show the resulting particle fractions, where a significant increase in the number of protons is clearly visible when kaons appear. In Fig. 4.8 we plot the symmetry energy as a function of n_B with and without condensed kaons.

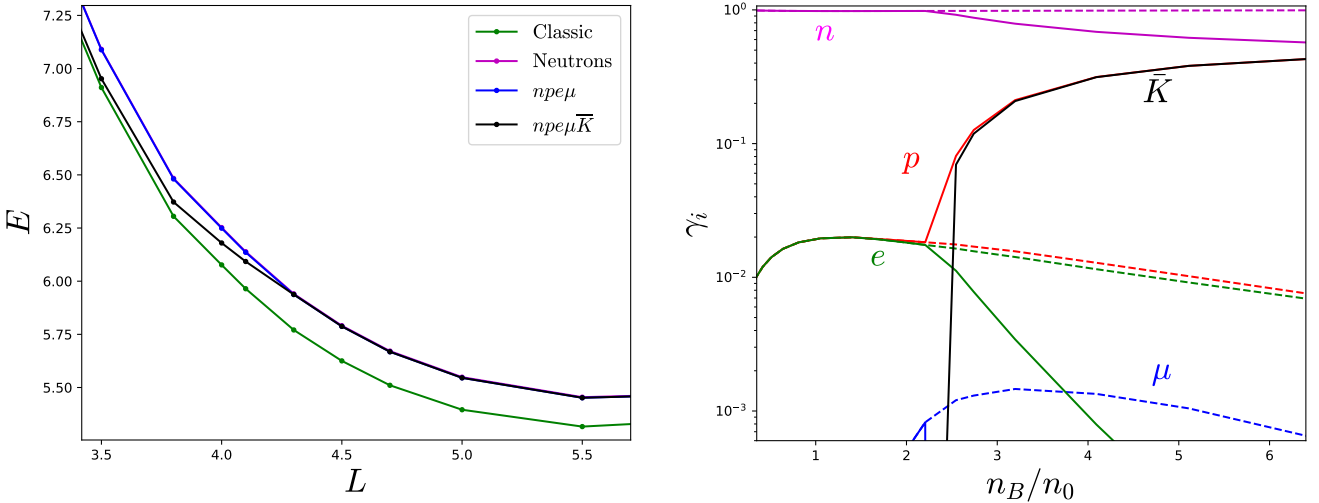


Figure 4.7: *Left:* Energy vs lattice length for the set 1 of parameters. The energy is shown for the classical crystal without isospin contributions (green), isospin asymmetric ($npe\mu$) matter with (black) and without (blue) kaons. We also plot the completely asymmetric neutron matter (magenta) which lies slightly above the blue curve. *Right:* Particle fractions as a function of baryon density for the set 1 of parameters, both with (solid lines) and without (discontinuous lines) kaon condensate.

Finally the interest of this work is to study the impact that kaon condensation have on the Skyrme NS, for which the EOS must be obtained. The $npe\mu$ matter case is easy to obtain using (4.34) for different values of L after solving the β -equilibrium and charge neutrality conditions for γ . However, once we include kaons, the change in the energy curve Fig. 4.7 may lead to a first or second order phase transition. To distinguish the order of the phase transition in our case, we need to know accurately the pressure near the condensation point. Therefore, we computed more points for the energy near the condensation value with

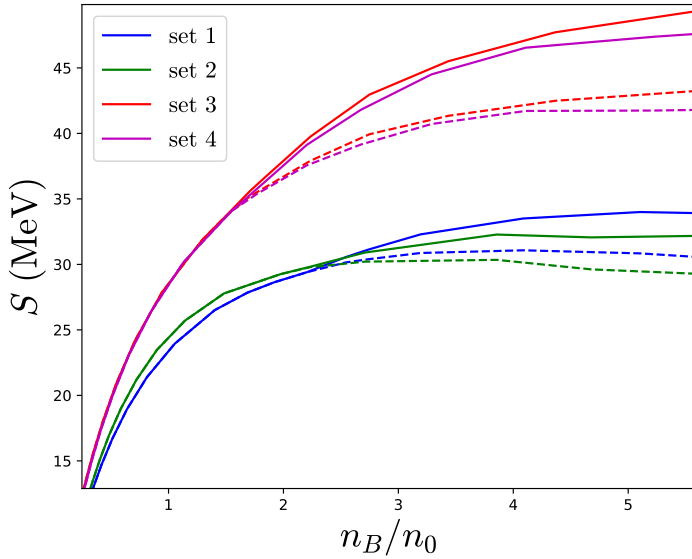


Figure 4.8: Symmetry energy of nuclear matter as a function of baryon density for the sets of parameters considered in this work. The thick line represents the symmetry energy when kaons are considered in the system and the dashed line does not include kaons.

higher accuracies, and we obtained the pressure using a numerical derivative. We conclude that the kaon condensation produces a first order phase transition for our choices of parameters in the Skyrme model. This can be seen in the right plot of Fig. 4.9, where we show the EOS for our best accuracy and for the set 1 of parameters. Clearly, there is a non-physical region which must be bridged by a first order phase transition. Similar results, indicating a first-order transition, are found for the other parameter sets.

The phase transition to kaon condensation has been investigated previously, e.g., within a relativistic mean field theory framework [101, 189]. The kaon optical potential, which is the relevant parameter for the phase transition, was allowed to vary within a rather large range in these investigations. This lead to a large variety of possible situations, from a second order phase transition for a weak optical potential to a strongly first-order transition for a strong one, where the number of protons outweighs the number of neutrons at sufficiently high density. For intermediate optical potentials, their results are similar to ours.

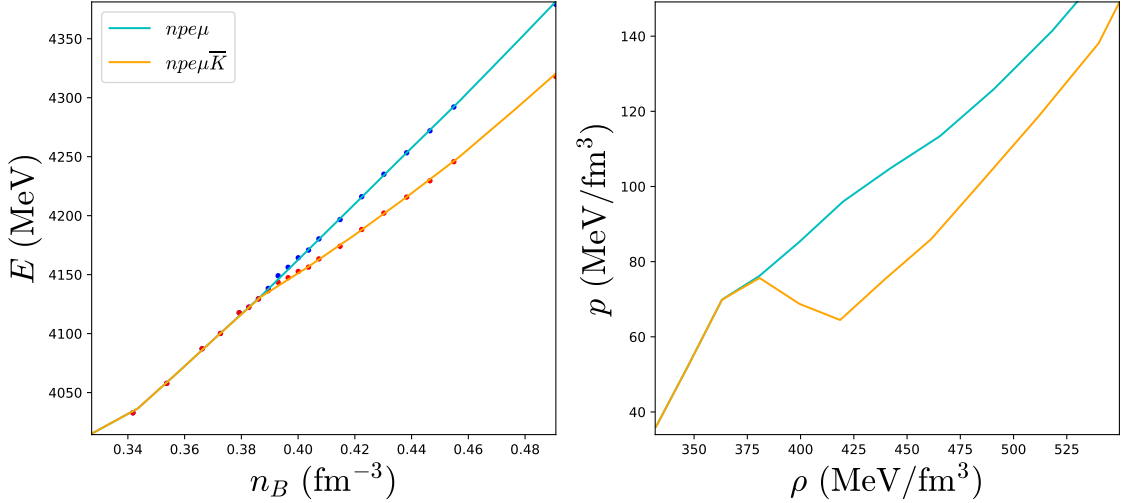


Figure 4.9: *Left:* Energy per baryon against the side length of the unit cell and their interpolations. *Right:* pressure against the energy density, from which we conclude that there is a first order phase transition. Both plots are for the set 1 of parameters.

Maxwell construction vs Gibbs construction

The Maxwell construction (MC) is typically used to obtain a physical equation of state when a first order transition is present. Indeed, the MC has been already studied in the Skyrme crystals context to describe the transition between crystals with different symmetries [24]. This construction is based on a mixed phase of constant pressure which connects the two solutions. However, the MC is only correct when there is a single conserved charge (in this case, the baryon number) for which the associated chemical potential is enforced to be common for both phases in the mixed phase [99]. If, instead, an additional charge is conserved, like the electric charge in the case of \$npe\mu\$ matter, the Gibbs conditions for the phase equilibrium,

$$p^I = p^{II}, \quad \mu_i^I = \mu_i^{II}, \quad i = B, q \quad (4.81)$$

cannot be both satisfied in a standard MC. In the last expression \$\mu_B\$ and \$\mu_q\$ represent the chemical potentials associated to the conserved baryon and electric charges, respectively. Instead, one should perform a Gibbs construction (GC) [99, 101]. Indeed, the GC has also been proven useful in the context of a hadron-to-quark phase transition inside NS [51].

We may write the chemical potential of each particle species as a linear com-

bination of the chemical potentials associated to the conserved charges of our system:

$$\mu_i = B_i \mu_B + q_i \mu_q, \quad (4.82)$$

where B_i and q_i are the baryon number and electric charge of the particle species i . Then we might identify the baryon and electric charge chemical potentials with the neutron and electron chemical potentials respectively. The main difference between MC and GC is that, in the mixed phase, the first one imposes charge neutrality locally, *i.e.* both phases are neutral independently, however in the GC it is imposed globally in the mixed phase. Considering a volume fraction χ of the kaon condensed phase, charge neutrality is imposed in the GC as:

$$n_q^{\text{MP}} = (1 - \chi)n_q^{\text{I}} + \chi n_q^{\text{II}} = 0. \quad (4.83)$$

The mixed phase in the GC is calculated by identifying first the contributions to the pressure and charge densities in each phase separately. Then we have to solve the system of equations composed by (4.81), (4.83) and (4.80). We use the unit cell length parameter of the first ($npe\mu$) phase L_{I} as the variable defining our position in the phase diagram, then the unknowns are the length in the second ($npe\mu\bar{K}$) phase L_{II} , the proton fractions γ_{I} , γ_{II} , the kaon field ϕ and the volume fraction χ .

We remark that we assumed in our calculations of the kaon condensate that the backreaction of the condensate on the crystal is negligible, such that our two phases are always considered in the same classical crystal background, and the energies per baryon of the two phases are compared for the same length L . As a result, we always should have $L_{\text{I}} = L_{\text{II}}$ and, consequently, $n_B^{\text{I}} = n_B^{\text{II}}$ by construction. On the other hand, the relation between L and the thermodynamical variables p , μ_i and ϕ used in (4.81), (4.83) and (4.80) is quite nontrivial in both phases. We, therefore, treat L_{II} as an independent variable in our numerical calculations. We find that always $L_{\text{I}} = L_{\text{II}}$ within our numerical precision, which provides us with an additional consistency check both for our numerics and for the thermodynamical transformations we used.

The results are shown in Fig. 4.10. Specifically, in the left plot of Fig. 4.10 the energy per baryon is shown as a function of the lattice parameter L both for the two pure phases and for the mixed phases resulting from a MC and a GC, respectively. We find that the mixed phase of the GC, and hence the values at which the kaon field becomes non-zero, starts at a smaller density than the value obtained in Table 4.5. This is also found in [101], for which the GC mixed phase extends to a larger region than the one obtained from the MC, because the mixed phase in the GC no longer is for constant pressure. In our case, even the minimum of $E(L)$ is shifted to slightly lower values and, hence, the use of the GC affects the low density regime of the EOS.

Once the energy is computed, the EOS is obtained in the standard procedure and the TOV system of equations may be solved to study the impact that kaons have in the Skyrme NS. The results of this computation are plotted in the right panel of Fig. 4.10 for the 4 sets of parameters. We compare the results obtained between the MC and GC as well as with the EOS without kaons but we also include the same GW and pulsar constraints from the previous section in the MR diagram. The first observation is that the addition of kaons to the EOS agrees with the expectation, reducing the achievable maximum mass. This represents the *hyperon puzzle*, in which the appearance of new strange degrees of freedom softens the EOS such that it may not lead to sufficiently massive NS ($\sim 2M_{\odot}$). As can be seen, this is not the case in the generalized Skyrme model since we may obtain very high masses easily due to the contribution of the sextic term. Furthermore the radii of NS are also reduced, which benefits our concrete model since the radii for skyrmion crystals are in some cases too large.

The main difference between the two different constructions is that the MC starts at a given density, hence it deviates from the $npe\mu$ EOS at a certain mass. On the other hand, since the GC changes the location of the minimum, it leads to different results also in the low mass region. However, both constructions practically merge in the high masses region, in which they follow the same $npe\mu\bar{K}$ EOS.

As already explained, the thermodynamically stable region of the $E(L)$ curves and the corresponding EOS based on Skyrme crystals is $L \leq L_*$ or, equivalently,

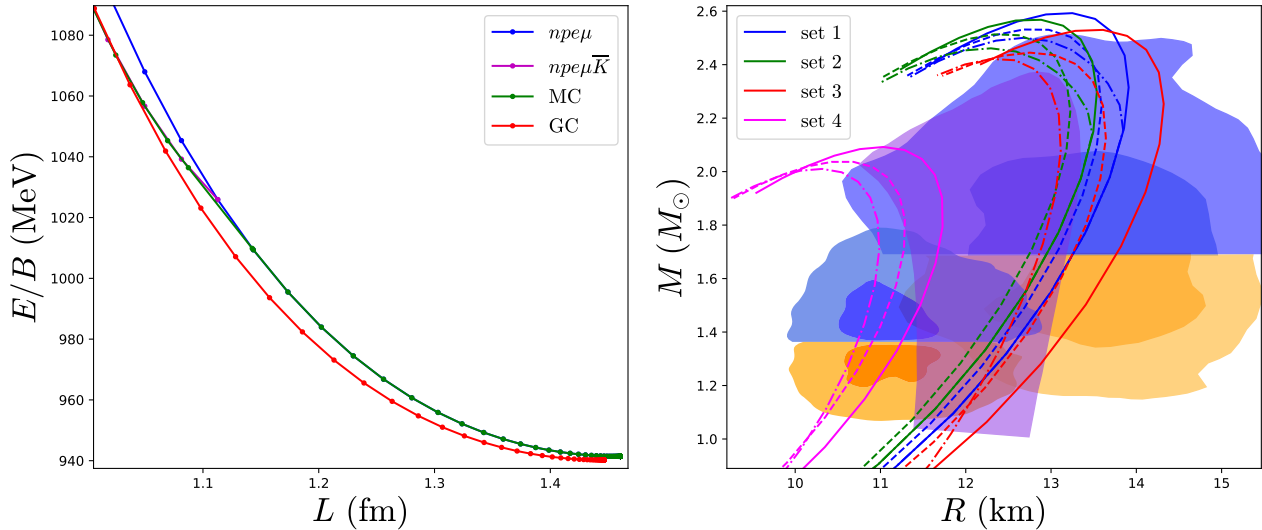


Figure 4.10: *Left:* $E(L)$ curves for the two phases and the two different constructions, for set 1 of the parameter values. *Right:* MR curves of NS with a kaon condensed core. The different sets of parameters that we consider are shown with different colors. Solid lines represent $npe\mu$ matter, dashed-dotted lines are obtained with a MC and the dashed with the GC.

$n_B \geq n_0$. As a consequence, NS based on Skyrme crystals have $n_B = n_0$ at the NS surface or, in other words, Skyrme crystal NS have no low-density region (outer core and crust).

It is possible to add a low-density region to the NS by joining the GC equations of state of the Skyrme crystal with a standard nuclear physics EOS for low densities as we explained in the second chapter of this thesis. This computation is performed in [21] using the same smooth interpolation between our kaon condensed Skyrme crystal EOS and the BCPM [208] EOS, with the value of p_* as the point where both EOS cut. In terms of the baryon density, the joining occurs at $n_B^* \sim 1.1n_0$ for the parameter sets 1-3, and for $n_B^* \sim 1.2n_0$ for the set 4. Nevertheless, we do not show the results from this effective construction since the goal of this section was the correct description of the high density regime in the EOS, which is the region affected by the presence of kaons.

4.3 The inclusion of ρ mesons in the Skyrme model

Throughout this chapter we have improved the description of matter inside NS by introducing new particle species in a consistent fashion entirely within the Skyrme model. However, even more particles are expected to be important in nuclear interactions and specially inside NS. Specifically, the inclusion of other

higher-mass mesons to mediate the interactions between nucleons is crucial in many theoretical approaches for nuclear matter. Indeed, it was argued by Witten that the deviations in the nuclear observables computed from the Skyrme model may be due to an incomplete theory of mesons.

Many extensions of the Skyrme model with vector mesons were proposed to improve the results of the solutions [26, 27, 161, 163]. Specifically, the inclusion of ρ mesons as an additional field with a particular interaction term with the pions in the Skyrme model was first proposed by Adkins in [26]. This is, indeed, the most natural choice since these are the next lightest mesons ($m_\rho = 775$ MeV) after the pions, however, the results obtained in this work were not so promising.

The inclusion of vector mesons in the Skyrme model gained substantial interest again from a BPS theory of skyrmions coupled to vector mesons proposed by Sutcliffe in [218]. Although this theory is obtained in the holographic approach it definitely suggested that the binding energies problem in the Skyrme model might be solved by the inclusion of vector mesons, besides, the interactions terms and coupling constants are naturally fixed by the theory. Indeed, even the inclusion of just the ρ mesons yielded remarkable results in the binding energies [219].

Later, the full numerical minimization of the solutions carried out by Naya and Sutcliffe [169] confirmed the improvement on the binding energies for the first $B = 1 - 8$ skyrmions. Moreover, the ρ mesons also influence the shapes of the minimal energy configurations, inducing a clustered structure which is closer to physical nuclei. This effect is actually observed even for the very small baryon number skyrmions $B \geq 5$.

In this final section we want to study, for the first time, the impact of the ρ mesons on the Skyrme α -lattice solution, to show the physical implications that they have on the other main longstanding problem in the Skyrme model, the compression modulus.

4.3.1 The compression modulus problem

The energy curve $E(n_B)$ of symmetric nuclear matter in (4.20) is also expanded in power series of the baryon density,

$$E(n_B) = E_0 + \frac{1}{2}K_0 \frac{(n_B - n_0)^2}{9n_0^2} + \mathcal{O}(n_B^3), \quad (4.84)$$

equivalently to the symmetry energy curve (4.21).

The first multipole in this expansion is the energy per baryon E_0 of symmetric nuclear matter at the saturation density. There is no linear term since symmetric nuclear matter reaches a minimum of the energy at saturation. The next multipole, K_0 is known as the compression modulus, it enters at second order in the energy curve, and it is directly related to the compressibility of nuclear matter, hence it determines the softness of the EOS near the minimum.

The compression modulus is not directly measured, but it may be extracted from the Isoscalar Giant Monopole Resonance (ISGMR) [97, 114, 239] frequency, ω_M . This resonance is a collective excitation of the nucleus, in which both protons and neutrons vibrate spherically in phase. It is measured through the low-momentum transfer in inelastic scattering collisions between isoscalar particles (like α particles or deuterons) and medium-heavy nuclei, $B \geq 90$. The frequency of this resonance for a given nucleus may be related to its compression modulus K [67],

$$\omega_M^2 = \frac{K}{m_N R^2}, \quad (4.85)$$

where R is the radius of the nucleus and m_N is the mass of the nucleon. The value of this frequency was experimentally determined for different nuclei, such that the following dependence on the baryon number was found,

$$\hbar\omega_M \sim 80B^{-1/3} \text{ MeV}. \quad (4.86)$$

Then, from the well-known relation between the radius of a nucleus and its baryon number, $R \approx 1.25B^{1/3}$ fm, we find the B -independent value for the

compression modulus,

$$K = K_0 \sim 240 \pm 20 \text{ MeV}. \quad (4.87)$$

Further numerical simulations from theoretical approaches yield a range of values for K which confirmed this value [52]. Nevertheless, given that we usually work in Skyrme units, we have the freedom to fit the energy at saturation, so it is more informative for us to consider the adimensional ratio, $\frac{K_0}{E_0} \sim 0.25$.

It is possible to compute the compression modulus from Skyrme crystals using the definition from the Taylor expansion (4.84),

$$K_0 = 9n_0^2 \frac{\partial^2 E}{\partial n_B^2} \Big|_{n_0} \equiv 9V^2 \frac{\partial^2 E}{\partial V^2} \Big|_{L_0}. \quad (4.88)$$

The last derivation of the compression modulus in terms of the unit cell volume (or equivalently, the lattice length L) is equivalent, given that L_0 is defined as the point at which the energy is minimal.

The numerical values are given in Table 4.6 for the crystals obtained in Chapter 3. Although we have fitted the parameters to reproduce the saturation point, the compression modulus is much larger than the experimental value. This is also a well-known problem in the Skyrme model, which seems to yield too stiff energy curves. This might be a problem of the specific solutions considered here, however, a simple derivation of the compression modulus, again under the perfect scaling approximation, is much more clarifying and shows that the ratio K_0/E_0 is quite far from the desired value.

Model	λ^2 (MeV fm ³)	K_0 (MeV)
\mathcal{L}_{24}	0	882
\mathcal{L}_{240}	0	1340
\mathcal{L}_{246}	3	1321
\mathcal{L}_{246}	7	1831
\mathcal{L}_{2460}	3	1794
\mathcal{L}_{2460}	7	2333

Table 4.6: Values for the compression modulus for the crystals studied in Chapter 3.

The energy of Skyrme crystals has been shown to follow with great accuracy,

at least around the minimum, the PS approximation (3.12). Under a Derrick scaling transformation of the Skyrme field at the minimal energy configuration $U(L_0) \rightarrow U(\Lambda L_0)$, the PS parametrization yields,

$$E(\Lambda) = \frac{E^{(2)}}{\Lambda} + \Lambda E^{(4)} + \Lambda^3 E^{(6)} + \frac{E^{(0)}}{\Lambda^3}. \quad (4.89)$$

Then, the compression modulus may be related to the second derivative of the energy with respect to the Derrick factor Λ ,

$$\begin{aligned} E(1) &= E_0, \quad E'(1) = 0, \quad E''(1) = E_0 + 8 \left(E^{(6)} + E^{(0)} \right) \\ K_0 &= 9V^2 \left. \frac{\partial^2 E}{\partial V^2} \right|_{L_0} = L_0^2 \left. \frac{\partial^2 E}{\partial L^2} \right|_{L_0} \xrightarrow{L=\Lambda L_0} E''(1). \end{aligned}$$

This result explains why we find $K_0/E_0 = 1$ in the standard massless Skyrme model, and the inclusion of further terms increases even more this ratio. Nevertheless, this argument is based on the PS approximated energy curve, which is expected to fail for very high values of c_6 and c_0 , for which we would recover the BPS model. In this model, the compression modulus is exactly zero for a wide variety of potential terms [9], hence a near-BPS model may be a solution for the compression modulus problem. However, the values of the parameters c_6 and c_0 to reach the BPS model must be extremely large, so that numerical computations become difficult in this regime.

We propose in this section to include the next lightest mesons in the model, motivated from previous studies, in order to find crystalline solutions with realistic values of K_0/E_0 .

4.3.2 Skyrme α -lattice coupled to ρ mesons

The inclusion of ρ mesons in the Skyrme model requires the extension of the Lagrangian with the standard kinetic and mass terms for a vector field,

$$\mathcal{L}_\rho = -\frac{1}{8} \text{Tr}\{R_{\mu\nu}^\dagger R^{\mu\nu}\} + \frac{m_\rho^2}{4} \text{Tr}\{R_\mu^\dagger R^\mu\}, \quad (4.90)$$

where $R^\mu = \rho_0^\mu \mathbb{I}_2 + i\rho_a^\mu \tau_a$ is the $SU(2)$ representation of the ρ mesons, but it is not an element of the group, and $R_{\mu\nu} = \partial_\mu R_\nu - \partial_\nu R_\mu$ is the corresponding field strength tensor.

The theory is completed with the coupling between pions and ρ mesons through the following interaction term,

$$\mathcal{L}_I = \frac{\alpha}{2} \text{Tr}\{R_{\mu\nu}[L^\mu, L^\nu]\} = \alpha \text{Tr}\{\partial_\mu R^\nu[L^\mu, L_\nu]\}. \quad (4.91)$$

We propose this interaction term which differs from the one proposed by Adkins in [26], since it leads to much simpler computations, specially out of spherical symmetry. The motivation for the interaction term considered by Adkins is to reproduce the $\rho \rightarrow \pi\pi$ decay which does not produce a quartic term \mathcal{L}_4 after integrating out the ρ mesons from the theory. We do not find the last restriction mandatory, so we may consider a different interaction term which also yields the same decay reaction. Besides, the interaction term (4.91) always decouples the ρ_0^μ field from the system, since R^μ is coupled to a $\mathfrak{su}(2)$ element. This property only occurs in the spherically symmetric case for the Adkins term, then a further constraint must be imposed to erase the unphysical component of the ρ mesons. In addition to these motivations for using this interaction term, the proposal arose from other studies that included vector mesons in chiral perturbation theory, in which this term is used [126].

Furthermore, a BPS bound may be defined in the full Skyrme – ρ theory if this specific coupling is considered. As we did in (2.16), we must express the energy as a combination of positive definite terms. We first write down the static energy functional,

$$E = E_{\text{Skyrme}} + \int d^3x \left[\frac{1}{8} \text{Tr}\{|R_{ij}|^2\} + \frac{m_\rho^2}{4} \text{Tr}\{|R_i|^2\} - \frac{\alpha}{2} \text{Tr}\{R_{ij}[L_i, L_j]\} \right]. \quad (4.92)$$

The kinetic and mass terms are always positive definite, but for the interaction term we must realize that it may be used to complete the perfect square between the kinetic energy of the ρ mesons and a quartic Skyrme term with a new

different coupling constant.

$$\begin{aligned} \text{Tr} \left\{ \left(\frac{1}{\sqrt{8}} R_{ij} + \frac{\alpha}{\sqrt{2}} [L_i, L_j] \right) \left(\frac{1}{\sqrt{8}} R_{ij} + \frac{\alpha}{\sqrt{2}} [L_i, L_j] \right)^\dagger \right\} = \\ \text{Tr} \left\{ \frac{1}{8} |R_{ij}|^2 + \frac{\alpha}{4} \left(R_{ij} [L_j, L_i] + R_{ij}^\dagger [L_i, L_j] \right) + \frac{\alpha^2}{2} |[L_i, L_j]|^2 \right\} = \\ \text{Tr} \left\{ \frac{1}{8} |R_{ij}|^2 - \frac{\alpha}{2} R_{ij} [L_i, L_j] + \frac{\alpha^2}{2} |[L_i, L_j]|^2 \right\}. \end{aligned} \quad (4.93)$$

Then, the energy of the ρ mesons plus the interaction term yield positive terms and a remaining quartic Skyrme term, which may be absorbed into the Skyrme energy part. Then, in the \mathcal{L}_{24} model, we recover the same BPS bound (2.16), but with a redefined Skyrme parameter,

$$E \geq \frac{3\pi^2 f_\pi}{\bar{e}} |B|, \quad (4.94)$$

$$\bar{e}^2 = \frac{e^2}{1 - 16\alpha^2 e^2}. \quad (4.95)$$

From this result, it is clear that larger values of the coupling constant α increase the Skyrme parameter, which reduces the importance of the quartic term. Indeed there is a limiting value for which the Skyrme term completely vanishes,

$$\bar{e}^2 \geq 0 \longrightarrow c_\alpha := \alpha e \leq \frac{1}{4}. \quad (4.96)$$

This feature has great importance since the energy curve of Skyrme crystals increase for $L < L_0$ due to the quartic term in the \mathcal{L}_{24} and \mathcal{L}_{240} models. How fast the energy increases depends on the importance of \mathcal{L}_4 with respect to the other terms, and we have seen from the too high values of K_0 that the curve must be flattened near the minimum. Therefore, the α coupling constant may be tuned to yield a smaller quartic term and to obtain better values for the compression modulus.

Then, we compute the static energy functional in Skyrme units,

$$E = E_{\text{Skyrme}} + \frac{1}{24\pi^2} \int d^3x \left[4 \left((\partial_i \rho_a^j)^2 - \partial_i \rho_a^j \partial_j \rho_a^i \right) + 2c_0^\rho (\rho_a^i)^2 + 32\alpha e \partial_i \rho_a^j S_{ij}^a \right]. \quad (4.97)$$

where we have defined the adimensional field, $R^\mu \rightarrow \frac{R^\mu}{f_\pi}$ and its adimensional mass constant $c_0^\rho = \frac{2m_\rho^2}{f_\pi^2 e^2}$. The ρ_0^i fields have been erased since they are not coupled to the pions, so that they only contribute positively to the energy, hence, the minimal static energy solution is trivially $\rho_0^i = 0$. At this point, we see that the constant of interest is the adimensional coupling constant c_α , which cannot be larger than 1/4, otherwise the Skyrme term vanishes and we do not have stable skyrmions anymore.

We have also defined the $S_{\mu\nu}$ tensor in the interaction term,

$$[L_\mu, L_\nu] = -2i(\partial_\mu \sigma \partial_\nu \pi_c - \partial_\nu \sigma \partial_\mu \pi_c + \epsilon_{abc} \partial_\mu \pi_a \partial_\nu \pi_b) \tau_c = -2i S_{\mu\nu}^c \tau_c. \quad (4.98)$$

The field equations for the ρ mesons and their contribution to the Skyrme part are obtained. Then, the minimal energy configuration of the α -lattice coupled to ρ mesons is computed for different values of L using the AGD algorithm.

We will consider the \mathcal{L}_{240} model since the gradient flow method is quite sensitive to the sextic term for small values of L and, given that the quartic term is reduced by the ρ mesons, it becomes numerically difficult to converge into the solution. The results for energy curve are shown in Fig. 4.11. In the left plot we show the adimensional total energy of the system against the lattice length, for different values of the coupling constant c_α . In this plot we see that the minimal energy configuration (E_{\min}, L_{\min}) shifts towards smaller values of the unit cell when the coupling is increased. The reason is that the quartic is a repulsive term, hence, smaller energy configurations are preferred if this term is reduced. Besides, the quartic term prevents the collapse of the skyrmion, therefore, in the limit $c_\alpha \rightarrow 1/4$ the minimum is shifted towards the point $(E = 0, L = 0)$. Indeed, since the skyrmion becomes unstable in this limit, an accurate convergence in the numerical computations is harder to achieve.

Furthermore, the numerical difficulty to compute the solutions with high coupling constant values may be also attributed to the different scales developed

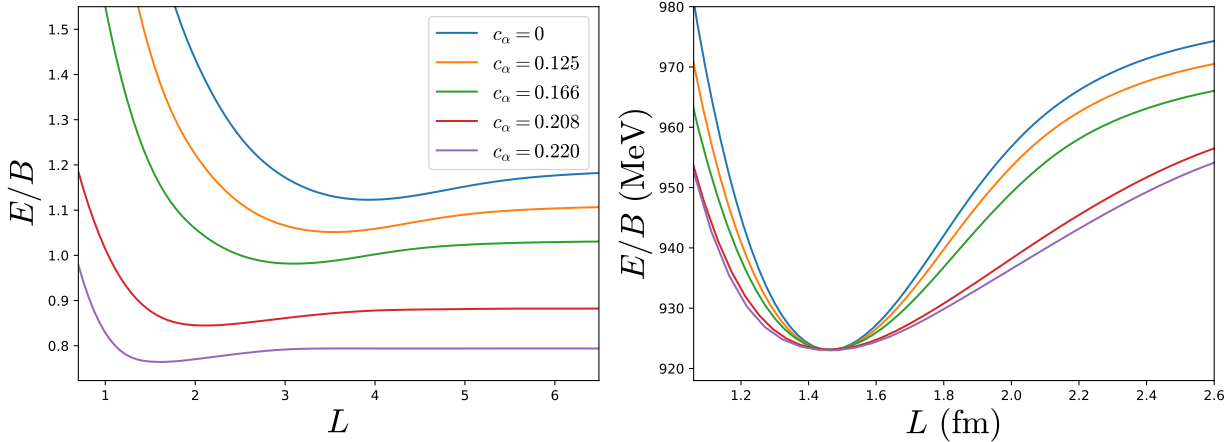


Figure 4.11: *Left:* Adimensional energy of the α -lattice for different values of the coupling with the ρ mesons. *Right:* The same curves when the minimum of each curve is fitted to the nuclear saturation point.

between the mesons. For increasing α , the ρ mesons accumulate in the centre of the box whilst the skyrmions remains practically unchanged in size. Therefore, a really accurate grid is needed to compute the small-size contributions from the ρ mesons, but it must be sufficiently large to contain the whole skyrmion.

In order to see the decrease in the K_0/E_0 ratio due to the increasing presence of the ρ mesons, we show in the right plot of Fig. 4.11 the same $E(L)$ curves but now in physical units. All the minima from each curve have been manually shifted to the saturation point (E_0, n_0) , so that the curvature around the minimum may be easily compared. In this plot we clearly see the decrease of the second derivative of the energy, the numerical values for the ratio K_0/E_0 are given in Table 4.7.

Additionally, we may also observe from the same plot that the binding energies, defined as the difference between the asymptotic energy and the minimum, also become smaller. Indeed, as we mentioned before, it was shown in [218] that the Skyrme model coupled to an infinite tower of vector mesons yields a BPS theory, implying that the binding energies are exactly zero. Although the BPS theory is only achieved with an infinite number of mesons, even the truncation to the first order, which are the ρ mesons, significantly enhances the binding energies [169]. Actually, the binding energies that we are considering here are not exactly those of the isolated nuclei, however, in the Skyrme model context, the minimum of the Skyrme crystal may be seen as the energy of the $B = \infty$ skyrmion, which is the lowest. Therefore, if the difference between the $B = 4$

skyrmion and the crystal decreases, the rest of the finite B isolated skyrmion binding energies will, by definition, decrease as well.

The specific values of the binding energies in our computations are given in Table 4.7, from where we confirm that the ρ mesons decrease this difference. This is also a great feature of this combined theory, since a sufficient reduction of this binding energy will allow the development of a crust for Skyrme NS. In addition, smaller values of this binding energy will also improve the surface term coefficient a_S obtained from the Skyrme lattices.

c_α	K_0/E_0	K_0 (MeV)	BE (%)	α
0	1.170	1080	5.54	0
0.125	0.985	909	5.36	0.031
0.166	0.778	718	5.00	0.046
0.208	0.461	425	4.25	0.075
0.220	0.381	351	3.85	0.095

Table 4.7: Values of the adimensional coupling constant between ρ mesons and pions with the corresponding values of the compression modulus and energy ratio. In the third column we show the value of the compression modulus once the minimum has been shifted to the saturation point. In the last two columns we compute the difference between the minimum and the $L \rightarrow \infty$ asymptotic energy and the corresponding value of the physical coupling constant, respectively.

As mentioned before we may extract from (4.91) the interaction vertex which describes the ρ meson decay into two pions. Then, it is possible to obtain the decay width, Γ_ρ in terms of α via standard QFT, and compute the physical value of the coupling from the experimental value of Γ_ρ . The derivation is quite straightforward and requires the field equation of the ρ field. The interaction vertex obtained is,

$$\mathcal{L}_{\text{vertex}} = 2\alpha m_\rho^2 \epsilon_{abc} \rho_c^\nu \pi_a \partial_\nu \pi_b. \quad (4.99)$$

Hence, from the most fiducial value of the decay width, $\Gamma_\rho = 147.4$ MeV, and the physical pion decay constant $f_\pi = 186$ MeV we obtain,

$$\alpha_{\text{exp.}} = 0.0427. \quad (4.100)$$

This value is smaller than those considered here in order to obtain a reasonable value of the ratio K_0/E_0 . However, we have only considered one physically

motivated interaction term between pion and ρ mesons, but we know that this is not the only possibility. In fact, we may find in the Lagrangian obtained from the holographic approach [219] an extensive list of the interaction terms which may be considered order by order in the ρ mesons. Hence, it may be argued that the inclusion of further terms will definitely contribute to the improvement of the compression modulus value, then, the value of α will approach the physical coupling constant. In this sense, we have shown the results at the first order, although there is an additional interaction term of the same order, besides, it may be identified with the $\rho \rightarrow 3\pi$ decay, although this process is highly suppressed.

As a final comment, the computation of NS is not performed in this section given that the absence of the sextic term will not produce maximal masses according to the experimental requirements. Furthermore, the inclusion of ρ mesons softens the EOS, which decrease even more the maximal masses. The inclusion of the sextic term will contend this effect, moreover, it allows to increase the value of c_α to reach the physical value of the compression modulus since the skyrmions will always remain stable. However, larger values of the ρ mesons coupling constant will require more presence of the sextic term, which may complicate the numerical computations using the AGD method.

Chapter 5

Conclusions and Outlook

Country roads, take me home. To the place I belong.

John Denver

The research work carried out throughout this thesis combines our most recent understanding about NS with the theoretical framework provided by the Skyrme model to develop an alternative description of ultra-dense nuclear matter. We conclude with some final remarks, including the best achievements and open problems, and further ideas to improve the results obtained.

The main conclusion that may be extracted is that the sextic term is necessary in the Skyrme model for a correct description of the high density regime in the EOS. This term does not only produce sufficiently high masses, but also induces interesting phenomenology, like the homogeneous fluid-like behaviour, which is expected in the internal regions of NS. Furthermore, when this term is combined with the standard Skyrme model, the properties of symmetric INM may be reproduced and the resulting NS are significantly improved in the sense that the MR curves get closer to the experimentally constrained region. However, we observe that the radii are slightly larger (between 1 – 2 km) than the expected values, which suggests a still high stiffness in the EOS obtained from the Skyrme crystals.

The quantization of the crystals enabled the computation, for the first time, of the symmetry energy curve within the Skyrme model. In fact, this curve may be accurately fitted in the whole range of densities and yields realistic particle fractions inside the NS. Besides, the contribution of these effects induces an interesting asymptotic decay in the energy curve in the zero density limit, which

may be crucial for the construction of a crust. The masses of the NS are hardly affected by this contribution and the radii increase in the whole MR curve, but less than some hundred meters. Therefore, the introduction of isospin-asymmetry effects yields a great improvement in the phenomenology of dense nuclear matter.

Additionally, the computation of the energy, baryon density and symmetry energy of INM at saturation opens the possibility to completely determine the free parameters in the generalized Skyrme model. Following this idea, we performed an extensive analysis on the nuclear observables mentioned before and the MR curves of the resulting NS in the pure neutron-matter case. In conclusion, we find difficulties in the simultaneous fit of the three observables with arbitrary accuracy, but we were able to establish upper and lower bounds for the sextic term coupling constant from the nuclear and NS observables respectively. Interestingly, even though the parameters are fixed by the nuclear saturation point, we still find a wide range of maximal masses for the NS between 2 and 2.5 solar masses. This is, indeed, a remarkable property of the Skyrme model, which may bring severe problems to other nuclear models if a sufficiently high mass NS is observed.

The Skyrme model also provides a natural extension to consider strange degrees of freedom. In particular, the kaon condensation is predicted at acceptable densities and it mainly reduces both the mass and radius of the NS, as expected. This effect has great implications since it shifts the MR curve closer to the experimental constraints. The condensation density is mainly affected by the symmetry energy, unfortunately, we find better values when the values at saturation are smaller than the experimental measurements.

Finally, motivated by the previous computations of isolated skyrmions including ρ mesons, we considered an interaction term between pions and ρ mesons in the lattice of α particles. This coupling is well motivated and it directly affects the two main problems found in the Skyrme model, *i.e.*, the compression modulus and the binding energies. Although our computations are just the first steps to approach this problem, the impressive results encourage the further development on the inclusion of vector mesons to achieve our final goal, the complete description of nuclear matter for all densities.

The main open problem which is present in many of the computations performed in this work is the absence of a crust in the low density regime of the EOS. Although this issue is localized in the zero pressure limit, it affects the radius in the whole MR curve. The addition of a crust by hand, as we did in Chapter 2, typically enlarges the radii in 1 km, which is not a desirable effect. However, this may not be the final answer since we do not actually know how a crust purely constructed from the Skyrme model would affect the radius of the NS. As explained in the text, this problem may be traced back to the high binding energies of isolated skyrmions, hence, any progress on the binding energies problem will favour the development of a crust. Nevertheless, as we have seen in the Introduction, the outer layers of NS are rather complicated systems in which different contributions are involved, therefore, the realistic description of the low density regime requires the inclusion of further effects.

Specifically, the Coulomb interaction is expected to have a significant impact at low densities, indeed, it is crucial for the shape of the nuclear pasta phases. This contribution may also be considered within the Skyrme model once the charge density is computed from the Gell-Mann–Nishijima formula [148]. The electrostatic contribution is usually added to the energy as a correction, however, in order to obtain the nuclear pasta shapes, the backreaction on the classical configuration must be taken into account.

Furthermore, the perturbative $SU(3)$ extension of the Skyrme model considered to compute the kaon condensation allows to obtain hyperon solutions as well [73]. Indeed, hyperons are expected to be produced even before the kaon condensation, but they would induce the same effect on the NS, so this is another source of improvement in the large values of the radii. Therefore, it is of great interest to compute the effects of hyperons in Skyrme crystals to study the impact on the particle fractions, on the NS and on the kaon condensation density, where the strange matter is completely determined by the Bound-State approach.

As a further suggestion, the inclusion of the sextic term in the Skyrme lattice coupled to ρ mesons is the most natural extension of this work. The NS masses will definitely grow if this term is added, but the compression modulus will deviate from the experimental value. Nevertheless, additional interaction terms

between pions and ρ mesons may compete with this deviation. Isospin quantum corrections may be also considered in the full Skyrme– ρ mesons system, but the time-dependence will excite the ρ_a^0 fields, implying a further minimization after the classical configuration has been obtained.

Additionally, all these computations may be reproduced in a new crystalline configuration recently proposed from the combined minimization of the Skyrme field and the geometry of space [116]. We want to remark this work since this configuration has the smallest asymptotic energy at the zero density limit and, therefore, it corresponds to the actual ground state of the Skyrme model in this regime.

We hope to have illustrated the importance on the physics of ultra-dense nuclear matter and NS with this thesis, and we motivate the reader to develop the computations here exposed to achieve a complete and realistic description of the nuclear matter in the whole range of densities based on the Skyrme model.

Appendix A

$B = 1$ skyrmion from Spectral Methods

Spectral methods were originally introduced in the context of numerical hydrodynamics, however, they were extensively developed in order to solve the highly non-linear Einstein equations within the Numerical Relativity framework. The main difference with respect to finite differences numerical methods is that spectral methods obtain a numerical approximation to the desired solution globally, rather than using local low degree approximations. This produces, in many cases, significantly better accuracies with moderate computational resources. In general, they can be used to solve any system of time-independent PDE, like in our case of interest, the Skyrme field equations. This appendix is not intended to be a rigorous mathematical and general presentation of spectral methods, but a practical and clarifying example. Specifically, we show the resolution of the $B = 1$ skyrmion using this numerical technique.

The main idea in which spectral methods are based is that any function $f(x)$ can be approximately interpolated by truncated series of a set of N_c orthogonal polynomials,

$$f(x) \approx \sum_{i=0}^{N_c-1} f_i T_i(x), \quad (\text{A.1})$$

where the coefficients f_i are the projection of the function f on each polynomial T_i .

In this case, the system of differential equations is converted into a system of algebraic equations in which the unknowns are the coefficients of the expan-

sion. This is due to the fact that we know how different operators act on the polynomials, T_i .

The two most frequent choices of polynomials are the Chebyshev and Legendre sets. Legendre polynomials are commonly used to expand the angular dependent part of the functions in some PDEs with axial symmetry. Since the angular variables will not enter in our specific problem we will focus on the Chebyshev polynomials, but the extension to other sets of polynomials is rather straightforward.

Then, we fix $\{T_i\}$ to be the set of Chebyshev polynomials, which are defined on a grid $x \in [-1, 1]$. We compute the coefficients f_i numerically on a discrete space grid via weighted Gaussian quadratures, which are a fast and accurate way to solve integrals,

$$f_i = \frac{\int_{-1}^1 \frac{dx}{\sqrt{1-x^2}} f(x) T_i(x)}{\int_{-1}^1 \frac{dx}{\sqrt{1-x^2}} T_i(x) T_i(x)} \approx \frac{\sum_{j=0}^{N_c-1} f(x_j) T_i(x_j) w_j}{\sum_{j=0}^{N_c-1} T_i(x_j) T_i(x_j) w_j}, \quad (\text{A.2})$$

where x_j and w_j are the collocation points of the discrete grid and the weights of the Chebyshev-Gauss-Lobatto (CGL) integral, respectively. The collocation points and weights for the Chebyshev polynomials are calculated as follows,

$$x_j = -\cos\left(\frac{j\pi}{N_c-1}\right), \quad w_0 = w_{N_c-1} = \frac{\pi}{2N_c}, \quad w_j = \frac{\pi}{N_c}. \quad (\text{A.3})$$

We denote with j the indices of the grid parameters since the number of points may be completely different to the number of polynomials, listed by i .

Chebyshev polynomials can also be classified by parity on the interval $[-1, 1]$: $T_{2i}(-x) = T_{2i}(x)$, $T_{2i+1}(-x) = -T_{2i+1}(x)$. Then, if we want to interpolate a function $f(x)$ with a definite parity, even or odd, on that interval we may directly use the polynomials with the same parity of $f(x)$.

We construct the polynomials from the recurrence relation, for Chebyshev poly-

nomials we have,

$$T_0(x) = 1, \quad T_1(x) = x, \quad T_i(x) = 2xT_{i-1}(x) - T_{i-2}, \quad (\text{A.4})$$

It is quite useful to define the orthogonality condition by hand, since it is faster than computing the discrete integrals, and an additional source of numerical errors is also erased,

$$\int_{-1}^1 \frac{dx}{\sqrt{1-x^2}} T_i(x) T_j(x) = \delta_{ij} \frac{\pi}{1 + \delta_{i0}}. \quad (\text{A.5})$$

The Skyrme field equation in the hedgehog ansatz reduces to an ODE for the profile function $f(r)$,

$$r^2 f'' + 2rf' - \sin(2f) + 8\sin^2(f)f'' + 4\sin(2f)(f')^2 - 4\sin^2 f \frac{\sin(2f)}{r} = 0. \quad (\text{A.6})$$

Given that the profile function extends up to infinity, the divergence of the radial coordinate requires a special treatment of the equation. To solve this issue, the space must be split in two different domains, $\mathcal{D}_1 : r_1 \in [0, r_c]$, and $\mathcal{D}_2 : r_2 \in [r_c, \infty)$, where r_c is a free choice. The number of coefficients $N_c^{\mathcal{D}_1}$ and $N_c^{\mathcal{D}_2}$ associated to each domain do not necessarily have to be equal.

Since the polynomials are defined on the interval $[-1, 1]$, we change the radial coordinate to an adimensional, well-behaved spatial coordinate for each domain,

$$\mathcal{D}_1 : \quad r_1 = \frac{r_c}{2}(1 + x_1), \quad x_1 \in [-1, 1], \quad (\text{A.7})$$

$$\mathcal{D}_2 : \quad r_2 = \frac{1}{u} = \frac{2r_c}{1 - x_2}, \quad u \in [\frac{1}{r_c}, 0], \quad x_2 \in [-1, 1]. \quad (\text{A.8})$$

As mentioned before, the main advantage of spectral methods is the expansion of the functions in polynomials, since we analytically know how some operators act on the polynomials. We show the three main linear operators that may be

written as linear combinations of the polynomials,

$$\frac{dT_i}{dx} = 2iT_{i-1} + \frac{i}{i-2} \frac{dT_{i-2}}{dx} = \sum_j L_{ij}^d T_j, \quad (\text{A.9})$$

$$xT_i = \frac{1}{2} (T_{i+1} + T_{i-1}) = \sum_j L_{ij}^x T_j, \quad (\text{A.10})$$

$$\frac{1}{x} T_i = 2T_{i-1} - \frac{1}{x} T_{i-2} = \sum_j L_{ij}^{1/x} T_j. \quad (\text{A.11})$$

We denote the linear operators with the superindices d , x and $1/x$ to distinguish them. The size of these operators depend on the number of polynomials considered, but the entries for a few number of coefficients may be found in [106]. Obviously, more complex computations may be obtained from the combinations of these operators, for instance, $\frac{d^2}{dx^2}$ is equivalent to $L_{ij}^{dd} = L_{ik}^d L_{kj}^d$.

Then, the field equation (A.6) is divided into a linear part in f and a source term, written in terms of the new coordinate. In the first domain we have,

$$x_1^2 f'' + 2x_1 f' = s_1, \quad (\text{A.12})$$

$$s_1 = \sin(2f) - 8\sin^2 f - 4\sin(2f)(f')^2 + 4\sin^2(f) \frac{\sin(2f)}{r^2}. \quad (\text{A.13})$$

Note that all the non-linear terms in f are grouped in the source part. The field equations in the second domain becomes,

$$(1-x_2)^2 f'' = s_2, \quad (\text{A.14})$$

$$s_2 = \sin(2f) (1 - 4u^4(f')^2) - 4u^2 \sin^2 f (2u - \sin(2f)) - 4\sin^2 f (2f' + uf''). \quad (\text{A.15})$$

The next step is to obtain the interpolation coefficients of the source term function, $s = \sum_i s_i T_i(x)$. However, the non-linearities of the Skyrme field equation introduces the function f , which is unknown, in the source term, therefore, an initial guess for the profile function is required to compute the coefficients s_i . Regarding the boundary conditions, $f(0) = \pi$ and $f(r \rightarrow \infty) \sim$

r^{-2} , we take the test function,

$$f(r) = \frac{\pi}{1 + r^2} \quad (\text{A.16})$$

Then, the equations are generically written in this simple form, $\sum_{ij} f_i L_{ij} T_j(x) = \sum_i s_i T_i(x)$, where L_{ij} is the total linear operator resulting from the left part of the equations (A.12) and (A.14).

Now, the boundary conditions must be implemented in the problem to ensure that the solution will always satisfy them. In this framework we adopt the tau-method, in which the last rows of the linear operators are used to fix the boundary conditions, given that these are the least relevant. For notational purposes, we use negative indices to refer to the last rows of the operator, so that the index $-1 := N_c - 1$, corresponds to the last row, and $-2 := N_c - 2$ is the previous one. Each condition belongs to a single domain, then, in the first domain we have,

$$f(r = 0) = \pi \rightarrow f^{(\mathcal{D}_1)}(x = -1) = \sum_i f_i^{(\mathcal{D}_1)} T_i(-1) = \sum_i f_i^{(\mathcal{D}_1)} (-1)^i, \quad (\text{A.17})$$

$$L_{-2j}^{(\mathcal{D}_1)} = (-1)^j, \quad s_{-2}^{(\mathcal{D}_1)} = \pi. \quad (\text{A.18})$$

Similarly, for the second domain we obtain,

$$f(r = \infty) = 0 \rightarrow f^{(\mathcal{D}_2)}(x = 1) = \sum_i f_i^{(\mathcal{D}_2)} T_i(1) = \sum_i f_i^{(\mathcal{D}_2)}, \quad (\text{A.19})$$

$$L_{-2j}^{(\mathcal{D}_2)} = 1, \quad s_{-2}^{(\mathcal{D}_2)} = 0. \quad (\text{A.20})$$

Actually, we have not used the last row of the linear operators, but the previous one to impose the boundary conditions. The reason is that we still need to impose continuity on the profile function and its first derivative between both domains. For this purpose, both operators are brought together in a larger square block-diagonal matrix, $L^{(\mathcal{D})}$, in which the matching conditions are im-

posed. The total operator is schematically represented below,

$$L^{(\mathcal{D})} = \left(\begin{array}{c|c} L^{(\mathcal{D}_1)} & 0 \\ \hline 0 & L^{(\mathcal{D}_2)} \end{array} \right)$$

The matching condition $f^{(\mathcal{D}_1)}(x = 1) = f^{(\mathcal{D}_2)}(x = -1)$ is easily imposed in the entire row of the total operator with index $N_c^{(\mathcal{D}_1)} - 1$, whilst the condition on the first derivative requires the corresponding L^d operators, and it is imposed in the last $N_c^{(\mathcal{D}_1)} + N_c^{(\mathcal{D}_2)} - 1$ row. The total linear operator for $N_c^{(\mathcal{D}_1)} = N_c^{(\mathcal{D}_2)} = 5$ is explicitly shown,

$$L^{(\mathcal{D})} = \left(\begin{array}{ccccccccc} 0 & 2 & 10 & 30 & 68 & 0 & 0 & 0 & 0 \\ 0 & 2 & 16 & 54 & 128 & 0 & 0 & 0 & 0 \\ 0 & 0 & 6 & 36 & 104 & 0 & 0 & 0 & 0 \\ 1 & -1 & 1 & -1 & 1 & 0 & 0 & 0 & 0 \\ -1 & -1 & -1 & -1 & -1 & 1 & -1 & 1 & 1 \\ 0 & 0 & 0 & 0 & 0 & 0 & 0 & 6 & -24 \\ 0 & 0 & 0 & 0 & 0 & 0 & 0 & -8 & 42 \\ 0 & 0 & 0 & 0 & 0 & 0 & 0 & 2 & -24 \\ 0 & 0 & 0 & 0 & 0 & 1 & 1 & 1 & 1 \\ 0 & 1 & 4 & 9 & 16 & 0 & -1 & 4 & -9 \\ & & & & & & & & 16 \end{array} \right) \quad (\text{A.21})$$

The final step, the resolution of the problem, consists in the computation of the coefficients f_i such that the residuals $R_i = L_{ij}^{(\mathcal{D})} f_j - s_i$ are nearly zero. This is achieved iteratively using a Newton-Raphson algorithm, starting from the initial seed (A.16).

The Newton-Raphson method proceeds as follows:

$$J_{ij}(f^n) := \frac{\partial R_i(f^n)}{\partial f_j^n} = L_{ij} - \frac{\partial s_i}{\partial f_j^n}, \quad X_i^n = \sum_j J_{ij}^{-1}(f^n) R_j(f^n) \quad (\text{A.22})$$

$$f_i^{n+1} = f_i^n - X_i^n. \quad (\text{A.23})$$

It states that the vector of coefficients $f^n = \{f_i^n\}$, calculated after n iterations,

makes R_i tend to zero, so that we will get closer to the true solution after each iteration.

The Jacobian matrix J_{ij} may be obtained analytically, however, if the source is sufficiently complicated, the numerical calculation of J is a more efficient choice. Using the discrete definition of the derivative we have,

$$J_{ij} \approx \frac{R_i(f^n + \epsilon f_j^n) - R_i(f^n - \epsilon f_j^n)}{2\epsilon}. \quad (\text{A.24})$$

We take the value $\epsilon \sim 1\%$ for a stable convergence of the method.

The profile function solution $f(r)$ in the \mathcal{L}_{24} model may be found in [154] as well as the resulting energy for the $B = 1$ skyrmion.

Appendix B

The TOV formalism

The TOV formalism is the standard procedure to describe stellar equilibrium in GR. It yields a system of ODEs for the spacetime metric functions and the pressure of a perfect fluid which is minimally coupled to gravity. Therefore, it solves the structure of a static, isotropic compact object under gravitational equilibrium. This formalism was developed by Oppenheimer and Volkoff [181] when they obtained and solved the system of differential equations, based on the previous works of Tolman [223] in the analysis of spherically symmetric spacetime metrics.

The starting point is the derivation of the field equations in GR from the EH action [166] in the presence of an energy distribution,

$$S = S_{\text{EH}} + S_{\text{matter}} = \frac{1}{16\pi G} \int d^4x \sqrt{|g|} R + S_{\text{matter}}. \quad (\text{B.1})$$

We will not consider the cosmological constant in this thesis, since it does not have an important impact on NS observables due its tiny value ($\Lambda \sim 10^{-52} \text{ m}^{-2}$) [61, 238].

In the EH action we find the determinant of the metric tensor, $g_{\mu\nu}$, which encodes the whole spacetime information. The Ricci scalar, denoted by R , is the trace of the Ricci curvature tensor, $R = R_{\mu\nu}g^{\mu\nu}$, and the Ricci tensor may be computed from the metric,

$$R_{\mu\nu} = \partial_\lambda \Gamma_{\mu\nu}^\lambda - \partial_\nu \Gamma_{\mu\lambda}^\lambda + \Gamma_{\lambda\rho}^\lambda \Gamma_{\nu\mu}^\rho - \Gamma_{\nu\rho}^\lambda \Gamma_{\lambda\mu}^\rho, \quad (\text{B.2})$$

where $\Gamma_{\mu\nu}^\alpha$ are the Christoffel symbols,

$$\Gamma_{\mu\nu}^\alpha = \frac{1}{2}g^{\alpha\beta}(\partial_\mu g_{\nu\beta} + \partial_\nu g_{\mu\beta} - \partial_\beta g_{\mu\nu}). \quad (\text{B.3})$$

Variations with respect to the metric on the EH action yield a system of field equations for each component of $g_{\mu\nu}$. We have,

$$\delta S_{\text{EH}} = \frac{1}{16\pi G} \int d^4x \left[\delta \sqrt{|g|} R + \sqrt{|g|} \delta R \right]. \quad (\text{B.4})$$

To proceed, the following results are used [53],

$$\delta \sqrt{|g|} = -\frac{1}{2}\sqrt{|g|}g_{\mu\nu}\delta g^{\mu\nu}, \quad (\text{B.5})$$

$$\delta R = R_{\mu\nu}\delta g^{\mu\nu} + \delta R_{\mu\nu}g^{\mu\nu}, \quad (\text{B.6})$$

$$\delta R_{\mu\nu} = \nabla_\lambda \delta \Gamma_{\mu\nu}^\lambda - \nabla_\nu \delta \Gamma_{\mu\lambda}^\lambda, \quad (\text{B.7})$$

where $\nabla_\mu a^\nu = \partial_\mu a^\nu + \Gamma_{\mu\alpha}^\nu a^\alpha$ represents the covariant derivative in a generic spacetime. The variations of the Christoffel symbols become easier to compute by expanding first the relation $\delta(\nabla_\lambda g_{\mu\nu}) = 0$,

$$\delta \Gamma_{\mu\nu}^\rho = \frac{1}{2}g^{\rho\lambda}(\nabla_\mu \delta g_{\nu\lambda} + \nabla_\nu \delta g_{\mu\lambda} - \nabla_\lambda \delta g_{\mu\nu}). \quad (\text{B.8})$$

Then, they are introduced in the last expression to obtain the final result,

$$\begin{aligned} g^{\mu\nu} \delta R_{\mu\nu} &= \nabla_\lambda (g^{\mu\nu} \delta \Gamma_{\mu\nu}^\lambda) - \nabla_\nu (g^{\mu\nu} \delta \Gamma_{\mu\lambda}^\lambda) = \\ &= (\nabla^\mu \nabla^\nu - \nabla^\alpha \nabla_\alpha g^{\mu\nu}) \delta g_{\mu\nu} = -(\nabla_\mu \nabla_\nu - \nabla^\alpha \nabla_\alpha g_{\mu\nu}) \delta g^{\mu\nu}. \end{aligned} \quad (\text{B.9})$$

This final expression exactly vanishes, given that the covariant derivative either applied on a constant or on the metric function is zero. Hence, the result of the variations on the EH action is obtained computing the ratio $\delta S_{\text{EH}}/\delta g^{\mu\nu}$.

Finally, the variational principle on the matter action yields, by definition, the stress-energy tensor $T_{\mu\nu}$. Then, the field equations obtained from the total EH

and matter actions give rise to the so-called Einstein equations,

$$R_{\mu\nu} - \frac{1}{2}g_{\mu\nu}R = 8\pi GT_{\mu\nu}. \quad (\text{B.10})$$

These equations relate the spacetime properties, in the left part, with the matter content which is described by the stress-energy tensor.

In the TOV formalism, the matter inside the star is assumed to be described by a perfect fluid stress-energy tensor,

$$T^{\mu\nu} = (\rho + p)u^\mu u^\nu - pg^{\mu\nu}, \quad (\text{B.11})$$

where u^μ is the four-velocity, which satisfies $g_{\mu\nu}u^\mu u^\nu = 1$ in the mostly minus metric convention.

Additionally, static and spherical symmetry conditions are imposed, then we use the standard spacetime metric parametrization,

$$g_{\mu\nu}dx^\mu dx^\nu = ds^2 = A(r)dt^2 - B(r)dr^2 - r^2d\theta^2 - r^2\sin^2\theta d\phi^2, \quad (\text{B.12})$$

Both the metric and the stress-energy tensor are introduced in the Einstein equations (B.10) and the system of ODEs is obtained from the (t, t) and (r, r) components [100],

$$A' = A \left(8\pi GBrp + \frac{B-1}{r} \right), \quad (\text{B.13})$$

$$B' = B \left(8\pi GBr\rho - \frac{B-1}{r} \right). \quad (\text{B.14})$$

Additional equations to describe how matter is affected by the gravitational field are required. A simple equation for the pressure may be obtained from the r component in the conservation of the stress-energy tensor,

$$\nabla_\mu T_r^\mu = 0 \longrightarrow p' = -\frac{\rho + p}{2} \frac{A'}{A}. \quad (\text{B.15})$$

Conversely, the energy density is fixed by the EOS, which directly relates p and ρ . At this point we may argue that the EOS previously obtained in a

flat spacetime is not the correct choice to solve the TOV equations. However, the equivalence principle ensures that a local Lorentz invariance frame exists in the neighbourhood of any point in spacetime. The metric change factor over a entire NS near the gravitational collapse may be computed, resulting in the tiny value of $\lesssim 10^{-19}$ factor in the metric over the space between nucleons. This negligible correction justifies the so-called bulk approximation to solve the TOV equations using the flat spacetime EOS [100]. Therefore, the system of ODEs is closed and ready to be solved once the correct initial conditions are given.

All the variables are expanded in power series of r up to quadratic order, but the linear order is suppressed by the smoothness condition around the origin,

$$A \sim a_0 + a_1 r^2 + \dots \quad (\text{B.16})$$

$$B \sim b_0 + b_1 r^2 + \dots \quad (\text{B.17})$$

$$p \sim p_c + p_1 r^2 + \dots \quad (\text{B.18})$$

$$\rho \sim \rho_c + \rho_1 r^2 + \dots \quad (\text{B.19})$$

We find from inserting the previous expansions into the equations that $B(0) = 1$, and $A(0)$ is irrelevant in the system. The reason is that A always appears in the combination A'/A , which is zero at $r = 0$, therefore we set $A(0) = 1$. Finally, the pressure at the origin, $p(0) = p_c$, is the input value that fixes the properties of the static spherically symmetric NS.

We use a 4th order Runge-Kutta method, with a constant step of $\Delta r = 10^{-3}$ km, to obtain the solutions for the metric functions and the pressure. The equation (B.15) indicates that the pressure is always a decreasing function inside the star, hence, the integration is stopped when the condition $p(r = R) = 0$ is satisfied, and R is defined as the radius of the star. Although we have used the same notation for the Ricci scalar and the radius of the star, we maintain R from now on to denote the radius since the Ricci scalar is not relevant in the TOV system.

The mass of the star is usually computed from the $B(r)$ function evaluated at the radius of the star. The reason is that for $r \geq R$, there is no star anymore,

so that the Einstein equation reduces to the vacuum field equations, for which the Schwarzschild metric [166] is the only solution. The Schwarzschild solution describes the spacetime surrounding an object with mass M and radius R . Specifically, the (r, r) component of the metric

$$B(r) = \left(1 - \frac{2GM}{r}\right)^{-1}, \quad r \geq R. \quad (\text{B.20})$$

In this way, we may extract the mass of our NS from this solution evaluated at the radius of the star.

Different NS are obtained from the one-parameter family of p_c values, such that the curves $M(p_c)$, $M(R)$ are built. Small values of p_c yield smaller masses, but the radii will strongly depend of the EOS. Specifically, the presence of a crust in the EOS, *i.e.*, the $\rho(p \rightarrow 0) \rightarrow 0$ limit, implies that the small mass region in the $M(R)$ curve develops a tail of increasing radius for decreasing mass. If there is not crust in the EOS, we obtain the opposite behaviour, in which both mass and radius increase together in the whole $M(R)$ curve. This effect is expected to occur in quark matter EOS [81, 185].

Increasing the value of p_c we obtain larger masses until we reach a maximal mass NS. Beyond this maximal mass, the resulting NS are unstable under radial perturbations. There is, indeed a theorem which states that the stability of the NS change if the condition,

$$\frac{dM}{d\rho_c} = 0, \quad (\text{B.21})$$

is attained. See [229] for a proof of this theorem, using a detailed perturbative study on the stability of the solutions under radial perturbation.

Appendix C

Gradient Flow methods in the Skyrme model

,Numerical methods are fundamental in the Skyrme model due to the complexity of the solutions. We saw that already for the simplest $B = 1$ skyrmion, either a shooting or spectral methods must be implemented to obtain the solution. Higher topological charge solutions do not share spherical symmetry, which implies that the angular variables appear in the field equations, therefore the problem is converted into a system of nonlinear PDEs.

A different approach might be considered in order to obtain solutions from the Skyrme model. The solutions in a field theory are actually minimizers of the energy functional. Hence, all the numerical techniques conceived for optimization problems may be applied to solutions in our context.

The gradient flow is a simple, but effective, minimization procedure to find the critical points of a scalar vector-valued function $f(\mathbf{x})$, and it is widely used, for instance, in machine learning algorithms training. It is based on the evolution of the coordinates x_i in the maximally decreasing direction, which is given by the partial derivatives,

$$\dot{x}_i = -\partial_i f(\mathbf{x}), \quad (\text{C.1})$$

starting from an initial seed. Here, x_i are the components of the \mathbf{x} vector.

The discrete version of the gradient flow is the gradient descent method, which solves the previous differential equation numerically, using the simplest discrete

time evolution, $x_i^{(n+1)} = x_i^{(n)} - \epsilon \partial_i f(\mathbf{x}^{(n)})$. The convergence rate of this method mainly depends on the value of $\partial_i f$, then, despite it is an effective method, it is not the most efficient choice to minimize a function given that the convergence soon slows down. The parameter ϵ is the time step in the gradient descent evolution, it is called learn rate in the machine learning context. Large values of the learn rate slightly speed up the minimization, but if the value is too high, the time evolution might diverge, hence, small values are usually taken for a stable convergence.

In 1983, Yuri Nesterov applied the concept of acceleration in convex optimization to find the optimal minimization algorithm. The accelerated gradient descent (AGD) [173, 226] was proposed as the optimal first-order (*i.e.*, only based on the gradient ∇f) minimization algorithm in convex optimization [174] when an upper bound for the velocity in the optimization was found. This method requires the introduction of an auxiliary variable y_i , it is explicitly implemented below,

$$x_i^{(n+1)} = y_i^{(n)} - \epsilon \partial_i f(\mathbf{y}^{(n)}), \quad (\text{C.2})$$

$$y_i^{(n)} = x_i^{(n)} + \frac{n}{n+3} \left(x_i^{(n-1)} - x_i^{(n-2)} \right). \quad (\text{C.3})$$

Note that the AGD is not a relaxation sequence in the sense that the next iteration is always better than the previous one, but it converges in a faster rate, therefore, we must be careful when the algorithm evolves into a worse iteration.

The AGD method is implemented in order to find solutions from the Skyrme model with $B \geq 1$. However, solutions are minimal energy configurations of the energy functional, which are infinitely extended in the three dimensional space. Then, the AGD algorithm must be applied on a functional, where the fields must be varied in the maximal decreasing energy direction. In this case, the gradient of the function $f(\mathbf{x})$ is substituted by the variations of the fields ϕ_a on the energy functional $E[\boldsymbol{\phi}, \partial\boldsymbol{\phi}]$,

$$\phi_a^{(n+1)} = \psi_a^{(n)} - \epsilon \frac{\delta E [\boldsymbol{\phi}, \partial\boldsymbol{\phi}]}{\delta \phi_a} \Big|_{\boldsymbol{\phi}^{(n)}}, \quad (\text{C.4})$$

where ψ_a is the auxiliar field in the AGD algorithm, which is updated equivalently to (C.3).

The starting point for the implementation of the AGD is the Skyrme model energy functional $E = \int d^3x \mathcal{E}$. We expand the integrand, and express the result in terms of the chiral vector $n_A = (\sigma, \pi_a)$,

$$\begin{aligned} \mathcal{E} = \frac{1}{24\pi^2} & \left[(\partial_i n_A)^2 + (\partial_i n_A \partial_j n_B - \partial_i n_B \partial_j n_A)^2 + \right. \\ & \left. + c_6 (\epsilon_{ABCD} n_A \partial_1 n_B \partial_2 n_C \partial_3 n_D)^2 + c_0 (1 - \sigma) \right], \end{aligned} \quad (\text{C.5})$$

where $A = 0, 1, 2, 3$. Computations are carried out much faster with the vector field n_A notation since the Lagrangian, except for the potential term, is chiral invariant. Therefore, the four fields are treated equivalently in almost all the mathematical and numerical computations, we identify $\phi_a := n_A$ in (C.4).

Variations of the energy functional with respect to the fields yields the Euler-Lagrange field equations,

$$\frac{\delta E [\mathbf{n}, \partial \mathbf{n}]}{\delta n_A} = \frac{\partial \mathcal{E}}{\partial n_A} - \partial_i \left(\frac{\partial \mathcal{E}}{\partial (\partial_i n_A)} \right). \quad (\text{C.6})$$

The chiral notation of the energy in terms of n_A becomes even more helpful when it comes to obtain the field equations. The expressions are given below,

$$\frac{\partial \mathcal{E}}{\partial n_E} = 2c_6 B^0 (\epsilon_{elmn} \partial_1 n_l \partial_2 n_m \partial_3 n_n) - c_0 \delta_0^e, \quad (\text{C.7})$$

$$\begin{aligned} \partial_s \left(\frac{\partial \mathcal{E}}{\partial (\partial_s n_E)} \right) = & 2\partial_s^2 n_E + 8 (2\partial_s \partial_i n_A \partial_i n_A \partial_s n_E + (\partial_i n_A)^2 \partial_s^2 n_E - \partial_i \partial_s n_E \partial_i n_A \partial_s n_A \\ & - \partial_i n_E \partial_i \partial_s n_A \partial_i n_A - \partial_s^2 n_A \partial_i n_A \partial_i n_E) + 2c_6 W_s V_s^e - 6c_6 B^0 (\epsilon_{elmn} \partial_1 n_l \partial_2 n_m \partial_3 n_n), \end{aligned} \quad (\text{C.8})$$

where we have defined W_s and V_s^e separately to speed up the numerical com-

putations,

$$W_s = \epsilon_{ABCD} n_A (\partial_s \partial_1 n_B \partial_2 n_C \partial_3 n_D + \partial_s \partial_2 n_C \partial_1 n_B \partial_3 n_D + \partial_s \partial_3 n_D \partial_1 n_B \partial_2 n_C), \quad (C.9)$$

$$V_s^e = \epsilon_{eabc} n_A (-\delta_s^1 \partial_2 n_B \partial_3 n_C + \delta_s^2 \partial_1 n_B \partial_3 n_C - \delta_s^3 \partial_1 n_B \partial_2 n_C). \quad (C.10)$$

Additionally, since the Skyrme field is unitary, this condition must be also imposed in the minimization, then the problem becomes a constrained minimization. For this purpose the energy density is redefined with the following Lagrange multiplier, $\mathcal{E} \rightarrow \mathcal{E} + \lambda(1 - n_A n_A)$. The value for λ may be solved using the equation of motion (C.1) and the unitary condition again,

$$\left. \begin{array}{l} n_A n_A = 1 \rightarrow 2n_A \dot{n}_A = 0 \\ \dot{n}_A = -\frac{\delta E[\mathbf{n}, \partial \mathbf{n}]}{\delta n_A} - 2\lambda n_A \end{array} \right\} \longrightarrow \lambda = -\frac{1}{2} \frac{\delta E[\mathbf{n}, \partial \mathbf{n}]}{\delta n_A} n_A \quad (C.11)$$

The minimization is performed on a finite size box of discrete space with step Δx . The energy and baryon number is computed in each iteration using Riemann sum definition to check the correct convergence of the algorithm. The typical value of the learn rate is $\epsilon \sim 10^{-5}$ for a grid spacing $\Delta x = 0.2$. For a better accuracy in the solution, we may decrease the grid spacing to $\Delta x = 0.1$, then a smaller $\epsilon \sim 10^{-6}$ must be used to ensure the convergence of the algorithm. Moreover, the discretization of the space yields some numerical errors such that the fields do not exactly satisfy unitarity, therefore we impose this condition renormalizing the fields after each iteration, $n_A \rightarrow \frac{n_A}{\sqrt{n_B n_B}}$.

We take the rational map configurations as the initial conditions, with an exponential or power-law decaying profile function $f(r)$, depending on the presence of the pion mass term. Then, the minimization starts and the energy decreases after each iteration, however we might find that the energy increases after some iterations. In this case we set n to zero in (C.4), and the minimization is restarted.

If the minimal energy configuration is obtained, the Derrick scaling argument

states that it must satisfy the so-called virial constraint [155],

$$E'(\sigma_s x) \Big|_{\sigma_s=1} = 0 \longrightarrow E_2 - E_4 - 3E_6 + 3E_0 = 0. \quad (\text{C.12})$$

We consider that the minimization algorithm has successfully converged when the accuracy of the last condition is 10^{-5} .

Bibliography

- [1] B. P. Abbott et al. Gravitational Waves and Gamma-rays from a Binary Neutron Star Merger: GW170817 and GRB 170817A. *Astrophys. J. Lett.*, 848(2):L13, 2017. [arXiv:1710.05834](https://arxiv.org/abs/1710.05834), doi:10.3847/2041-8213/aa920c.
- [2] B. P. Abbott et al. GW170817: Observation of Gravitational Waves from a Binary Neutron Star Inspiral. *Phys. Rev. Lett.*, 119(16):161101, 2017. [arXiv:1710.05832](https://arxiv.org/abs/1710.05832), doi:10.1103/PhysRevLett.119.161101.
- [3] B. P. Abbott et al. Properties of the binary neutron star merger GW170817. *Phys. Rev. X*, 9(1):011001, 2019. [arXiv:1805.11579](https://arxiv.org/abs/1805.11579), doi:10.1103/PhysRevX.9.011001.
- [4] B. P. Abbott et al. GW190425: Observation of a Compact Binary Coalescence with Total Mass $\sim 3.4M_{\odot}$. *Astrophys. J. Lett.*, 892(1):L3, 2020. [arXiv:2001.01761](https://arxiv.org/abs/2001.01761), doi:10.3847/2041-8213/ab75f5.
- [5] R. Abbott et al. GW190814: Gravitational Waves from the Coalescence of a 23 Solar Mass Black Hole with a 2.6 Solar Mass Compact Object. *Astrophys. J. Lett.*, 896(2):L44, 2020. [arXiv:2006.12611](https://arxiv.org/abs/2006.12611), doi:10.3847/2041-8213/ab960f.
- [6] C. Adam, C. D. Fosco, J. M. Queiruga, J. Sanchez-Guillen, and A. Wereszczynski. Symmetries and exact solutions of the BPS Skyrme model. *J. Phys. A*, 46:135401, 2013. [arXiv:1210.7839](https://arxiv.org/abs/1210.7839), doi:10.1088/1751-8113/46/13/135401.
- [7] C. Adam, T. Klähn, C. Naya, J. Sanchez-Guillen, R. Vazquez, and A. Wereszczynski. Baryon chemical potential and in-medium properties of BPS skyrmions. *Phys. Rev. D*, 91(12):125037, 2015. [arXiv:1504.05185](https://arxiv.org/abs/1504.05185), doi:10.1103/PhysRevD.91.125037.
- [8] C. Adam, P. Klimas, J. Sanchez-Guillen, and A. Wereszczynski. Pullback of the Volume Form, Integrable Models in Higher Dimensions and Exotic

- Textures. *J. Math. Phys.*, 50:022301, 2009. arXiv:0810.1943, doi:10.1063/1.3075572.
- [9] C. Adam, C. Naya, J. Sanchez-Guillen, J. M. Speight, and A. Wereszczynski. Thermodynamics of the BPS Skyrme model. *Phys. Rev. D*, 90:045003, 2014. arXiv:1405.2927, doi:10.1103/PhysRevD.90.045003.
- [10] C. Adam, C. Naya, J. Sanchez-Guillen, R. Vazquez, and A. Wereszczynski. BPS Skyrmions as neutron stars. *Phys. Lett. B*, 742:136–142, 2015. arXiv:1407.3799, doi:10.1016/j.physletb.2015.01.027.
- [11] C. Adam, C. Naya, J. Sanchez-Guillen, R. Vazquez, and A. Wereszczynski. Neutron stars in the Bogomol’nyi-Prasad-Sommerfield Skyrme model: Mean-field limit versus full field theory. *Phys. Rev. C*, 92(2):025802, 2015. arXiv:1503.03095, doi:10.1103/PhysRevC.92.025802.
- [12] C. Adam, C. Naya, J. Sanchez-Guillen, R. Vazquez, and A. Wereszczynski. The Skyrme model in the BPS limit. 11 2015. arXiv:1511.05160.
- [13] C. Adam, C. Naya, J. Sanchez-Guillen, and A. Wereszczynski. Bogomol’nyi-Prasad-Sommerfield Skyrme Model and Nuclear Binding Energies. *Phys. Rev. Lett.*, 111(23):232501, 2013. arXiv:1312.2960, doi:10.1103/PhysRevLett.111.232501.
- [14] C. Adam, C. Naya, J. Sanchez-Guillen, and A. Wereszczynski. Nuclear binding energies from a Bogomol’nyi-Prasad-Sommerfield Skyrme model. *Phys. Rev. C*, 88(5):054313, 2013. arXiv:1309.0820, doi:10.1103/PhysRevC.88.054313.
- [15] C. Adam, J. Sanchez-Guillen, R. Vazquez, and A. Wereszczynski. Adding crust to BPS Skyrme neutron stars. *Phys. Rev. D*, 102(2):023019, 2020. arXiv:2004.03610, doi:10.1103/PhysRevD.102.023019.
- [16] C. Adam, J. Sanchez-Guillen, and A. Wereszczynski. A BPS Skyrme model and baryons at large N_c . *Phys. Rev. D*, 82:085015, 2010. arXiv:1007.1567, doi:10.1103/PhysRevD.82.085015.
- [17] C. Adam, J. Sanchez-Guillen, and A. Wereszczynski. A Skyrme-type proposal for baryonic matter. *Phys. Lett. B*, 691:105–110, 2010. arXiv:1001.4544, doi:10.1016/j.physletb.2010.06.025.
- [18] C. Adam and A. Wereszczynski. Topological energy bounds in generalized Skyrme models. *Phys. Rev. D*, 89(6):065010, 2014. arXiv:1311.2939,

- doi:10.1103/PhysRevD.89.065010.
- [19] Christoph Adam, Alberto García Martín-Caro, Miguel Huidobro, Ricardo Vázquez, and Andrzej Wereszczynski. Quasiuniversal relations for generalized Skyrme stars. *Phys. Rev. D*, 103(2):023022, 2021. arXiv: 2011.08573, doi:10.1103/PhysRevD.103.023022.
 - [20] Christoph Adam, Alberto García Martín-Caro, Miguel Huidobro, Ricardo Vázquez, and Andrzej Wereszczynski. Quantum skyrmion crystals and the symmetry energy of dense matter. *Phys. Rev. D*, 106(11):114031, 2022. arXiv:2202.00953, doi:10.1103/PhysRevD.106.114031.
 - [21] Christoph Adam, Alberto García Martín-Caro, Miguel Huidobro, Ricardo Vázquez, and Andrzej Wereszczynski. Kaon condensation in skyrmion matter and compact stars. *Phys. Rev. D*, 107(7):074007, 2023. arXiv: 2212.00385, doi:10.1103/PhysRevD.107.074007.
 - [22] Christoph Adam, Alberto Garcia Martin-Caro, Miguel Huidobro, and Andrzej Wereszczynski. Skyrme Crystals, Nuclear Matter and Compact Stars. *Symmetry*, 15(4):899, 2023. arXiv:2305.06639, doi:10.3390/sym15040899.
 - [23] Christoph Adam, Mareike Haberichter, and Andrzej Wereszczynski. Skyrme models and nuclear matter equation of state. *Phys. Rev. C*, 92(5):055807, 2015. arXiv:1509.04795, doi:10.1103/PhysRevC.92.055807.
 - [24] Christoph Adam, Alberto Garcia Martin-Caro, Miguel Huidobro, Ricardo Vazquez, and Andrzej Wereszczynski. Dense matter equation of state and phase transitions from a generalized Skyrme model. *Phys. Rev. D*, 105(7):074019, 2022. arXiv:2109.13946, doi:10.1103/PhysRevD.105.074019.
 - [25] D. Adhikari et al. Accurate Determination of the Neutron Skin Thickness of ^{208}Pb through Parity-Violation in Electron Scattering. *Phys. Rev. Lett.*, 126(17):172502, 2021. arXiv:2102.10767, doi:10.1103/PhysRevLett.126.172502.
 - [26] Gregory S. Adkins. ρ Mesons in the Skyrme Model. *Phys. Rev. D*, 33:193, 1986. doi:10.1103/PhysRevD.33.193.
 - [27] Gregory S. Adkins and Chiara R. Nappi. Stabilization of Chiral Solitons

- via Vector Mesons. *Phys. Lett. B*, 137:251–256, 1984. doi:10.1016/0370-2693(84)90239-9.
- [28] Gregory S. Adkins and Chiara R. Nappi. The Skyrme Model with Pion Masses. *Nucl. Phys. B*, 233:109–115, 1984. doi:10.1016/0550-3213(84)90172-X.
- [29] Gregory S. Adkins, Chiara R. Nappi, and Edward Witten. Static Properties of Nucleons in the Skyrme Model. *Nucl. Phys. B*, 228:552, 1983. doi:10.1016/0550-3213(83)90559-X.
- [30] Sinan Altiparmak, Christian Ecker, and Luciano Rezzolla. On the Sound Speed in Neutron Stars. *Astrophys. J. Lett.*, 939(2):L34, 2022. arXiv:2203.14974, doi:10.3847/2041-8213/ac9b2a.
- [31] P. W. Anderson and N. Itoh. Pulsar glitches and restlessness as a hard superfluidity phenomenon. *Nature*, 256:25–27, 1975. doi:10.1038/256025a0.
- [32] Eemeli Annala, Tyler Gorda, Aleksi Kurkela, Joonas Nätilä, and Aleksi Vuorinen. Evidence for quark-matter cores in massive neutron stars. *Nature Phys.*, 16(9):907–910, 2020. arXiv:1903.09121, doi:10.1038/s41567-020-0914-9.
- [33] John Antoniadis et al. A Massive Pulsar in a Compact Relativistic Binary. *Science*, 340:6131, 2013. arXiv:1304.6875, doi:10.1126/science.1233232.
- [34] Miguel Aparicio Resco, Álvaro de la Cruz-Dombriz, Felipe J. Llanes Estrada, and Víctor Zapatero Castrillo. On neutron stars in $f(R)$ theories: Small radii, large masses and large energy emitted in a merger. *Phys. Dark Univ.*, 13:147–161, 2016. arXiv:1602.03880, doi:10.1016/j.dark.2016.07.001.
- [35] A. Savas Arapoglu, Cemsinan Deliduman, and K. Yavuz Eksi. Constraints on Perturbative $f(R)$ Gravity via Neutron Stars. *JCAP*, 07:020, 2011. arXiv:1003.3179, doi:10.1088/1475-7516/2011/07/020.
- [36] Artyom V. Astashenok, Salvatore Capozziello, and Sergei D. Odintsov. Nonperturbative models of quark stars in $f(R)$ gravity. *Phys. Lett. B*, 742:160–166, 2015. arXiv:1412.5453, doi:10.1016/j.physletb.2015.01.030.

- [37] Artyom V. Astashenok, Sergei D. Odintsov, and Alvaro de la Cruz-Dombriz. The realistic models of relativistic stars in $f(R) = R + \alpha R^2$ gravity. *Class. Quant. Grav.*, 34(20):205008, 2017. [arXiv:1704.08311](https://arxiv.org/abs/1704.08311), doi:10.1088/1361-6382/aa8971.
- [38] Walter Baade and Fritz Zwicky. On super-novae. *Proceedings of the National Academy of Sciences*, 20(5):254–259, 1934.
- [39] M. Bailes et al. Gravitational-wave physics and astronomy in the 2020s and 2030s. *Nature Rev. Phys.*, 3(5):344–366, 2021. doi:10.1038/s42254-021-00303-8.
- [40] M. Baldo and G. F. Burgio. The nuclear symmetry energy. *Prog. Part. Nucl. Phys.*, 91:203–258, 2016. [arXiv:1606.08838](https://arxiv.org/abs/1606.08838), doi:10.1016/j.ppnp.2016.06.006.
- [41] Marcello Baldo and Fiorella Burgio. Microscopic theory of the nuclear equation of state and neutron star structure. *Lect. Notes Phys.*, 578:1–29, 2001. [arXiv:nucl-th/0012014](https://arxiv.org/abs/nucl-th/0012014).
- [42] W. K. Baskerville. Making nuclei out of the Skyrme crystal. *Nucl. Phys. A*, 596:611–630, 1996. [arXiv:nucl-th/9510047](https://arxiv.org/abs/nucl-th/9510047), doi:10.1016/0375-9474(95)00432-7.
- [43] W. K. Baskerville. Quantization of global isospin in the Skyrme crystal. *Phys. Lett. B*, 380:106–112, 1996. [arXiv:hep-ph/9603216](https://arxiv.org/abs/hep-ph/9603216), doi:10.1016/0370-2693(96)00409-1.
- [44] Richard Battye, Nicholas S. Manton, and Paul Sutcliffe. Skyrmions and the alpha-particle model of nuclei. *Proc. Roy. Soc. Lond. A*, 463:261–279, 2007. [arXiv:hep-th/0605284](https://arxiv.org/abs/hep-th/0605284), doi:10.1098/rspa.2006.1767.
- [45] Richard Battye and Paul Sutcliffe. Skyrmions and the pion mass. *Nucl. Phys. B*, 705:384–400, 2005. [arXiv:hep-ph/0410157](https://arxiv.org/abs/hep-ph/0410157), doi:10.1016/j.nuclphysb.2004.11.018.
- [46] Richard Battye and Paul Sutcliffe. Skyrmions with massive pions. *Phys. Rev. C*, 73:055205, 2006. [arXiv:hep-th/0602220](https://arxiv.org/abs/hep-th/0602220), doi:10.1103/PhysRevC.73.055205.
- [47] Richard M. Battye and Paul M. Sutcliffe. Solitonic fullerenes. *Phys. Rev. Lett.*, 86:3989–3992, 2001. [arXiv:hep-th/0012215](https://arxiv.org/abs/hep-th/0012215), doi:10.1103/PhysRevLett.86.3989.

- [48] Gordon Baym, Tetsuo Hatsuda, Toru Kojo, Philip D. Powell, Yifan Song, and Tatsuyuki Takatsuka. From hadrons to quarks in neutron stars: a review. *Rept. Prog. Phys.*, 81(5):056902, 2018. [arXiv:1707.04966](https://arxiv.org/abs/1707.04966), doi:10.1088/1361-6633/aaaе14.
- [49] Marc-Olivier Beaudoin and Luc Marleau. Near-BPS Skyrmions: Constant baryon density. *Nucl. Phys. B*, 883:328–349, 2014. [arXiv:1305.4944](https://arxiv.org/abs/1305.4944), doi:10.1016/j.nuclphysb.2014.03.025.
- [50] Paulo Bedaque and Andrew W. Steiner. Sound velocity bound and neutron stars. *Phys. Rev. Lett.*, 114(3):031103, 2015. [arXiv:1408.5116](https://arxiv.org/abs/1408.5116), doi:10.1103/PhysRevLett.114.031103.
- [51] Abhijit Bhattacharyya, Igor N. Mishustin, and Walter Greiner. Deconfinement Phase Transition in Compact Stars : Maxwell vs. Gibbs Construction of the Mixed Phase. *J. Phys. G*, 37:025201, 2010. [arXiv:0905.0352](https://arxiv.org/abs/0905.0352), doi:10.1088/0954-3899/37/2/025201.
- [52] Jean-Paul Blaizot. Nuclear compressibilities. *Physics Reports*, 64(4):171–248, 1980.
- [53] Matthias Blau. *Lecture notes on general relativity*. Albert Einstein Center for Fundamental Physics Bern Germany, 2011.
- [54] U. Blom, K. Dannbom, and D.O. Riska. Hyperons as bound states in the skyrme model. *Nuclear Physics A*, 493(3):384–396, 1989. URL: <https://www.sciencedirect.com/science/article/pii/0375947489900936>, doi:[https://doi.org/10.1016/0375-9474\(89\)90093-6](https://doi.org/10.1016/0375-9474(89)90093-6).
- [55] A. R. Bodmer. Collapsed nuclei. *Phys. Rev. D*, 4:1601–1606, 1971. doi:10.1103/PhysRevD.4.1601.
- [56] Slavko Bogdanov et al. Snowmass 2021 Cosmic Frontier White Paper: The Dense Matter Equation of State and QCD Phase Transitions. In *Snowmass 2021*, 9 2022. [arXiv:2209.07412](https://arxiv.org/abs/2209.07412).
- [57] E. B. Bogomolny. Stability of Classical Solutions. *Sov. J. Nucl. Phys.*, 24:449, 1976.
- [58] Ignazio Bombaci. The Hyperon Puzzle in Neutron Stars. *JPS Conf. Proc.*, 17:101002, 2017. [arXiv:1601.05339](https://arxiv.org/abs/1601.05339), doi:10.7566/JPSCP.17.101002.
- [59] Silvano Bonazzola, Eric Gourgoulhon, and Jean-Alain Marck. Numerical

- models of irrotational binary neutron stars in general relativity. *Phys. Rev. Lett.*, 82:892–895, 1999. arXiv:gr-qc/9810072, doi:10.1103/PhysRevLett.82.892.
- [60] Eric Bonenfant and Luc Marleau. Nuclei as near BPS-Skyrmions. *Phys. Rev. D*, 82:054023, 2010. arXiv:1007.1396, doi:10.1103/PhysRevD.82.054023.
- [61] G. H. Bordbar, S. H. Hendi, and B. Eslam Panah. Neutron stars in Einstein- Λ gravity: the cosmological constant effects. *Eur. Phys. J. Plus*, 131(9):315, 2016. arXiv:1502.02929, doi:10.1140/epjp/i2016-16315-0.
- [62] Eric Braaten and Larry Carson. The Deuteron as a Soliton in the Skyrme Model. *Phys. Rev. Lett.*, 56:1897, 1986. doi:10.1103/PhysRevLett.56.1897.
- [63] Eric Braaten and Larry Carson. The Deuteron as a Toroidal Skyrmion. *Phys. Rev. D*, 38:3525, 1988. doi:10.1103/PhysRevD.38.3525.
- [64] Eric Braaten, Steve Townsend, and Larry Carson. Novel Structure of Static Multi - Soliton Solutions in the Skyrme Model. *Phys. Lett. B*, 235:147–152, 1990. doi:10.1016/0370-2693(90)90111-I.
- [65] C. Brans and R. H. Dicke. Mach’s principle and a relativistic theory of gravitation. *Phys. Rev.*, 124:925–935, Nov 1961. URL: <https://link.aps.org/doi/10.1103/PhysRev.124.925>, doi:10.1103/PhysRev.124.925.
- [66] D.M. Brink, H. Friedrich, A. Weiguny, and C.W. Wong. Investigation of the alpha-particle model for light nuclei. *Physics Letters B*, 33(2):143–146, 1970. URL: <https://www.sciencedirect.com/science/article/pii/0370269370902844>, doi:[https://doi.org/10.1016/0370-2693\(70\)90284-4](https://doi.org/10.1016/0370-2693(70)90284-4).
- [67] K. A. Brueckner, M. J. Giannoni, and R. J. Lombard. Statistical estimate of the breathing mode energy. *Phys. Lett. B*, 31:97–98, 1970. doi:10.1016/0370-2693(70)90119-X.
- [68] G. F. Burgio, H. J. Schulze, I. Vidana, and J. B. Wei. Neutron stars and the nuclear equation of state. *Prog. Part. Nucl. Phys.*, 120:103879, 2021. arXiv:2105.03747, doi:10.1016/j.ppnp.2021.103879.

- [69] G. F. Burgio and I. Vidana. The Equation of State of Nuclear Matter : from Finite Nuclei to Neutron Stars. *Universe*, 6(8):119, 2020. arXiv: 2007.04427, doi:10.3390/universe6080119.
- [70] A. Burrows. Supernova explosions in the universe. *Nature*, 403:727–733, 2000. doi:10.1038/35001501.
- [71] Adam Burrows and David Vartanyan. Core-Collapse Supernova Explosion Theory. *Nature*, 589(7840):29–39, 2021. arXiv:2009.14157, doi:10.1038/s41586-020-03059-w.
- [72] Curtis G. Callan, Jr., Kent Hornbostel, and Igor R. Klebanov. Baryon Masses in the Bound State Approach to Strangeness in the Skyrme Model. *Phys. Lett. B*, 202:269–275, 1988. doi:10.1016/0370-2693(88)90022-6.
- [73] Curtis G. Callan, Jr. and Igor R. Klebanov. Bound State Approach to Strangeness in the Skyrme Model. *Nucl. Phys. B*, 262:365–382, 1985. doi:10.1016/0550-3213(85)90292-5.
- [74] M. E. Caplan and C. J. Horowitz. Colloquium : Astromaterial science and nuclear pasta. *Rev. Mod. Phys.*, 89(4):041002, 2017. arXiv:1606.03646, doi:10.1103/RevModPhys.89.041002.
- [75] Monica Capone and Matteo Luca Ruggiero. Jumping from Metric $f(R)$ to Scalar-Tensor Theories and the relations between their post-Newtonian Parameters. *Class. Quant. Grav.*, 27:125006, 2010. arXiv:0910.0434, doi:10.1088/0264-9381/27/12/125006.
- [76] Salvatore Capozziello and Mariafelicia De Laurentis. Extended Theories of Gravity. *Phys. Rept.*, 509:167–321, 2011. arXiv:1108.6266, doi:10.1016/j.physrep.2011.09.003.
- [77] L. Castillejo, P. S. J. Jones, A. D. Jackson, J. J. M. Verbaarschot, and A. Jackson. Dense skyrmion systems. *Nucl. Phys. A*, 501:801–812, 1989. doi:10.1016/0375-9474(89)90161-9.
- [78] N. Chamel and P. Haensel. Physics of Neutron Star Crusts. *Living Rev. Rel.*, 11:10, 2008. arXiv:0812.3955, doi:10.12942/lrr-2008-10.
- [79] Katerina Chatzioannou. Neutron star tidal deformability and equation of state constraints. *Gen. Rel. Grav.*, 52(11):109, 2020. arXiv:2006.03168, doi:10.1007/s10714-020-02754-3.

- [80] M. Chemtob. Skyrme Model of Baryon Octet and Decuplet. *Nucl. Phys. B*, 256:600–608, 1985. doi:10.1016/0550-3213(85)90409-2.
- [81] A. Chodos, R. L. Jaffe, K. Johnson, C. B. Thorn, and V. F. Weisskopf. New extended model of hadrons. *Phys. Rev. D*, 9:3471–3495, Jun 1974. URL: <https://link.aps.org/doi/10.1103/PhysRevD.9.3471>, doi:10.1103/PhysRevD.9.3471.
- [82] H. T. Cromartie et al. Relativistic Shapiro delay measurements of an extremely massive millisecond pulsar. *Nature Astron.*, 4(1):72–76, 2019. arXiv:1904.06759, doi:10.1038/s41550-019-0880-2.
- [83] T. Damour and Gerhard Schaefer. Higher Order Relativistic Periastron Advances and Binary Pulsars. *Nuovo Cim. B*, 101:127, 1988. doi:10.1007/BF02828697.
- [84] Paweł Danielewicz and Jenny Lee. Symmetry Energy II: Isobaric Analog States. *Nucl. Phys. A*, 922:1–70, 2014. arXiv:1307.4130, doi:10.1016/j.nuclphysa.2013.11.005.
- [85] Antonio De Felice and Shinji Tsujikawa. $f(R)$ theories. *Living Rev. Rel.*, 13:3, 2010. arXiv:1002.4928, doi:10.12942/lrr-2010-3.
- [86] Cemsinan Deliduman, K. Y. Eksi, and Vildan Keles. Neutron star solutions in perturbative quadratic gravity. *JCAP*, 05:036, 2012. arXiv:1112.4154, doi:10.1088/1475-7516/2012/05/036.
- [87] Paul Demorest, Tim Pennucci, Scott Ransom, Mallory Roberts, and Jason Hessels. Shapiro Delay Measurement of A Two Solar Mass Neutron Star. *Nature*, 467:1081–1083, 2010. arXiv:1010.5788, doi:10.1038/nature09466.
- [88] G. H. Derrick. Comments on Nonlinear Wave Equations as Models for Elementary Particles. *Journal of Mathematical Physics*, 5(9):1252–1254, 12 2004. arXiv:https://pubs.aip.org/aip/jmp/article-pdf/5/9/1252/11363337/1252_1_online.pdf, doi:10.1063/1.1704233.
- [89] E. Epelbaum, J. Gegelia, N. Lange, U. G. Meißner, and M. V. Polyakov. Definition of Local Spatial Densities in Hadrons. *Phys. Rev. Lett.*, 129(1):012001, 2022. arXiv:2201.02565, doi:10.1103/PhysRevLett.129.012001.
- [90] Valerio Faraoni. Scalar field mass in generalized gravity. *Class. Quant.*

- Grav.*, 26:145014, 2009. arXiv:0906.1901, doi:10.1088/0264-9381/26/14/145014.
- [91] D. T. J. Feist, P. H. C. Lau, and N. S. Manton. Skyrmions up to Baryon Number 108. *Phys. Rev. D*, 87:085034, 2013. arXiv:1210.1712, doi:10.1103/PhysRevD.87.085034.
- [92] D. Finkelstein and J. Rubinstein. Connection between spin, statistics, and kinks. *J. Math. Phys.*, 9:1762–1779, 1968. doi:10.1063/1.1664510.
- [93] Eanna E. Flanagan and Tanja Hinderer. Constraining neutron star tidal Love numbers with gravitational wave detectors. *Phys. Rev. D*, 77:021502, 2008. arXiv:0709.1915, doi:10.1103/PhysRevD.77.021502.
- [94] Emmanuel Fonseca et al. The NANOGrav Nine-year Data Set: Mass and Geometric Measurements of Binary Millisecond Pulsars. *Astrophys. J.*, 832(2):167, 2016. arXiv:1603.00545, doi:10.3847/0004-637X/832/2/167.
- [95] Kenji Fukushima and Tetsuo Hatsuda. The phase diagram of dense QCD. *Rept. Prog. Phys.*, 74:014001, 2011. arXiv:1005.4814, doi:10.1088/0034-4885/74/1/014001.
- [96] Apratim Ganguly, Radouane Gannouji, Rituparno Goswami, and Subharthi Ray. Neutron stars in the Starobinsky model. *Phys. Rev. D*, 89(6):064019, 2014. arXiv:1309.3279, doi:10.1103/PhysRevD.89.064019.
- [97] Umesh Garg and Gianluca Colò. The compression-mode giant resonances and nuclear incompressibility. *Prog. Part. Nucl. Phys.*, 101:55–95, 2018. arXiv:1801.03672, doi:10.1016/j.ppnp.2018.03.001.
- [98] Riccardo Giacconi, Herbert Gursky, Frank R. Paolini, and Bruno B. Rossi. Evidence for x rays from sources outside the solar system. *Phys. Rev. Lett.*, 9:439–443, Dec 1962. URL: <https://link.aps.org/doi/10.1103/PhysRevLett.9.439>, doi:10.1103/PhysRevLett.9.439.
- [99] Norman K. Glendenning. First order phase transitions with more than one conserved charge: Consequences for neutron stars. *Phys. Rev. D*, 46:1274–1287, 1992. doi:10.1103/PhysRevD.46.1274.
- [100] Norman K Glendenning. *Compact stars: Nuclear physics, particle physics and general relativity*. Springer Science & Business Media, 2012.

- [101] Norman K. Glendenning and Jurgen Schaffner-Bielich. First order kaon condensate. *Phys. Rev. C*, 60:025803, 1999. [arXiv:astro-ph/9810290](https://arxiv.org/abs/astro-ph/9810290), doi:10.1103/PhysRevC.60.025803.
- [102] T. Gold. Rotating neutron stars as the origin of the pulsating radio sources. *Nature*, 218:731–732, 1968. doi:10.1038/218731a0.
- [103] Alfred S. Goldhaber and N. S. Manton. Maximal Symmetry of the Skyrme Crystal. *Phys. Lett. B*, 198:231–234, 1987. doi:10.1016/0370-2693(87)91502-4.
- [104] J. Goldstone. Field Theories with Superconductor Solutions. *Nuovo Cim.*, 19:154–164, 1961. doi:10.1007/BF02812722.
- [105] P. Grandclement, S. Bonazzola, E. Gourgoulhon, and J. A. Marck. A Multidomain spectral method for scalar and vectorial Poisson equations with noncompact sources. *J. Comput. Phys.*, 170:231–260, 2001. [arXiv:gr-qc/0003072](https://arxiv.org/abs/gr-qc/0003072), doi:10.1006/jcph.2001.6734.
- [106] Philippe Grandclement. Introduction to spectral methods. *EAS Publ. Ser.*, 21:153–180, 2006. [arXiv:gr-qc/0609020](https://arxiv.org/abs/gr-qc/0609020), doi:10.1051/eas:2006112.
- [107] Philippe Grandclement and Jerome Novak. Spectral methods for numerical relativity. *Living Rev. Rel.*, 12:1, 2009. [arXiv:0706.2286](https://arxiv.org/abs/0706.2286), doi:10.12942/lrr-2009-1.
- [108] Philippe Grandclement, Claire Somé, and Eric Gourgoulhon. Models of rotating boson stars and geodesics around them: new type of orbits. *Phys. Rev. D*, 90(2):024068, 2014. [arXiv:1405.4837](https://arxiv.org/abs/1405.4837), doi:10.1103/PhysRevD.90.024068.
- [109] S. K. Greif, K. Hebeler, J. M. Lattimer, C. J. Pethick, and A. Schwenk. Equation of state constraints from nuclear physics, neutron star masses, and future moment of inertia measurements. *Astrophys. J.*, 901(2):155, 2020. [arXiv:2005.14164](https://arxiv.org/abs/2005.14164), doi:10.3847/1538-4357/abaf55.
- [110] Sven Bjarke Gudnason. Loosening up the Skyrme model. *Phys. Rev. D*, 93(6):065048, 2016. [arXiv:1601.05024](https://arxiv.org/abs/1601.05024), doi:10.1103/PhysRevD.93.065048.
- [111] Sven Bjarke Gudnason and Chris Halcrow. A Smörgåsbord of Skyrmions. *JHEP*, 08:117, 2022. [arXiv:2202.01792](https://arxiv.org/abs/2202.01792), doi:10.1007/JHEP08(2022)

117.

- [112] Sven Bjarke Gudnason and Chris Halcrow. Quantum binding energies in the Skyrme model. 7 2023. [arXiv:2307.09272](#).
- [113] P. Haensel, A. Y. Potekhin, and D. G. Yakovlev. *Neutron stars 1: Equation of state and structure*, volume 326. Springer, New York, USA, 2007. [doi:10.1007/978-0-387-47301-7](#).
- [114] M. N. Harakeh, K. van der Borg, T. Ishimatsu, H. P. Morsch, A. van der Woude, and F. E. Bertrand. Direct Evidence for a New Giant Resonance at A-80-13 MeV in the Lead Region. *Phys. Rev. Lett.*, 38:676–679, 1977. [doi:10.1103/PhysRevLett.38.676](#).
- [115] Derek Harland. Topological energy bounds for the Skyrme and Faddeev models with massive pions. *Phys. Lett. B*, 728:518–523, 2014. [arXiv:1311.2403](#), [doi:10.1016/j.physletb.2013.11.062](#).
- [116] Derek Harland, Paul Leask, and Martin Speight. Skyrme crystals with massive pions. *J. Math. Phys.*, 64:103503, 2023. [arXiv:2305.14005](#), [doi:10.1063/5.0159674](#).
- [117] James B. Hartle. Slowly rotating relativistic stars. 1. Equations of structure. *Astrophys. J.*, 150:1005–1029, 1967. [doi:10.1086/149400](#).
- [118] Alexander Heger, C. L. Fryer, S. E. Woosley, N. Langer, and D. H. Hartmann. How massive single stars end their life. *Astrophys. J.*, 591:288–300, 2003. [arXiv:astro-ph/0212469](#), [doi:10.1086/375341](#).
- [119] Jason W. T. Hessels, Scott M. Ransom, Ingrid H. Stairs, Paulo Cesar Carvalho Freire, Victoria M. Kaspi, and Fernando Camilo. A radio pulsar spinning at 716 Hz. *Science*, 311:1901–1904, 2006. [arXiv:astro-ph/0601337](#), [doi:10.1126/science.1123430](#).
- [120] A. Hewish, S. J. Bell, J. D. H Pilkington, P. F. Scott, and R. A. Collins. Observation of a rapidly pulsating radio source. *Nature*, 217:709–713, 1968. [doi:10.1038/217709a0](#).
- [121] Tanja Hinderer, Benjamin D. Lackey, Ryan N. Lang, and Jocelyn S. Read. Tidal deformability of neutron stars with realistic equations of state and their gravitational wave signatures in binary inspiral. *Phys. Rev. D*, 81:123016, 2010. [arXiv:0911.3535](#), [doi:10.1103/PhysRevD.81.123016](#).
- [122] G. Holzwarth and B. Schwesinger. Baryons in the Skyrme Model. *Rept.*

- Prog. Phys.*, 49:825, 1986. doi:10.1088/0034-4885/49/8/001.
- [123] C. J. Horowitz, J. Piekarewicz, and Brendan Reed. Insights into nuclear saturation density from parity violating electron scattering. *Phys. Rev. C*, 102(4):044321, 2020. arXiv:2007.07117, doi:10.1103/PhysRevC.102.044321.
- [124] Conor J. Houghton, Nicholas S. Manton, and Paul M. Sutcliffe. Rational maps, monopoles and Skyrmions. *Nucl. Phys. B*, 510:507–537, 1998. arXiv:hep-th/9705151, doi:10.1016/S0550-3213(97)00619-6.
- [125] S. Huth et al. Constraining Neutron-Star Matter with Microscopic and Macroscopic Collisions. *Nature*, 606:276–280, 2022. arXiv:2107.06229, doi:10.1038/s41586-022-04750-w.
- [126] Elizabeth Ellen Jenkins, Aneesh V. Manohar, and Mark B. Wise. Chiral perturbation theory for vector mesons. *Phys. Rev. Lett.*, 75:2272–2275, 1995. arXiv:hep-ph/9506356, doi:10.1103/PhysRevLett.75.2272.
- [127] Nan Jiang and Kent Yagi. Analytic I-Love-C relations for realistic neutron stars. *Phys. Rev. D*, 101(12):124006, 2020. arXiv:2003.10498, doi:10.1103/PhysRevD.101.124006.
- [128] D. B. Kaplan and A. E. Nelson. Kaon Condensation in Dense Matter. *Nucl. Phys. A*, 479:273c, 1988. doi:10.1016/0375-9474(88)90442-3.
- [129] Ryotaro Kase and Shinji Tsujikawa. Neutron stars in $f(R)$ gravity and scalar-tensor theories. *JCAP*, 09:054, 2019. arXiv:1906.08954, doi:10.1088/1475-7516/2019/09/054.
- [130] Igor R. Klebanov. Nuclear Matter in the Skyrme Model. *Nucl. Phys. B*, 262:133–143, 1985. doi:10.1016/0550-3213(85)90068-9.
- [131] Igor R. Klebanov. Strangeness in the Skyrme model. In *NATO ASI: Hadrons and Hadronic Matter*, 12 1989.
- [132] Vladimir B. Kopeliovich. The Bubbles of matter from multiskyrmions. *JETP Lett.*, 73:587–591, 2001. arXiv:hep-ph/0105102, doi:10.1134/1.1392417.
- [133] Vladimir B. Kopeliovich. MultiSkyrmions and baryonic bags. *J. Phys. G*, 28:103–120, 2002. arXiv:hep-ph/0109229, doi:10.1088/0954-3899/28/1/308.

- [134] Steffen Krusch. Homotopy of rational maps and the quantization of skyrmions. *Annals Phys.*, 304:103–127, 2003. [arXiv:hep-th/0210310](https://arxiv.org/abs/hep-th/0210310), doi:10.1016/S0003-4916(03)00014-9.
- [135] Steffen Krusch. Finkelstein–Rubinstein constraints for the Skyrme model with pion masses. *Proc. Roy. Soc. Lond. A*, 462:2001–2016, 2006. [arXiv: hep-th/0509094](https://arxiv.org/abs/hep-th/0509094), doi:10.1098/rspa.2006.1664.
- [136] M. Kugler and S. Shtrikman. A new skyrmion crystal. *Phys. Lett. B*, 208:491–494, 1988. doi:10.1016/0370-2693(88)90653-3.
- [137] M. Lacombe, B. Loiseau, J. M. Richard, R. Vinh Mau, J. Côté, P. Pirès, and R. de Tourreil. Parametrization of the paris $n - n$ potential. *Phys. Rev. C*, 21:861–873, Mar 1980. URL: <https://link.aps.org/doi/10.1103/PhysRevC.21.861>, doi:10.1103/PhysRevC.21.861.
- [138] Philippe Landry, Reed Essick, and Katerina Chatzioannou. Nonparametric constraints on neutron star matter with existing and upcoming gravitational wave and pulsar observations. *Phys. Rev. D*, 101(12):123007, 2020. [arXiv:2003.04880](https://arxiv.org/abs/2003.04880), doi:10.1103/PhysRevD.101.123007.
- [139] J. M. Lattimer. Neutron Stars and the Nuclear Matter Equation of State. *Ann. Rev. Nucl. Part. Sci.*, 71:433–464, 2021. doi:10.1146/annurev-nucl-102419-124827.
- [140] J. M. Lattimer and M. Prakash. The physics of neutron stars. *Science*, 304:536–542, 2004. [arXiv:astro-ph/0405262](https://arxiv.org/abs/astro-ph/0405262), doi:10.1126/science.1090720.
- [141] James M. Lattimer. Symmetry energy in nuclei and neutron stars. *Nucl. Phys. A*, 928:276–295, 2014. doi:10.1016/j.nuclphysa.2014.04.008.
- [142] James M Lattimer. A rapidly cooling neutron star. *Physics*, 11:42, 2018.
- [143] Hee-Jung Lee, Byung-Yoon Park, Dong-Pil Min, Mannque Rho, and Vicente Vento. A Unified approach to high density: Pion fluctuations in skyrmion matter. *Nucl. Phys. A*, 723:427–446, 2003. [arXiv: hep-ph/0302019](https://arxiv.org/abs/hep-ph/0302019), doi:10.1016/S0375-9474(03)01452-0.
- [144] Bao-An Li, Bao-Jun Cai, Wen-Jie Xie, and Nai-Bo Zhang. Progress in Constraining Nuclear Symmetry Energy Using Neutron Star Observables Since GW170817. *Universe*, 7(6):182, 2021. [arXiv:2105.04629](https://arxiv.org/abs/2105.04629), doi:10.3390/universe7060182.

- [145] Jia Jie Li, Armen Sedrakian, and Fridolin Weber. Competition between delta isobars and hyperons and properties of compact stars. *Phys. Lett. B*, 783:234–240, 2018. [arXiv:1803.03661](https://arxiv.org/abs/1803.03661), doi:10.1016/j.physletb.2018.06.051.
- [146] Z. H. Li, U. Lombardo, H.-J. Schulze, and W. Zuo. Consistent nucleon-nucleon potentials and three-body forces. *Phys. Rev. C*, 77:034316, Mar 2008. URL: <https://link.aps.org/doi/10.1103/PhysRevC.77.034316>, doi:10.1103/PhysRevC.77.034316.
- [147] M. Loewe, S. Mendizabal, and J. C. Rojas. Skyrme model and isospin chemical potential. *Phys. Lett. B*, 632:512–516, 2006. [arXiv:hep-ph/0508038](https://arxiv.org/abs/hep-ph/0508038), doi:10.1016/j.physletb.2005.10.082.
- [148] Nana Ma, Chris James Halcrow, and Hongfei Zhang. Effect of the Coulomb energy on Skyrmions. *Phys. Rev. C*, 99(4):044312, 2019. [arXiv:1901.06025](https://arxiv.org/abs/1901.06025), doi:10.1103/PhysRevC.99.044312.
- [149] Yong-Liang Ma and Masayasu Harada. Lecture notes on the Skyrme model. 4 2016. [arXiv:1604.04850](https://arxiv.org/abs/1604.04850).
- [150] R. Machleidt and D. R. Entem. Chiral effective field theory and nuclear forces. *Phys. Rept.*, 503:1–75, 2011. [arXiv:1105.2919](https://arxiv.org/abs/1105.2919), doi:10.1016/j.physrep.2011.02.001.
- [151] Olga V. Manko, Nicholas S. Manton, and Stephen W. Wood. Light nuclei as quantized skyrmions. *Phys. Rev. C*, 76:055203, 2007. [arXiv:0707.0868](https://arxiv.org/abs/0707.0868), doi:10.1103/PhysRevC.76.055203.
- [152] N. S. Manton. A Remark on the Scattering of BPS Monopoles. *Phys. Lett. B*, 110:54–56, 1982. doi:10.1016/0370-2693(82)90950-9.
- [153] N. S. Manton. Is the $B = 2$ Skyrmion Axially Symmetric? *Phys. Lett. B*, 192:177, 1987. doi:10.1016/0370-2693(87)91162-2.
- [154] N. S. Manton and P. Sutcliffe. *Topological solitons*. Cambridge Monographs on Mathematical Physics. Cambridge University Press, 2004. doi:10.1017/CBO9780511617034.
- [155] Nicholas S. Manton. Scaling Identities for Solitons beyond Derrick’s Theorem. *J. Math. Phys.*, 50:032901, 2009. [arXiv:0809.2891](https://arxiv.org/abs/0809.2891), doi:10.1063/1.3089582.

- [156] Nicholas S. Manton. *Skyrmions – A Theory of Nuclei*. World Scientific, 3 2022. doi:10.1142/q0368.
- [157] Nicholas S. Manton and Bernard M. A. G. Piette. Understanding skyrmions using rational maps. *Prog. Math.*, 201:469–479, 2001. arXiv: hep-th/0008110, doi:10.1007/978-3-0348-8268-2_27.
- [158] Toshiki Maruyama, Toshitaka Tatsumi, Dmitri . N. Voskresensky, Tomonori Tanigawa, and Satoshi Chiba. Nuclear pasta structures and the charge screening effect. *Phys. Rev. C*, 72:015802, 2005. arXiv: nucl-th/0503027, doi:10.1103/PhysRevC.72.015802.
- [159] Larry McLerran and Robert D. Pisarski. Phases of cold, dense quarks at large N_c . *Nucl. Phys. A*, 796:83–100, 2007. arXiv:0706.2191, doi: 10.1016/j.nuclphysa.2007.08.013.
- [160] Larry McLerran and Sanjay Reddy. Quarkyonic Matter and Neutron Stars. *Phys. Rev. Lett.*, 122(12):122701, 2019. arXiv:1811.12503, doi: 10.1103/PhysRevLett.122.122701.
- [161] U. G. Meissner and I. Zahed. Skyrmions in the Presence of Vector Mesons. *Phys. Rev. Lett.*, 56:1035, 1986. doi:10.1103/PhysRevLett.56.1035.
- [162] Ulf G. Meissner. Low-Energy Hadron Physics from Effective Chiral Lagrangians with Vector Mesons. *Phys. Rept.*, 161:213, 1988. doi: 10.1016/0370-1573(88)90090-7.
- [163] Ulf G. Meissner, Norbert Kaiser, Andreas Wirzba, and Wolfram Weise. Skyrmions With ρ and ω Mesons as Dynamical Gauge Bosons. *Phys. Rev. Lett.*, 57:1676, 1986. doi:10.1103/PhysRevLett.57.1676.
- [164] M. C. Miller et al. PSR J0030+0451 Mass and Radius from NICER Data and Implications for the Properties of Neutron Star Matter. *Astrophys. J. Lett.*, 887(1):L24, 2019. arXiv:1912.05705, doi:10.3847/2041-8213/ab50c5.
- [165] M. C. Miller et al. The Radius of PSR J0740+6620 from NICER and XMM-Newton Data. *Astrophys. J. Lett.*, 918(2):L28, 2021. arXiv:2105.06979, doi:10.3847/2041-8213/ac089b.
- [166] Charles W. Misner, K. S. Thorne, and J. A. Wheeler. *Gravitation*. W. H. Freeman, San Francisco, 1973.

- [167] Joachim Naf and Philippe Jetzer. On the $1/c$ Expansion of $f(R)$ Gravity. *Phys. Rev. D*, 81:104003, 2010. [arXiv:1004.2014](https://arxiv.org/abs/1004.2014), doi:10.1103/PhysRevD.81.104003.
- [168] Yoichiro Nambu. Quasiparticles and Gauge Invariance in the Theory of Superconductivity. *Phys. Rev.*, 117:648–663, 1960. doi:10.1103/PhysRev.117.648.
- [169] Carlos Naya and Paul Sutcliffe. Skyrmions and clustering in light nuclei. *Phys. Rev. Lett.*, 121(23):232002, 2018. [arXiv:1811.02064](https://arxiv.org/abs/1811.02064), doi:10.1103/PhysRevLett.121.232002.
- [170] John A. Nelder and Roger Mead. A simplex method for function minimization. *Comput. J.*, 7:308–313, 1965.
- [171] S. G. Nelmès and B. M. A. G. Piette. Phase Transition and Anisotropic Deformations of Neutron Star Matter. *Phys. Rev. D*, 85:123004, 2012. [arXiv:1204.0910](https://arxiv.org/abs/1204.0910), doi:10.1103/PhysRevD.85.123004.
- [172] Susan Nelmès and Bernard M. A. G. Piette. Skyrmion stars and the multilayered rational map ansatz. *Phys. Rev. D*, 84:085017, 2011. doi:10.1103/PhysRevD.84.085017.
- [173] Yurii Nesterov. A method for unconstrained convex minimization problem with the rate of convergence $\mathcal{O}(1/k^2)$. In *Dokl. Akad. Nauk. SSSR*, volume 269, page 543, 1983.
- [174] Yurii Nesterov. *Introductory lectures on convex optimization: A basic course*, volume 87. Springer Science & Business Media, 2003.
- [175] Shin’ichi Nojiri and Sergei D. Odintsov. Unified cosmic history in modified gravity: from F(R) theory to Lorentz non-invariant models. *Phys. Rept.*, 505:59–144, 2011. [arXiv:1011.0544](https://arxiv.org/abs/1011.0544), doi:10.1016/j.physrep.2011.04.001.
- [176] Jerome Novak. Spherical neutron star collapse in tensor-scalar theory of gravity. *Phys. Rev. D*, 57:4789–4801, 1998. [arXiv:gr-qc/9707041](https://arxiv.org/abs/gr-qc/9707041), doi:10.1103/PhysRevD.57.4789.
- [177] E. M. Nyman and D. O. Riska. Low-energy Properties of Baryons in the Skyrme Model. *Rept. Prog. Phys.*, 53:1137–1182, 1990. doi:10.1088/0034-4885/53/9/001.

- [178] Anne Marie Nzioki, Rituparno Goswami, and Peter K. S. Dunsby. Jebsen–Birkhoff theorem and its stability in $f(R)$ gravity. *Phys. Rev. D*, 89(6):064050, 2014. [arXiv:1312.6790](https://arxiv.org/abs/1312.6790), doi:10.1103/PhysRevD.89.064050.
- [179] M. Oertel, M. Hempel, T. Klähn, and S. Typel. Equations of state for supernovae and compact stars. *Rev. Mod. Phys.*, 89(1):015007, 2017. [arXiv:1610.03361](https://arxiv.org/abs/1610.03361), doi:10.1103/RevModPhys.89.015007.
- [180] M. Oertel, M. Hempel, T. Klähn, and S. Typel. Equations of state for supernovae and compact stars. *Rev. Mod. Phys.*, 89:015007, Mar 2017. URL: <https://link.aps.org/doi/10.1103/RevModPhys.89.015007>, doi:10.1103/RevModPhys.89.015007.
- [181] J Robert Oppenheimer and George M Volkoff. On massive neutron cores. *Physical Review*, 55(4):374, 1939.
- [182] M. Ostrogradsky. Mémoires sur les équations différentielles, relatives au problème des isopérimètres. *Mem. Acad. St. Petersbourg*, 6(4):385–517, 1850.
- [183] Feryal Özal and Paulo Freire. Masses, Radii, and the Equation of State of Neutron Stars. *Ann. Rev. Astron. Astrophys.*, 54:401–440, 2016. [arXiv:1603.02698](https://arxiv.org/abs/1603.02698), doi:10.1146/annurev-astro-081915-023322.
- [184] Frits Paerels. Pressure broadening of absorption lines in neutron star atmospheres and prospects for measuring neutron star masses and radii. *The Astrophysical Journal*, 476(1):L47, 1997.
- [185] L. Paulucci, Efrain J. Ferrer, Vivian de la Incera, and J. E. Horvath. Equation of state for the magnetic-color-flavor-locked phase and its implications for compact star models. *Phys. Rev. D*, 83:043009, Feb 2011. URL: <https://link.aps.org/doi/10.1103/PhysRevD.83.043009>, doi:10.1103/PhysRevD.83.043009.
- [186] C. J. Pethick and D. G. Ravenhall. Matter at large neutron excess and the physics of neutron-star crusts. *Ann. Rev. Nucl. Part. Sci.*, 45:429–484, 1995. doi:10.1146/annurev.ns.45.120195.002241.
- [187] J. Piekarewicz and G. Toledo Sanchez. Proton fraction in the inner neutron-star crust. *Phys. Rev. C*, 85:015807, 2012. [arXiv:1107.2638](https://arxiv.org/abs/1107.2638), doi:10.1103/PhysRevC.85.015807.

- [188] Bernard M. A. G. Piette and Gavin I. Probert. Towards skyrmion stars: Large baryon configurations in the Einstein–Skyrme model. *Phys. Rev. D*, 75:125023, 2007. [arXiv:0704.0527](https://arxiv.org/abs/0704.0527), doi:10.1103/PhysRevD.75.125023.
- [189] Jose A. Pons, Sanjay Reddy, Paul J. Ellis, Madappa Prakash, and James M. Lattimer. Kaon condensation in proto neutron star matter. *Phys. Rev. C*, 62:035803, 2000. [arXiv:nucl-th/0003008](https://arxiv.org/abs/nucl-th/0003008), doi:10.1103/PhysRevC.62.035803.
- [190] M. K. Prasad and Charles M. Sommerfield. Exact classical solution for the 't Hooft monopole and the Julia–Zee dyon. *Phys. Rev. Lett.*, 35:760–762, Sep 1975. URL: <https://link.aps.org/doi/10.1103/PhysRevLett.35.760>, doi:10.1103/PhysRevLett.35.760.
- [191] Michal Praszalowicz. A Comment on the Phenomenology of the SU(3) Skyrme Model. *Phys. Lett. B*, 158:264–269, 1985. doi:10.1016/0370-2693(85)90968-2.
- [192] William H. Press, Saul A. Teukolsky, William T. Vetterling, and Brian P. Flannery. Numerical Recipes in FORTRAN: The Art of Scientific Computing. 9 1992.
- [193] R. Rajaraman. *Solitons and instantons. An introduction to solitons and instantons in Quantum Field Theory*. 1982.
- [194] Angels Ramos, Jurgen Schaffner-Bielich, and Jochen Wambach. Kaon condensation in neutron stars. *Lect. Notes Phys.*, 578:175–202, 2001. [arXiv:nucl-th/0011003](https://arxiv.org/abs/nucl-th/0011003).
- [195] Luciano Rezzolla, Elias R. Most, and Lukas R. Weih. Using gravitational-wave observations and quasi-universal relations to constrain the maximum mass of neutron stars. *Astrophys. J. Lett.*, 852(2):L25, 2018. [arXiv:1711.00314](https://arxiv.org/abs/1711.00314), doi:10.3847/2041-8213/aaa401.
- [196] Luciano Rezzolla, Pierre Pizzochero, David Ian Jones, Nanda Rea, and Isaac Vidaña, editors. *The Physics and Astrophysics of Neutron Stars*, volume 457. Springer, 2018. doi:10.1007/978-3-319-97616-7.
- [197] Thomas E. Riley et al. A NICER View of PSR J0030+0451: Millisecond Pulsar Parameter Estimation. *Astrophys. J. Lett.*, 887(1):L21, 2019. [arXiv:1912.05702](https://arxiv.org/abs/1912.05702), doi:10.3847/2041-8213/ab481c.
- [198] Thomas E. Riley et al. A NICER View of the Massive Pulsar PSR

- J0740+6620 Informed by Radio Timing and XMM-Newton Spectroscopy. *Astrophys. J. Lett.*, 918(2):L27, 2021. [arXiv:2105.06980](#), doi:10.3847/2041-8213/ac0a81.
- [199] Francesca Sammarruca. The Symmetry Energy: Current Status of Ab Initio Predictions vs. Empirical Constraints. *Symmetry*, 15(2):450, 2023. [arXiv:2212.13304](#), doi:10.3390/sym15020450.
- [200] Fulvio Sbisà, Pedro O. Baqui, Tays Miranda, Sergio E. Jorás, and Oliver F. Piattella. Neutron star masses in R^2 -gravity. *Phys. Dark Univ.*, 27:100411, 2020. [arXiv:1907.08714](#), doi:10.1016/j.dark.2019.100411.
- [201] Jürgen Schaffner-Bielich. *Compact star physics*. Cambridge University Press, 2020.
- [202] J. Schechter and H. Weigel. The Skyrme model for baryons. pages 337–369, 7 1999. [arXiv:hep-ph/9907554](#).
- [203] Mark A. Scheel, Michael Boyle, Tony Chu, Lawrence E. Kidder, Keith D. Matthews, and Harald P. Pfeiffer. High-accuracy waveforms for binary black hole inspiral, merger, and ringdown. *Phys. Rev. D*, 79:024003, 2009. [arXiv:0810.1767](#), doi:10.1103/PhysRevD.79.024003.
- [204] Andreas Schmitt. *Dense matter in compact stars: A pedagogical introduction*, volume 811. 2010. [arXiv:1001.3294](#), doi:10.1007/978-3-642-12866-0.
- [205] A. S. Schneider, C. J. Horowitz, J. Hughto, and D. K. Berry. Nuclear “pasta” formation. *Phys. Rev. C*, 88(6):065807, 2013. [arXiv:1307.1678](#), doi:10.1103/PhysRevC.88.065807.
- [206] Irwin I. Shapiro. Fourth test of general relativity. *Phys. Rev. Lett.*, 13:789–791, Dec 1964. URL: <https://link.aps.org/doi/10.1103/PhysRevLett.13.789>, doi:10.1103/PhysRevLett.13.789.
- [207] S. L. Shapiro and S. A. Teukolsky. *Black holes, white dwarfs, and neutron stars: The physics of compact objects*. 1983.
- [208] B. K. Sharma, M. Centelles, X. Viñas, M. Baldo, and G. F. Burgio. Unified equation of state for neutron stars on a microscopic basis. *Astron. Astrophys.*, 584:A103, 2015. [arXiv:1506.00375](#), doi:10.1051/0004-6361/201526642.
- [209] J. Silva Lobo. Deformed Skyrme Crystals. *JHEP*, 10:029, 2010. [arXiv:](#)

- 1010.0619, doi:10.1007/JHEP10(2010)029.
- [210] T. H. R. Skyrme. A Nonlinear field theory. *Proc. Roy. Soc. Lond. A*, 260:127–138, 1961. doi:10.1098/rspa.1961.0018.
- [211] T. H. R. Skyrme. A Unified Field Theory of Mesons and Baryons. *Nucl. Phys.*, 31:556–569, 1962. doi:10.1016/0029-5582(62)90775-7.
- [212] D. T. Son and Misha A. Stephanov. QCD at finite isospin density. *Phys. Rev. Lett.*, 86:592–595, 2001. arXiv:hep-ph/0005225, doi:10.1103/PhysRevLett.86.592.
- [213] Thomas P. Sotiriou and Valerio Faraoni. $f(R)$ Theories Of Gravity. *Rev. Mod. Phys.*, 82:451–497, 2010. arXiv:0805.1726, doi:10.1103/RevModPhys.82.451.
- [214] H. C. Spruit. Origin of neutron star magnetic fields. *AIP Conf. Proc.*, 983(1):391–398, 2008. arXiv:0711.3650, doi:10.1063/1.2900262.
- [215] Alexei A. Starobinsky. A New Type of Isotropic Cosmological Models Without Singularity. *Phys. Lett. B*, 91:99–102, 1980. doi:10.1016/0370-2693(80)90670-X.
- [216] Kalin V. Staykov, Daniela D. Doneva, Stoytcho S. Yazadjiev, and Kostas D. Kokkotas. Slowly rotating neutron and strange stars in R^2 gravity. *JCAP*, 10:006, 2014. arXiv:1407.2180, doi:10.1088/1475-7516/2014/10/006.
- [217] T. E. Sterne. The equilibrium theory of the abundance of the elements. *Phys. Rev.*, 43:585–586, Apr 1933. URL: <https://link.aps.org/doi/10.1103/PhysRev.43.585.2>, doi:10.1103/PhysRev.43.585.2.
- [218] Paul Sutcliffe. Skyrmions, instantons and holography. *JHEP*, 08:019, 2010. arXiv:1003.0023, doi:10.1007/JHEP08(2010)019.
- [219] Paul Sutcliffe. Skyrmions in a truncated BPS theory. *JHEP*, 04:045, 2011. arXiv:1101.2402, doi:10.1007/JHEP04(2011)045.
- [220] Gerard 't Hooft. A Planar Diagram Theory for Strong Interactions. *Nucl. Phys. B*, 72:461, 1974. doi:10.1016/0550-3213(74)90154-0.
- [221] I. Tews, T. Krüger, K. Hebeler, and A. Schwenk. Neutron matter at next-to-next-to-next-to-leading order in chiral effective field theory. *Phys. Rev. Lett.*, 110(3):032504, 2013. arXiv:1206.0025, doi:10.1103/

- PhysRevLett.110.032504.
- [222] Kip S. Thorne and James B. Hartle. Laws of motion and precession for black holes and other bodies. *Phys. Rev. D*, 31:1815–1837, 1984. doi: 10.1103/PhysRevD.31.1815.
 - [223] Richard C Tolman. Static solutions of Einstein’s field equations for spheres of fluid. *Physical Review*, 55(4):364, 1939.
 - [224] Laura Tolos and Laura Fabbietti. Strangeness in Nuclei and Neutron Stars. *Prog. Part. Nucl. Phys.*, 112:103770, 2020. arXiv:2002.09223, doi:10.1016/j.ppnp.2020.103770.
 - [225] Isaac Vidaña. Hyperons in Neutron Stars. *J. Phys. Conf. Ser.*, 668(1):012031, 2016. arXiv:1509.03587, doi:10.1088/1742-6596/668/1/012031.
 - [226] Noel J Walkington. Nesterov’s method for convex optimization. *SIAM Review*, 65(2):539–562, 2023.
 - [227] M. Warda, X. Vinas, X. Roca-Maza, and M. Centelles. Neutron skin thickness in droplet model with surface width dependence: Indications of softness of the nuclear symmetry energy. *Phys. Rev. C*, 80:024316, 2009. arXiv:0906.0932, doi:10.1103/PhysRevC.80.024316.
 - [228] Fridolin Weber, Alexander Ho, Rodrigo P. Negreiros, and Philip Rosenfield. Strangeness in Neutron Stars. *Int. J. Mod. Phys. D*, 16:231–245, 2007. arXiv:astro-ph/0604422, doi:10.1142/S0218271807009966.
 - [229] Steven Weinberg. Gravitation and cosmology: principles and applications of the general theory of relativity. 1972.
 - [230] J. Wess and B. Zumino. Consequences of anomalous ward identities. *Physics Letters B*, 37(1):95–97, 1971. URL: <https://www.sciencedirect.com/science/article/pii/037026937190582X>, doi: [https://doi.org/10.1016/0370-2693\(71\)90582-X](https://doi.org/10.1016/0370-2693(71)90582-X).
 - [231] Robert B. Wiringa, V. G. J. Stoks, and R. Schiavilla. An Accurate nucleon-nucleon potential with charge independence breaking. *Phys. Rev. C*, 51:38–51, 1995. arXiv:nucl-th/9408016, doi:10.1103/PhysRevC.51.38.
 - [232] Edward Witten. Current Algebra, Baryons, and Quark Confinement. *Nucl. Phys. B*, 223:433–444, 1983. doi:10.1016/0550-3213(83)

90064–0.

- [233] Edward Witten. Global Aspects of Current Algebra. *Nucl. Phys. B*, 223:422–432, 1983. doi:10.1016/0550-3213(83)90063-9.
- [234] Edward Witten. Cosmic Separation of Phases. *Phys. Rev. D*, 30:272–285, 1984. doi:10.1103/PhysRevD.30.272.
- [235] Richard P. Woodard. Avoiding dark energy with $1/r$ modifications of gravity. *Lect. Notes Phys.*, 720:403–433, 2007. arXiv:astro-ph/0601672, doi:10.1007/978-3-540-71013-4_14.
- [236] Jun Xu, Wen-Jie Xie, and Bao-An Li. Bayesian inference of nuclear symmetry energy from measured and imagined neutron skin thickness in $^{116,118,120,122,124,130,132}\text{Sn}$, ^{208}Pb , and ^{48}Ca . *Phys. Rev. C*, 102:044316, Oct 2020. URL: <https://link.aps.org/doi/10.1103/PhysRevC.102.044316>, doi:10.1103/PhysRevC.102.044316.
- [237] Kent Yagi and Nicolas Yunes. I-Love-Q Relations in Neutron Stars and their Applications to Astrophysics, Gravitational Waves and Fundamental Physics. *Phys. Rev. D*, 88(2):023009, 2013. arXiv:1303.1528, doi:10.1103/PhysRevD.88.023009.
- [238] T. Yazdizadeh, G. H. Bordbar, and B. Eslam Panah. The structure of hybrid neutron star in Einstein- Λ gravity. *Physics of the Dark Universe*, 35:100982, March 2022. arXiv:1902.04887, doi:10.1016/j.dark.2022.100982.
- [239] D. H. Youngblood, C. M. Rozsa, J. M. Moss, D. R. Brown, and J. D. Bronson. Isoscalar breathing-mode state in ^{144}Sm and ^{208}Pb . *Phys. Rev. Lett.*, 39:1188–1191, Nov 1977. URL: <https://link.aps.org/doi/10.1103/PhysRevLett.39.1188>, doi:10.1103/PhysRevLett.39.1188.
- [240] I. Zahed and G. E. Brown. The Skyrme Model. *Phys. Rept.*, 142:1–102, 1986. doi:10.1016/0370-1573(86)90142-0.



IGFAE

Instituto Galego de Física de Altas Enerxías

The present thesis aims to develop a realistic description of highly dense nuclear matter and neutron stars within the Skyrme model. For this purpose, the properties of neutron stars and the problem of ultra-dense nuclear matter are introduced.

The main features of the Skyrme model and the previous attempts to reproduce neutron stars are reviewed to introduce a physically motivated generalization of the model that yields remarkable results for the neutron stars observables.

We establish the basis for a consistent description of infinite nuclear matter at each range of densities and perform the standard quantization procedure to account for the isospin-asymmetric effects. Finally, we consider the kaon condensation in the neutron star cores, and we include ρ mesons as a viable solution to the compression modulus problem.